PAUL SCHERRER INSTITUT

PSI

ETH Eidgenössische
Technische Hochschule
Zürich

Diss. No. 18400

Charge storage and aging phenomena in
electrochemical double layer capacitors

Patrick Ruch

Cuvillier Verlag Göttingen
Internationaler wissenschaftlicher Fachverlag

DISS. ETH NO. 18400

CHARGE STORAGE AND AGING PHENOMENA IN ELECTROCHEMICAL DOUBLE LAYER CAPACITORS

A dissertation submitted to

ETH ZURICH

for the degree of

Doctor of Sciences

presented by

PATRICK W. RUCH

M.Sc., ETH ZURICH

Born on March 17th, 1981

Citizen of Germany / USA

accepted on the recommendation of

Prof. Alexander Wokaun
Dr. Rüdiger Kötz
Prof. Reinhard Nesper

2009

Le savant doit ordonner; on fait la science avec des faits comme une maison avec des pierres; mais une accumulation de faits n'est pas plus une science qu'un tas de pierres n'est une maison.

The scientist must set in order. Just as houses are made of stones, so is science made of facts; but a pile of stones is not a house and a collection of facts is not necessarily science.

Henri Poincaré (1854–1912)
La Science et l'Hypothèse (1902)

Summary

The storage of electrical charge in electrochemical double layer capacitors (EDLCs) is ideal for short-term energy storage in stationary and mobile or portable applications in which intermittent power demands and reliability are of prime importance. A significant limitation of the currently employed EDLC technology is the low energy density, whereby a promising approach towards increasing the energy content of present EDLC systems is a widening of the operational voltage window. However, a significant reduction of the device lifetime is observed under elevated voltage conditions.

In the present work, the contribution of interfacial charge transfer towards charge storage in and aging of EDLCs based on non-aqueous electrolyte solutions at elevated voltages is considered. The possible charge transfer mechanisms are thus conveniently classified as ionic or electronic. Through an improved understanding of these processes, possible routes for optimizing charge storage and avoiding aging at elevated voltages may be developed.

A coconut shell derived activated carbon was selected as electrode material in non-aqueous solutions of $1\,M\ Et_4NBF_4$ in acetonitrile (AN) and in propylene carbonate (PC). Through an electrochemical characterization of these systems via cyclic voltammetry, the potential regions of essentially ideal polarizability could be identified and separated from the regions in which irreversible charge transfer took place.

The region of ideal polarizability was characterized by in situ Raman spectroscopy, electrical resistance measurements and electrochemical dilatometry. The results are discussed in the context of those obtained on single-walled carbon nanotubes (SWCNTs) in order to establish a comparison with a high surface area electrode material of well-defined geometric and electronic structure. Fundamental differences in the reversible doping behavior of the two materials were observed, indicating that a conceptual representation of the carbonaceous framework of the activated carbon must take into account the presence of significant disorder and deviations from the idealized assembly of graphene fragments. Differences in the capacitive charging behavior could be attributed to the different electronic density of states of the materials, thus

highlighting the importance of the electronic structure of carbonaceous electrodes for the storage of charge in EDLCs.

In order to investigate the possibility of ionic charge transfer in EDLC systems, the contribution of ion insertion processes to the charge storage and electrode degradation of both graphitic and activated carbon electrodes was studied using in situ electrochemical dilatometry, X-ray diffraction and small-angle X-ray scattering. It was found that the insertion of ions into graphite proceeds via well-defined intercalation sites, with the electrochemical intercalation of BF_4^- leading to staging and solvent cointercalation for both AN- and PC-based electrolytes. Further, the crystallinity of the graphitic electrodes was found to degrade markedly in the direction perpendicular to the graphene sheets, which could largely be attributed to the electrochemical decomposition of intercalated electrolyte species, i.e. a combination of ionic and electronic charge transfer.

On the the other hand, ion insertion processes in activated carbon could be attributed to the accumulation of ions within the confined insertion sites offered by micropores during charging. The steric requirements of these ions result in a macroscopically observable, reversible electrode expansion. A comparison with the expansion of entangled SWCNT electrodes and an expanded graphite electrode proved that the occupation of insertion sites depends directly on the electrode potential and the accessibility of the insertion site. As a particular example of this behavior, it was shown that the interstitial porosity of SWCNT bundles can be made accessible by electrochemical polarization, leading to an intrinsic capacitance enhancement. As an important conclusion, the accessibility of such sites must be evaluated in situ in order to determine their possible contribution to charge storage within the stability limits of the electrolyte solution.

Studies of the electronic charge transfer contribution towards the aging of EDLCs in the present work emphasized the possible formation of insoluble solid electrolyte degradation products. Systematic aging experiments using laboratory-scale test cells at elevated voltages enabled to distinguish between the loss of electrochemical performance and physicochemical modification of the activated carbon electrodes on the single electrode level. The rapid rate of aging at elevated voltages was

found to depend notably on the solvent. In the AN-based electrolyte solution, the performance loss at a cell voltage of 3.5 V could be primarily attributed to the blockage of porosity at the positive electrode by the formation of solid degradation products within the porous structure of the activated carbon, most likely due to the oxidation of AN. This aging mechanism is promoted by the defluorination of the polymeric binder at the negative electrode, which results in unfavorable potential window shifts during aging. Preliminary studies regarding aging in the PC-based electrolyte indicated a different primary aging mechanism, likely due to reductive processes involving PC at the negative electrode. Notably, the detrimental effects of electrolyte degradation on the EDLC performance appeared to be significantly more pronounced than the contribution of ion insertion processes to aging.

Finally, suggestions for future research are made in order to deepen and exploit the insights gained regarding the insertion of ions in carbonaceous electrodes as well as the aging of EDLCs at elevated voltages.

Zusammenfassung

Die Ladungsspeicherung in elektrochemischen Doppelschichtkondensatoren (DSKs) bietet sich für die kurzfristige Speicherung von Energie in stationären und mobilen oder tragbaren Anwendungen an, in denen zwischenzeitliche Leistungsspitzen und Zuverlässigkeit von Bedeutung sind. Gegenwärtig wird der Einsatz von DSKs oft durch ihre beschränkte Energiedichte benachteiligt, wobei ein vielversprechender Ansatz zur Erhöhung derselbigen durch eine Vergrößerung der Betriebsspannung dargestellt wird. Allerdings wird unter diesen Bedingungen eine ausgeprägte Abnahme der Lebensdauer festgestellt.

In der vorliegenden Arbeit wurde der Einfluss von Ladungsdurchtritt auf die Ladungsspeicherung und Alterung von DSKs in nichtwässrigen Elektrolytlösungen untersucht. Dabei bietet sich die Unterteilung der Durchtrittsströme in ionische und elektronische Beiträge an. Anhand eines tieferen Verständnisses dieser Prozesse können mögliche Strategien zur Optimierung der Ladungsspeicherung und Verhinderung der Alterung bei erhöhten Spannungen vorgebracht werden.

Eine kommerzielle, aus Kokosnussschale gewonnene Aktivkohle wurde als Elektrodenmaterial in $1\,M$ Lösungen von Et_4NBF_4 in Acetonitril (AN) und in Propylencarbonat (PC) verwendet. Durch elektrochemische Charakterisierung dieser Systeme mittels Zyklovoltammetrie wurden die Potentialbereiche idealer Polarisierbarkeit sowie die Potentialbereiche mit irreversiblem Ladungstransfer identifiziert.

Der Bereich idealer Polarisierbarkeit wurde mittels in situ Ramanspektroskopie, Widerstandsmessungen und elektrochemischer Dilatometrie untersucht. Die Ergebnisse wurden im Zusammenhang mit denjenigen von Kohlenstoffnanoröhrchen (*single-walled carbon nanotubes*, SWCNTs) diskutiert, um einen Vergleich mit einem hochporösen Elektrodenmaterial mit definierter geometrischer und elektronischer Struktur herzustellen. Fundamentale Unterschiede im elektrochemischen Dotierungsverhalten dieser beiden Materialien wurden festgestellt, was für Aktivkohle nur durch eine Berücksichtigung von erheblicher Unordnung und Abweichungen von der idealisierten Graphenstruktur zu erklären ist. Unterschiede in der kapazitiven Ladungsspeicherung konnten auf die elektronische Zustandsdichte des jeweiligen

Materials zurückgeführt werden, wodurch die Bedeutung der elektronischen Eigenschaften der Elektrode für die Ladungsspeicherung in DSKs hervorgehoben wird.

Um mögliche ionische Ladungstransfermechanismen in DSKs zu beschreiben, wurden die Beiträge von Ioneninsertionsprozessen zur Ladungsspeicherung und Elektrodenalterung für Graphit und Aktivkohle mittels in situ Dilatometrie, Röntgenbeugung und Kleinwinkelröntgenstreuung verglichen. Es wurde gezeigt, dass die Insertion von Ionen in Graphit durch die vorhandenen, wohldefinierten Interkalationsplätze fortschreitet, wobei die elektrochemische Interkalation von BF_4^- zur Stufenbildung und Lösungsmittelkointerkalation sowohl im AN- wie auch im PC-basierten Elektrolyten führte. Weiterhin wurde eine bemerkenswerte Abnahme der Periodizität senkrecht zu den Graphenebenen der Graphitelektroden durch die Interkalation festgestellt, was größtenteils auf die elektrochemische Zersetzung der interkalierten Elektrolytspezies zurückgeführt wurde, d.h. auf eine Kombination aus ionischem und elektronischem Ladungstransfer.

Auf der anderen Seite konnte die Ioneninsertion in Aktivkohle primär der Anreicherung von Ionen innerhalb der nur begrenzt zugänglichen Mikroporosität zugeordnet werden. Der Platzbedarf der Ionen verursacht eine makroskopisch messbare, reversible Ausdehnung der Elektrode. Im Vergleich mit der Ausdehnung von SWCNTs und einer aufgeweiteten Graphitelektrode wurde gezeigt, dass die Ausnutzung der Insertionsplätze der Elektrode vom Elektrodenpotential und der Zugänglichkeit dieser Plätze abhängt. Als spezielles Beispiel für dieses Verhalten wurde die Ausnutzung der interstitiellen Porosität innerhalb von seilähnlichen SWCNT-Agglomeraten durch elektrochemische Polarisierung gezeigt, was zu einer Zunahme der Doppelschichtkapazität führte. Als wichtige Schlussfolgerung wird festgehalten, dass der Zugang zu solchen Insertionsplätzen notwendigerweise in situ bewertet werden muss, um den entsprechenden Beitrag zur Ladungsspeicherung innerhalb des Betriebsspannungsfensters zu bestimmen.

Untersuchungen zu den Folgen des elektronischen Ladungstransfers bei erhöhten Spannungen zielten insbesondere auf die Bildung von festen, unlöslichen Zersetzungsprodukten der Elektrolytlösung ab. Durch systematische Versuche zur Alterung von symmetrischen DSK-

Systemen im Labormaßstab konnte der Kapazitätsverlust sowie physikochemische Veränderungen den einzelnen Aktivkohle-Elektroden zugeordnet werden. Die erhöhte Alterungsrate bei hohen Spannungen wurde maßgeblich durch das verwendete Lösungsmittel beeinflusst. Im AN-basierten Elektrolyten konnte die Kapazitätsabnahme bei einer Zellspannung von 3.5 V primär einer Porenverstopfung an der positiven Elektrode durch feste Zersetzungsprodukte zugewiesen werden, wobei letztere höchstwahrscheinlich durch die Oxidation von AN zustande kommen. Dieser Alterungsmechanismus wurde durch die Entfluorinierung des polymeren Binders an der negativen Elektrode gefördert, welches zu ungünstigen Potentialverschiebungen der Elektroden während der Alterung führte. Erste Messergebnisse zur Alterung im PC-basierten Elektrolyten wiesen auf einen anderen Alterungsmechanismus hin, welcher vermutlich auf der Reduktion von PC an der negativen Elektrode beruht. Als wichtige Erkenntnis gilt festzuhalten, dass die Alterung von DSKs im Wesentlichen von der Elektrolytzersetzung beeinflusst wird und die Ioneninsertion im Vergleich dazu einen verschwindend kleinen Beitrag zu leisten scheint.

Anhand der gewonnenen Erkenntnisse werden Vorschläge zu weiterführenden Untersuchungen gemacht, um die Insertion von Ionen sinnvoll auszunutzen sowie der Alterung von DSKs bei erhöhten Spannungen entgegenzuwirken.

Acknowledgments

This work was carried out at the Paul Scherrer Institut in Villigen, Switzerland, within the Electrochemistry Laboratory of the General Energy Department from November 2005 to April 2009.

I would like to express my gratitude to my thesis advisor, Alexander Wokaun, for enabling this research and his continued interest in the present work. It was a pleasure being a member of the Interfaces and Capacitors Group led by Rüdiger Kötz, to whom I am very grateful for his enjoyable supervision, constructive input and guidance at all times. Also, I thank Reinhard Nesper of the Laboratory of Inorganic Chemistry at ETH Zurich for accepting the coexamination of this work and for inspirational discussions.

I am particularly thankful for meeting Matthias Hahn and benefiting from his expert mentoring and practical wisdom. His dedicated efforts enabled the dilatometry and resistance experiments conducted in this work, and our stimulating discussions sparked many new experimental ideas. Also, I would like to thank Dario Cericola for all discussions, experimental support and enjoyable teamwork in the lab. The great dedication of Annette Foelske-Schmitz in performing the numerous XPS measurements is gratefully acknowledged, as well as the contributions of Anastasia Savouchkina. I also benefited from the guidance and experience of former group members, in particular Flavio Campana (AFM), Jean-Claude Sauter (LabView programming) and Olivier Barbieri (gas adsorption).

The close collaborations and shared infrastructure with the Battery Group headed by Petr Novák were indispensable for the present work. In particular, I would like to highlight the invaluable technical advice of Werner Scheifele and Hermann Kaiser as well as important joint efforts with Laurence Hardwick (Raman spectroscopy), Fabio Rosciano (X-ray diffraction at the SLS), Desmond Ng and Sophie Chew (both SWCNTs).

Further, the realization of numerous in situ cells would not have been possible without the expert help of Marcel Hottiger and the entire PSI workshop. In this respect, I would like to thank Christian Marmy for his assistance in countless practical situations as well as Jörg Schneebeli

Contents

Part I.

Introduction

Chapter 1.

Motivation and scope

1.1. General introduction

There are two prominent challenges facing the global energy economy in the present century. First, the continued depletion of economically viable supplies of fossil fuels is irreconcilable with the significant increase in the world energy consumption [1, 2]. Second, the anthropogenic emissions are, for the first time, of equal magnitude as the natural fluxes and are therefore expected to have a notable impact on the global climate [3]. Thus, it is essential for future energy economies to feature an increased contribution from renewable energy technologies and improved means for efficient energy storage.

As electrical energy storage devices, electrochemical double layer capacitors (EDLCs) can provide valuable contributions to the power quality of grids based on decentralized electricity production as well as to the efficiency of portable and mobile applications which rely on electrical energy. A summary of the properties and application fields of EDLCs is given in Chapter 2. In this context, the limited energy density of EDLCs will be identified as a key weakness of the technology.

By describing the scientific principles underlying the electrochemical energy storage in EDLCs in Chapter 3 and reviewing the properties of the most important electrode material, carbon, in Chapter 4, strategies for increasing the energy density of EDLCs can be outlined. In describing the most promising approaches, the necessity for a more detailed understanding of the charge storage and aging mechanisms of EDLCs at elevated voltages becomes apparent (Chapter 5). An investigation into these mechanisms and their consequences for energy storage in EDLCs is the focus of the present work.

1.2. Scope of this work

An increase in the specific energy of EDLCs is a key research area for the advancement of this electrochemical energy storage technology. A promising approach to achieve this goal is an increase in the device voltage (Chapter 5). However, under these conditions, a significant reduction in the lifetime of EDLCs occurs (Section 5.2.2).

The aim of the present work was to identify the dominant aging mechanisms of EDLCs based on non-aqueous electrolytes in order to describe the processes which lead to performance loss over time at elevated device voltages. Hence, two main experimental strategies were pursued:

1. in situ investigations of potential-dependent structural changes of carbonaceous electrodes, and

2. electrochemical aging of laboratory-scale EDLCs and correlation of the performance loss of single electrodes with the according structural changes.

As reviewed in Section 5.2.2, the majority of irreversible charge loss at elevated voltages does not appear to contribute towards the formation of gaseous reaction products. Hence, no investigations into the gas evolution or pressure build-up in EDLCs were performed in the present work. Also, the influence of temperature on the aging mechanisms of EDLCs was not studied as it does not directly contribute towards an increase in specific energy.

Instead, the experimental efforts focused on less established research areas such as the in situ investigation of the electrochemical charging mechanism in highly porous activated carbon electrodes, dimensional changes of such electrodes as a consequence of electrochemical charging, and the deposition of insoluble electrolyte degradation products on such electrodes. The experimental techniques employed in these studies are described in Part II of this thesis, while the according results are presented in Part III under the following classification:

- characterization of an activated carbon, YP17, in terms of structure, porosity and electrochemical performance in EDLC electrolytes (Chapter 9),

- study of the reversible electrochemical doping mechanism of this carbon and comparison with a model carbonaceous electrode consisting of single-walled carbon nanotubes using in situ Raman spectroscopy and resistance measurements (Chapter 10),

- investigation of the dimensional changes during electrochemical charging of YP17 and single-walled carbon nanotubes via electrochemical dilatometry, as well as of graphite via electrochemical dilatometry and in situ X-ray diffraction (Chapter 11),

- assessment of irreversible changes on the length scale of the microporosity of YP17 using in situ small-angle X-ray scattering (Chapter 12),

- study of solid deposits on a model carbonaceous electrode, highly oriented pyrolytic graphite, after electrolyte degradation at elevated negative and positive potentials, respectively, using atomic force microscopy and X-ray photoelectron spectroscopy (Chapter 13), and

- effects of elevated float voltages on the single electrode capacitance and electrochemical performance of YP17, as well as an ex situ characterization of these electrodes following aging at elevated voltages (Chapter 14).

Each of the chapters listed above contains a concluding section in which the relevant results are briefly summarized. Finally, in Part IV, the insights gained by the various approaches are combined to enable a more complete description of the electrochemical charging and aging of EDLCs based on non-aqueous electrolytes.

Chapter 2.

Practical aspects of energy storage in EDLCs

2.1. Electrical energy storage systems and their applications

The importance of electrical energy has been rising steadily over the past century. While the global consumption of electrical energy was 9.4 % of the world total final energy consumption in 1973, this figure rose to 16.7 % in 2006 [1] and is expected to increase at an even faster rate in future years [4]. This prognosis results from several aspects:

- the rising importance of renewable energy technologies in order to provide a sustainable energy economy which is neutral in anthropogenic emissions,

- the increased use of electrical devices in both industrial and consumer applications, and

- the prospect of zero emissions during local consumption of electrical energy.

Many forms of renewable energy (wind, wave, tidal, solar and run-of-river hydro) result in an electrical energy output which is intermittent or at least variable according to the availability of the resource [5, 6]. Given the importance of a reliable supply of electric power within a stable power network, the need for efficient electrical energy storage techniques is evident.

In Figure 2.1, an overview is given of different electrical energy storage systems currently used in stationary applications for power grids. The wide range of energy content and power output can be explained by the different purposes these systems serve in the context of grid electricity. While pumped hydro, compressed air energy storage (CAES)

and flow batteries are best suited for high-energy storage applications (in the order of MWh to GWh), conventional electrochemical batteries and superconducting magnetic energy storage (SMES) are preferred for small and intermediate energy storage systems (few kWh to several hundred kWh).

EDLCs, along with flywheels, fill a particular niche in the context of grid electricity management due to their high efficiencies, high power capabilities and long cycle lives (up to several 10^6 cycles) [4, 8]. Both systems have the disadvantage of energy losses over time with initial rates of ca. 50 % per day for flywheels due to friction and ca. 5 % per day for EDLCs due to electrochemical discharge [4]. Both figures are unsuitable for long-term energy storage. However, EDLCs and flywheels are ideal for power quality management in the form of load leveling during peak power demand, where power in the order of MW needs to be supplied in the time frame of seconds to minutes (Figure 2.2). Regarding applications in which such power capability is the key performance parameter, EDLCs are usually the most cost-effective energy storage (Figure 2.3).

In portable and mobile applications which rely on an integrated or on-board source of electrical energy, it is usually necessary to consider the energy and power content of energy storage devices normalized to their mass or volume in a Ragone plot [9, 10]. In Figure 2.4, the maximum specific power and energy which are obtained with EDLCs at the present state of technology are compared to the corresponding values for other capacitor types and a series of common batteries. For sake of comparison, fuel cells and the internal combustion engine (ICE), which are both energy conversion systems, have also been included in the Ragone plot. In the case of the latter two, the specific properties depend directly on how the fuel is stored prior to conversion within the device itself.

From Figures 2.2 and 2.4, it is clear that EDLCs fill a particular energy storage niche in which power pulses need to be supplied for durations of a few seconds or tens of seconds. Such power demand is required for a range of different systems covering a wide span of total energy content, which has led to the implementation of EDLCs in a number of applications as diverse as memory backup in consumer electronics [11],
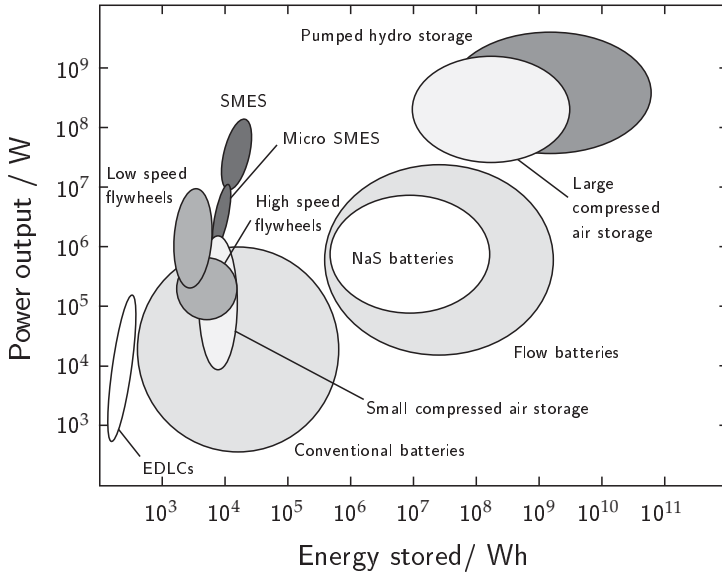
Figure 2.1.: Electrical energy storage systems for grid applications according to their energy content and power output. Adapted from [4].
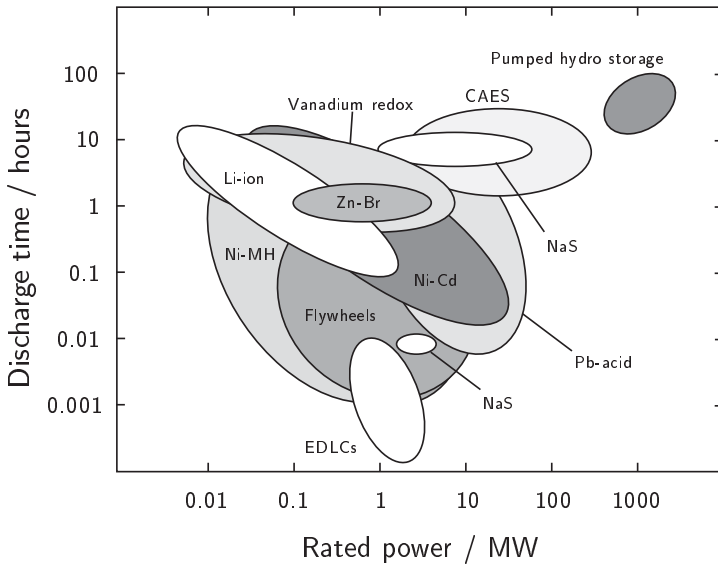
Figure 2.2.: Characteristic discharge time for electrical energy storage installations with varying power ratings as of 2008. Adapted from [7].
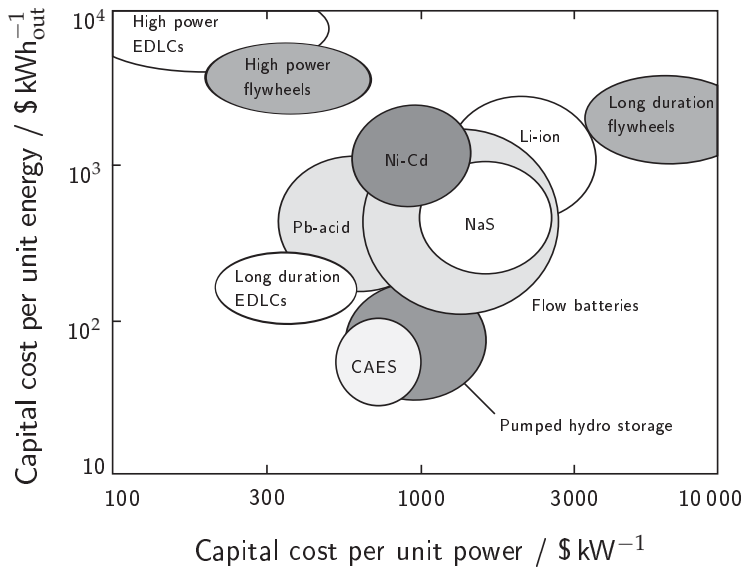
Figure 2.3.: Capital cost per unit energy and power for different electrical energy storage systems. Adapted from [7].
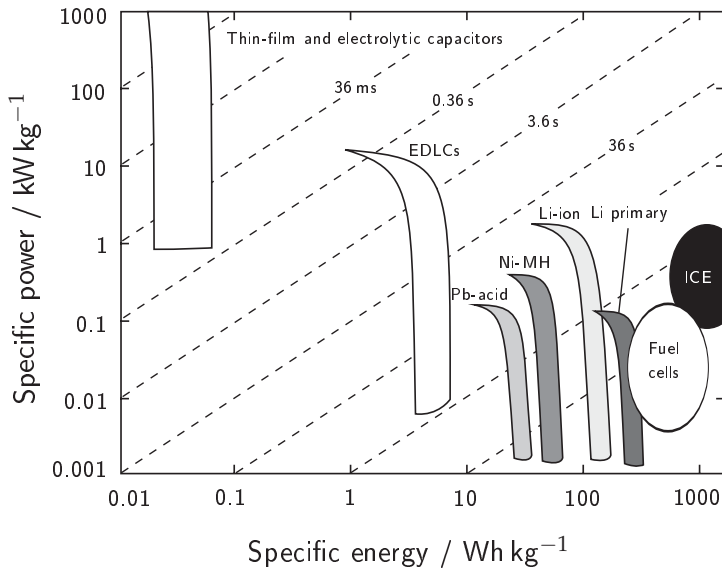
Figure 2.4.: Schematic Ragone plot for EDLCs in relation to other energy storage and conversion devices. The dashed lines indicate time constants for certain combinations of energy and power. Adapted from [4, 11–15].

energy recuperation and boost in electric vehicles [16–20], and load leveling in decentralized power microgrids [21]. A selection of these applications, which vary in maturity from the stage of single prototypes to the extent of mass production, is given in Table 2.1.

In most applications, EDLCs supply the peak loads and act complementary to high-energy storage or conversion devices which supply the bulk of the energy demand. This combination of energy sources which are effective on different timescales permits a downscaling of the primary energy source and thereby improves the overall energy efficiency and cost. Similarly, short interruptions in the main power supply can be compensated through EDLCs which provide the necessary bridge power, thus forming an uninterruptable power supply (UPS). In many cases, peak power loads can be detrimental when applied to a single high-energy device (such as an electrochemical battery), leading to the advantage of a prolonged lifetime of the primary energy source when combined with EDLCs.

In the context of public and individual transport, EDLCs possess a number of advantageous characteristics. They can be both charged and discharged at high rates with high efficiency and cycle life irrespective of their actual state-of-charge, which does not hold for high-power batteries. Thus, they are suitable for repeated recuperation and delivery of

Table 2.1.: Applications of EDLCs listed according to their approximate maximum energy content.

Stored energy	Application	Function	Ref.
< 1 mWh	Consumer electronics	Memory backup	[11]
< 100 mWh	Wireless sensor nodes	Energy harvesting	[22]
0.5–5 Wh	Power tools	Main power source	[23]
	Electric scooters	Peak load supply	[24]
5–20 Wh	Hybrid vehicles	Start-stop	[16]
50–250 Wh	Wind turbines	Blade rotation	[25]
	Hybrid vehicles	Power assist	[16–18, 26]
250–500 Wh	Trolley buses	Recuperation	[27]
	Microgrids	Power quality	[28–30]
> 1 kWh	Light rail vehicles	Recuperation	[31–33]
	Gantry cranes	Recuperation	[23, 34]

energy as is the case for successive deceleration and acceleration cycles in electric vehicles (regenerative braking) [11, 26]. Also, the determination of the state-of-charge of EDLCs is uncomplicated since the voltage of EDLCs increases roughly linearly with increasing state-of-charge (Chapter 3), which facilitates power management significantly. EDLCs using acetonitrile-based electrolytes (Section 3.4) retain their properties down to -40 °C [35], making them ideal for cold starting of engines.

Finally, it must be emphasized that future applications for EDLCs are closely linked to the necessity of electrical energy storage. Given the above prospects in stationary as well as in mobile applications, an increase in the importance of energy storage systems in general and of EDLCs in particular can be expected.

However, despite the various successful applications listed in Table 2.1, the low energy density of EDLCs remains a key limitation which hinders their widespread implementation, as will be briefly highlighted in the next section.

2.2. The specific energy of EDLCs

In the year 2000, it was suggested that the specific energy of EDLCs would exceed $10\,\mathrm{Wh\,kg^{-1}}$ by improving the EDLC technology which existed at the time [36]. However, after nearly one decade, commercially available EDLCs still exhibit rated specific energies in the range of only 5–$6\,\mathrm{Wh\,kg^{-1}}$ (Figure 2.5), which are well below those of electrochemical batteries (Figure 2.4). From this observation, it appears as though the specific energy of devices based solely on double layer charging has currently reached saturation. This conclusion is supported by measurements of the capacitance of electrodes with increasing surface area (Section 3.5) and by rough estimates of the maximum theoretical capacitance of carbon-based electrode materials (Section 5.1).

The low specific energy of EDLCs, along with the high cost of the carbonaceous electrode material and the electrolytes, is thus generally identified as the main weakness of these devices [8, 39]. Various strategies may be proposed for improving the specific energy of EDLCs (Section 5.1), but usually at the expense of favorable attributes such as specific power and cycle life. In this context, knowledge about the aging mechanisms which limit the operating range of EDLCs is lacking. In recent years, a number of studies have been conducted to explain the
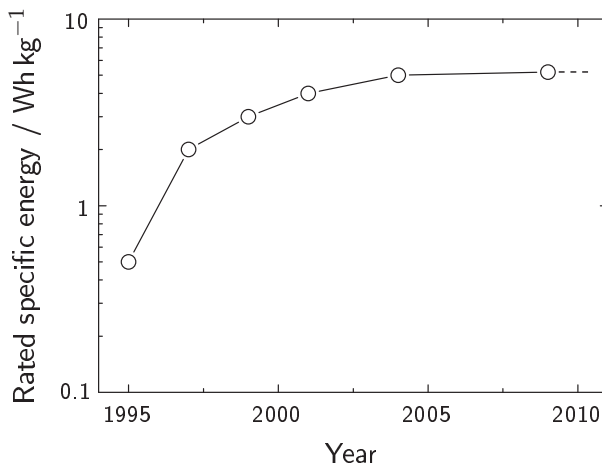
Figure 2.5.: Saturation of the specific energy of commercially available EDLCs (product data from Nippon Chemi-Con Corporation [37, 38]).

degradation of EDLCs (Section 5.2.2), but a consensus on the relationship between physicochemical changes within EDLCs and their loss of electrochemical performance has not yet been established.

In order to treat these issues in more detail in Chapter 5, it is convenient to first describe some practical aspects and the scientific fundamentals of EDLCs (Chapter 3) and the structural properties of carbonbased electrodes (Chapter 4) in the following.

Chapter 3.

Fundamentals of EDLCs

3.1. Introduction and nomenclature

The first patent application for an energy storage device based on double layer charging was granted to Becker of General Electric in 1957 [40], followed by patents of Rightmire (1966) [41] and Boos (1970) [42], both of the Standard Oil Company of Ohio (SOHIO), upon the basis of which first commercial devices were produced and sold. Since then, a number of companies [11, 37] have entered the market of energy storage based on electrochemical double layer charging, which has affected a number of applications (Table 2.1) and spurred research in this field. Corresponding overviews have been given by Raistrick [43], Conway [44], Kötz and Carlen [11], Frackowiak and Béguin [45] and Simon and Gogotsi [15], among others.

Over the years, the technology has been provided with various names by the industrial and scientific communities, the most frequent descriptions being supercapacitors and ultracapacitors. While the origin of this nomenclature may be attributed to the very high specific capacitance of these devices in comparison to conventional thin-film capacitors, it is important to note that the electrochemical charge storage mechanisms of devices described by these names may differ fundamentally from each other.

The terms supercapacitor and ultracapacitor describe devices which exhibit approximatively capacitive behavior, i.e. for which the change in the amount of charge stored, dQ, is proportional to the change in the applied voltage, dU:

$$dQ = C\, dU \qquad (3.1)$$

where C is the capacitance of the device. When a potential difference is applied across the electrochemical double layer (Section 3.3) of an

electrode, charge is accumulated within the double layer according to Equation (3.1). This mechanism of charge storage is nonfaradaic, since no charge transfer takes place across the electrode/electrolyte interface. However, a number of electrode/electrolyte combinations exhibit faradaic reactions for which Equation (3.1) is also fulfilled well over a range of applied voltages. Such behavior is described as pseudocapacitive and arises due to a distribution of redox states in the electrode material. The most important materials of this class include hydrous ruthenium dioxide, $RuO_2 \cdot xH_2O$ [46], in protic electrolytes, and electroactive polymers such as polypyrrole, polyaniline or polythiophene and their derivatives in various electrolytes [47].

Hence, the terms supercapacitor and ultracapacitor describe any electrochemical system which stores charge in a capacitive manner, be it via nonfaradaic or faradaic processes. This includes so-called hybrid or asymmetric devices in which a nonfaradaic (double layer) charge storage material is combined with a faradaic (battery) material. In this sense, it is clear that the properties of supercapacitors and electrochemical batteries, the latter of which rely almost exclusively on faradaic charge storage at well-defined electrode potentials, may overlap.

In order to distinguish between supercapacitors based on pseudocapacitance and those which are based on double layer capacitance, the latter are referred to as electrochemical double layer capacitors, or EDLCs. This class of capacitors represents the object of interest in this thesis. When additional faradaic processes contribute to charge storage, usage of the more general term electrochemical capacitors is preferred (Table 3.1).

The aim of this chapter is to describe the nature of and the interaction between the main components of the most successful class of EDLCs on

Table 3.1.: Classification of capacitive electrochemical energy storage devices.

Electrochemical capacitor	
EDLC	Pseudocapacitor Hybrid
Nonfaradaic charge storage	*Nonfaradaic + faradaic charge storage*

the market today, which are based on carbonaceous electrodes and non-aqueous electrolytes.

3.2. Basic assembly and properties of EDLCs

Commercial EDLCs consist of carbon-coated aluminum current collectors with a porous, often cellulose-based membrane serving as a separator between the positive and negative terminals. The active electrode material is highly porous (Section 3.5), held together by a polymeric binder such as poly(tetrafluoroethylene) (PTFE) and often contains an additional conductive agent such as carbon black or graphite. In order to improve mechanical adhesion and electrical contact between the porous electrode material and current collector, the latter is often roughened [48] and covered with a conductive layer of carbon black or graphite which also contains a polymeric binder [49]. Details of commercial production processes may be found in numerous patents, for instance that by Nanjundiah et al. [50] of Maxwell Technologies.

The final assembly of these components may be spiral-wound (Figure 3.1) or stacked within an aluminum can, a prismatic enclosure or flexible pouch. Since most commercial EDLCs rely on non-aqueous electrolyte solutions (Section 3.4), the materials are thoroughly dried, usually under vacuum at temperatures above $100\,°C$ in order to remove moisture. Under an inert gas environment, the non-aqueous electrolyte is subsequently injected into the can, which is then hermetically sealed in order to prevent moisture from entering into and electrolyte from leaking out of the device.

Considerations regarding the cost of the various components have been given by Burke [8]. The most expensive components are the carbonaceous electrodes, mainly due to the carbonization and activation steps (see Section 4.5), and the non-aqueous electrolyte solution, mainly due to the rigorous procedures necessary to achieve the technical specifications regarding impurity levels and water content.

It is convenient to picture an EDLC in terms of a simplified equivalent circuit in which the capacitive contributions of the negative and positive electrodes are denoted by C_{neg} and C_{pos}, respectively, while all resistive components are lumped together in R_S (Figure 3.2).
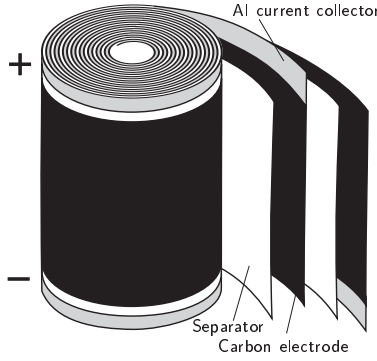
Figure 3.1.: Illustration of a spiral-wound EDLC without housing.

For the total device, the capacitance C_{cell} is obtained according to

$$\frac{1}{C_{\text{cell}}} = \frac{1}{C_{\text{neg}}} + \frac{1}{C_{\text{pos}}} \tag{3.2}$$

or, for $C_{\text{neg}} = C_{\text{pos}} = C_{\text{single}}$,

$$\frac{C_{\text{cell}}}{2\, m_{\text{single}}} = \frac{1}{4} \frac{C_{\text{single}}}{m_{\text{single}}} \tag{3.3}$$

where m_{single} and C_{single} are the mass and capacitance, respectively, of a single electrode. Equation (3.3) states that the gravimetric capacitance of the full cell with respect to the active electrode mass is equal to a quarter of the gravimetric capacitance of a single electrode for a completely symmetric EDLC device.

Assuming ideal capacitive behavior according to Equation (3.1), the energy content W of an EDLC is given by
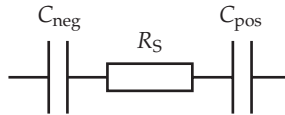
Figure 3.2.: Simplified equivalent circuit of an EDLC device.

$$
\begin{aligned}
dW &= dQ\,dU \\
dW &= C\,dU^2 \\
W &= \frac{1}{2}CU^2
\end{aligned}
\tag{3.4}
$$

where U is the voltage of the EDLC. Consider now the discharge of the equivalent circuit in Figure 3.2 over a constant load resistance R_L. In order to determine an expression for the maximum source power of the EDLC, the current I is written as

$$
I = \frac{U}{R_S + R_L}
\tag{3.5}
$$

The source power P_S is then given by

$$
\begin{aligned}
P_S &= UI \\
&= R_S I^2 \\
&= \frac{U^2}{R_S + 2R_L + R_L^2 / R_S}
\end{aligned}
\tag{3.6}
$$

The denominator in Equation (3.6) is minimal for $R_S = R_L = R$, which represents the so-called matched impedance condition. The power delivered to the load resistor in this case immediately follows as

$$
P_{\max} = I^2 R = \frac{U^2}{4R}
\tag{3.7}
$$

It is worth noting that the operation of an EDLC under conditions of $P_{\max}$ results in an energetic efficiency of only 50 %, as the power delivered to the load is equal to the power loss due to Joule heating across the internal resistance of the EDLC.

In order to obtain higher efficiencies, the load power must be less than $P_{\max}$. An energetic efficiency ζ_W for the constant power discharge of an EDLC may be defined as

$$
\zeta_W = \frac{P_L}{P_L + P_S}
\tag{3.8}
$$

where P_L is the power dissipated at the load. It follows that

$$R_{\mathrm{L}} = \left(\frac{\zeta_W}{1 - \zeta_W} \right) R_{\mathrm{S}} \tag{3.9}$$

Thus, the useful power P_{L} and ohmic losses P_{S} for a given efficiency ζ_W can be written as

$$P_{\mathrm{L}} = \frac{U^2 \zeta_W (1 - \zeta_W)}{R_{\mathrm{L}}} \tag{3.10}$$

$$P_{\mathrm{S}} = \frac{U^2 (1 - \zeta_W)^2}{R_{\mathrm{S}}} \tag{3.11}$$

It is worth noting that in practical applications, EDLCs are often only cycled between the nominal voltage, U_{nom}, and $U_{\mathrm{nom}}/2$, which results in a usable energy fraction which is 3/4 of the total energy content given in (3.4):

$$\mathrm{d}W = C \, \mathrm{d}U^2$$
$$W_{\mathrm{nom}} = C \iint_{U_{\mathrm{nom}}/2}^{U_{\mathrm{nom}}} \mathrm{d}U^2$$
$$W_{\mathrm{nom}} = \frac{3}{8} C U_{\mathrm{nom}}^2 \tag{3.12}$$

The expressions (3.4) and (3.12) for the energy content as well as (3.7) and (3.10) for the power capability of EDLCs are useful in justifying strategies to improve the specific energy and power of EDLCs. Thus, the following may be concluded:

- the specific energy of EDLCs may be increased proportionally to the specific total capacitance and proportionally to the square of the device voltage, and

- the specific power of EDLCs may be increased proportionally to the inverse total resistance and proportionally to the square of the voltage of the device.

However, the crude calculations given above are based on the assumption of idealized capacitive and resistive behavior which is rate-independent. Further, the actual operating limits of the device are not taken into consideration. Important information regarding these latter

issues can be gathered in the following by discussing the structure of the electrochemical double layer and the influence of the electrolyte as well as of the electrode and its porosity.

3.3. The electrochemical double layer

3.3.1. The electrode potential

The electrode potential is a central term in electrochemistry and one that has been influenced by the fields of electrochemistry and solid state physics alike. Since a description of the potential profile across the electrode/solution interface is a prerequisite for describing the properties of the electrochemical double layer, it is appropriate to establish the necessary nomenclature and conventions at this point. In this respect, the recommendations given by the International Union of Pure and Applied Chemistry (IUPAC) will be followed [51].

For sake of simplicity, the interface between an ideal metal and vacuum is considered (Figure 3.3). First, it is assumed that there is no difference between surface and bulk properties and that the metal carries no net charge (Figure 3.3a). In this case, the electron density n_e is constant within the metal ($x \leq 0$) and zero outside of it ($x > 0$). The electron energy consists of a potential energy, V, due to the interaction with the metallic nuclei and other electrons in the system, and a kinetic energy.

According to the Pauli exclusion principle, only two electrons with opposing spin may occupy the same energy level, for which reason the electrons are filled into the band structure [53] with successively higher energies until the Fermi level is reached. At the Fermi level, the kinetic energy of an electron is ε_F (the kinetic Fermi energy [54]) and the probability of finding an electron at this energetic level is 0.5, according to the Fermi-Dirac distribution:

$$f = \frac{1}{1 + \exp\left(\frac{\varepsilon - \varepsilon_F}{k_B T}\right)} \tag{3.13}$$

which gives the probability f of finding an electron with the energy ε, where k_B is the Boltzmann constant and T is the temperature [53, 55].
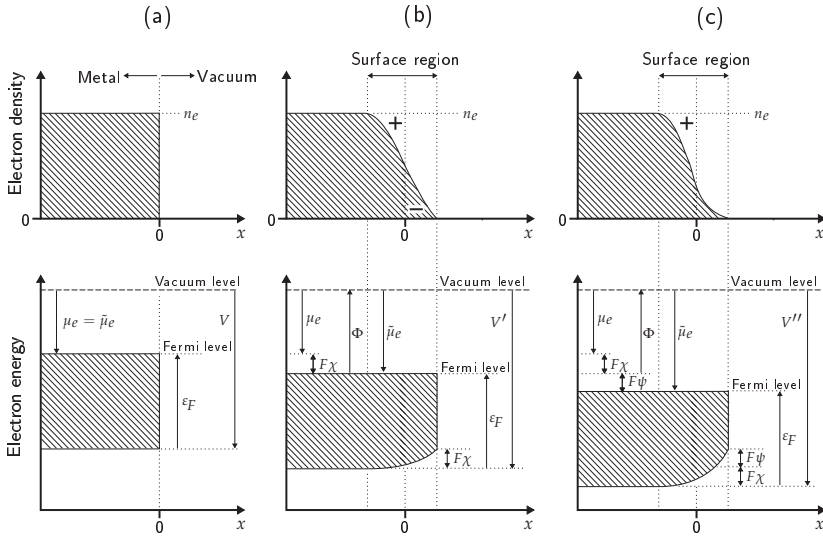
Figure 3.3.: Simplified diagrams of the electron density and electron energy at the interface between a metal and vacuum for (a) an ideal metal, (b) the same metal with a surface dipole, and (c) the same metal with a surface dipole and a net positive surface charge. The hatched regions indicate states occupied by electrons. Adapted from [52].

The energy that binds electrons to the interior of a phase is generally called the electrochemical potential $\tilde{\mu}_e$.

In the absence of a surface electric potential (Figure 3.3a), $\tilde{\mu}_e$ is equal to the chemical potential, μ_e [54]. However, there is usually an imbalance of charge at real surfaces as there is a finite probability of finding electrons beyond the surface plane of the localized positive charge of metallic nuclei [52], resulting in a double layer of charge in the surface region (Figure 3.3b). This double layer is associated with a surface electric potential, χ, which effectively lowers the entire band structure of the metal with respect to the vacuum level. More work is now needed to remove an electron from the metal across the surface, which is expressed by the work function Φ [56].

Per definition, Φ is only valid for metals in the uncharged state, i.e. carrying no net charge [51]. This is no longer the case in Figure 3.3c, where a net positive charge has been applied to the metal. The charge is localized in the surface region and results in an additional outer po-

tential, ψ, also called the Volta potential [51, 56]. The electric potential in the bulk of the metal is called the Galvani potential, ϕ, and may be regarded as the sum of the contributions of the Volta potential (due to the net charge on the phase) and the surface electric potential (due to the surface dipole), $\phi = \psi + \chi$ [51]. Hence, the Galvani potential ϕ describes the difference between the electrochemical and the chemical potential, $\phi = (\tilde{\mu}_e - \mu_e)/F$, where F is Faraday's constant [51, 57, 58].

The principle of electrode potential measurements involves an experimental arrangement as schematically shown in Figure 3.4. The measurement of the electrode potential of a material M (the working electrode) is performed against a practical point of reference, in this case the electrode potential of a reference material, R (the reference electrode). Both are immersed in an electrolyte, S, and contacted by the potential probes M' and M'' of the measuring instrument. The probes are made of the same material, but will in general differ in their electrical state [59]. None of the Galvani potentials ϕ_i can be measured directly, and even the Galvani potential differences $\Delta_i^j \phi$ can not be measured in-
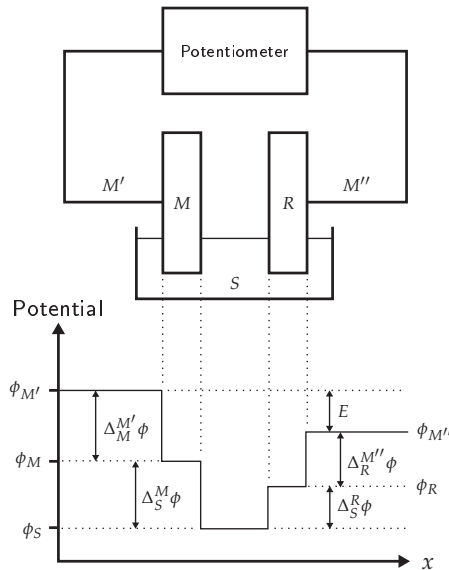
Figure 3.4.: Practical determination of the electrode potential E of the working electrode M against a reference electrode R.

dependently [57, 58, 60]. The measured electrode potential E is in fact equal to the sum of all Galvani potential differences (or Volta potential differences [61]) in the system, and therefore it depends on the choice of electrolyte, reference electrode and the potential probes.

Hence, an electrode potential measurement implies that all Galvani potential differences other than the one of interest are kept constant. The junctions between the potential probes and the electrodes remain constant (at constant temperature) without attention, and if the composition of the electrolyte solution is not changed and the reference electrode remains unaltered, then any measured change in E must be attributed to a change in the Galvani potential difference $\Delta_S^M \phi$ at the electrode/solution boundary [60]. As a consequence, it is imperative that all electrode potentials are quoted against the type of reference electrode which was used in the measurement (i.e. the reference material/electrolyte combination).

In electrochemistry, the standard hydrogen electrode (SHE) has become the internationally accepted primary reference whose own electrode potential has been defined as zero. It consists of a platinum electrode in an aqueous electrolyte solution which contains hydrogen (H_2) and protons (H^+) at unit activity [60]. For the SHE, Trasatti has assigned a value of +4.44 V against the vacuum level [59]. However, the SHE can not always be easily implemented in electrochemical systems, which will be addressed in Section 7.2.

Having identified the relevant physical quantities involved in electrode potential measurements, it is now possible to conduct a closer examination of the interface between electrode and electrolyte solution.

3.3.2. The electrode/solution interface

When an electrode is immersed into an electrolyte solution, charge is accumulated at the interface due to the presence of mobile electronic and ionic charge carriers, respectively, within the two phases. The interfacial region or electrified *interphase* is the spatial region in which the properties vary between those of the bulk phases. In contrast to this interphase, the *interface* is taken to be an infinitely thin, two-dimensional plane which represents the formal boundary between the two phases [62]. The classical double layer model [60] assumes that

no charged species can cross the interface regardless of the potential of the electrode. The electrode is thus said to be ideally polarizable [51], which implies that it behaves like an ideal capacitor without the leakage of charge across the interface.

The interfacial region between electrode and electrolyte is commonly referred to as the electrochemical double layer, even though it may be thought to consist of more than two layers. An illustration of the electrochemical double layer is given in Figure 3.5, in which a perfectly flat electrode surface is in contact with an aqueous solution of an electrolyte.

On the electrode side of the interface, an excess (or deficiency) of electronic charge with respect to the bulk results in a free charge density per unit interfacial area of the electrode, σ_{SC}. On the solution side of the interface, the electrode surface is covered by a compact layer
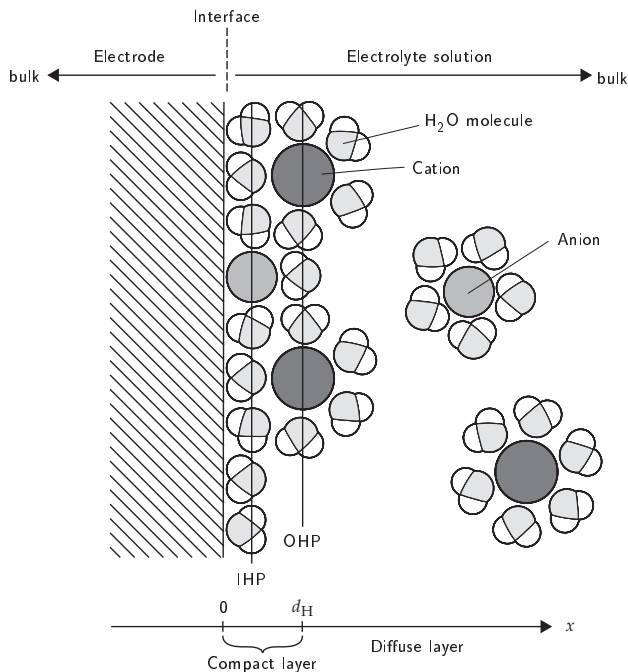
Figure 3.5.: Classical model of the electrochemical double layer in which an electrode is in contact with an electrolyte solution. The inner and outer Helmholtz planes are denoted by IHP and OHP, respectively.

referred to as the Helmholtz (or Stern) layer [58, 60] which contains solvent molecules and possibly also partially desolvated ions which are then said to be specifically adsorbed [63]. The locus of the electrical centers of the specifically adsorbed ions defines the position of the inner Helmholtz plane (IHP). Further, long-range coulombic interactions may also affect the distribution of solvated ions in the solution, which is termed non-specific adsorption. The distance of closest approach of the electrical centers of the solvated ions to the electrode defines the outer Helmholtz plane (OHP), and the specific charge contained within the Helmholtz layer per unit interfacial area is denoted as σ_H. The thickness of the Helmholtz layer is denominated d_H. The region in which the concentration of the non-specifically adsorbed ions differs from the bulk concentration of the solution is called the diffuse (or Gouy-Chapman) layer [58, 60, 62]. The excess charge per unit interfacial area in the diffuse layer is σ_d.

Electroneutrality requires that the total charge in the interphase is zero, so that the charge σ_{SC} on the electrode is balanced by the total charge in the electrolyte solution:

$$\sigma_{SC} = -(\sigma_H + \sigma_d) \tag{3.14}$$

The interfacial charge densities are allocated to the volumetric charge density ρ in the different regions of the electrochemical double layer (Figure 3.5):

$$\sigma_{SC} = \int_{-\infty}^{0} \rho(x)\, dx \tag{3.15}$$

$$\sigma_H = \int_{0}^{d_H} \rho(x)\, dx \tag{3.16}$$

$$\sigma_d = \int_{d_H}^{\infty} \rho(x)\, dx \tag{3.17}$$

When Helmholtz proposed the first conceptual model for the electrochemical double layer, the charges σ_{SC} and σ_H were envisaged as infinitely extended parallel sheets of charge separated by a distance of molecular order, analogous to a parallel-plate capacitor [58, 60]. In this case, σ_H can be obtained using Gauss' law (e.g. [64]):

$$\iiint \rho \, dV = \epsilon\epsilon_0 \iint \mathcal{E} \, dA \tag{3.18}$$

$$\sigma_H = \epsilon_H\epsilon_0\mathcal{E}_H \tag{3.19}$$

where ρ is the volumetric charge density within the volume $\iiint dV$ enclosed by the Gaussian surface $\iint dA$, ϵ is the relative permittivity of the medium (ϵ_H in the Helmholtz layer), ϵ_0 is the permittivity constant and $\mathcal{E}$ the electric field ($\mathcal{E}_H$ in the Helmholtz layer). Assuming a linear potential drop within this layer, $\mathcal{E}_H$ is constant and equal to $-\Delta\phi_H/d_H$, where $\Delta\phi_H$ is the potential difference across the Helmholtz layer and d_H its thickness. Then, Equation (3.19) becomes

$$\sigma_H = -\epsilon_H\epsilon_0\frac{\Delta\phi_H}{d_H} \tag{3.20}$$

In the Helmholtz model, the corresponding charge on the electrode is $-\sigma_H$. Using $C_H = d(-\sigma_H)/d(\Delta\phi_H)$ for the Helmholtz capacitance (in $F\,m^{-2}$), one obtains

$$C_H = \frac{\epsilon_H\epsilon_0}{d_H} \tag{3.21}$$

For the diffuse layer, Gouy and Chapman proposed that the charge density should be greatest close to the electrode surface, where the electrostatic forces of attraction are able to overcome thermal processes, and progressively less charge would be found at greater distances from the electrode [58, 60]. Accordingly, a Boltzmann distribution of ions as a function of the potential ϕ in the diffuse layer is assumed:

$$n_i = n_i^0 \exp\left(\frac{-z_ie\phi}{k_BT}\right) \tag{3.22}$$

with n_i^0 being the bulk concentration of the ion i, z_i its valency, e denoting the elementary charge and n_i the concentration of i at the potential ϕ. For clarity, $\phi = 0$ has been assumed for the bulk electrolyte solution ($x \to \infty$). The charge density in the solution, ρ_S, can then be expressed as

$$\begin{aligned} \rho_S(x) &= \sum_i z_i e n_i \\ &= \sum_i z_i e n_i^0 \exp\left(\frac{-z_i e \phi}{k_B T}\right) \end{aligned} \qquad (3.23)$$

From electrostatics, the potential ϕ associated with a charge density ρ is governed by the Poisson equation, which follows from the differential form of Gauss' law (3.18) and can be written in the one-dimensional form as (e.g. [55])

$$\rho(x) = -\epsilon\epsilon_0 \frac{d^2\phi}{dx^2} \qquad (3.24)$$

The combination of (3.24) with (3.23) results in the Poisson-Boltzmann equation. Using the identity

$$\frac{d^2\phi}{dx^2} = \frac{1}{2}\frac{d}{d\phi}\left(\frac{d\phi}{dx}\right)^2 \qquad (3.25)$$

and considering the boundary conditions $\phi = 0$ and $(d\phi/dx) = 0$ for the bulk electrolyte solution, the Poisson-Boltzmann equation can be written in a reduced form as

$$\left(\frac{d\phi}{dx}\right)^2 = \frac{2k_B T}{\epsilon_d \epsilon_0}\sum_i n_i^0\left[\exp\left(\frac{-z_i e \phi}{k_B T}\right) - 1\right] \qquad (3.26)$$

where ϵ_d is the relative permittivity of the solution in the diffuse layer, which is approximated to be constant. Now, assuming a symmetrical electrolyte ($z = z_1 = -z_2$) and applying the identity $\sinh x = \frac{e^x - e^{-x}}{2}$,

$$\frac{d\phi}{dx} = -\left(\frac{8k_B T n^0}{\epsilon_d \epsilon_0}\right)^{1/2}\sinh\left(\frac{ze\phi}{2k_B T}\right) \qquad (3.27)$$

Integration of (3.27) results in the following expression for the potential profile in the diffuse layer:

$$\frac{\tanh(ze\phi/4k_B T)}{\tanh(ze\Delta\phi_d/4k_B T)} = e^{-\kappa x} \qquad (3.28)$$

with

$$\kappa = \left(\frac{2n^0 z^2 e^2}{\epsilon_d \epsilon_0 k_B T}\right)^{1/2} = \frac{1}{L_D} \qquad (3.29)$$

where $\Delta\phi_d$ is the potential in the diffuse layer at the point $x = d_H$. The Debye-length L_D is a measure of the spatial decay of potential in the diffuse charge layer. Similar to (3.20), the charge density of the diffuse layer at $x = d_H$ can be written as:

$$\sigma_d = \epsilon_d \epsilon_0 \left(\frac{d\phi}{dx} \right)_{x=d_H} \tag{3.30}$$

and, through substitution of (3.27) in (3.30),

$$\sigma_d = -(8k_B T \epsilon_d \epsilon_0 n^0)^{1/2} \sinh \left(\frac{ze\Delta\phi_d}{2k_B T} \right) \tag{3.31}$$

In the Gouy-Chapman model, the charge on the electrode surface is $-\sigma_d$ [58, 60]. Thus, the diffuse layer capacitance can be obtained by differentiation of (3.31):

$$C_d = \frac{d(-\sigma_d)}{d(\Delta\phi_d)} = \left(\frac{2z^2 e^2 \epsilon_d \epsilon_0 n^0}{k_B T} \right)^{1/2} \cosh \left(\frac{ze\Delta\phi_d}{2k_B T} \right) \tag{3.32}$$

Conveniently, the capacitance contribution of the electrode, C_{SC}, can be derived in an analogous manner when the charge carriers are thermally activated, as is the case for intrinsic semiconductors [60, 65]. Noting that $z = 1$ in this case, (3.32) can be rewritten as

$$C_{SC,S} = \left(\frac{2e^2 \epsilon_{SC,S} \epsilon_0 n}{k_B T} \right)^{1/2} \cosh \left(\frac{e\Delta\phi_{SC,S}}{2k_B T} \right) \tag{3.33}$$

where $\epsilon_{SC,S}$ is the dielectric constant of the semiconductor, n is its charge carrier density, and $\Delta\phi_{SC,S}$ is the potential drop in the electrode due to the surface charge σ_{SC}. Equivalently, a Debye length can be defined for the semiconducting electrode according to (3.29) by replacing ϵ_d with $\epsilon_{SC,S}$. The region of potential decay in the semiconductor is commonly referred to as the space charge layer [65].

For metallic electrodes, the Boltzmann distribution of charge carriers does not apply. The charge carrier density for a metal is given by

$$n_e = \int_{-\infty}^{\infty} D(\varepsilon) f(\varepsilon) d\varepsilon \tag{3.34}$$

where $D(\varepsilon)$ is the density of electronic states (DOS) [53] and f is the probability of occupation of a particular electronic state according to the

Fermi-Dirac distribution (3.13). A net surface charge may be applied to the metal by increasing the charge carrier density by the amount n_e':

$$n_e' = \int_{\varepsilon_F}^{\varepsilon_F'} D(\varepsilon) f(\varepsilon) \, d\varepsilon \tag{3.35}$$

where ε_F' is the Fermi energy of the charged metal relative to the band edge at the metal surface ($x = 0$). Under the assumption that the DOS is constant in the range of integration given in (3.35), and replacing $f(\varepsilon)$ by its zero-temperature equivalent, $f = 1$ in the range $0 \leq \varepsilon \leq \varepsilon_F'$ and zero at every other energy, (3.35) can be written as

$$n_e' = \int_{\varepsilon_F}^{\varepsilon_F'} D(\varepsilon_F) \, d\varepsilon \tag{3.36}$$

or

$$dn_e = D(\varepsilon_F) \, d\varepsilon_F \tag{3.37}$$

Noting that $d\varepsilon_F$ is equal to $e \, d\phi$, the net charge density on the metal ρ_M is obtained through

$$
\begin{aligned}
d\rho_M &= e \, dn_e \\
&= e^2 D(\varepsilon_F) \, d\phi \\
\rho_M &= e^2 D(\varepsilon_F) \phi
\end{aligned}
\tag{3.38}
$$

Equation (3.38) can be inserted into the Poisson equation (3.24) and, with the help of (3.25) and the boundary conditions $\phi = \Delta\phi_{SC,M}$ at $x = 0$ and $(d\phi/dx) = \phi = 0$ in the bulk metal, the potential profile in the metal is obtained for $x \leq 0$ as

$$\phi = \Delta\phi_{SC,M} \, e^{(\kappa_M x)} \tag{3.39}$$

with

$$\kappa_M = \left(\frac{D(\varepsilon_F) e^2}{\epsilon_{SC,M} \epsilon_0} \right)^{1/2} = \frac{1}{L_{TF}} \tag{3.40}$$

where $\epsilon_{SC,M}$ is the dielectric constant of the metal. L_{TF} is the Thomas-Fermi screening length which is analogous to the Debye-length (3.29)

for the diffuse layer. Similar to Equations (3.30) and (3.20), the charge density of the metal electrode is given as

$$\sigma_{SC} = \epsilon_{SC,M}\epsilon_0 \left(\frac{d\phi}{dx}\right)_{x=0} \tag{3.41}$$

Combining (3.41) with (3.39), the capacitance contribution of the space-charge layer of the metal is given as

$$C_{SC,M} = \frac{d(\sigma_{SC})}{d(\Delta\phi_{SC,M})} = e\sqrt{D(\varepsilon_F)\epsilon_{SC,M}\epsilon_0} \tag{3.42}$$

Neglecting capacitance contributions from surface states [66], the total capacitance C of the electrochemical double layer is expressed as a series connection of the three capacitive contributions from the space-charge, Helmholtz and diffuse layers, respectively:

$$\frac{1}{C} = \frac{1}{C_{SC}} + \frac{1}{C_H} + \frac{1}{C_d} \tag{3.43}$$

It is now possible to discuss the potential profile across the electrochemical double layer using Equations (3.20), (3.28) and (3.39) for three illustrative situations (Figure 3.6), taking into account that $(d\phi/dx)$ at the boundaries between the space-charge, Helmholtz and diffuse layers must be continuous. In all cases, a Helmholtz layer thickness of 1 nm and a constant Galvani potential difference between electrode and bulk electrolyte of $\Delta_S^M\phi$ were assumed.

In Figure 3.6a, a dilute electrolyte based on acetonitrile as solvent (concentration 0.01 M, $\epsilon_d = 36$ [67], $\epsilon_H = 10$ [68], $z = 1$) is in contact with a metallic electrode with a density of states of $10^{22}\ \mathrm{eV^{-1}\,cm^{-3}}$ [53] at the Fermi level. The relative permittivity of the electrode was taken to be 3, representative of graphite [69]. The Debye length L_D under these conditions is 2 nm and roughly half of the potential drop occurs across the diffuse layer. The capacitance C_d is the smallest term in (3.43) and therefore limits the total capacitance, C.

In Figure 3.6b, the concentration of the electrolyte is increased to 1 M, which reduces L_D to 0.2 nm and renders the potential drop across the diffuse layer negligible. Thus, the term C_d^{-1} may usually be neglected in concentrated electrolytes [60]. In this case, the capacitance of the Helmholtz layer, C_H, is the limiting capacitance in Equation (3.43).
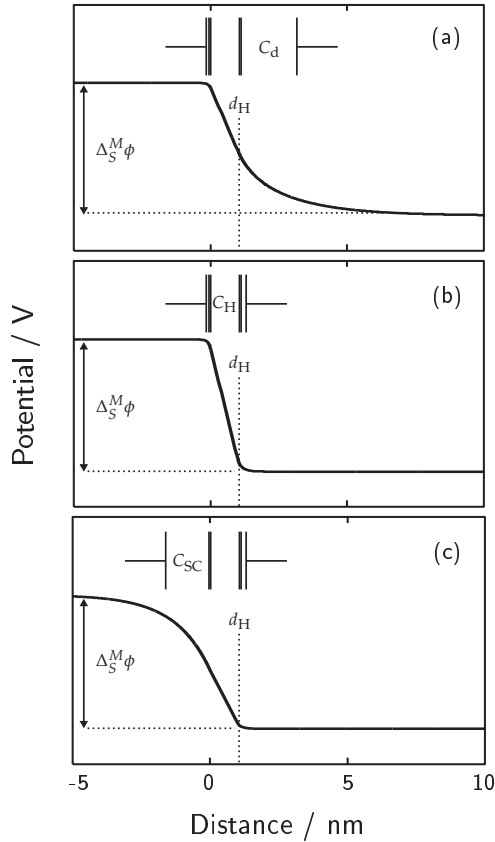
Figure 3.6.: Calculated potential profiles across the electrochemical double layer for (a) a metallic electrode and a dilute electrolyte (0.01 M), (b) an increased electrolyte concentration (1 M), and (c) a semi-metal in the concentrated electrolyte (1 M). In each case, the smallest capacitance of the different electrode/electrolyte contributions is given and visualized as the capacitance between two parallel plates.

In the third case (Figure 3.6c), the metallic electrode has been given a relatively low DOS of 10^{20} eV^{-1} cm^{-3}, a typical value for the semi-metal graphite [66, 70]. The screening length L_{TF} increases from 0.13 nm, i.e. less than the C–C bond length in graphite [71], to 1.3 nm. The corresponding potential decay in the space charge layer of the electrode is significant and results in a limiting space charge capacitance C_{SC} under

these conditions, as has been shown by Gerischer et al. for graphite electrodes [66, 70].

Finally, it should be mentioned that the potential profiles shown in Figure 3.6 do not take into account the specific adsorption of ions. In this respect, Bockris et al. [72] have reported the following important trends for aqueous solutions:

- anions are specifically adsorbed 3-4 times as much as cations of the same radius at a given charge, and

- ions of the same type are more easily specifically adsorbed with increasing ionic radius.

The above observations led Bockris et al. [72] to suggest the degree of solvation of the ions to be the decisive parameter for specific adsorption. In water, anions tend to be solvated less than cations, and larger ions tend to be solvated less than smaller ions. Hence, the enthalpy of solvation of ions may be used as a measure of the ease of specific adsorption. These trends apply likewise to non-aqueous electrolytes, with the degree of specific adsorption usually being greater than in aqueous electrolytes due to the smaller solvation number of the former [73]. It is worth noting that specific adsorption of ions can occur even on electrode surfaces carrying charge of the same sign [63, 72]. It is only upon sufficiently high polarization of the electrode that specifically adsorbed ions with the same sign of charge may be repelled.

Grahame [63] has shown how the potential profile across the electrochemical double layer can change dramatically due to specific adsorption. In Figure 3.7, the potential profiles across a model electrochemical system are shown schematically in which two identical electrodes are charged towards positive and negative potentials, respectively, starting from their electrode potentials immediately following immersion in the solution, E_{im}. In this particular example, anions are adsorbed at the electrode to which a positive charge has been applied, leading to a drastic change in the potential profile across the inner layer. Specific adsorption leads to a higher capacitance per unit interfacial area than non-specific adsorption due to the closer distance of approach of ions to the electrode, and may be envisaged as an additional capacitance in parallel with the inner Helmholtz layer [74].
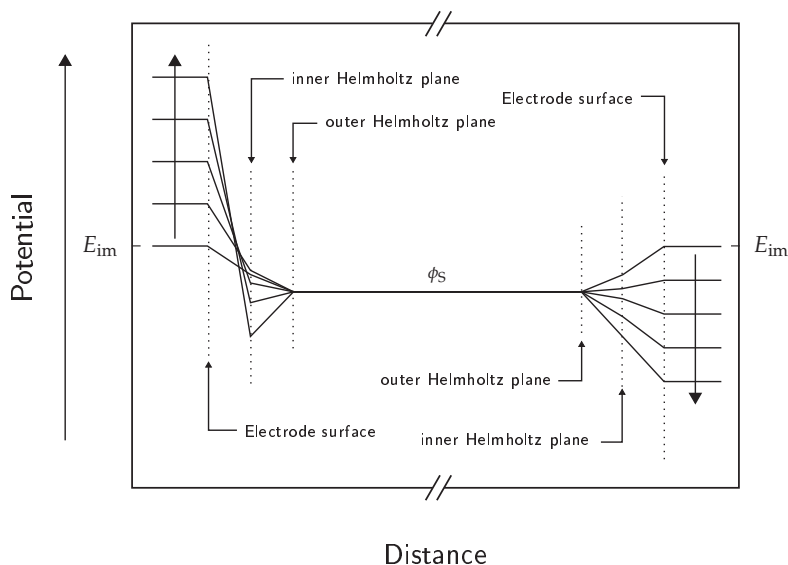
Figure 3.7.: Schematic potential profile of two identical electrodes upon polarization towards positive and negative potentials, respectively. Note the effect of specific adsorption of anions upon positive polarization. Adapted from [63].

For an ideally polarizable electrode, there exists one potential at which the interfacial charge of the electrode, σ_{SC}, is zero. This potential is referred to as the potential of zero charge (pzc) [51]. However, zero charge does not imply zero potential difference across the electrode/electrolyte interface [63], as oriented solvent dipoles within the inner Helmholtz layer result in a potential drop despite carrying no net charge.

If specific adsorption occurs, the number of adsorbed ions exceeds the corresponding counter-charge on the electrode due to the presence of covalent bonding in addition to electrostatic forces [63, 72]. In this case, the remaining net charge may be formally attributed to the electrode and is balanced by the total charge in the diffuse layer. The additional potential drop due to specific adsorption then occurs between the IHP and the solution bulk. Accordingly, the specific adsorption of anions results in a shift of the electrode potential towards more negative values, while for the specific adsorption of cations the electrode

potential shifts to more positive values [60, 75]. This is equivalent to stating that the pzc is shifted to more negative potentials for the specific adsorption of anions and to more positive potentials for the specific adsorption of cations [63, 72, 76].

3.4. Electrolytes in EDLCs

By referring to electrolytes in electrochemical systems, both the salt which provides the ions and the solvent in which the salt is dissolved are considered. Stringent use of the term electrolyte refers only to the salt, but it may also be used loosely as a convenient general description for the solution or medium which enables ionic conductivity.

The selection of electrolytes for EDLCs is centered around a few important criteria regarding their physical properties. From the discussion in Section 3.2, it is clear that the ionic conductivity should be as high as possible to minimize ohmic losses during current flow. Further, both high oxidative and reductive stability of the electrolyte is desirable in order to maximize the operating voltage window of the EDLC, which is beneficial for both energy content and power capability according to Equations (3.4) and (3.10). In order to provide a high capacitance contribution, a high electrolyte concentration, high dielectric constant and short distance of approach to the electrode appear favorable (Section 3.3). The electrolyte should maintain these properties in a wide operating temperature range, which for automotive applications has been targeted to lie between -30 °C and 52 °C [16]. Finally, the electrolyte should not pose a safety threat when the EDLC is used beyond specification limits and should have no harmful environmental impact during its synthesis and disposal.

Ue [77] has reviewed the properties of electrolytes for EDLCs and proposed the classification given in Table 3.2. Since electrodes in EDLCs possess a pronounced porosity (Section 3.5), solid electrolytes are generally deemed unsuitable. In the following, the basic properties of liquid electrolytes for EDLCs will be reviewed with respect to the selection criteria mentioned above.

Table 3.2.: Classification of electrolytes for electrochemical systems [77].

Aggregate state	Type	
Liquid	Aqueous	Acidic
		Alkaline
		Neutral
	Non-aqueous	Organic
		Inorganic
		Molten salt
Solid		Organic
		Inorganic

Regarding electrolyte conductivity, the following force balance may be considered when a potential difference is applied between two (parallel) electrodes:

$$ze\mathcal{E} = 6\pi\eta r v_{max} \tag{3.44}$$

where $ze\mathcal{E}$ is the force acting on an ion of valency z in the electric field $\mathcal{E}$, while the term on the right hand side is the opposing drag force acting on the same ion, where r is the effective radius and v_{max} its terminal velocity in the solution with dynamic viscosity η [78]. The ionic current I flowing in an electrolyte through a cross-section A is then the sum of the contributions of the negatively and positively charged ions which travel in opposite directions under the influence of the electric field:

$$I = Ae(n^+ z^+ v_{max}^+ + n^- z^- v_{max}^-) \tag{3.45}$$

in which n, z and v_{max} are the number concentration, valency and terminal velocity of the cations ($+$) and anions ($-$), respectively. For large parallel plate electrodes, the electric field $\mathcal{E}$ is related to the applied potential difference U between the electrodes by $U = \mathcal{E}d$, where d is the distance between the electrodes. Thus, substituting the expression for v_{max} from (3.44) into (3.45),

$$I \quad = \quad \frac{A}{d} \frac{e^2}{6\pi\eta} \left(\frac{n^+(z^+)^2}{r^+} + \frac{n^-(z^-)^2}{r^-} \right) U \qquad (3.46)$$

$$= \quad \frac{A}{d}\sigma U \qquad (3.47)$$

where σ is the conductivity of the electrolyte independent of the geometry of the electrode arrangement. Thus, in order to obtain a high electrolyte conductivity, a low viscosity (η), high charge concentrations (z^+n^+, z^-n^-) and small ionic radii (r) are desirable. It should be noted that the effective ionic radius depends on the extent of solvation of the ion, which tends to be greater with decreasing radius of the ion itself. Further, the charge concentration does not increase monotonically with the molarity of the electrolyte, since coulombic forces of attraction between charges of opposite sign become significant as the mean distance between ions decreases. This ion association effectively results in a screening of the ionic charge, causing the resulting ion pair to behave like a neutral molecule when the distance of approach becomes less than the Bjerrum critical distance q [79, 80]:

$$q = \frac{| z^+z^- | e^2}{8\pi\epsilon_0\epsilon k_B T} \qquad (3.48)$$

According to (3.48), ion association is most likely to occur in electrolytes with a low dielectric constant ϵ and ionic valencies $z > 1$. Ion association can be avoided when the distance of closest ionic approach, which is the sum of the effective ionic radii, is greater than q. It should be mentioned that it is rather difficult to engineer these ionic radii and dielectric constants when dealing with electrodes which confine the electrolyte in very narrow pores, as is the case in EDLCs (Section 3.5). This is due to the uncertainty involved in the extent of ion solvation under these circumstances [81] and the fact that the dielectric constants of electrolyte species in the Helmholtz layer are significantly reduced [68].

Apart from ionic conductivity, the maximum operating voltage of an electrolyte is one of the most important characteristics for electrochemical energy storage. Unfortunately, the measurement of this property is very sensitive to the experimental conditions, including the kind of electrode employed, and is subject to more or less arbitrary experimental criteria. For instance, stability windows of electrolytes are often

assessed by applying linear potential ramps to a flat electrode such as glassy carbon or platinum against a reference electrode, both of which are immersed in the electrolyte under investigation. An increase in current flow is taken to be a measure for the onset of faradaic charge transfer across the electrode/electrolyte interface, thus signaling the decomposition of the electrolyte. However, it will be shown in the following that this measurement usually grossly overestimates the electrolyte stability window.

Xu et al. [82, 83] have proposed a more relevant criterion for the electrochemical stability window of electrolytes, which is based on the coulombic discharge efficiency (CDE) of technically relevant electrodes in progressively larger potential windows. For instance, the electrochemical stability window of a 1 M solution of Et_4NBF_4 in propylene carbonate (PC) has been reported to be 6.65 V [77] on glassy carbon using a cut-off current criterion of 1 mA per cm^2 of geometric electrode area. This voltage is far beyond the operating voltages of any commercially available electrochemical cell. Based on an operating window in which 90 % of the charge is recovered upon discharge, Xu et al. [82] find a value of 2.2 V for a similar electrolyte, 1 M Et_4NPF_6/PC, on an activated carbon electrode. The latter value is more representative of practically relevant conditions encountered in EDLCs, which typically have a specified operating voltage window of 2.7 V [8].

Despite the above complications in relation to potential window measurements, it has been found that the trends in electrochemical stability windows which have been measured on nonporous electrodes such as glassy carbon or platinum using arbitrary cut-off criteria often reflect the trends encountered under more technically relevant conditions [82]. For this reason, it is convenient to give an overview of aqueous and non-aqueous electrolytes in terms of their conductivities and voltage windows (Figure 3.8), noting that the experimental voltage windows depend critically on the measurement conditions and that the bulk specific conductivities of the electrolytes may be significantly reduced within porous electrodes (Section 3.5). From Figure 3.8, it is clear that aqueous electrolytes are advantageous in terms of conductivity, while the non-aqueous electrolytes are superior in terms of electrochemical stability. The thermodynamic stability of aqueous electrolytes is mostly

limited by the onsets of H^+ reduction, resulting in H_2 evolution at $0\,V$ vs. SHE, and H_2O oxidation, resulting in O_2 evolution at $+1.23\,V$ vs. SHE [60, 78].

In addition to their high conductivity, aqueous electrolytes generally offer advantages in terms of cost and environmental impact in comparison with non-aqueous electrolytes. Further, the capacitance of activated carbon electrodes in aqueous electrolytes is typically twice as large as in non-aqueous electrolytes [90], which may be attributed to the protonation of oxygen-containing surface functional groups or basal planes of graphene (Section 4.6), smaller effective ion size and higher dielectric constant in aqueous solutions. This protonation may be regarded as the localized specific adsorption of hydrogen ions onto the carbon through covalent bond formation, which contributes capacitance according to the discussion in Section 3.3. Hence, the capacitive behavior of activated carbons in aqueous electrolytes consists of a considerable pseudocapacitive contribution.
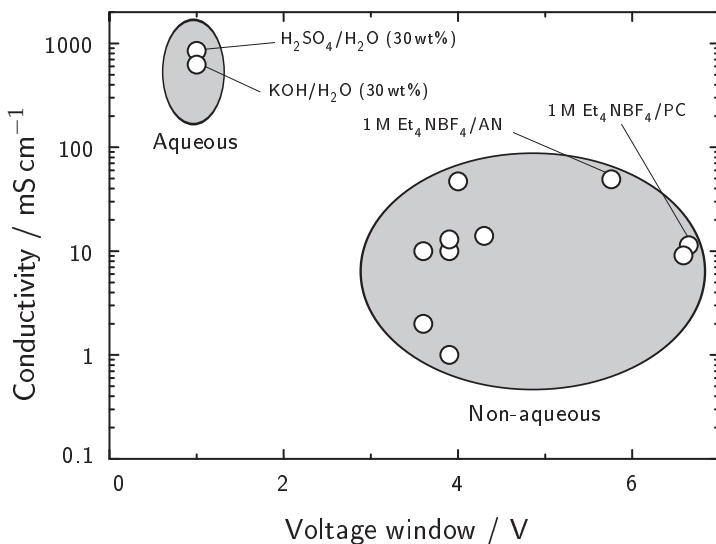
Figure 3.8.: Approximate specific conductivities and voltage windows of a selection of electrolytes for EDLCs measured on glassy carbon [77, 84–89].

However, aqueous electrolytes also exhibit several drawbacks. Besides the significantly lower voltage window in comparison with non-aqueous electrolytes (Figure 3.8), corrosion of the metallic current collectors is often problematic. Also, it has been shown that the ionic conductivity of electrolytes in micropores is considerably lower than in the bulk, as will be discussed further in Section 3.5. For aqueous electrolytes, Kastening et al. [91] have estimated a drop in conductivity by one order of magnitude when the electrolyte is confined within micropores. For a carbon electrode with a given porosity, a similar behavior is also observed in non-aqueous electrolytes, for even though the interaction between ions and functional groups on the carbon is expected to be less than in aqueous systems, the steric hinderance due to the functional groups remains [90].

In Figure 3.9, the specific energy and power are plotted as a function of the EDLC voltage using representative values for aqueous and non-aqueous systems. This rough comparison illustrates how the larger voltage window of non-aqueous electrolytes provides a significantly higher specific energy than aqueous electrolytes while maintaining a comparable specific power. Thus, it is understandable that the use of non-aqueous electrolytes such as $1\,M$ solutions of Et_4NBF_4 in acetonitrile (AN) or PC has become the industrial standard for EDLCs.

Regarding the temperature sensitivity of these electrolytes, it has been shown that the AN-based electrolyte retains its properties to a considerable extent down to -30 °C, while the PC-based electrolyte features a significant loss of performance below 0 °C [35, 92]. Regarding the upper temperature limit, it has been established that a temperature increase of 10 °C results in a lifetime reduction by a factor of approximately 2 [35] (see also discussion in Section 5.2.2). It is worth noting that a critical upper limit for AN-based electrolytes is the boiling temperature of AN at 82 °C [77]. For comparison, the boiling temperature of PC is 242 °C [77]. These and other properties of the two solvents are compiled in Table 3.3.

Finally, it is instructive to highlight a key difference between electrolytes used in lithium-ion batteries (LIBs) and EDLCs. While faradaic reactions are avoided in the latter, they are an essential part of LIB chemistry in order to obtain a passivating film on both the neg-
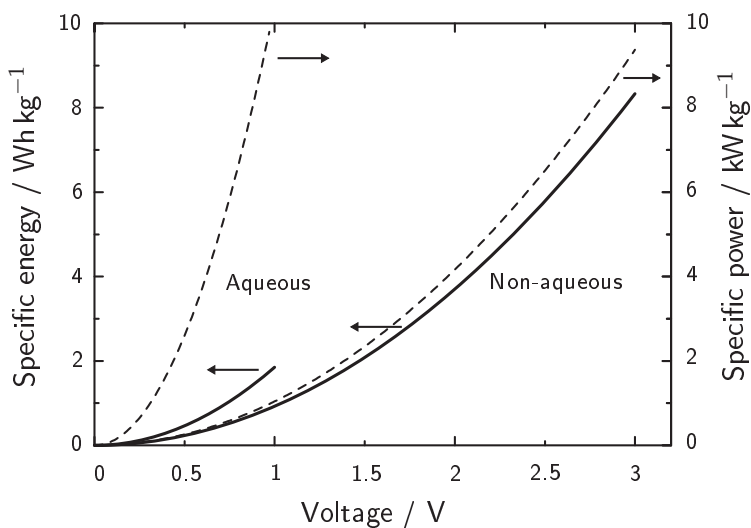
Figure 3.9.: Comparison of aqueous and non-aqueous electrolytes in terms of estimated specific energy and matched impedance power based on Equations (3.4) and (3.7). For the non-aqueous electrolyte, a specific capacitance of 20 F/g and specific resistance of 0.08 Ω g [8] (referring to total electrode mass) were assumed, while twice this capacitance and a tenth of this resistance were assumed for the aqueous electrolyte. The plotted curves take into account additional packaging components by multiplying the total electrode mass by a factor of 3.

ative [97, 98] and positive Li$^+$ insertion electrodes, as extensively reviewed by Xu [99]. The thus obtained solid electrolyte interphase (SEI), a term initially coined by Peled [100] for alkali and alkaline earth metal batteries, prevents further decomposition of the electrolyte and cointercalation of solvent, enabling operating voltages in the order of 4 V.

Jänes and Lust [86] evaluated a series of organic carbonates and esters as solvents and co-solvents for EDLCs in various binary, tertiary and quaternary mixtures similar to those used in LIBs. While some of these mixtures were competitive with the PC-based electrolyte used in EDLCs, the electrolyte resistance within pores was found to increase significantly at higher cell voltages with respect to both the AN- and PC-based electrolytes. Therefore, there appear to be no advantages of these solvent mixtures over the currently employed EDLC electrolytes,

Table 3.3.: Selected properties of acetonitrile (AN) and propylene carbonate (PC) [77, 86, 93, 94].

	AN	PC
Molecular formula	CH_3CN	$CH_3C_2H_3CO_3$
Melting temperature / °C	-44	-49
Boiling temperature / °C	82	242
Density at 25 °C / $g\,cm^{-3}$	0.776	1.20
Relative permittivity ϵ / –	35.9	62.9
Dipole moment[a] / D	3.95	4.77
Molar volume / $cm^3\,mol^{-1}$	52.9	85.1
Conductivity[b] σ at 10 °C / $mS\,cm^{-1}$	56	13
Polarity[c] E_T / $kcal\,mol^{-1}$	45.6	46.0
Donicity[d] DN / $kcal\,mol^{-1}$	14.6	14.9
Vapor pressure[e] / Pa	9710	17
Viscosity[e] / mPa s	0.37	2.5

[a] D stands for the debye unit, $1D \approx 3.34 \cdot 10^{-30}\,C\,m^{-1}$.
[b] Measured in a solution containing $1\,M\,Et_4NBF_4$ [95, 96].
[c] Widely used empirical solvent polarity scale [93]. E_T is defined as the molar transition energy for the long wavelength electronic transition of a particular dye [93] as a solution in the solvent.
[d] Widely used donicity scale for solvents [93]. DN is defined as $-\Delta H^{\circ}_{SbCl_5}$, where $\Delta H^{\circ}_{SbCl_5}$ is the standard enthalpy change for the formation of a 1:1 adduct between $SbCl_5$ and the solvent [93].
[e] Values at 20 °C.

apart from concerns regarding the toxicity of AN for certain applications [8].

3.5. Electrodes in EDLCs

In this section, the basic requirements for electrodes in EDLCs will be outlined. Based on the previous discussions in this chapter, these requirements may be formulated without specifying the actual electrode material itself. In fact, it will become apparent that carbonaceous materials in various forms represent ideal electrode materials for EDLCs. Due to the diversity of carbonaceous materials and their importance in

EDLCs, a review of their relevant properties will be presented separately in Chapter 4.

As defined in Section 3.1, true non-faradaic charge storage relies on an ideal capacitive behavior of the electrochemical double layer. Hence, electrode materials in EDLCs must exhibit the characteristics of an ideally polarizable electrode (Section 3.3.2) as closely as possible. In order to obtain a system in which no faradaic reactions occur over the entire operating potential window, it is the choice of the electrode/electrolyte combination which is essential. For the combination of certain carbon materials with the preferred non-aqueous electrolytes presented in Section 3.4, a relatively wide potential range seems to exist in which the conditions of the ideally polarizable electrode are closely met.

In addition to ideal polarizability, the electrode material must have a high electrical conductivity in order to minimize ohmic losses during current flow and exhibit a high space-charge capacitance through a high charge carrier density (Section 3.3.2). Assuming this condition to be fulfilled, and that the electrolyte used exhibits a sufficiently high concentration, the double layer capacitance is dominated by the capacitance of the Helmholtz layer. Recalling Equation (3.21), this capacitance is proportional to the interfacial area between the electrode and the electrolyte. Assuming a perfect wettability of the electrode by the electrolyte, it appears as though a maximization of the electrode surface area is essential to achieve a high capacitance, all the other parameters in (3.21) being given by the choice of the electrolyte.

However, a saturation of the gravimetric capacitance with increasing gravimetric surface area as measured by gas adsorption has been observed experimentally [101, 102]. As the gravimetric surface area increases for a material of given porosity, both the pore size and size of the solid domains are reduced. As the pore size drops to comparable dimensions as the ions or even lower, the surface area within these pores becomes inaccessible to the electrolyte and provides no additional capacitance contribution [81, 102]. In this case, ion-sieving occurs in which larger ions do not occupy small pores [101, 103–107]. Further, the size of the solid domains may approach the extension of the space-charge layer (Section 3.3), in which case the capacitance limitation is on the electrode side [101, 108].

The maximization of the electrode surface area is therefore not the essential parameter resulting in a high capacitance, but rather an optimization of the pore size distribution with respect to the ions involved in double layer charging along with a sufficiently high space-charge capacitance. As will be shown later in this work, both of these properties in fact depend on the electrode potential and require in situ studies in order to obtain information which is practically relevant for EDLCs.

It should also be noted that a pore size which is considerably larger than the entire electrochemical double layer may result in an appreciable amount of volume which does not contribute to the capacitance, with the consequence of low values for the volumetric capacitance in $F\,cm^{-3}$, but also a low gravimetric capacitance when the voids are filled with excess electrolyte. However, a certain electrolyte reservoir is needed to provide a sufficient number of ions for charging of the double layer and avoid a depletion of the electrolyte (electrolyte starvation) [109].

Bearing in mind the above considerations with respect to the pore size distribution and space-charge limitation of the electrode, it is important to highlight that the transient behavior of EDLCs is dominated by the pronounced porosity of the electrode. As a result, the effective usable depth of the pores depends on the rate at which current is drawn from the EDLC. This situation may be represented by an *RC* transmission line as shown in Figure 3.10. Notably, the application of this equivalent circuit to porous electrodes in electrochemical systems was treated by De Levie [110, 111] and later extended by Keiser et al. [112] to include the effects of varying pore shapes.

It is illustrative to describe the behavior of the equivalent circuit in Figure 3.10 at different frequencies of alternating current or potential (corresponding to different rates of charge and discharge). Assuming a cylindrical pore with radius *r* and depth *l*, the total capacitance of the pore can be written as:

$$C_{\text{pore}} = 2\pi r l C_{\text{S}} \tag{3.49}$$

where C_{S} is the specific capacitance in $F\,m^{-2}$. The capacitance contribution of the pore bottom has been neglected, which is justifiable for
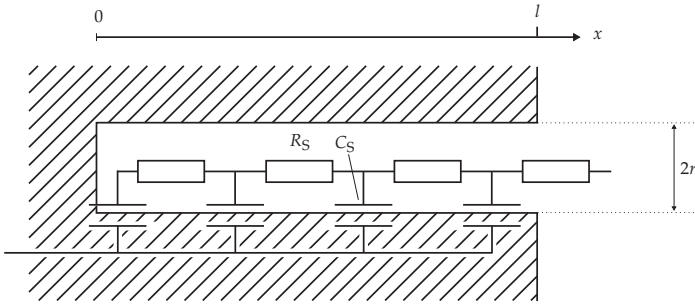
Figure 3.10.: Distribution of resistive and capacitive components within a pore for an ideally polarizable electrode.

pores with large aspect ratios. The total resistance of the pore is given by

$$R_{\text{pore}} \quad = \quad \frac{l}{\sigma \pi r^2} \tag{3.50}$$

in which σ is the conductivity of the electrolyte in $(\Omega\,\text{cm})^{-1}$. Now, the equivalent circuit in Figure 3.11 is considered.

Following the approach of De Levie [110, 111], the potential and current along the transmission line are denoted by E and I, respectively. R' and Z' denote the respective impedances (Section 7.5) per unit pore length, whereby all R' are connected in series while all Z' are connected in parallel. If a homogeneous distribution of R' and Z' is assumed along the entire length l of the pore, R' and Z' are given by
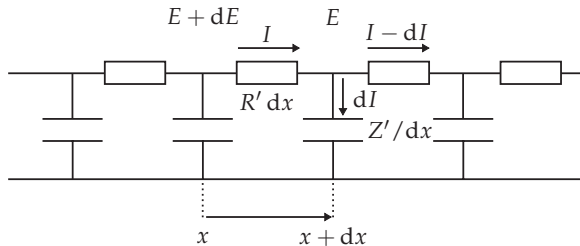
Figure 3.11.: Potentials, currents and impedances involved in an infinitesimally small segment of an RC transmission line circuit. Adapted from [110, 111].

$$R' = \frac{R_{\text{pore}}}{l} \tag{3.51}$$

$$Z' = \frac{l}{i\omega C_{\text{pore}}} \tag{3.52}$$

where ω is the angular frequency of the applied alternating potential. The impedance of EDLCs will be described in more detail in Section 7.5. Referring to Figure 3.11, the following differential equations are valid:

$$
\begin{aligned}
dE &= -IR'\,dx \\
\frac{dE}{dx} + IR' &= 0
\end{aligned}
\tag{3.53}
$$

and

$$
\begin{aligned}
dI &= -\frac{E}{Z'}\,dx \\
\frac{dI}{dx} + \frac{E}{Z'} &= 0
\end{aligned}
\tag{3.54}
$$

By differentiating (3.53) and (3.54) with respect to x and combining the resulting equations, one obtains

$$\frac{d^2E}{dx^2} - \frac{R'}{Z'}E = 0 \tag{3.55}$$

$$\frac{d^2I}{dx^2} - \frac{R'}{Z'}I = 0 \tag{3.56}$$

The case is considered in which $E(x = 0) = E_0$ at one end of the transmission line and $(dE/dx)_{x=l} = 0$ at the entrance of the pore. Using the ansatz

$$E = K_1 \sinh\left(x\sqrt{\frac{R'}{Z'}}\right) + K_2 \cosh\left(x\sqrt{\frac{R'}{Z'}}\right) \tag{3.57}$$

the following solution for E is obtained:

$$E = E_0 \cosh\left(x\sqrt{\frac{R'}{Z'}}\right) - E_0 \tanh\left(l\sqrt{\frac{R'}{Z'}}\right) \sinh\left(x\sqrt{\frac{R'}{Z'}}\right) \tag{3.58}$$

It follows that

$$
\begin{aligned}
I &= -\frac{1}{R'}\frac{\mathrm{d}E}{\mathrm{d}x} \tag{3.59}\\
&= -\frac{E_0}{\sqrt{R'Z'}}
\end{aligned}
$$

$$
\cdot\left[\sinh\left(x\sqrt{\frac{R'}{Z'}}\right) - \tanh\left(l\sqrt{\frac{R'}{Z'}}\right)\cosh\left(x\sqrt{\frac{R'}{Z'}}\right)\right] \tag{3.60}
$$

When evaluating the current I at the end of the pore, $x = 0$, (3.60) becomes

$$
I(x = 0) = \frac{E_0}{\sqrt{R'Z'}\coth\left(l\sqrt{\frac{R'}{Z'}}\right)} \tag{3.61}
$$

From Equation (3.61), it can be seen that the pore behaves like an impedance Z_{pore} defined by

$$
Z_{\mathrm{pore}} = \sqrt{R'Z'}\coth\left(l\sqrt{\frac{R'}{Z'}}\right) \tag{3.62}
$$

In the case of multiple (identical) pores, these may be considered as connected in parallel, resulting in a total impedance $Z_n = Z_{\mathrm{pore}}/n$ for n pores.

Despite the crude approximation of perfect cylindrical channels in place of real pore shapes, Equation (3.62) provides a convenient means of describing the effect of the porous electrode structure on the transient behavior of EDLCs. For a fixed porosity of $\pi r^2 n/A = 0.8$, where n/A is the number of pores per unit geometric area, the capacitance can be plotted as a function of the frequency $f = 2\pi/\omega$ under different conditions (Figure 3.12). The total capacitance was calculated from the imaginary part of the impedance, $C = 1/\omega\,\mathrm{Im}(Z_n)$.

An immediate consequence of the *RC* transmission line is that the maximum capacitance is not accessible at all frequencies. In the high frequency limit, only a fraction of the theoretical double layer capacitance is available due to the distributed resistance within the porous electrode. At a given frequency, the effectively used surface area within the pores decreases with decreasing electrolyte conductivity and pore

radius and with increasing pore length (Figure 3.12). One can define a penetration depth, λ, which describes the fraction of the pore length actually involved in double layer charging [111, 112]. The expression $\sqrt{Z'/R'}$ in Equation (3.62) has the dimension of a length and may be used as a measure for the penetration depth into a single pore according to

$$\lambda = \sqrt{\frac{l^2}{\omega C_{\mathrm{pore}} R_{\mathrm{pore}}}} = \sqrt{\frac{\sigma r}{2\omega C_{\mathrm{S}}}} \tag{3.63}$$

For $\lambda > l$, virtually all of the pore is accessible. In conclusion, it must be recognized that the dimensioning of electrodes for EDLCs is ultimately a compromise between a high rate capability and high capacitance. From Figure 3.12c, it can be seen that an increase in volumetric capacitance at a given porosity may be achieved by employing an electrode with a more finely distributed porosity, so that the ratio of internal surface area to total electrode volume is high. However, such an electrode features a more pronounced distributed resistance, resulting in an advantage over electrodes with larger pore dimensions only at sufficiently low frequencies. Therefore, an electrode must not only be tailored according to the electrolyte (Section 3.4), but also according to the power demand of the intended application.
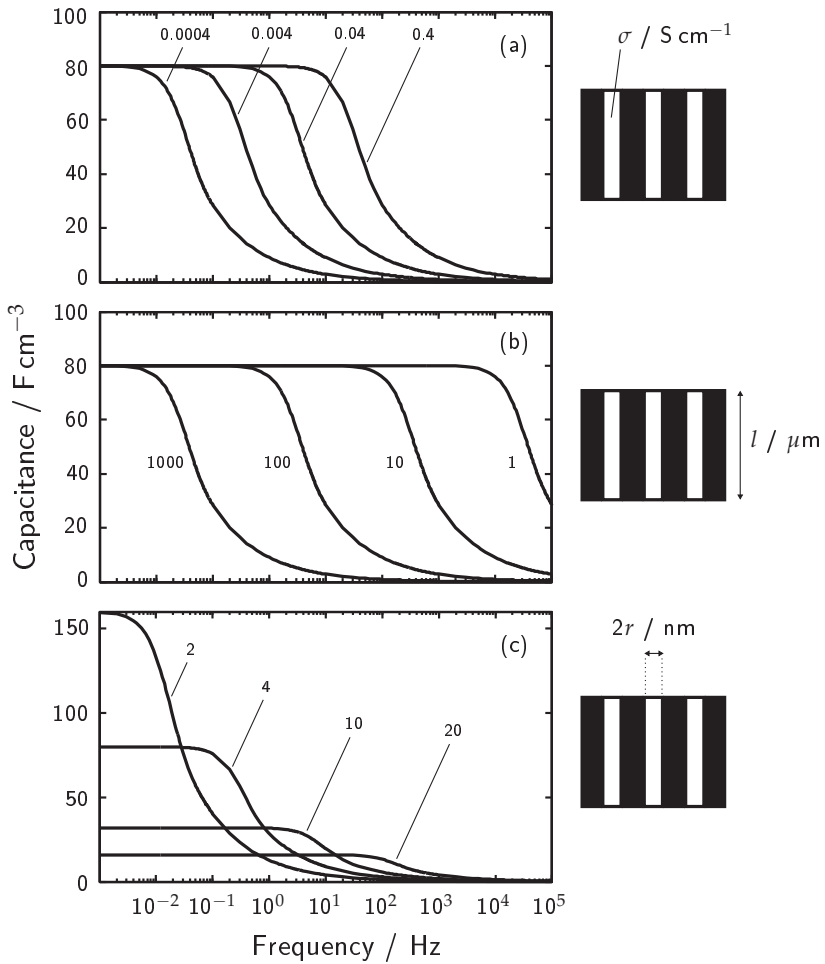
Figure 3.12.: Effect of electrolyte conductivity σ (a), pore length l (b) and pore diameter $2r$ (c) on the volumetric double layer capacitance as a function of frequency. Unless otherwise specified, $\sigma = 40\,\mathrm{mS\,cm^{-1}}$, $r = 2\,\mathrm{nm}$, $C_S = 10\,\mu\mathrm{F\,cm^{-2}}$ and $l = 100\,\mu\mathrm{m}$. The porosity of the electrode was fixed at 0.8 in all cases.

Chapter 4.

The structure of carbons used in EDLCs

4.1. The element carbon

The element carbon forms the basis of a vast range of compounds which span a considerable spectrum of properties. Being the sixth element of the periodic table, carbon has six electrons with the ground state configuration of $1s^2 2s^2 2p^2$. In the formation of bonds, an electron from the 2s orbital may be promoted to an empty 2p orbital, after which different hybridizations of the 2s and 2p orbitals may take place. The energy required for promotion and hybridization is more than compensated for by the formation of bonds with other atoms [113–115]. The hybrid orbitals result from the combination of one 2s orbital with n 2p orbitals, resulting in $n + 1$ sp^n orbitals with $n = 1$, 2 or 3 [115]. The shapes of these hybrid orbitals are shown in Figure 4.1.

In the sp^3 configuration, each of the four valence electrons of carbon is assigned to a hybrid sp^3 orbital which is separated by the nearest neighboring orbital by an angle of 109.5 °. Each of the sp^3 orbitals can participate in a strong σ bond with an adjacent atom. A solid made of purely sp^3 hybridized, tetrahedrally coordinated carbon may form the
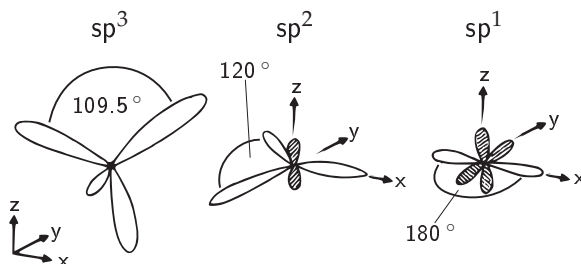
Figure 4.1.: Schematic representation of sp^3, sp^2 and sp^1 hybridized carbon atoms and corresponding atomic orbitals. Adapted from [116].

cubic (diamond) or hexagonal (lonsdaleite) structures which differ in their stacking order (ABCABC vs. ABAB, respectively) [114].

For sp^2 hybridized carbon, three valence electrons are assigned to the trigonally directed sp^2 orbitals which can participate in σ bonds within the same plane, while the fourth electron lies in the p$_z$ orbital perpendicular to the bonding plane and can participate in weaker π bonds with adjacent orbitals [116]. In the sp^1 configuration, two valence electrons in two sp orbitals can participate in σ bonds which are oriented at 180 $^\circ$ to each other, and the remaining two valence electrons are assigned to the p$_z$ orbitals which can contribute to π bonds.

The chemical bonding between two carbon atoms via both a σ and a π bond is called a double bond. In the sp^2 and sp^1 configurations, only one electron is available per π orbital to bond to all neighboring atoms. Thus, when more than two carbon atoms are involved in such binding configurations, there exist multiple possible arrangements in-

Table 4.1.: Possible classification of mainly sp^2 hybridized carbonaceous solids. Different types of carbon fibers have not been included. Adapted from [117–120].

Graphitic	Natural graphite		
	Synthetic graphite		
Non-graphitic	Graphitizable	Cokes	Petroleum based
			Coal-based
		Pitches	Petroleum based
			Coal tar based
			Synthetic
		Mesocarbon microbeads	
	Non-graphitizable	Synthetic polymers	Thermoplasts
			Thermosets
		Carbon blacks	
		Glassy carbon	
		Chars	
		Coals	Anthracitic
			Bituminous
			Subbituminous
			Lignite
		Activated carbons	
		Fullerenes	

volving different placements of the π electrons, leading to a delocalization of the π electrons in so-called resonance structures [113]. These structures are particularly stable when they are aromatic, which is the case when carbon atoms form cyclic compounds in which there are ($4N$ + 2) π electrons. This is known as Hückel's rule of aromaticity, where N is a whole number [121].

All carbonaceous materials which are electronically conducting, and hence candidate electrode materials for EDLCs, contain a significant fraction of sp^2 hybridized carbon and delocalized π electrons. An overview of a possible classification of sp^2 hybridized carbons is given in Table 4.1. In the following section, the basic properties of the simplest form of sp^2 bonded carbon, graphene, will be discussed. Afterwards, some important characteristics of graphitic and different types of non-graphitic carbon will be described. In this context, the review by Pandolfo and Hollenkamp [122] concerning different carbonaceous materials used in EDLCs is also worth mentioning.

4.2. Graphene: building block for carbon electrodes

The term graphene describes a single layer of polycyclic aromatic hydrocarbon of a size much larger than the constituent individual aromatic rings [118]. It may be viewed as the basic two-dimensional building block for all sp^2 hybridized carbonaceous materials [123]. A stacked arrangement of about ten or more graphene layers tends to exhibit the bulk properties of graphite [124]. Hence, it has become colloquial custom to refer to single-, double- and few-layer graphene [123]. In the present work, however, graphene is used exclusively as the description of the strictly two-dimensional sheet of aromatic carbon.

Graphene has received increasing attention in recent years, partly due to the advancement of techniques for its synthesis on the laboratory scale. These techniques include annealing of silicon carbide at elevated temperatures under vacuum [125, 126], repeated cleaving of highly oriented pyrolytic graphite [123] and the reduction of graphite oxide [127, 128].

Considering an idealized, free-standing graphene sheet (Figure 4.2), there are two carbon atoms per unit cell of area $3\sqrt{3}(d_{C-C})^2/2$. The

mass of the two carbon atoms is $2 \cdot 12 \, \text{g} \, \text{mol}^{-1}/N_A$, where N_A is Avogadro's number. The specific geometric surface area of one side of graphene thus amounts to $1315 \, \text{m}^2\text{g}^{-1}$, or $2630 \, \text{m}^2\text{g}^{-1}$ for both sides. The Connolly surface area of graphene, which takes into account the atomic roughness by means of a hypothetical probe molecule, is even higher ($2965 \, \text{m}^2\text{g}^{-1}$) [129].

First studies of the electronic structure of graphene were performed by Wallace [130] in 1947 in the context of investigations on the electronic properties of graphite. In the tight-binding approximation, also referred to as the linear combination of atomic orbitals (LCAO) [53], a superposition of individual atomic orbitals results in the band structure of the extended graphene sheet. Per unit cell, each of the two carbon atoms contributes a p_z orbital and one π electron, leading to the formation of the π and π^* bands in graphene. Since each band may accommodate two electrons per unit cell, the lower energy π band will be completely filled and the π^* band will be completely empty (neglecting temperature and doping effects).

Often, it is convenient to express the band structure as a function of the electron wave vector, k, whose magnitude is related to the electron wavelength λ by $|k| = 2\pi/\lambda$. For this purpose, a reciprocal lattice is constructed according to Figure 4.2b with the unit cell vectors defined by $b_{1,2} \perp a_{2,1}$ and $|b_{1,2}| = 2\pi/|a_{2,1}|$. For a given reciprocal lattice point, it is useful to define the first Brillouin zone [53] which contains all values of k which are closer to this reciprocal lattice point than to any other reciprocal lattice point. The first Brillouin zone contains all information about the band structure of the lattice. The band dispersion of graphene [131, 132] within the first Brillouin zone is plotted in Figure 4.3.

From Figure 4.3, it can be deduced that the π and π^* bands touch at the K point of the Brilloin zone, coinciding with the Fermi level ε_F. Hence, graphene behaves like a zero-gap semiconductor or zero-overlap semimetal in which electronic conduction is only enabled by thermally excited electrons (and holes) with wavevectors near the K point. The π and π^* bands are the valence and conduction bands, respectively, while the contribution of the σ and σ^* bands towards conductivity can

(a) (b)
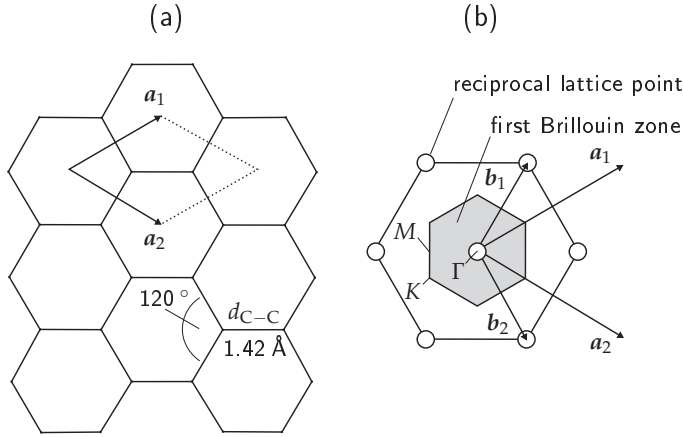
Figure 4.2.: (a) C−C bonding framework in a graphene fragment along with the corresponding bond length and angle, respectively. The unit cell vectors in real space are denoted by a_1 and a_2, where $|a_1| = |a_2| = \sqrt{3}\,d_{C-C}$. (b) Reciprocal lattice with the unit cell vectors b_1 and b_2 and the corresponding Brillouin zone.

be neglected. Near the K point, the valence and conduction bands are practically symmetrical with respect to the Fermi level.

The number of allowed electronic states per unit cell for a given energy ε is summarized in the DOS, $D(\varepsilon) \propto 1\,/\,\mathrm{grad}_k \varepsilon(k)$. Using the tight-binding approximation and assuming symmetric π and π^* bands, Robertson [116] calculated the DOS of graphene sheets with an increasing number of aromatic rings (Figure 4.4). In this case, the energy has been expressed in units of the overlap integral γ_0 (C−C nearest-neighbor interaction energy). It is clear that the DOS may be significantly modified for graphene clusters less than approximately 10 nm in size, with the possible emergence of a band gap. Also, it has been shown that the presence of defects such as vacancies [133] or sp^3 clusters [116] within graphene can increase the density of states at the Fermi level significantly [116, 134, 135]. Upon stacking of several graphene sheets, the valence and conduction bands experience an increasing overlap until the band structure of bulk graphite is obtained (band overlap of a few tens of meV depending on the stacking order) [124, 131, 136–138].
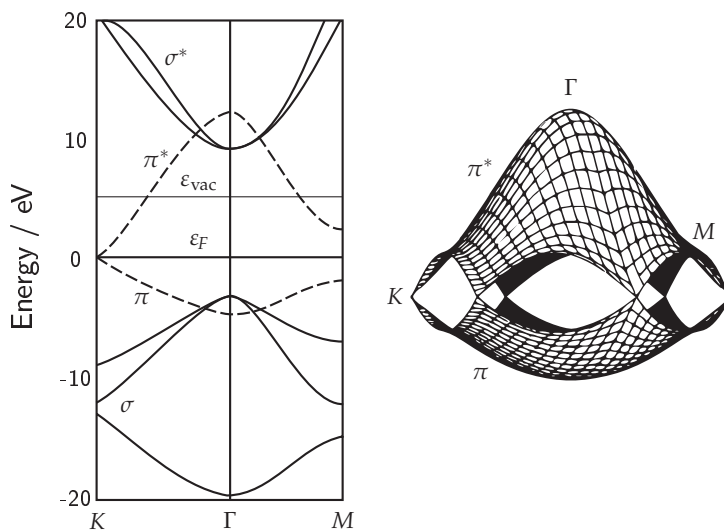
Figure 4.3.: Energy dispersion of graphene within the first Brillouin zone [131, 132] for the σ and σ^* bands (solid lines) as well as the π and π^* bands (dashed lines). The Fermi level is denoted by ε_F while the vacuum level is represented by $\varepsilon_{\mathrm{vac}} \approx \varepsilon_F + 4.7\,\mathrm{eV}$ [116].

Due to the electronic conductivity and high specific surface area of graphene, it is an obvious candidate electrode material for EDLCs. However, the first trial experiments in this direction report specific capacitances of $99\,\mathrm{F\,g^{-1}}$ (using $1\,\mathrm{M}$ Et_4NBF_4 in AN [139]) and $117\,\mathrm{F\,g^{-1}}$ (in H_2SO_4 [140]), which is at best similar to existing electrode materials made of activated carbon [90]. It should be noted that the measured specific surface areas of the electrodes in both cases were below $1000\,\mathrm{m^2\,g^{-1}}$, i.e. significantly less than the theoretical value for a free-standing graphene sheet.

A practical concern related to graphene electrodes may be the fact that the thickness of a graphene sheet is clearly less than the thickness of the according space charge layer in the uncharged state, as was discussed for graphite in Section 3.3.2. The double layer capacitance is thus certainly limited by the graphene electrode at low polarizations. This limitation might be overcome through the modification of the density of states through defects, as mentioned above, or through doping with foreign atoms. However, in the case of materials with a low DOS
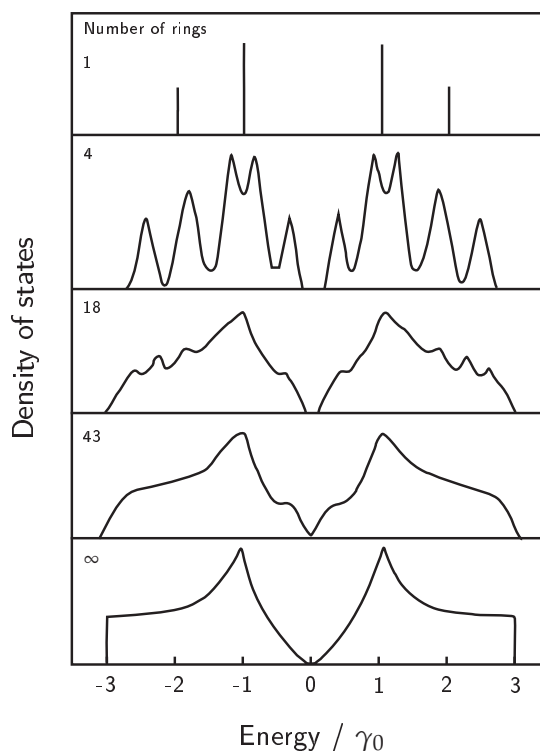
Figure 4.4.: Density of states for graphene sheets of increasing size plotted against the energy relative to the Fermi level in units of $\gamma_0 = 2.9\,\text{eV}$. Only the π and π^* bands are shown. After Robertson [116].

at the Fermi level (such as graphene and graphite), it should be noted that the position of the Fermi level within the band structure changes with the electrode potential, leading to an increase in the DOS and a corresponding increase in the space charge capacitance. Therefore, the space charge limitation tends to be more pronounced when the electrode is in the uncharged state, which is a situation rarely encountered in practical applications.

4.3. Fullerenes and nanotubes

While graphene is the prototypical planar sp^2 hybridized carbon material, there is evidence suggesting that a pronounced curvature of

graphene-like structures occurs in systems confined to the nanometer scale [141]. Although hexagonal graphite (Section 4.4) is the thermodynamically stable form of carbon under ambient conditions, the driving force towards curvature of small graphene fragments is the elimination of unpaired electrons (dangling bonds). Marsh and Rodríguez-Reinoso [142] argue that this process is very fast, and may thus take place irreversibly before graphitic structures are formed.

Originally, the class of fullerenes described strictly cage-like, polycyclic structures consisting of twelve five-membered rings and the rest six-membered rings [143]. The first reported representative of this class was the molecule C_{60}, named buckminsterfullerene by Kroto et al. [144]. However, the family of fullerenes has been extended to include all closed-cage structures consisting entirely of three-fold coordinated carbon atoms [143].

In fact, such closed cages were already reported to exist within the inner core of common carbon fibers in 1976 in form of a hollow central tube [145]. As a byproduct of experiments aiming at the synthesis of fullerenes through arc discharge evaporation, Iijima [146] presented the first transmission electron microscopy (TEM) images of carbon tubes consisting of a small number of concentric graphene cylinders. Two years later, Iijima and Ichihashi [147] and Bethune et al. [148] reported the synthesis of carbon tubes consisting of single graphene cylinders using Fe or Co as catalysts for their growth, respectively. Figure 4.5 shows the original TEM micrographs of these materials, which came to be widely known as multi-walled carbon nanotubes (MWCNTs) and single-walled carbon nanotubes (SWCNTs), respectively. Due to their unique electronic properties and potentially high accessible surface area, the rest of this section will focus on SWCNTs only.

SWCNT powders are readily available commercially and are mainly produced via four synthesis routes: pulsed laser vaporization [149], electric arc discharge [150], gas phase decomposition [151–153] and chemical vapor deposition (CVD) on a solid support [154]. The growth mechanism is generally accepted to be root-based, i.e. hemispherical fullerene caps form on a metal catalyst (sometimes referred to as the yarmulke mechanism [151]), followed by saturation of the metal
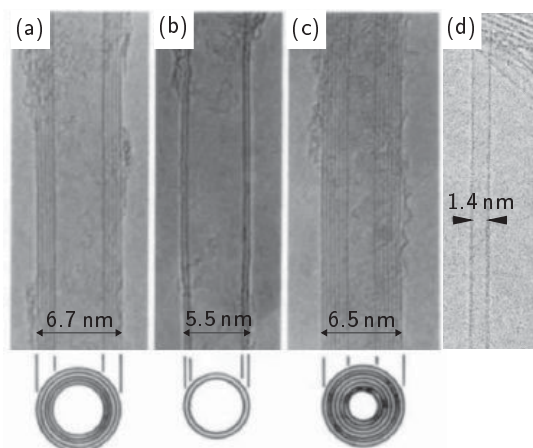
Figure 4.5.: Transmission electron micrographs of MWCNTs of different diameters (a–c) and a SWCNT (d). From [146, 147].

with carbon and growth of the SWCNTs outward from the metal particle [155].

As-grown SWCNTs consist of a mixture of close-capped and open-ended tubes [156]. In close-capped SWCNTs, only the outer surface area of the tubes is considered to be accessible, resulting in a specific surface area equivalent to one side of a graphene sheet ($1315\,\mathrm{m^2\,g^{-1}}$, see Section 4.2). The caps may be removed by oxidative treatment in air, O_2 or CO_2 [156–160] as well as by mechanical abrasion [161], whereby the generation of defects along the tube are also possible. However, oxidation of SWCNTs may result in the formation of bulky functional groups at the tube ends which effectively prevent species from entering into the inner part of the tubes [156, 160]. In addition, SWCNTs have a strong tendency to agglomerate into bundles or ropes (Figure 4.6) containing from less than ten up to several hundred SWCNTs depending on the synthesis method [149, 152, 162]. This spontaneous arrangement of individual SWCNTs into a triangular close-packed lattice can be detected by X-ray diffraction (XRD) [149, 156, 162]. In the course of thermal treatments and purification steps, the SWCNTs may be partially debundled and oxidized both at the ends and along the tube surface [163].

In gas adsorption measurements, often only the external bundle surface area is stated to be easily accessible [164], but gas adsorption within bundles has also been reported [165]. The accessible porosity of SWCNTs may thus depend on the size of the bundles, the concentration and type of defects along the tubes and tube ends, and the type of adsorbate.

Formally, a SWCNT can be constructed by rolling a graphene sheet seamlessly into a cylinder (Figure 4.7). There are a number of possible configurations for the chiral vector $C_h = na_1 + ma_2$, and the electronic properties of the resulting SWCNT may vary considerably. The diameter of a SWCNT can be expressed in terms of the (n, m) indices as

$$d_t = \frac{|C_h|}{\pi} = \frac{\sqrt{3}\,d_{C-C}}{\pi}\sqrt{n^2 + nm + m^2} \tag{4.1}$$

Note that, due to symmetry, only chiral angles $0° \leq \theta \leq 30°$ need to be considered (Figure 4.7). The special cases $\theta = 0°$ and $\theta = 30°$ are referred to as non-chiral tubes and are called zig-zag and armchair SWCNTs, respectively.

The length of a SWCNT is typically in the order of μm [167], i.e. significantly larger than the graphene unit cell, resulting in a quasi-continuum of allowed electronic states along the tube. However, the tube diameter is close to 1 nm, leading to a discretization of allowed wavevectors along the circumference of the tube. The strong curva-

5 nm
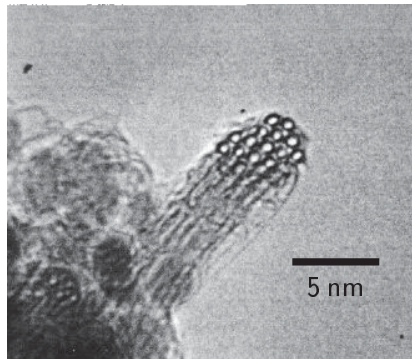
Figure 4.6.: Transmission electron micrograph of a bundle of SWCNTs produced by the catalytic gas phase decomposition of CO [152].
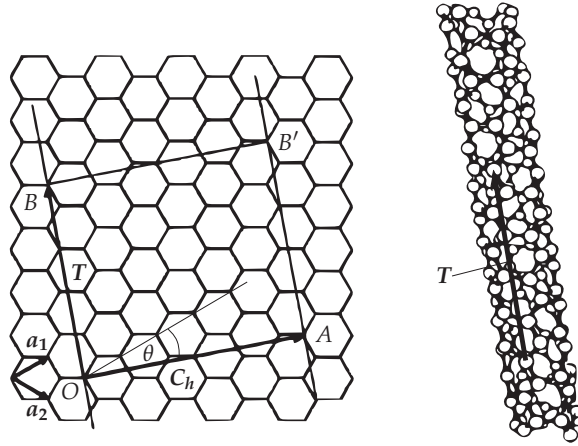
Figure 4.7.: One possibility to roll up a graphene sheet into a SWCNT [166]. The vectors OB and AB' are brought on top of each other so that the SWCNT axis is coaxial with the unit cell vector T. The chirality of the SWCNT is defined through the chiral angle θ or the chiral vector $C_h = na_1 + ma_2$, where (n, m) are the Hamada indices of the SWCNT. Accordingly, the SWCNT generated in the above example is denominated a (4, 2) tube.

ture of SWCNTs results in some mixing of the π and σ orbitals which is more pronounced for tubes with smaller diameters, but can be neglected near the Fermi level [168]. The effect of curvature on the $C-C$ interaction energy γ_0 is a decrease in the order of only 2 % [132]. Thus, the electronic band structure of SWCNTs can be obtained from that of graphene by considering the appropriate periodic boundary conditions [132, 168, 169]. This procedure is called zone-folding of graphene. As a result, a quasi-continuum of allowed k values is obtained in axial direction but only certain values for the electron wave vector k are allowed in the circumferential direction, which can be represented by cutting lines within the first Brilloin zone (Figure 4.8).

For a SWCNT of a given chirality, a non-vanishing density of states at the Fermi level thus only occurs when the K point represents an allowed value for k. Due to the periodic boundary condition $C_h \cdot k = 2\pi j$, where j is an integer, it turns out that this is only the case when $n - m$ is zero (airmchair SWCNTs) or a multiple of 3, while all other (n, m) tubes
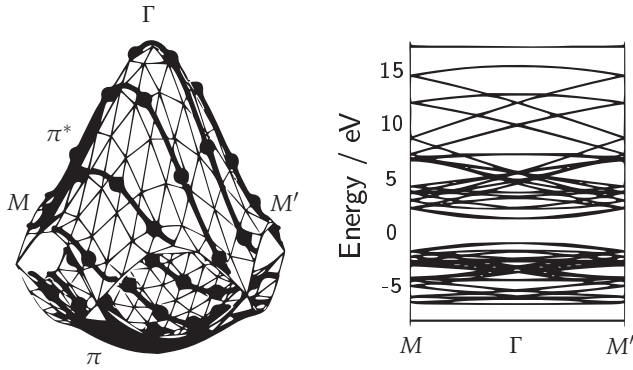
Figure 4.8.: Schematic derivation of the band structure of SWCNTs from graph-
ene [166]. Left: The π and π^* bands in the first Brillouin zone. Solid
lines represent allowed k values. Right: Corresponding band disper-
sion for a part of the first Brillouin zone. The energy is given relative
to the Fermi level.

are semiconducting [167, 168]. This pronounced difference in electronic
properties follows only from the geometrical arrangement of carbon
atoms in the SWCNTs, without the consideration of differences in the
local bonding arrangement or doping with foreign atoms.

As $D(\varepsilon) \propto 1 \,/\, \mathrm{grad}_k\,\varepsilon(k)$, the DOS of SWCNTs becomes large as the
energy dispersion as a function of k becomes flat, resulting in sharp
peaks in the DOS which are called van Hove singularities (vHs) [132].
A comparison with the DOS of graphene is shown in Figure 4.9 for dif-
ferent SWCNTs. For all (n, m) combinations, the energy gaps between
vHs in the π and π^* bands can be calculated using the tight-binding
approximation in conjunction with the zone-folding of graphene. The
result can be conveniently summarized in a Kataura plot [171] such as
the one depicted in Figure 4.10. Note that metallic SWCNTs which are
chiral ($n \neq m$, $m \neq 0$) exhibit a very small energy gap of a few meV due
to the SWCNT curvature, leading to quasi-metallic behavior at lower
temperatures [166].

It should be noted that the electronic structure of SWCNTs within
bundles can be significantly modified through interaction with neigh-
boring SWCNTs. Generally, the $E_{\mathrm{ii}}^{M,S}$ spacings tend to decrease as a con-
sequence of bundling [172, 173]. Theoretical studies have shown that
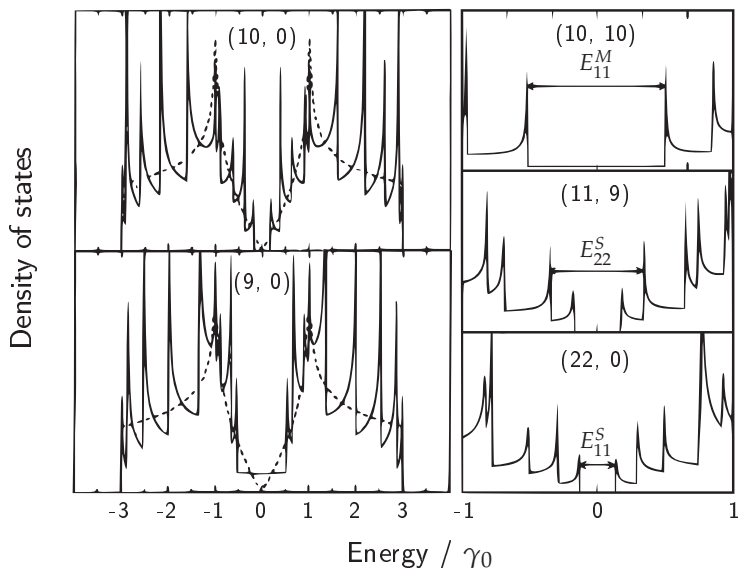
Figure 4.9.: Density of states for different (n, m) SWCNTs as a function of the energy relative to the Fermi level in units of the overlap integral γ_0 [168, 170]. Note the non-vanishing density of states for metallic SWCNTs, for which $n - m$ is zero or a multiple of 3. $E_{ii}^{M,S}$ denotes the gap between the ith vHs in the π and π^* bands for metallic (M) and semi-conducting (S) tubes, respectively. The dashed lines represent the band structure of graphene.

semiconducting SWCNTs may even become metallic as a consequence of bundling [174]. In order to take these effects into consideration, experimental Kataura plots have been compiled on samples consisting of bundled and dispersed SWCNTs using optical spectroscopy techniques to determine the transition energies [175].

Due to the dependence of the electronic properties and the effective surface area on the extent of bundling and presence of defects, it is difficult to predict the suitability of SWCNTs for EDLCs. Several experimental studies which incorporate SWCNTs as the active electrode material in EDLCs have been reported (e.g. [176, 177]). However, many studies present varying results and are sometimes even controversial. In the present work, SWCNTs will be used as a model electrode to obtain insights into the charging mechanisms in EDLCs (Chapters 10
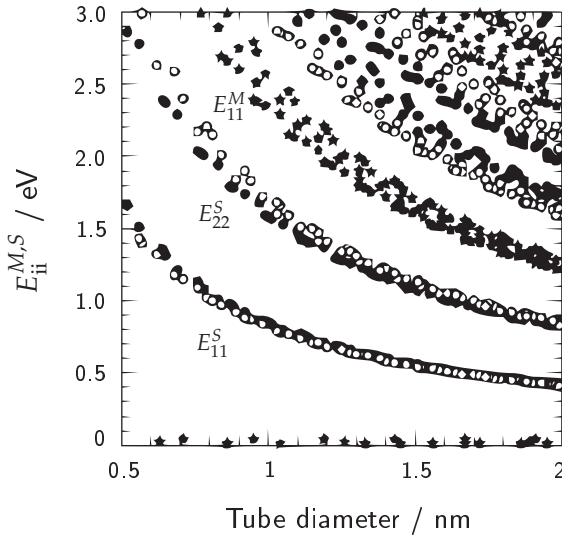
Figure 4.10.: Kataura plot of transition energies $E_{ii}^{M,S}$ between mirror-image vHs for individual SWCNTs with diameters between 0.5 and 2 nm according to the tight-binding approximation [166]. The filled and open circles represent semiconducting SWCNTs while the stars represent metallic SWCNTs.

and 11). In this context, an evaluation of the suitability of SWCNTs for application as the active electrode material in EDLCs will be given.

4.4. Graphitic carbon

Graphite consists of several graphene layers stacked in a well-defined manner. Its crystal structure may be based on either a hexagonal or a rhombohedral lattice (Figure 4.11), whereby the two differ only in the stacking order of the graphene layers [114, 178]. The rhombohedral phase (ABCABC) is thermodynamically unstable with respect to the hexagonal phase (ABAB) and thus usually transforms to this phase upon annealing at heat treatment temperatures above 1300 °C [114]. Through grinding, stacking faults may be introduced into hexagonal graphite, resulting in an increased fraction of rhombohedral graphite of up to 20 % [71, 179]. The density of graphite regardless of the stacking order is 2.26 g cm^{-3} [179].
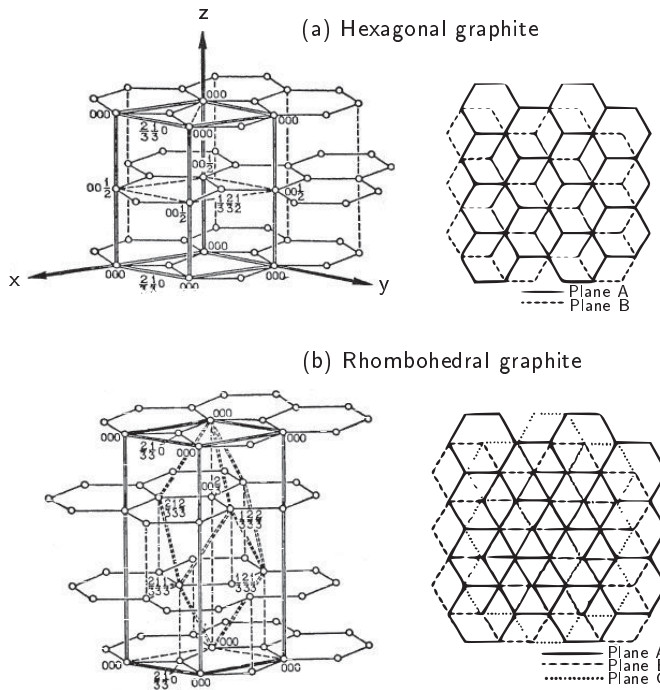
Figure 4.11.: The hexagonal (a) and rhombohedral (b) lattices of graphite with indicated unit cells and stacking order [114, 178]. The coordinates of the carbon atoms are given in terms of the unit cell parameters along the x-, y- and z-axis, respectively.

Graphite features essentially the same in-plane bonding as graphene (Figure 4.2). For hexagonal graphite, which is the more abundant modification [71], the height of the unit cell perpendicular to the graphene sheets (along the z- or c-axis) is 6.71 Å, with the corresponding distance d_{002} between graphene sheets being 3.35 Å [71, 114]. The bonding between planes due to overlapping of the π orbitals is essentially van der Waals bonding, which is much weaker than the in-plane σ bonding [114]. This anisotropy between intra- and interplane bonding explains the anisotropic properties of graphite such as its electronic conductivity (Table 4.2). Due to the weak interaction between layers, the electronic properties of graphite essentially correspond to those of a graphene sheet [124, 130, 131, 137], with a slight overlap of the valence

and conduction bands resulting as an effect of the interplane interaction as stated in Section 4.2.

The size of graphite crystallites is usually characterized by parameters which quantify the stacking height, L_c, and the lateral extension, L_a (Figure 4.12). In polycrystalline samples, a distribution of these parameters is usually observed, whereby the anisotropy of the individual crystallites is usually also reflected macroscopically in the polycrystalline sample due to the preferential orientation of individual crystallites with respect to each other due to their high aspect ratios.

The symmetric density of states near the Fermi level results in the ability of graphite to accommodate both electron donors and acceptors in the interlayer spacings, leading to a rich intercalation chemistry. Comprehensive reviews in the field of graphite intercalation compounds (GICs) have been given by Ebert [181], Herold [182], Dresselhaus and Dresselhaus [183] and Solin [184]. For electrochemical energy storage, graphite has gained significant importance as an intercalation electrode in batteries, notably as a Li^+ host in LIBs [185–187]. A dependence of the intercalation mechanism of Li^+ on the structure and chemistry of the carbonaceous electrode has been reported, notable parameters being the extent of stacking order, hydrogen content and porosity [188]. It should be noted that the surface chemistry of the electrode, in combination with the passivating properties of the electrolyte (Section 3.4), play a crucial part in the performance of intercalation electrodes for LIBs [97, 98, 189].

Table 4.2.: Comparison of some properties of the graphite (sp^2) and diamond (sp^3) allotropes of carbon [114, 116, 179].

	Diamond	Graphite
Density / $g\,cm^{-3}$	3.52	2.26
C–C bond length / pm	154	142
Melting point / K	4500	4450
Electronic conductivity at 298 K / $S\,cm^{-1}$	10^{-20}	2000^a, 3^b
Thermal conductivity at 298 K / $W\,m^{-1}\,K^{-1}$	2000	400^a, 2^b

[a] Perpendicular to the c-axis.
[b] Parallel to the c-axis.
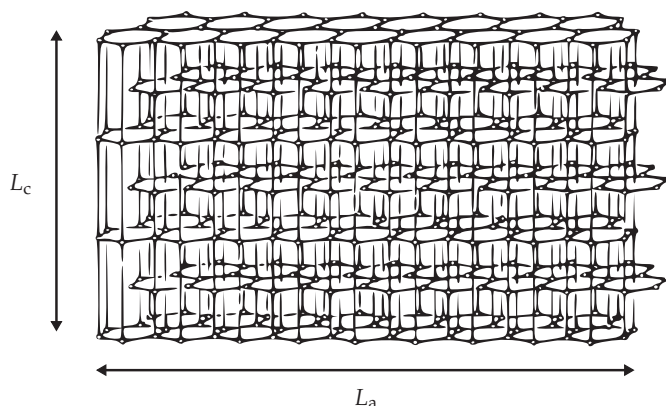
Figure 4.12.: Crystallite size parameters L_c and L_a for graphite. From [180].

The influence of ion intercalation on the stability and charge storage capability of carbonaceous electrodes used in EDLCs has only recently been considered [190–195] and will be studied in more detail in the present work (Chapter 11).

4.5. Non-graphitic carbon

The term non-graphitic carbon encompasses all carbonaceous solids with an extended two-dimensional order of the carbon atoms in sp^2 bonded, planar hexagonal networks, but without any measurable stacking order of these sheets [118]. A suitable technique to determine the extent of stacking order in graphite is XRD, in which the absence of ($h\,k\,l$) reflexions (where $l \neq 0$) indicates the absence of such three-dimensional ordering.

In 1951, Franklin [196] proposed a classification of non-graphitic carbon into two main groups based upon experimental evidence—those carbons which can be converted to graphitic carbon through conventional heat treatment (up to 3000 °C under atmospheric or lower pressure) and those which cannot. Franklin's original two-dimensional representations of these two forms of carbon are still widely used today and are shown in Figure 4.13.
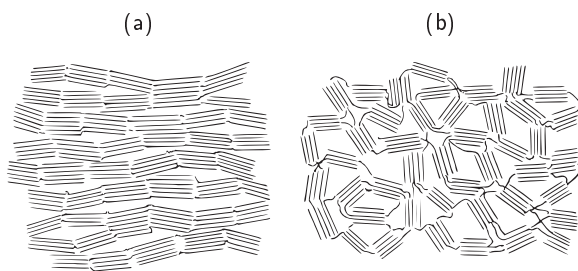
Figure 4.13.: Two-dimensional structural models for (a) graphitizing and (b) non-graphitizing carbons after Franklin [196]. Note the relative arrangement of domains consisting of approximately parallel graphene sheets joined by cross-links of unspecified nature.

In both cases, the heat treatment of the starting organic material usually takes place in an inert atmosphere (pyrolysis). A review of the processes occurring under these conditions has been given by Marsh and Rodríguez-Reinoso in their book on activated carbon [142]. The organic material is decomposed to a solid residue of high carbon content through the removal of volatile compounds and a series of complex processes including dehydrogenation, condensation, hydrogen transfer and isomerization [114, 118]. The overall process is called carbonization and is similar to the naturally occurring coalification of biomass after its biochemical degradation, whereby coalification occurs at more moderate temperatures, higher pressures and many orders of magnitude more slowly than carbonization [118].

The differences in the pyrolysis of non-graphitizable and graphitizable carbons are briefly outlined in the following.

4.5.1. Non-graphitizable carbon

The carbonization step, which occurs in a temperature range of up to about 1300 °C, may take place entirely in the solid phase, in which case the resulting material is a pseudomorph of the parent material, i.e. it retains its original shape to a large extent and there is no introduction of additional anisotropy. The loss of heteroatoms without collapse of the remaining carbonaceous structure results in a significant porosity, which is directly measurable as a decrease in the apparent density of

the material. The porous carbonaceous residue obtained after decomposition is called a char, and its specific surface area may be up to $1000\,\mathrm{m^2 g^{-1}}$ or even higher [142].

Referring to Table 4.1, certain non-graphitizing carbons are not classified as chars. Glass-like (or glassy) carbon [197] is a particular class of non-graphitizable carbon produced by the carbonization of resins. In these resins, the release of small molecules upon volatization is hindered, resulting in a closed porosity which is inaccessible to helium [118, 142].

A completely different structure is exhibited by carbon blacks, which are formed by the incomplete combustion or cracking (thermal decomposition) of hydrocarbon gases and vapors derived from petroleum sources [142]. Carbon black is colloidal, i.e. it consists of spherical particles (typically between 10 nm and 500 nm in diameter depending on the production method) which are fused together in larger aggregates [118, 142]. The layered arrangement of graphene layers in carbon black results in some degree of graphitizability, a severe limitation in this case being the restricted size and spherical structure of the primary carbon black particles [142, 198, 199].

Coals are the result of the geochemical process of coalification [119, 200]. They are inherently microporous and thus non-graphitizable. In order of increasing degree of coalification, coal can be classified into the ranks of lignite, sub-bituminous, bituminous and anthracitic coal [119, 142]. The concentration of polar functional groups (containing predominantly oxygen, nitrogen and sulfur) is highest in the lower rank coals, leading to a pronounced swelling of these coals in polar media as discussed by Hall [201] and critically reviewed by Given et al. [202]. Upon further carbonization of coals, the bituminous coals stand out in that they are fusible, leading to a collapse of the porous structure upon heat treatment [142]. Despite the formation of a fluid phase (Section 4.5.2) during carbonization, they are non-graphitizable. Another case in which a material passes through a fluid phase upon carbonization without subsequent graphitization is the pyrolysis of sucrose [203], in which an immediate cross-linking takes place upon melting, thus preventing the formation of graphitic domains.

The particular structures of glass-like carbon and carbon blacks will not be treated in more depth here, but instead the general non-graphitic structure of chars will be discussed as they form the basis for most activated carbon electrodes used in EDLCs. In chars, there exist local domains with approximately parallel graphene sheets. Due to the essentially random disorder of these domains with respect to each other, the properties of non-graphitizable carbon are usually isotropic. The density of parallel graphene sheets is significantly less than in graphitized samples [142, 196]. There is no apparent stacking order, a property which has been termed turbostratic (e.g. [114]). However, this terminology has been criticized by Marsh and Rodríguez-Reinoso [142] since it presumes a parallel arrangement of stiff graphene layers, and it is actually not part of the IUPAC recommendations for the description of carbonaceous solids [118]. Another widely used term for non-graphitizable carbon is hard carbon, although the hardness of a carbon is not necessarily directly related to its ease of graphitization [142].

A number of structural models for non-graphitizing carbons have been proposed which take into consideration the flexibility of individual graphene sheets, and, more recently, the discovery of fullerenes and experimental evidence for significant curvature of graphene on the nanometer scale [208]. The common feature of these models is the existence of small domains with a roughly parallel arrangement of graphene sheets. These models, coupled with TEM studies, suggest
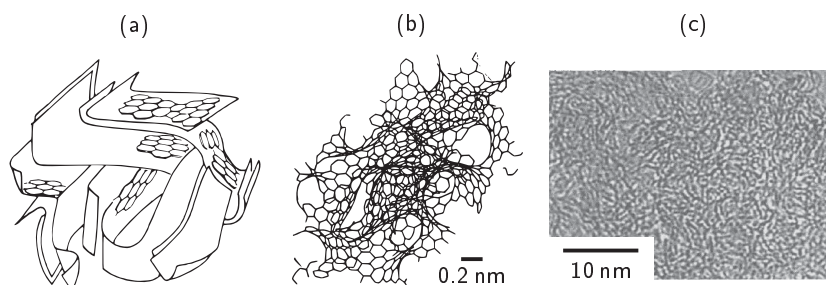
Figure 4.14.: Structural models of non-graphitizable carbon. (a) Graphene sheet model by Stoeckli [204], (b) fullerene-based model by Townsend [205, 206], and (c) transmission electron micrograph of a commercial porous carbon [142, 207].

that one should not envisage non-graphitizing carbons as consisting of very small graphite microcrystallites, as critically reviewed by Marsh and Rodríguez-Reinoso [142], but rather as a disorganized assembly of sp^2 hybridized, aromatic carbon in different bent and twisted configurations (Figure 4.14).

4.5.2. Graphitizable carbon

Contrary to the vast majority of non-graphitizable carbons, all graphitizable carbons soften upon carbonization. In the softened state, the self-assembly of individual aromatic molecules (called mesogens) results in the formation of an anisotropic nematic liquid crystal system called mesophase [209, 210]. Brooks and Taylor [211] were the first to conclude that the formation of mesophase is the common step in the graphitization of all graphitizable carbons regardless of their source. Whereas nucleation centers are not necessary for the formation of mesophase, they can promote its growth [203, 212].

The complete process of carbonization and graphitization of mesophase has been summarized graphically by Marsh [142, 203, 213] and is reproduced in Figure 4.15.

Prior to carbonization, the starting material is a pitch, which is a non-graphitic, graphitizable carbon consisting, in general, of a complex mixture of essentially aromatic hydrocarbons and heterocyclic compounds [118]. It may be obtained as a residue from the pyrolysis of organic material or from tar distillation. Pitches are usually solid at room temperature and exhibit a broad softening range when heated. Upon carbonization above 400 °C, the formation of mesophase begins, resulting in an increase in the anisotropic fraction consisting of aromatic carbon sheets arranged roughly in parallel. After heat treatment in the temperature range between the onset of fusion of mesogens and complete devolatization, the material is called a semicoke [118, 203]. After removal of all volatile species, a green (or raw) coke is obtained.

Green coke is essentially non-porous and can be graphitized at temperatures above about 2200 °C. During graphitization, the spacing between parallel graphene layers is gradually reduced until the characteristic d_{002} value of 3.35 Å for graphite is reached [212, 214, 215]. This is usually only achieved at temperatures close to 3000 °C. In addition, the
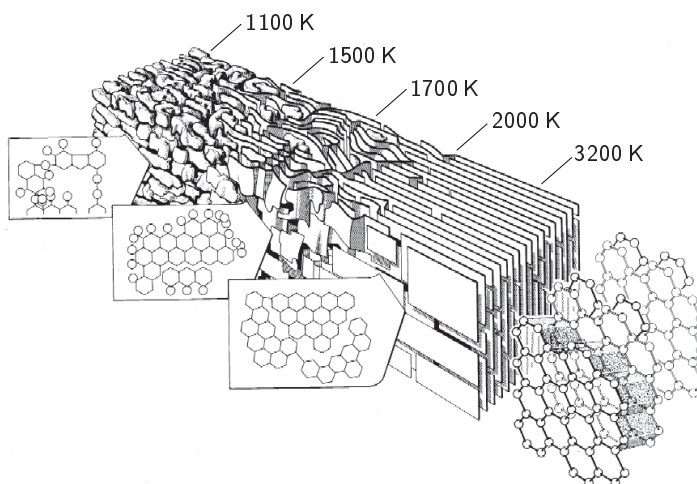
Figure 4.15.: Overview of the graphitization of mesophase according to Marsh [142, 203, 213]. The initial stages involve a stacking of the mesogens with significant buckling and defects. With increasing heat treatment temperature, the planarity increases and the defect density decreases, until finally a graphitic structure is obtained.

crystallite size parameters L_c and L_a (Section 4.4) increase continuously in course of graphitization [196, 216, 217].

4.5.3. Development of porosity

As discussed in Section 3.5, a key requirement for electrodes in EDLCs is a high surface area which is accessible to the electrolyte. An increase in surface area can be achieved via so-called activation processes regardless of whether a carbon is non-graphitizing or graphitizing and independent of its extent of carbonization. As a result, an activated (or active) carbon is obtained. Some carbonaceous materials exhibit an intrinsically high surface area following carbonization, such as poly(vinylidene chloride) (PVDC) [218, 219] or polyfurfuryl alcohol (PFA) [142], as long as the heat treatment temperature does not exceed the temperature required for significant cross-linking and collapse of the carbon structure. In any case, the surface area can be enhanced via activation, leading to a pronounced porosity. The conventions regard-

ing the description of porosity on different length scales are summarized in Table 4.3.

Activation treatments may be classified as either physical (thermal) or chemical, as reviewed by Marsh and Rodríguez-Reinoso [142].

Physical activation involves the use of a carbon gasification reactant, usually CO_2 or H_2O, with or without catalyst at temperatures of 800–1000 °C. O_2 is usually not used as an activating agent since its reaction with carbon is highly exothermic and hence difficult to control [142]. The activation is usually preceded by a separate carbonization step [220, 221]. The according porosity of the activated carbon increases with the amount of burn-off [142, 221, 222]. At burn-offs below about 30 %, the activated carbon is predominantly microporous. At higher burn-offs, the meso- and finally macroporosity becomes more pronounced [220].

The essential chemical reactions involved in the physical activation of carbons with CO_2 and H_2O are endothermic [142] and can be written as follows:

$$C_{(s)} + CO_{2\,(g)} \quad \longrightarrow \quad 2\,CO_{(g)} \tag{4.2}$$
$$C_{(s)} + H_2O_{(g)} \quad \longrightarrow \quad CO_{(g)} + H_{2\,(g)} \tag{4.3}$$
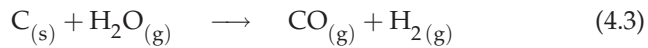
Both reactions occur during activation with either gasification agent, since it is difficult to exclude water in the case of CO_2 activation and, in the case of H_2O activation, the water gas shift reaction produces CO_2 according to

$$CO_{(g)} + H_2O_{(g)} \longrightarrow CO_{2\,(g)} + H_{2\,(g)} \tag{4.4}$$
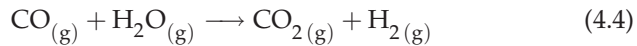
During chemical activation, the carbonization and activation steps are usually carried out simultaneously in a single heating step by pyrolyzing the carbonaceous feedstock which has been impregnated with a

Table 4.3.: The nomenclature of porosities for different pore widths according to IUPAC [223].

Micropores	Mesopores	Macropores
< 2 nm	2…50 nm	> 50 nm

suitable chemical activation agent. Besides temperature, the intimacy of mixing of the two components as well as their mass ratio and the activation time determine the extent of activation [142]. The most frequently employed activation agents for chemical activation are $ZnCl_2$ [220, 221, 224], H_3PO_4 [225] and KOH [220, 226].

$ZnCl_2$ and H_3PO_4 begin to act below $500\,°C$, thus influencing the process of carbonization. Both chemicals are dehydrating agents, promoting a collapse of the carbonaceous structure during carbonization. In the case of $ZnCl_2$, a relatively uniform dispersion of small $ZnCl_2$ molecules locally prevents the fusing of the carbon, thus acting as templates for the subsequently formed, relatively uniform microporosity. For H_3PO_4, a mixture of molecules with different sizes exist, thus usually resulting in a wider distribution of pore sizes [142].

KOH does not act as a dehydrating agent and does not inhibit the contraction of the carbon structure upon carbonization [142]. It only begins to react above $700\,°C$, i.e. after the formation of the char or coke. According to Lillo-Ródenas et al. [227], the activation reaction initially consists of carbon oxidation and the generation of metallic potassium:

$$6\,KOH_{(l)} + 2\,C_{(s)} \longrightarrow 2\,K_{(l)} + 2\,K_2CO_{3\,(s)} + 3\,H_{2\,(g)} \qquad (4.5)$$
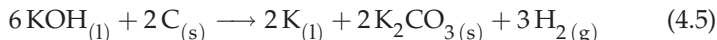
Accordingly, some microporosity is created during Reaction (4.5). At the reaction temperatures involved, metallic potassium may intercalate between graphene layers and force these apart, leading to a further enhancement of microporosity [226] and in some cases even resulting in a disintegration of the carbonaceous solid to powder [142].

As opposed to physical activation, chemical activation has the advantages of higher yield (no burn-off), a single combined carbonization/activation step, and a well-defined resulting microporosity with little or no meso- and macroporosity. As a disadvantage, the product salts or excess activation agent must be washed out of the solid after activation. Also, the corrosive nature of the chemical activation agent may present practical difficulties. The obtained micropore volumes are in the order of $0.4\,cm^3\,g^{-1}$ for KOH, $0.5\,cm^3\,g^{-1}$ for $ZnCl_2$ and $0.6\,cm^3\,g^{-1}$ for H_3PO_4 [142].

There exist some additional techniques which permit the generation of carbonaceous solids with well-defined pore structures and high

specific surface areas, but which have not yet achieved the industrial importance of the traditional activation procedures described above. These approaches include templating techniques by which porous carbons are derived from carbides under chlorination [228] or from the carbonization of a suitable precursor within the existing porosity of a template material such as expanded mica [229], silica [230, 231], alumina [232] or zeolites [233]. Reviews of these fields have been given by Lee et al. [234] and Kyotani [235]. The common disadvantages of most of these methods compared to the traditional activation procedures are the increased cost and difficulty of mass production.

4.6. Surface functionalities

Carbonaceous electrodes in EDLCs do not consist entirely of carbon. At the edges of graphene sheets, which may be of the zig-zag or armchair type, the carbon atoms only possess a two-fold coordination with other carbon atoms. In such a configuration, the resulting unpaired electrons (dangling bonds) are highly reactive and inevitably terminated by heteroatoms or, as discussed recently by Radovic and Bockrath [236], they might lead to the formation of carbene/carbyne-type bonding at hydrogen-free edges. The latter would only be possible through significant mixing of the σ and π orbitals at the edges of graphene.

Under ambient conditions, the saturation of dangling bonds by hydrogen and oxygen is the most likely scenario. A range of surface functional groups may therefore exist at the edges of graphene sheets, as reviewed by Boehm [237]. An illustration of this edge plane functionalization is given in Figure 4.16. Accordingly, carbons may exhibit acidic or basic behavior depending on the concentration of the corresponding surface groups. It should be mentioned that, even in the absence of such groups, the basal plane of graphene exhibits an intrinsic basicity due to the electron-donating properties of the π orbitals [238].

As a consequence of functionalization, surface dipoles can induce a change in the surface potential, χ (Section 3.3.1). Accordingly, carbons with varying degrees of functionalization will exhibit different electrode potentials, namely more positive potentials in the case of a partial positive charge on the carbon (e.g. $C^{\delta+}O^{\delta-}$ dipoles) and more
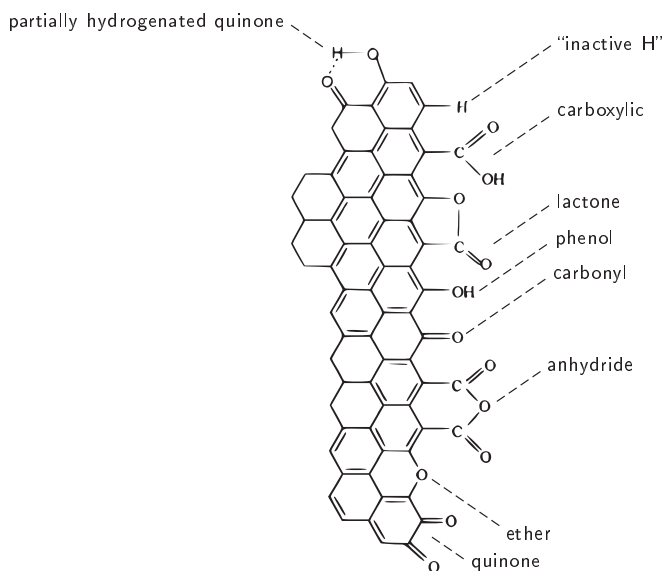
Figure 4.16.: Nomenclature of surface groups at edge sites of graphene. Adapted from [239].

negative potentials when a partial negative charge is imparted on the carbon (e.g. $C^{\delta-}H^{\delta+}$ dipoles), as discussed by Tobias and Soffer [240].

In aqueous electrolytes, a pseudocapacitive contribution to the electrode capacitance may result as a consequence of protonation and deprotonation of surface groups, such as the quinone-hydroquinone half-reaction [241]

$$Q + 2\,H^+ + 2\,e^- \longrightarrow QH_2 \tag{4.6}$$

where Q represents the quinone group (Figure 4.16). H^+ may also be inserted in between graphene layers as described by Qu [242], which has led to proposals of carbon-based electrochemical hydrogen storage [243, 244]. At any rate, the capacitance of activated carbons in protic electrolytes has been shown to increase with the concentration of oxygen-containing surface groups [90]. In aprotic electrolytes, such as those preferred for EDLCs (Section 3.4), no such enhancement of capacitance is observed, which supports the notion of pseudocapacitive contributions of carbon surface groups in aqueous electrolytes.

In fact, functional groups appear to impose only disadvantages in non-aqueous electrolytes. Centeno et al. [90, 245] have shown that the ionic mobility is reduced with increasing concentration of surface groups in both protic and aprotic electrolytes, apparently due to the steric hindrance imposed by these groups within micropores. In addition, surface groups may participate in irreversible faradaic reactions with electrolyte and solvent species, thus catalyzing aging processes (Section 5.2.2).

Finally, it should be noted that further types of heteroatoms besides oxygen and hydrogen may be incorporated into the carbonaceous network depending on the precursor material. For instance, nitrogen is relatively abundant in lignite and poly(acrylonitrile) (PAN) [246, 247] as well as in polymerized melamine [229]. Pels et al. [246] showed that nitrogen replaces carbon both at the edges and in the interior of graphene layers.

Chapter 5.

Increasing the operating voltage of EDLCs

5.1. Improving the energy density of EDLCs

In Section 2.2, an apparent saturation of the specific energy of commercially available EDLCs was presented. Having discussed the fundamental properties of the electrochemical double layer, electrolytes and porous electrodes in EDLCs (Chapter 3) as well as the characteristics of the most versatile electrode material, carbon (Chapter 4), the theoretical limits of the specific energy of EDLCs as well as possible strategies to overcome them may be discussed in the following.

In an initial approach, the maximum theoretical energy is considered without taking into account the influence of different rates of charge and discharge. Likewise, an improvement in design parameters such as the mass of auxiliary components or packaging density is disregarded. In this case, it is useful to recall the expression for the energy content of a capacitor:

$$W = \frac{1}{2}CU^2 \qquad (3.4)$$

An increase in specific energy of EDLCs may therefore be achieved by two main routes: an increase in the capacitance C or an increase in the operating voltage window U. In the implementation of so-called hybrid (or asymmetric) electrochemical capacitors, both of these parameters may be enhanced. In these systems, an EDLC-type electrode material is paired with a battery-type electrode material such as those used in Li-ion batteries (e.g. graphite [248–250], $Li_4Ti_5O_{12}$, $LiCoO_2$, $LiMnO_4$ [14, 251]). Other proposed battery-type electrodes for hybrid electrochemical capacitors include MnO_2 [252–254], Pb/PbO_2, $Ni(OH)_2$ [255], and conductive polymers [47, 254, 256]. The common feature of these battery-type materials is faradaic charge storage which

is linked to a change in the structure and chemical composition of the bulk electrode material. Due to the solid-state diffusion of reactants in such systems and the irreversibility of faradaic reactions in comparison with pure double layer charging, the currently proposed hybrids are disadvantageous in terms of power capability and cycle life compared to EDLCs. In order to focus on the capacitive charge storage characteristics of EDLC systems and the related benefits, the wide field of hybrid electrochemical capacitors will not be pursued further in this work.

In the case of symmetric electrodes and a limiting Helmholtz capacitance, the specific capacitance C_S (in $F\,m^{-2}$) of an EDLC electrode can be written as

$$C_S = C_H = \frac{\epsilon_H\,\epsilon_0}{d_H} \tag{3.21}$$

The total gravimetric capacitance is then given by $C_{single} = C_S A$, where A is the specific surface area of the electrode (in $m^2\,g^{-1}$). A maximum electrode capacitance is therefore achieved by maximizing C_S and the specific interfacial area between electrode and electrolyte. Setting $d_H = 0.35\,nm$ and $\epsilon_H = 8$ as the dielectric permittivity of the Helmholtz layer, a specific capacitance close to $20\,\mu F\,cm^{-2}$ is obtained. For carbonaceous electrodes, the specific surface area of a graphene sheet, $2630\,m^2\,g^{-1}$ (Section 4.2), may be taken as an upper limit for A. In this case, a capacitance of $C_{single} = 532\,F\,g^{-1}$ is obtained for the single electrode or, according to Equation (3.3), $C_{cell} = 133\,F\,g^{-1}$ for the full cell capacitance based on the total electrode mass.

At a voltage of $U = 2.7\,V$, a capacitor consisting of two such electrodes holds a charge of $Q = C_{cell}U = 359\,C\,g^{-1}$ with respect to the total electrode mass. An according minimum amount of electrolyte must be present in order to balance the electronic charge on the electrode, i.e. $m = QM_W/F = 0.81\,g$ of electrolyte per g total electrode mass for a molecular mass M_W of $216.8\,g\,mol^{-1}$ and monovalent ions, representing Et_4NFB_4. In addition, the mass of the solvent must be taken into account. A $1\,M$ solution of Et_4NBF_4 in a low density solvent such as AN has a density close to $0.85\,g\,cm^{-3}$, leading to mass contribution of the solvent of $3.9\,g$ per g of salt. Thus, the minimum amount of solution for the electrode pair described above increases the mass of the

system by a factor of $(0.81 + 0.81 \cdot 3.9) = 3.97$, resulting in an effective capacitance of $C_{\text{cell}} = 33.5\,\text{F}\,\text{g}^{-1}$.

Assuming an optimistic additional 50 % of packaging mass to account for separator, excess electrolyte, current collectors and housing, the theoretical maximum specific energy of the EDLC described above is $17\,\text{Wh}\,\text{kg}^{-1}$ at 2.7 V. Lewandowski and Galiński arrive at a similar value ($14.4\,\text{Wh}\,\text{kg}^{-1}$) for their estimation of the theoretical maximum energy content of EDLCs [257].

The specific energy of commercial EDLCs in the order of $5\,\text{Wh}\,\text{kg}^{-1}$ represents approximately 29 % of the theoretical maximum value estimated above. However, adopting a specific double layer capacitance of $C_S = 10\,\mu\text{F}\,\text{cm}^{-2}$, which is a more reasonable estimate [90] due to the larger effective ion size and smaller value for the relative permittivity ϵ_H in the double layer, a maximum theoretical specific energy of $8.5\,\text{Wh}\,\text{kg}^{-1}$ is obtained. This value is not far above the present specific energies of commercial EDLCs. From these rough calculations, it appears as though the specific energy limit of EDLC systems has indeed nearly been reached, in support of the trend observed in Figure 2.5. Hence, a further increase in specific surface area of the carbonaceous electrodes in order to enhance the specific capacitance appears neither plausible nor beneficial for EDLCs based on the current electrolytes and nominal voltages.

The second route towards an improvement of the specific energy of EDLCs is an increase of the operating voltage. This is a particularly attractive approach as $W \propto U^2$ and an increase in specific power could also be expected as $P \propto U^2$. Starting from a cell voltage of 2.7 V, a widening of the potential window by 500 mV would result in an increase in the specific energy and power by 40 % each. Under the condition that there is no decline in other favorable properties of the device, an increase in the voltage window is the most promising strategy to increase the specific energy and power of EDLCs.

However, the operation of EDLCs at voltages beyond the nominal voltage usually results in a rapid decline of the device lifetime. There is currently no consensus on the mechanisms by which this lifetime reduction occurs and detailed studies in this respect are lacking. Establishing an understanding of the aging processes is essential for the

development of suitable strategies with which to obtain higher device voltages.

A review of the state of research regarding aging phenomena in EDLCs is given in the next section.

5.2. Aging of EDLCs

5.2.1. Introduction

The end-of-life of EDLCs is defined by the occurrence of any one of the following measurable device parameters with respect to their respective initial values (e.g. [258]):

- a loss of capacitance of 20 %,

- an increase in the internal resistance by a factor of 2, or

- an increase in the self-discharge rate by a factor of 2.

Testing protocols in this respect have not yet been sufficiently standardized, leading to varying testing conditions in past studies concerning the aging of EDLCs. In the following, the available scientific literature dealing with the aging and degradation mechanisms of EDLCs will be reviewed, taking into account both investigations on commercial devices and on laboratory test cells. An overview of the corresponding literature is given in Table 5.1. The list may not be exhaustive, but is considered to contain the most important published information regarding the aging of EDLCs based on non-aqueous electrolyte solutions to date. The experimental details and most important findings of these publications are summarized in the following.

5.2.2. Literature review

Morimoto et al. [259] from the companies Asahi Glass and Elna, both based in Japan, published one of the first studies regarding the performance and aging of EDLCs using a number of different activated carbons as electrodes and various electrolytes based on PC as the solvent. Among the systems investigated, EDLCs containing the quaternary onium salts Et_4NBF_4 or Et_4PBF_4 exhibited the best conductivities

Table 5.1.: Selection of published scientific articles on the aging and degradation mechanisms of EDLCs including the respective focal points of investigation. The analytical techniques are classified into in situ and ex situ methods.

Year	Solvent	Performance loss		Effect of temperature	Effect of voltage	Pressure build-up	Electrolyte degradation	Carbon degradation	Ref.
		Device	Electrode						
1996	PC	✓	(✓)						[259]
2003	PC	✓	(✓)		✓			ex situ	[260]
2005	PC	(✓)	(✓)		✓		in situ		[261]
2006	PC	✓		✓	✓	in situ			[262]
2009	PC	✓			✓		in situ	ex situ	[263]
2009	PC	✓	(✓)			in situ	in situ	ex situ	[264]
2003	AN	✓			✓			ex situ	[265, 266]
2006	AN	(✓)	(✓)		✓		in situ		[190]
2006	AN	✓		✓					[35]
2006	AN	(✓)		(✓)	(✓)			ex situ	[267, 268]
2007	AN	✓		(✓)	(✓)				[269, 270]
2008	AN				(✓)		ex situ		[271]

and highest electrochemical stability, with a capacitance loss of about 15 % and an internal resistance increase of a factor 2 after 1000 hours at 2.8 V and 70 °C. Further, the authors found that the capacitance loss was clearly more pronounced for activated carbons with higher initial oxygen contents as measured by X-ray photoelectron spectroscopy (XPS).

Umemura et al. [260] investigated a series of non-specified commercial EDLCs containing Et_4NBF_4 in PC as the electrolyte. These authors tested the EDLCs at temperatures between 40 °C and 60 °C at device voltages ranging from 2.1 V to 2.7 V. During aging under the imposed conditions, the rate of capacitance fading and resistance increase was found to become higher after an aging time in the order of 1000 hours (at 60 °C). Using an end-of-life criterion of 10 % capacitance loss, lifetimes in the order of 10^5 hours were measured under nominal conditions. Under the testing conditions employed, an increase in device voltage by 0.2 V or an increase in temperature by 20 °C both led to a decrease in lifetime by a factor of 10, respectively.

In the same investigation [260], an analysis of the gases evolved during EDLC aging was performed using an unspecified experimental setup. It was found that the main gaseous decomposition product was CO, followed by CO_2 and H_2, which were attributed quite generally to the electrochemical and/or thermal degradation of the electrolyte. Employing XPS to investigate a pair of electrodes after one particular set of aging conditions, an increase in the oxygen content of both the positive and negative electrode was measured, which was attributed to either the oxidation of the electrode surfaces or to the presence of $C-O$ containing degradation products on the electrodes. Further, Umemura et al. [260] showed a possible topographical change of the positive electrode material using atomic force microscopy (AFM) on an aged sample, as well as small changes in the micropore size distribution of the electrodes using gas adsorption.

Although the measurement technique was not specified, Umemura et al. [260] state that the capacitance loss of the negative electrode was more pronounced than for the positive electrode for a single set of aging parameters, and that some of the capacitance could be recovered by replacing the electrolyte. Although no correlation was established between the capacitance fading and the observed changes of single elec-

trodes, the authors concluded that the observed aging of commercial EDLCs was due to a degradation of the electrolyte solution and the associated formation of degradation products within the electrodes and a loss of ionic charge carriers.

In a Ph.D. thesis by Azaïs [265] and a later publication by Azaïs et al. [266], the aging of commercial EDLCs (SAFT, France) based on Et_4NBF_4 in AN was studied for three different carbonaceous electrode materials at room temperature and different aging conditions [265] for each electrode material (2.8 V/4000 h, 2.8 V/7000 h, 2.5 V/10 000 h). For these particular carbons, it was found that capacitance loss over time was favored by a higher amount of oxygen-containing surface functional groups (analogous to the studies of Morimoto et al. [259] described above for PC-based electrolytes). The presence of trace amounts of water was proposed to enhance the aging rate [266], although no evidence was presented in this respect. The high initial rate of self-discharge (which is not strictly an aging phenomenon according to the definition at the beginning of this section) of carbons originating from biomass was attributed to the migration of cationic metallic impurities from the positive to the negative electrode.

Azaïs et al. [265, 266] also investigated the positive and negative electrodes after each of the above aging experiments via XPS, finding increased amounts of fluorine and nitrogen at both the negative and positive electrode, as well as trace amounts of boron on the negative electrode. It was concluded that electrochemical reactions involving the anion BF_4^- and cation Et_4N^+ occurred at both electrodes. Using the sodium salt of carboxymethylcellulose (CMC) as polymeric binder for both electrodes, it was found that Na^+ migrated from the positive to the negative electrode during the aging treatments. A decrease in the surface area of both the negative and the positive electrode due to aging was measured using nitrogen gas adsorption, indicating the blockage of porosity due to electrolyte degradation products. The loss of surface area was more pronounced for the positive electrode, which was tentatively attributed to a more significant influence of trace water on the electrochemical stability window in the positive potential range. However, no single electrode capacitances were measured to support this hypothesis.

Hahn et al. [261] studied the gaseous decomposition products of Et_4NBF_4/PC with activated carbon electrodes using on-line mass spectrometry for the first few charge/discharge cycles. While the evolution of small amounts of propene ($H_2C=CHCH_3$) was already detected at cell voltages below 1 V, significant gas evolution occurred above 2.6 V in the form of CO_2, formed by solvent oxidation at the positive electrode, as well as propene and H_2, both formed by solvent reduction at the negative electrode. The onset of gas evolution coincided with faradaic losses. The decrease in faradaic losses with increasing cycle number indicated either a form of surface passivation of the electrodes or an electrochemical consumption of impurities.

In a subsequent study, the pressure increase associated with gas evolution in Et_4NBF_4/PC for durations of about 10 hours was measured at different float voltages [262]. The rate of pressure build-up was found to increase by a factor of 6–7 when increasing the cell voltage from 2.5 V to 3 V. Also, it was deduced that most of the irreversible faradaic current did not contribute to gas formation. In a follow-up study, Kötz et al. [272] confirmed this result and found that the pressure build-up in cells containing Et_4NBF_4/AN is lower than for the PC-based electrolyte above ca. 3 V, despite a higher leakage current of the former. Therefore, it must be concluded that the majority of charge consumption does not result in the formation of gaseous degradation products.

Hahn et al. [190] also suggested the possibility of another degradation mechanism in which the repeated insertion and deinsertion of ions in between graphene layers could affect the electrode stability during cycling. This hypothesis was based on in situ dilatometry measurements of activated carbon electrodes using Et_4NBF_4 in AN as the electrolyte, in which a measurable expansion of the electrodes occurred well below 2 V cell voltage for the first charge/discharge cycles. The intercalation of Et_4N^+ into highly oriented pyrolytic graphite (HOPG) in Et_4NBF_4/PC was later demonstrated by Campana et al. [273] using in situ AFM. In the same study, first evidence was presented for the formation of insoluble degradation products on the HOPG surface when used as the negative electrode in this electrolyte. The effect of positive polarization was not studied. The influence of these insertion processes

and degradation products on the charge storage and lifetime of EDLCs has not yet been clarified.

Kötz et al. [35] studied the influence of temperature (between -40 °C and 60 °C) and cell voltage (between 2.5 V and 3 V) on the leakage current of commercial EDLCs (Maxwell, Switzerland) based on Et_4NBF_4 in AN. The leakage current can be considered a combination of self-discharge and faradaic processes. By extrapolation, the lifetime under nominal conditions was found to be more than 300 years and limited by the capacitance fading rather than the other two end-of-life criteria listed in Section 5.2.1. Under the assumption that the leakage current is proportional to the rate of aging, it was found that an increase in the voltage by 0.1 V or in the temperature by 10 °C led to a decrease in the lifetime by a factor of around 2. However, it was also found that higher voltages led to leakage currents higher than those expected by extrapolation from lower voltages, indicating that the aging mechanism depends on the applied voltage.

It is worth noting that the influence of voltage and temperature on the EDLC lifetime in the studies by Kötz et al. [35] differs slightly from the findings of Umemura et al. [260] with respect to the device lifetime. Company data published by EPCOS, Germany (cited by Linzen et al. [258]) on EDLCs using Et_4NBF_4/AN support the findings of Kötz et al. [35]. Differences between these studies may be due to a number of reasons, including different end-of-life criteria and testing conditions, but also electrolyte composition and properties of the carbonaceous electrodes.

The aging of commercial EDLCs based on Et_4NBF_4/AN (EPCOS, Germany) was studied by Zhu et al. [267, 268]. In this work, six devices were aged at voltages between 2.3 V and 2.8 V at different temperatures in the range 50–80 °C for ca. 3000 hours. In addition, three different activated carbons were aged in laboratory cells at 2.9 V for 1080 hours. Subsequent analysis via gas adsorption measurements suggested a blocking or destruction of micro- and mesopores within the electrodes, with the loss of surface area being more pronounced for the positive electrode (in agreement with the studies by Azaïs et al. [265]). XPS and infrared spectroscopy mainly indicated the formation of C−H bonds on the negative electrode due to a protonation of edge plane car-

bon atoms. Changes on the positive electrode were more pronounced, indicating the formation of C−N and C−F bonds, tentatively assigned to the polymerization of the solvent AN and decomposition of the anion BF_4^-. C−O species in aged samples were suggested to originate from trace water, which could also act as a proton donor. A correlation with the electrochemical performance of the individual electrodes was not carried out.

The aging of three EDLCs provided by different manufacturers (EP-COS, Germany as well as NessCap, Korea, and Maxwell, Switzerland) was investigated by Bohlen et al. [269, 270] using electrochemical impedance spectroscopy (EIS). The authors found that the aging under nominal conditions can be represented by a linear decrease in conductances and capacitances over time within a simple equivalent circuit, but emphasized that extrapolations to other voltages and temperatures must be performed with caution. The most significant change over time was found in the equivalent series resistance, which represents the electrolyte and contact resistances within an EDLC. No interpretation of the impedance data in terms of aging mechanisms was given. However, in their simulations, the authors found that an increase in the internal resistance led to an accelerated rate of aging due to the local temperature rise as a consequence of resistive heating.

A similar conclusion was drawn by Lajnef et al. [274] in their study on EDLCs provided by EPCOS, Germany. In their study, Lajnef et al. [274] also highlighted the importance of the testing conditions on the measured capacitance loss. In particular, a recovery of the capacitance was observed during rest periods between cycling experiments. Schiffer et al. [275] investigated the heat generation of EDLCs in more detail, finding that the total heat generation is a superposition of ohmic heating due to the internal resistance and a small reversible temperature change in the order of $1\,°C$. The latter is an entropy effect due to the ordering of ions upon charging (leading to a temperature increase) and disordering of ions upon discharging (leading to a temperature decrease) of the electrochemical double layer. Due to the adverse effect of elevated temperatures on the lifetime of EDLCs, active or passive cooling of EDLC modules which are subjected to rapid charge/discharge cycles is recommended [276, 277].

Kurzweil and Chwistek [271] analyzed the solid, crystalline residue protruding from a failed EDLC (EPCOS, Germany) and the electrolysis products of Et_4NBF_4/AN at voltages of 4 V and 6 V. According to these authors, AN (CH_3CN) decomposes to acetamide (CH_3CONH_2), acetic acid (CH_3COOH) and fluoroacetic acid (CFH_2COOH), while the cation $(C_2H_5)_4N^+$ is decomposed at elevated temperatures by the Hofmann elimination of ethene, producing $(C_2H_5)_3N$ and H^+. The anion BF_4^- may be decomposed to BF_3 and F^-, leading to the formation of HF and boric acid derivatives. The presence of $BF_xO_y{}^-$ anions within aged electrodes was also suggested in the study by Azaïs et al. [266]. Kurzweil and Chwistek [271] thus concluded that the brownish salt residue in burst EDLCs is a heterogeneous mixture of a variety of compounds. In the liquid phase, soluble heterocyclic compounds such as pyrazines could be formed. However, the formation of these compounds was neither discriminated with respect to the operating voltage nor was their influence on the EDLC performance discussed.

Ishimoto et al. [263] investigated the degradation of EDLC systems in Et_4NBF_4/PC. The authors propose that, at a cell voltage of 3 V, H_2, CO and CO_2 are evolved from the EDLC and an exfoliation of graphene layers at the positive electrode due to trapped water takes place. At 3.3 V, degradation of the binder (PTFE) is believed to occur, coupled with a detachment of the electrode materials from the current collectors [278]. Finally, at 4 V, the additional gas evolution of propene is measured at the negative electrode, and the coverage of both electrodes by solid degradation products (described by the authors as SEI-like films [263, 279] in analogy to LIB chemistry) was observed. By spatial separation of the positive and negative electrodes, it was found that the water content of the anolyte (electrolyte volume near the positive electrode where electrolyte oxidation takes place) increased significantly after 50 hours at 4 V while the water content of the catholyte (electrolyte volume near the negative electrode where electrolyte reduction takes place) decreased [280]. The increase in water content of the anolyte was attributed to the liberation of trapped water within the micropores of the activated carbon working as the positive electrode, causing an exfoliation of the carbon in the process. However, it should be noted that the mechanism by which this happens is unclear, and the observation of

exfoliated activated carbon using scanning electron microscopy (SEM) is at least debatable.

Nozu et al. [264] investigated the aging of laboratory-scale EDLCs at 3 V and 60 °C or 80 °C using a PC-based electrolyte with the somewhat unconventional cation $(Et_2MeNEtOMe)^+$ and the anions BF_4^- or $(CF_3SO_2)_2N^-$. The aging, quantified by a loss in discharge energy, was found to be greatly accelerated by a factor of at least 5 when operating the EDLC in ambient air. The potentials of the negative and positive electrodes were measured separately and found to shift non-monotonically over time. The specific surface areas of both electrodes were found to decrease after 1000 hours of aging. From visual examination, the authors proposed that material from the negative electrode was transferred to the positive electrode. The deposition of solid degradation products on both the positive and the negative electrode was observed using SEM. Based on XPS measurements, the formation of $C-F$ species on the positive and negative electrode was proposed.

Finally, it is worth mentioning the importance of the aging of EDLC modules or stacks which consist of a large number of individual EDLCs connected in series in order to obtain high voltages. For most practical applications, this is an aspect of considerable relevance. Due to the unavoidable scattering of properties of industrially manufactured EDLCs in terms of capacitance and leakage resistance, the cell voltages of individual EDLCs within a module may progressively deviate with time. However, during the implementation of an EDLC module in a hybrid fuel cell car [17], it could be shown that additional on-board auxiliary components to actively manage individual EDCL voltages are not necessary to avoid single cell excursions to unacceptably high voltages. Instead, a suitable initialization [281] of the EDLCs to equal voltages appears to be sufficient, mainly due to a self-regulating effect as a consequence of an increasing leakage current at higher voltages. Since the aging of EDLC modules will not be treated further in the present work, the details of the calculations [17] are not reproduced here.

5.2.3. Conclusions

From the overview given in the previous section, it is difficult to draw general conclusions regarding the aging of EDLCs due to the variety

of testing conditions employed. The following findings appear to be established:

- the presence of oxygen-containing functional groups on activated carbon electrodes reduces the lifetime of EDLCs based on non-aqueous electrolytes,

- electrolyte degradation may lead to gas evolution and pressure build-up,

- electrolyte degradation may lead to the formation of insoluble depositions on the surface of carbonaceous electrodes,

- the accessible surface area of aged electrodes may be reduced due to blocking or destruction of porosity, and

- new covalently bound species may form at the electrode surfaces upon aging.

Unfortunately, most previous studies did not correlate the physical and chemical changes to the according capacitance changes of single electrodes. It is expected that the mechanisms of capacitance loss with time differ depending on the electrode polarization. Also, the role of structural changes of the carbonaceous electrodes due to repeated expansion and contraction cycles has been neglected so far. In fact, the mechanism of expansion has not been settled satisfactorily yet, with possible explanations including the change in surface tension of the carbon [282] and intercalation into graphitic domains [190]. Further, the correlation between the working voltage of the EDLC and the degradation processes occurring at each electrode has not been sufficiently addressed to date.

The remainder of the present work will describe the experiments undertaken to clarify the mechanism of electrode expansion in EDLCs as well as the relationship between performance loss and physicochemical modifications on the single electrode level at elevated voltages.

Part II.

Experimental methods

Chapter 6.

Electrode materials and electrolytes

6.1. Electrode materials

6.1.1. Activated carbon

The activated carbon used in this work was YP17 (Kuraray Chemical, Japan), which is produced via the steam activation of pyrolyzed coconut shell. It is highly porous, as indicated by its benzene and iodine adsorption capacities as well as the high specific surface area given by the manufacturer (Table 6.1).

Table 6.1.: Properties of YP17 as given by Kuraray Chemical.

Iodine adsorption / $mg\,g^{-1}$	1700–1800
Benzene adsorption / wt%	45–55
Total surface area / $m^2\,g^{-1}$	1600–1700
pH	5–8
Ash content / %	max. 1.0
Particle diameter / µm	3–20

YP17 was used either as a powder in the as-received form or as a free-standing sheet bound with PTFE. The bound sheet was produced from a slurry consisting of 25 wt% YP17 in a 1:1 mixture by mass of isopropanol and distilled water. Under constant stirring, a suspension of 35.5 wt% PTFE in water (TE 3554-N, DuPont) was added dropwise until an equivalent of 10 wt% of PTFE with respect to YP17 was obtained. In order to achieve a precipitation of PTFE, acetone was then added to the suspension in a mass ratio of 2:1 with respect to YP17. After 15 minutes of vigorous stirring, the suspension was heated to 150 °C until a dough-like mass was obtained. The moist dough was kneaded repeatedly and rolled into flat sheets of different thicknesses. Finally,

the self-supporting sheets were left to dry under ambient conditions overnight before being dried at 120 °C under a vacuum of 10^3 Pa for several days. The thus produced bound activated carbon was denominated YP17/PTFE.

6.1.2. Graphite

In this work, the behavior of the synthetic graphite TIMREX® SFG44 (TIMCAL, Switzerland) in EDLC electrolytes was investigated. According to the manufacturer, SFG44 is manufactured by the graphitization of coke, which is performed at temperatures of at least 2800 °C during 3–4 weeks. After graphitization, the cooling of the material requires 2–3 weeks before unloading. The final graphite powder is essentially obtained by crushing, milling and sieving.

Table 6.2.: Properties of SFG44 as given by TIMCAL.

BET surface area[a] / $m^2\,g^{-1}$	5
Ash content / %	max. 0.1
Moisture content / %	max. 0.5
Particle diameter[b] / µm	44–53
d_{002} / Å	3.35
L_c / nm	min. 200
Scott density[c] / $g\,cm^{-3}$	0.19
Xylene density[d] / $g\,cm^{-3}$	2.26

[a] See Section 8.4 for a description of the BET method.
[b] Represents the 90th percentile of the particle size distribution (D90).
[c] Represents the bulk density of the tap-packed powder.
[d] Represents the apparent density of the graphite particles.

The nominal properties of SFG44 as given by the manufacturer are summarized in Table 6.2. The powder was used either as-received or in the form of bound electrodes based on poly(vinylidene fluoride) (PVDF). In order to produce the latter, a solution of 20 wt% PVDF (SOLEF® PVDF 1015 from Solvay, Belgium) in *N*-methyl-2-pyrrolidone (NMP) was prepared. The graphite powder was added to this solution so as to obtain a SFG44:PVDF mass ratio of 9:1. The resulting slurry was doctor-bladed onto baking paper and dried at 80 °C for 12 hours, after

which the electrode thickness was $(135 \pm 10)\,\mu m$. This self-supporting electrode was denominated SFG44/PVDF.

6.1.3. Highly oriented pyrolytic graphite

HOPG is a monolithic piece of graphite derived from pyrolytic carbon [118]. In the present work, HOPG was used as a model system providing a nearly atomically flat surface consisting almost entirely of graphitic basal planes highly suitable for imaging via AFM (Section 8.2). The manufacturing of HOPG and its resulting properties has been reviewed by Moore [283] and is briefly summarized in the following.

The production of pyrolytic carbon involves CVD of hydrocarbons such as methane, propane and benzene onto suitable substrates such as graphite, metals or ceramics at temperatures in the range of 700–2200 °C. Pyrolytic carbon itself has a preferential orientation of graphitic domains parallel to the substrate surface with a very low stacking order of the graphene layers. The full width at half maximum (FWHM) of the $0\,0\,2$ reflexion determined by Cu K_α radiation is referred to as the mosaic angle or mosaic spread of monolithic carbon or graphitic materials. Correspondingly, the mosaic structure of a monolithic crystalline material describes the misorientation of individual crystallites within the material with respect to each other.

Through graphitization heat treatment of the pyrolytic carbon, so-called pyrolytic graphite with a mosaic spread of approximately $2\,°$ is obtained. HOPG is produced by annealing at approximately 3000 °C under compressive stress (stress-annealing), resulting in a reduction of the mosaic spread to about $0.2°$. In HOPG, the misorientation of the c-axes of the individual crystallites with respect to each other is generally less than $1\,°$ [118].

Due to the weak bonding between the graphite layers (Section 4.4), fresh surfaces may be obtained by cleaving of HOPG. The cleaving procedure usually involves peeling off the uppermost layers of graphite using conventional adhesive tape. Due to the mosaic structure of HOPG, even a perfectly cleaved HOPG surface will never be atomically flat due to the protrusion of individual crystallites to different extents, resulting in the presence of steps on the surface.

The HOPG used in this work was of the ZYA grade (Tectra, Germany, or Advanced Ceramics, USA) and was always freshly cleaved prior to experiments. For experiments involving electrochemical treatment in non-aqueous electrolytes, the cleaving was performed in an argon-filled glovebox with less than $1\,ppm$ H_2O and O_2, respectively. The manufacturer's data is listed in Table 6.3.

Table 6.3.: Properties of HOPG-ZYA as given by Advanced Ceramics.

Mosaic spread	$0.4\pm0.1\,°$
Thickness / mm	2
Size / mm^2	12×12
Thermal conductivity / W (m K)$^{-1}$	1600-2000[a], 8[b]
Electrical resistivity / $\Omega\,cm^{-1}$	$3.5\text{-}4.5^{a}\cdot10^{-5}$, 0.15-0.25[b]
Density / $g\,cm^{-3}$	2.26

[a] Perpendicular to the c-axis.
[b] Parallel to the c-axis.

6.1.4. Single-walled carbon nanotubes

SWCNTs were obtained from Carbon Nanotechnologies (now Unidym, USA) in the purified form (P grade). The purification of the SWCNTs involves an oxidative treatment [157] which preferentially removes catalyst particles and non-SWCNT carbon. The ash content of the purified SWCNTs is less than $15\,wt\%$, of which $5\,wt\%$ is non-SWCNT carbon according to the manufacturer.

The SWCNTs were produced by the HiPco process, which involves the high-pressure decomposition of CO [152, 153]. In this process, the feedstock gas is a mixture of CO and $Fe(CO)_5$ which passes through a heated reactor. Rapid thermal decomposition of $Fe(CO)_5$ occurs above 250–300 °C, leading to the formation of catalytically active iron clusters. SWCNTs grow on these clusters via the disproportionation of CO (the Boudouard reaction):

$$2\,CO_{(g)} \longrightarrow C_{(s)} + CO_{2\,(g)} \tag{6.1}$$
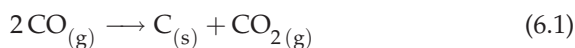
Evidence for the formation of SWCNTs is provided by TEM [152] and the presence of radial breathing modes (RBMs) in the Raman spectrum [157].

The SWCNT powder was used either as-received or in form of a self-supporting electrode. In order to produce the latter, a SWCNT dispersion was prepared by adding 0.1 wt% of SWCNT powder to ultra-high purity water (Purelab UHQ from ELGA LabWater, UK) under the addition of 1 wt% of the surfactant Triton X-100 (Sigma-Aldrich). After 2 hours of ultrasonication, the dispersion was filtrated through a PVDF membrane with a pore size of 0.22 µm (Durapore membrane filter from Millipore, USA) and the thus obtained SWCNT mat (also termed buckypaper) washed thoroughly with water and methanol. Finally, the self-supporting mat was dried for several days at 120 °C under a vacuum of 10^3 Pa. This fabrication process was adapted from a procedure given previously in [284].
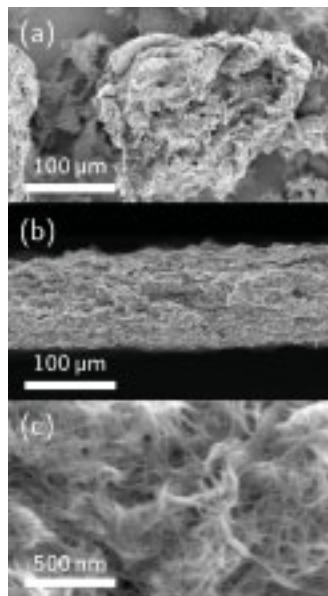
Figure 6.1.: SEM micrographs of a self-supporting SWCNT mat. (a) As-received SWCNT powder, (b) cross-section of filtrated SWCNT mat, and (c) view perpendicular to the SWCNT mat surface.

SEM micrographs of one of the SWCNT mats produced by the above process are shown in Figure 6.1. The thickness was in the order of $100\,\mu m$ (Figure 6.1b). The reason for the structural stability in the absence of any binder is the breaking up of large agglomerates in the as-received powder (Figure 6.1a) and the formation of an entangled SWCNT network (Figures 6.1b, c). In Figure 6.1c, bundles consisting of several tightly packed SWCNTs are visible. The typical bundle diameter in the samples studied in the present work was less than $10\,nm$.

6.2. Electrolyte solutions

Electrolyte solutions consisting of $1\,M\ Et_4NBF_4$ in AN and in PC (brand name DIGIRENA®) were provided by Honeywell Specialty Chemicals Seelze, Germany. Except where noted otherwise, these solutions were used in all experiments in the present work. The sealed bottles were opened and stored in an argon-filled glovebox with less than $1\,ppm$ H_2O and O_2, respectively. The manufacturers data is given in Table 6.4.

Table 6.4.: Properties of electrolyte solutions used in this work as provided by Honeywell Specialty Chemicals Seelze. Additional information regarding the pure solvents can be found in Table 3.3.

	$1\,M\ Et_4NBF_4$/AN	$1\,M\ Et_4NBF_4$/PC
Density at $20\,°C$ / $g\,cm^{-3}$	0.847	1.196
Flashpoint / $°C$	2	ca. 130
Hazard warnings	Highly flammable (F) Harmful (Xn)	Irritant (Xi)

Chapter 7.

Electrochemical characterization

7.1. Electrochemical cell design and assembly

The principle of electrochemical characterization by means of a three-electrode setup [60] is illustrated in Figure 7.1. The current is passed through the working (or indicator) and counter (or auxiliary) electrode while the electrode potential E of the working electrode is measured with respect to that of the reference electrode. Requirements regarding the nature of the reference electrode will be discussed in the next section. The cell voltage U is measured as the potential difference between the working and the counter electrode. In practice, a potentiostat or
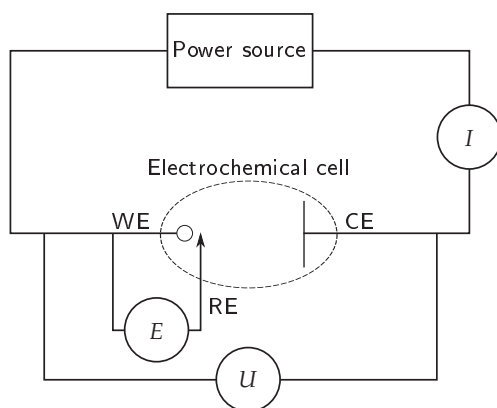
Figure 7.1.: Electrochemical characterization using a three-electrode setup. The working electrode (WE), counter electrode (CE) and reference electrode (RE) are indicated along with the low-impedance current (I) and high-impedance voltage (E and U) measurements. After Bard and Faulkner [60].

galvanostat simultaneously fulfills the functions of power source, volt- and ammeter.

During current flow, there is a potential drop within the electrochemical cell due to the ohmic resistance of the electrolyte. For this reason, the reference electrode should be placed as closely as possible to the working electrode to minimize the error in the measurement of E.

The test cell used for electrochemical characterization in this work is shown in Figure 7.2. The electrode stack has a maximum diameter of 13 mm and is compressed by a spring-loaded piston. The lower position of the working electrode within the cell is fixed in this construction, achieving a close positioning with respect to the reference electrode. To minimize the contact resistance between the electrodes and the titanium pistons which acted as current collectors, either platinum discs or carbon-coated aluminum foil (Gaia Akkumulatorenwerke, Germany) were placed between the two. The separator used was either a proprietary cellulose-based paper separator provided by Maxwell Technologies, Switzerland, or an unbound glass fiber separator (type EUJ116) obtained from Hollingsworth & Vose, UK. Hermetic sealing of the titanium wire feedthrough used for contacting the reference electrode was achieved by means of chromatography fittings (types P-259 or P-200 from Upchurch Scientific, USA). Further sealing was achieved by means of EPDM (ethylene propylene diene M-class rubber from Angst & Pfis-
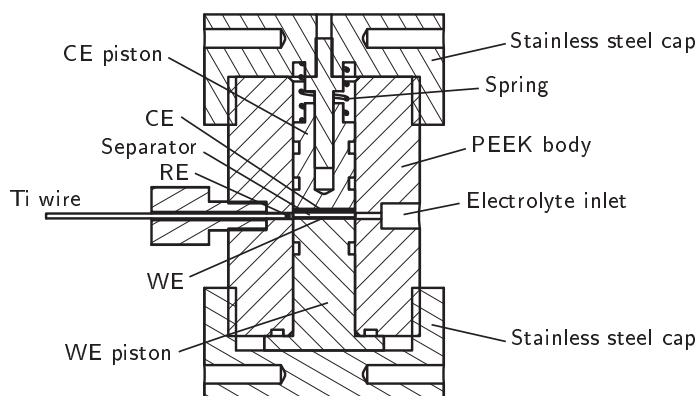
Figure 7.2.: Three-electrode cell for electrochemical measurements.

ter, Switzerland) O-rings for the pistons and EPDM or silicone seals for the electrolyte inlets. Poly(aryletheretherketone) (PEEK) was chosen as electronically insulating construction material due to its chemical inertness, high stiffness and stability up to its glass transition temperature of about 140 °C [94].

For assembly, the cell was fully assembled under ambient conditions and then dried for at least 24 hours at 120 °C and 10^3 Pa prior to experiments. After this period, the cell was vented with argon, hermetically sealed and transferred to an argon-filled glovebox with less than 1 ppm of H_2O and O_2, respectively. Inside the glovebox, the cell volume was filled with the desired electrolyte and resealed. Unless otherwise mentioned, the above procedure was also applied for the assembly of all other electrochemical cells used in this work.

7.2. Choice of reference electrode

In electrochemistry, reference electrodes must exhibit a constant electrode potential over the entire duration of an experiment and are usually chosen among three main types [80]:

- redox electrodes, in which the electrode material itself is inert under the experimental conditions,

- electrodes of the first kind, in which the metallic cation of the electrode material is involved in the potential-determining redox reaction, and

- electrodes of the second kind, in which the activity of the metallic cation of the electrode material depends on the activity of an anion in solution.

In all three cases, the electrode potential E is given by the Nernst equation [60, 78, 80]:

$$E = E^0 + \frac{RT}{zF} \ln \frac{a_{\text{Ox}}}{a_{\text{Red}}} = E^{0\prime} + \frac{RT}{zF} \ln \frac{c_{\text{Ox}}}{c_{\text{Red}}} \qquad (7.1)$$

in which E^0 and $E^{0\prime}$ are the standard electrode potential and formal electrode potential, respectively, R and T are the gas constant and tem-

perature, z is the number of electrons exchanged during the redox reaction and F is the Faraday constant. a_{Ox} and a_{Red} are the activities of the oxidized and reduced species, respectively, and c_{Ox} and c_{Red} the corresponding concentrations.

The primary reference electrode is the SHE as mentioned in Section 3.3.1. It is a redox electrode in which the electrode material, platinum, is not itself involved in the potential-determining reaction. Instead, the half-cell reaction $2\,H^+_{(aq)} + 2\,e^- \rightleftharpoons H_{2\,(g)}$ which occurs at the platinum electrode determines the electrode potential. For the SHE, $a_{H^+} = a_{H_2} = 1$.

An example of a commonly employed electrode of the first kind is a silver wire immersed directly into the electrolyte solution, for which the potential-determining half-cell reaction is $Ag^+_{(aq)} + e^- \rightleftharpoons Ag_{(s)}$.

A popular electrode of the second kind is obtained by coating the silver wire with AgCl, the activity of Ag^+ ions in solution thus depending on the anion concentration via the solubility product constant $K_{sp} = a_{Ag^+}\,a_{Cl^-}$. In order to maintain approximately constant ionic activities, the reference electrode is immersed in a separate electrolyte solution which does not participate in the electrochemical system of interest and is connected to the electrochemical system via a salt bridge [60, 80].

Often, quasi-reference electrodes (QREs) are employed for which no redox potential can be readily defined using the Nernst equation [60]. QREs are usually immersed directly into the test solution and are often employed in non-aqueous electrolytes in order to avoid contamination of the test solution with foreign species and eliminate liquid junction potentials. Unfortunately, there is no accepted primary reference electrode in non-aqueous solutions as discussed by Izutsu [80]. The electrode potential of the most popular QRE, a silver wire, is relatively stable in AN- but not in PC-based electrolytes due to the weak solvation of Ag^+ and hence high sensitivity to trace water and impurities in the latter [80].

In the present work, activated carbons such as YP17/PTFE were found to represent convenient QREs. As opposed to the reference electrodes mentioned above, the electrode potential of activated carbon in non-aqueous solutions is not governed by Equation (7.1) since the ma-

terial is ideally polarizable over a wide potential range. In this case, the potential of an activated carbon electrode is given by its Galvani potential (Section 3.3.1). Due to the high double layer capacitance C, any transfer of a small amount of charge dQ to the QRE due to spontaneous redox reactions of trace impurities are not expected to significantly affect the electrode potential according to $dE = dQ/C$. When $dE \approx 0$ for the duration of an experiment, the potential of the activated carbon QRE is essentially equal to its immersion potential [240].

In order to assess the stability of the potential of YP17/PTFE as a suitable reference potential in AN- and PC-based EDLC electrolytes, it was calibrated against the reference redox system ferrocene/ferricenium ion as recommended by IUPAC [285]. Ferrocene (Sigma-Aldrich, purum, $\geq 98.0\,\%$ Fe) is designated by $Fe(C_5H_5)_2$ or Fc, and is an organometallic compound consisting of a central iron atom sandwiched between two cyclopentadienyl rings. The results of the YP17/PTFE calibration and stability assessment are presented in Section 9.2.6.

7.3. Cyclic voltammetry

Cyclic voltammetry is a commonly employed form of linear sweep chronoamperometry (also referred to as linear sweep voltammetry) [60] in which the voltage of an electrochemical system is changed by a constant rate, dU/dt, between two arbitrary vertex voltages.

In the case of an electrode without any faradaic contributions over the entire investigated potential range, the current response I is purely capacitive and follows from the derivative of Equation (3.1) with respect to time:

$$\frac{dQ}{dt} = I = C\frac{dU}{dt} \tag{7.2}$$

The current response of an ideal capacitor of capacitance C with leakage resistance R_p and series resistance R_s is shown in a series of cyclic voltammograms (CVs) in Figure 7.3. Deviations from the ideal capacitive box shape become more pronounced with increasing series resistance and increasing potential sweep rate, while a decrease in leakage resistance results in a tilting of the CV.
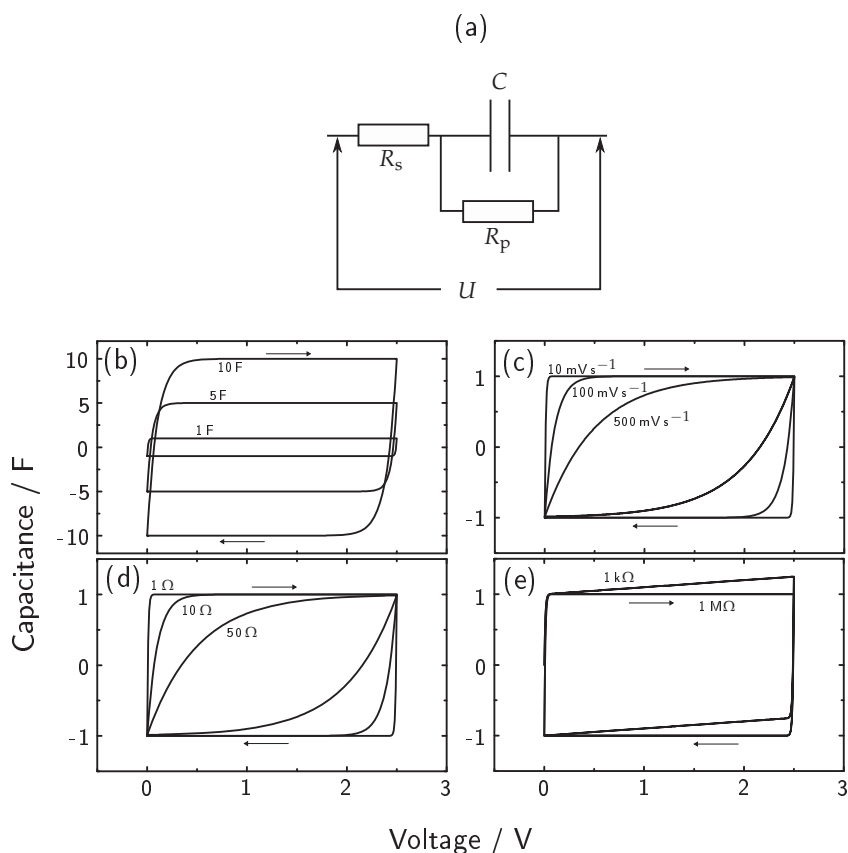
Figure 7.3.: Series of CVs for the electrical circuit shown in (a) obtained by simulation with MATLAB/Simulink™. The parameters used were $C = 1\,\mathrm{F}$, $R_\mathrm{p} = 1\,\mathrm{M\Omega}$, $R_\mathrm{s} = 1\,\Omega$ and a potential sweep rate of $10\,\mathrm{mV\,s^{-1}}$. The direction of the potential sweep is indicated by arrows. The current is normalized to the sweep rate and thus is equal to the differential capacitance given in F. The effect of parameter variation is shown in (b) for C, (c) for the sweep rate, (d) for R_s, and (e) for R_p.

In practice, an increased series resistance may be the result of an increased electrolyte resistance or contact resistance between grains of electrode material or between these grains and the current collector, resulting in a delayed current response for a given sweep rate as shown in Figure 7.3d. A low leakage resistance may result from the presence of

a faradaic reaction besides double layer charging or a path of electronic conductivity between the working and counter electrode.

Unless mentioned otherwise, all CVs in this work were recorded with an IM6e or IM6ex electrochemical workstation (Zahner-Elektrik, Germany).

7.4. Galvanostatic cycling

In this work, galvanostatic cycling refers to the technique of constant-current chronopotentiometry [60]. A constant current I flows through the working and counter electrodes, which in the case of a purely capacitive system leads to a change in voltage according to (7.2), which may be rewritten as

$$\frac{\mathrm{d}U}{\mathrm{d}t} = \frac{1}{C}\,I \tag{7.3}$$

For a given applied current I, a plot of the voltage U against time therefore has a slope $\mathrm{d}U/\mathrm{d}t$ which is inversely proportional to the capaci-
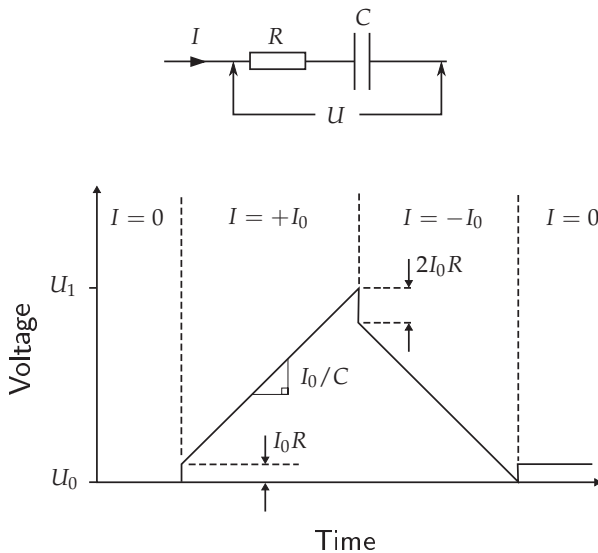
Figure 7.4.: A galvanostatic cycle obtained by applying the current I to the electrical circuit shown above within the potential range $U_0 \leq U \leq U_1$.

tance C. A single galvanostatic cycle is schematically depicted in Figure 7.4 for the series connection of a resistance R with a capacitance C.

In the present work, all galvanostatic measurements were performed using a battery cycler (Computer Controlled Cell Capture, CCCC) from Astrol Electronics, Switzerland.

7.5. Impedance spectroscopy

The impedance Z of an electrical system describes the relationship between the applied voltage, U, and the current flow, I, according to

$$I = \frac{U}{Z} \tag{7.4}$$

Widely used in electrochemistry, the technique of EIS involves the study of the impedance of an electrochemical system, usually by measuring the current response to an applied sinusoidal voltage perturbation at different frequencies. An introduction to EIS is given by Bard and Faulkner [60] in their electrochemistry textbook, while a more comprehensive treatment is presented in the book edited by Barsoukov and MacDonald [286]. The application of EIS to the study of EDLCs has also been described by Conway [44].

The principle of an EIS measurement is shown in Figure 7.5. A voltage perturbation $U(t)$ of amplitude U_0 and angular frequency ω (in $\mathrm{rad\,s^{-1}}$) results in a current response with amplitude I_0 which is of the
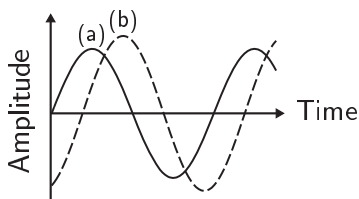
Figure 7.5.: Measurement principle of an EIS experiment. A sinusoidal perturbation in the voltage, (a) $U = U_0 \sin(\omega t)$, results in a current response (b) $I = I_0 \sin(\omega t + \phi)$, which is shifted in phase with respect to the perturbation signal by the phase angle ϕ.

same frequency but, in general, out of phase with the voltage perturbation as given by the phase angle ϕ.

For a pure resistance R, $Z = R$ in Equation 7.4 according to Ohm's law. For a pure capacitance, $Q = CU$ and hence $I = C\,dU/dt$, so that

$$
\begin{aligned}
I &= C\omega U_0 \cos(\omega t) & (7.5) \\
&= C\omega U_0 \sin\left(\omega t + \frac{\pi}{2}\right) & (7.6) \\
&= \frac{U_0 \sin(\omega t + \frac{\pi}{2})}{X_{\mathrm{c}}} & (7.7)
\end{aligned}
$$

in which $X_{\mathrm{c}} = 1/\omega C$ is called the capacitive reactance. Hence, for a pure capacitance, the current response is exactly $90\,^\circ$ out of phase with the voltage perturbation and the impedance is given by $Z = X_{\mathrm{c}}$. In general, it is convenient to map the impedance of a given electrochemical system in a complex plane (Nyquist) plot in which all components with $\phi \neq 0$ are assigned as imaginary and projected along the y-axis, while all components with $\phi = 0$ are assigned as real and projected along the x-axis. Formally, the impedance Z therefore consists of a real part, Z_{Re}, and an imaginary part, Z_{Im}, represented by

$$
Z = Z_{\mathrm{Re}} - iZ_{\mathrm{Im}} \tag{7.8}
$$

Hence, for a series connection of a resistance R and capacitance C, the impedance is given by $Z = R - iX_{\mathrm{c}}$ and the phase angle by $\phi = \tan Z_{\mathrm{Im}}/Z_{\mathrm{Re}}$. Due to the presence of the capacitive component, the impedance is a function of the frequency. An idealized equivalent circuit of an EDLC is shown in Figure 7.6a consisting of a component R_{e} describing the electrolyte resistance and the impedance of a porous electrode Z_n as derived in Section 3.5. Also, the contact between the electrode and the current collector is approximated by the contact resistance R_{c}, which is in parallel with the capacitance of the current collector, C_{c}.

In Figure 7.6b–e, the influence of various parameters on the shape of the Nyquist plot of an EDLC is shown based on the equivalent circuit in Figure 7.6a. Characteristic for all plots is the $45\,^\circ$ slope at high frequencies, which arises due to the distributed resistive and capacitive
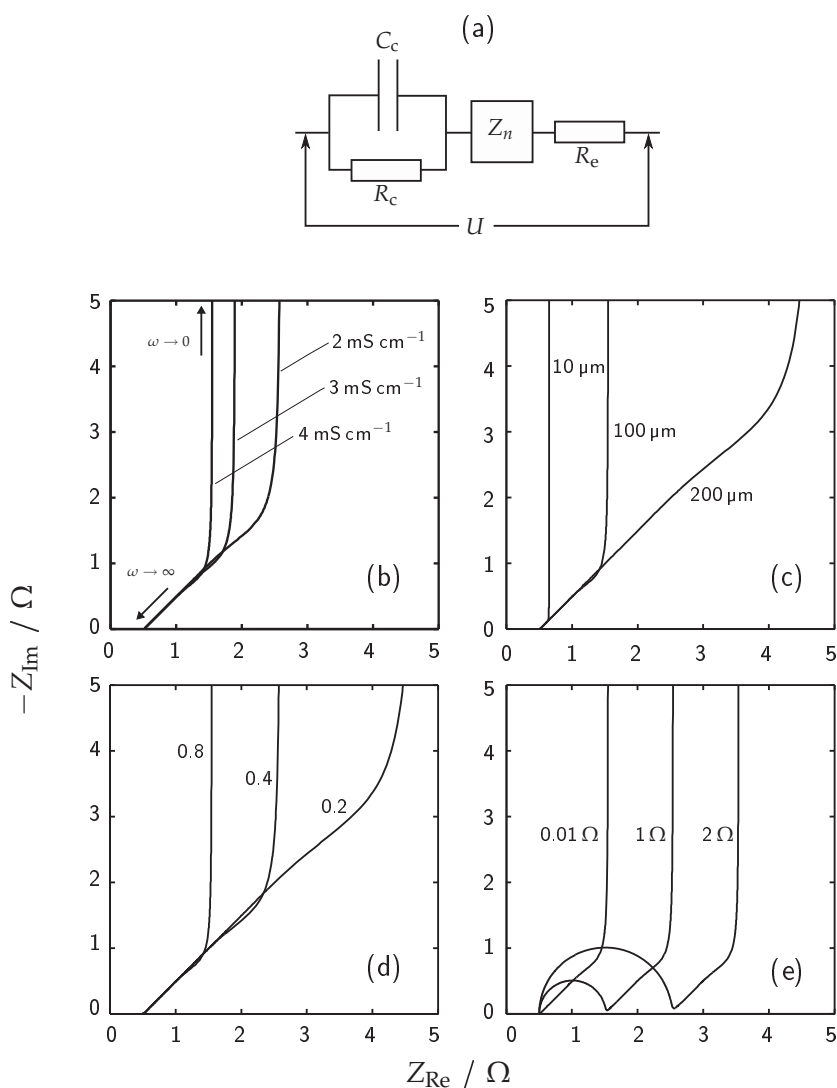
Figure 7.6.: Calculated Nyquist plots of the equivalent circuit shown in (a). For the electrode, a porosity of 0.8, pore radius of 1 nm and thickness of 100 µm was assumed. For the electrolyte, a bulk conductivity of 40 mS cm^{-1}, pore conductivity of 4 mS cm^{-1} and effective volume of 0.1 cm^{-3} was used. The contact between electrode and current collector was modeled by a resistance of 10 mΩ and the capacitance of the current collector was taken to be 20 µF for a geometric area of 1 cm^2. The parameters varied were (b) the electrolyte conductivity in the pores, (c) the electrode thickness, (d) the electrode porosity, and (e) the contact resistance between electrode and current collector.

network within the pores of the electrode as modelled by the transmission line discussed in Section 3.5, and its contribution to Z_{Re} is often termed the equivalent distributed resistance (EDR) [11]. As the frequency of the perturbation voltage approaches zero, the phase angle approaches 90 $^\circ$ as for an ideal capacitor.

The resistance of the electrolyte solution has the effect of shifting the entire curve in the Nyquist plot along the real axis due to the series connection of R_e. An increased electrolyte resistance within the pores increases the resistive contribution of the 45 $^\circ$ region as shown in Figure 7.6b. By increasing the electrode thickness, the region of distributed resistance is also increased (Figure 7.6c). The same effect is achieved by reducing the porosity of the electrode while maintaining a constant pore diameter (Figure 7.6d). It is worth noting that a change in pore diameter while maintaining a constant porosity has no effect on the shape of the Nyquist plot, but results in a different frequency dependence as was shown in Figure 3.12 in Section 3.5.

The effect of poor electrical contact between electrode and current collector is highlighted in Figure 7.6e, where the parallel configuration of the current collector capacitance and contact resistance between current collector and electrode results in a more or less pronounced semi-circle in the Nyquist plot. For all plots, an increase in the real component of the impedance corresponds to an increase of the equivalent series resistance (ESR) at a given frequency.

Hence, EIS enables the characterization of capacitive and resistive components of EDLCs and is particularly sensitive to the pore structure of the electrodes. In this work, all impedance spectra were measured with an IM6e or IM6ex electrochemical workstation (Zahner-Elektrik, Germany). Due to the high sensitivity of the impedance spectrum of single electrodes on the exact position of the reference electrode [287], only EIS measurements on symmetric full cells are reported in the present work.

Chapter 8.

Analytical techniques

8.1. Electrochemical dilatometry

Dimensional changes of single electrodes were measured in situ using an electrochemical dilatometer which was developed in-house by Hahn et al. [190, 288]. A cross-sectional view of the apparatus used in the present work is shown in Figure 8.1.

All components were dried and assembled as outlined in Section 7.1. In the electrochemical dilatometer shown in Figure 8.1, a stiff glass frit
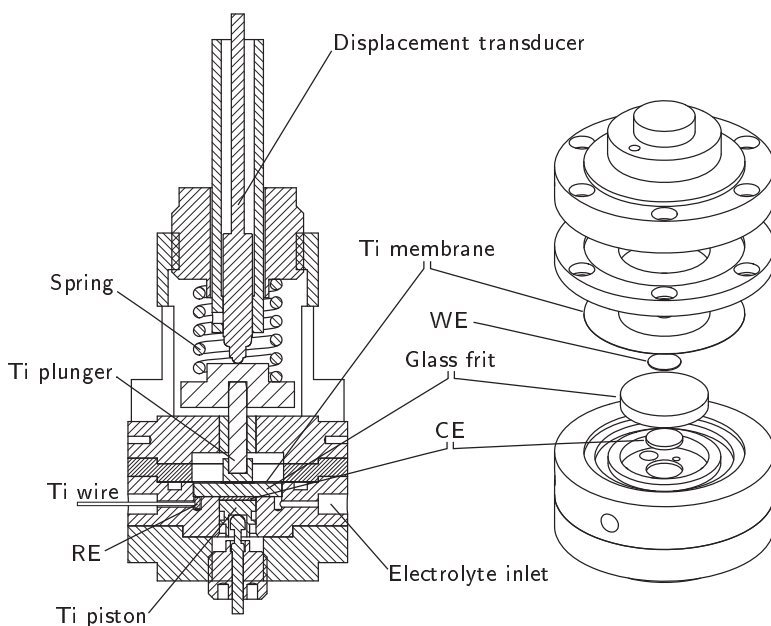
Figure 8.1.: Main components of the electrochemical dilatometer used in this work.

was fixed in position and served as the separator between working and counter electrode. Hence, the height change of the working electrode alone could be resolved. A titanium plunger weighted with a total load of 10 N transmitted the change in thickness of the working electrode through a flexible titanium membrane (thickness 50 µm) to a displacement transducer (DP/1/S, Solartron Metrology, England, specified resolution 60 nm). The relative height changes were normalized to the dry electrode thickness which was measured prior to the experiment. Alternatively, the height of unbound electrodes could be measured through the titanium membrane using a micrometer gauge mounted on a tripod.

The electrochemical dilatometer was placed inside a temperature-controlled test chamber (BINDER, Germany) set to 25 °C for the duration of the experiment. After a settling period of 2–6 hours, the measured experimental drift was less than 100 nm per hour. The working electrode potential was controlled against a YP17/PTFE QRE using the same potentiostat as for the CV (Section 7.3) and EIS (Section 7.5) measurements.

8.2. Atomic force microscopy

8.2.1. Background

The technique of AFM was first reported by Binnig, Quate and Gerber in 1986 [289]. The versatility of AFM is demonstrated by its capability to achieve atomic scale resolution under ambient conditions [290] for electronically conductive and insulating samples alike as well as the possibility to probe mechanical properties on the nanometer scale [291]. In the present work, AFM was applied to obtain topographical images of surfaces with the scale of roughness ranging from below 1 nm up to about 1 µm.

The working principle of AFM is outlined in Figure 8.2. A fine tip is mounted on a cantilever which has a spring constant below that of the interatomic bonds of the sample, leading to a deflection of the cantilever upon interaction with the sample surface. The extent of deflection is often measured using the optical lever technique, in which a laser beam is focused onto the end of the cantilever and the position of the reflected

beam measured by a position sensitive detector such as a segmented photodiode. The relative position of the sample with respect to the cantilever along the z-axis is varied by means of a piezo. Other piezo elements also enable a scanning of the tip across the sample surface in the x- and y-directions (Figure 8.2). The piezos are integrated in a scanner which may be located within the stage (sample-scanning) or at the cantilever (tip-scanning).

Usually, van der Waals forces account for the attractive component between the tip and the sample, while the dominant repulsive component arises due to the overlapping of electron orbitals of tip and sample (Born repulsion) [291]. The van der Waals interaction is essentially the sum of three attractive interactions: dipole-dipole interactions (Keesom potential), dipole-induced dipole interactions (Debye potential) and dispersion (London) forces due to instantaneously fluctuating charge density in all matter.

All of the corresponding potentials describing the attractive interaction are proportional to r^{-6}, where r is the distance between the tip and sample surfaces. The Born repulsion dominates the short range interaction, being proportional to r^{-12}. In Figure 8.3, a schematic plot of the cantilever deflection as a function of the z-piezo displacement is shown. Beyond the range of significant tip-sample interaction due to van der Waals forces, the cantilever deflection is constant. Attractive
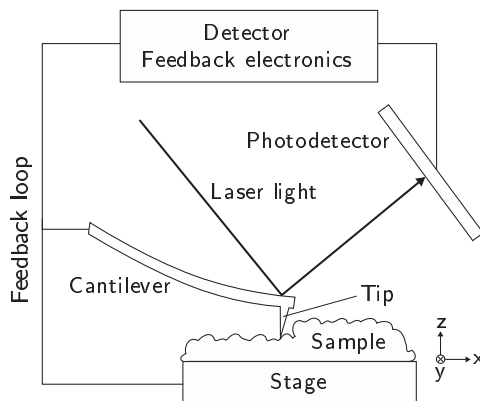
Figure 8.2.: Topographical measurement of a sample surface using AFM.

(Figure 8.3b and d) or repulsive forces (Figure 8.3c) are balanced by the deflection of the cantilever multiplied by its spring constant. Hence, the measured deflection is a measure of the forces acting between tip and sample.

Three fundamentally different modes of AFM operation may be distinguished. In non-contact or frequency modulated AFM, the cantilever is mounted on an additional piezo which is made to oscillate near the resonant frequency of the cantilever. The cantilever oscillation is progressively damped upon tip-sample approach due to variations in the force gradient acting between tip and sample, whereby the operating regime for true non-contact AFM is that of attractive tip-sample forces (Figure 8.3b).

In tapping mode or intermittent contact AFM, the amplitude of cantilever oscillation is typically larger than in non-contact AFM and the operating regime is extended to include one tip-sample contact per oscillation cycle. Both of the frequency modulated techniques are intended to minimize the shear forces acting on the sample surface which may lead to deformation or displacement of soft or mobile surface
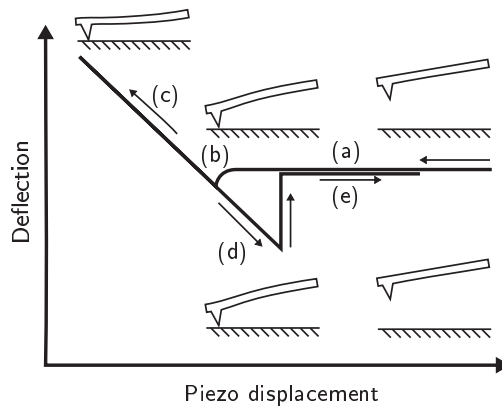
Figure 8.3.: Cantilever deflection as a function of piezo displacement during approach between tip and sample. (a) No interaction between tip and sample, (b) van der Waals attraction between tip and sample is dominant , (c) Born repulsion between tip and sample is dominant, (d) hysteresis during retraction due to adhesion between tip and sample, and (e) detachment of tip from sample.

species. Due to the difficulty in distinguishing between non-contact and intermittent contact AFM during an experiment, these techniques are simply referred to as frequency modulated AFM in the present work.

The third operating mode of AFM does not involve frequency modulation of the cantilever and is therefore referred to as static or contact mode. It is performed in the regions c and d of Figure 8.3, whereby the adhesive regime was preferred in the present work in the case of easily deformable sample surfaces. Imaging of the sample topography in contact mode may be achieved by either maintaining a constant tip height and recording the change in cantilever deflection during x–y scanning or by maintaining a constant cantilever deflection and adjusting the tip height accordingly during x–y scanning by means of an electronic feedback loop. Due to a greater z-range during imaging in the latter mode, this was the preferred method of topographical imaging used in the present work.

Generally, both frequency modulated and contact mode AFM were used to image sample topography in this work. Usually, images of higher contrast were obtained in contact mode without noticeable differences in the surface topography with respect to the frequency modulated mode. Therefore, unless otherwise mentioned, all images shown were obtained in contact mode in the adhesive regime.

8.2.2. Methodology

AFM was applied in the present work in order to investigate changes in the surface topography of a model carbonaceous electrode, HOPG, in EDLC electrolytes. In particular, the possibility of solid deposits on the electrode due to electrolyte degradation was investigated. As mentioned in Section 5.2.2, first in situ AFM experiments on HOPG in $1\,M\,Et_4NBF_4$ in PC were performed by Campana et al. [273, 292] in recent years using an open electrochemical cell within a flow-through glovebox. The advantage of PC-based electrolytes in this context is their relatively low vapor pressure (see also Table 3.3), leading to an approximately constant solution volume for the duration of the in situ experiment. Significant difficulties in this respect were encountered when using AN-based electrolytes, but also when significant gas evolution hindered satisfactory imaging of the HOPG surface. In order to

perform comparable electrochemical treatments of HOPG in both AN- and PC-based EDLC electrolytes, an ex situ topographical analysis of HOPG after electrochemical treatment was the preferred experimental strategy in this work.

An electrochemical cell was designed specifically for the electrochemical treatment of monolithic electrodes with planar surfaces, as shown in Figure 8.4. The absence of a separator facilitates the removal and surface analysis of the working electrode after treatment. In contrast to the procedure outlined in Section 7.1, the cell assembly and electrochemical treatment was carried out entirely within an argon-filled glovebox with less than $1\,ppm$ H_2O and O_2, respectively. YP17/PTFE was used as counter and reference electrode and was stored in the glovebox in a sealed container after drying at $120\,°C$ and $10^3\,Pa$ for several days, while freshly cleaved HOPG was used as the working electrode. A $1\,M$ solution of Et_4NBF_4 in either AN or PC was filled into the cell, and the working electrode potential was scanned to -2.3 V or +2 V for cathodic and anodic treatment, respectively, at a sweep rate of $10\,mV\,s^{-1}$ using an electrochemical workstation (Zahner IM6ex from Zahner-Elektrik, Germany). After a holding time of 30 minutes at these potentials, the working electrode potential was swept back to $0\,V$ at $10\,mV\,s^{-1}$ and held at this potential for 5 minutes. Finally, the potentiostatic control was interrupted and the HOPG removed from the electrochemical system. The HOPG surface was rinsed 3–5 times with pure AN or PC within the glovebox, according to the electrolyte solution used during electrochemical treatment, before transferring the HOPG to air and drying it carefully under a stream of dry nitrogen gas.

The AFM measurements were subsequently performed under ambient conditions using either an Autoprobe CP from Park Scientific Instruments (now Veeco Instruments, USA) or a PicoSPM LE from Molecular Imaging (now Agilent Technologies, USA). Both the tapping and contact modes were used for topographical imaging as discussed in the previous section. The scanners used were calibrated in the x-, y- and z-directions by means of a silicon grid (type TGZ01 from NT-MDT, Russia). For frequency modulated AFM, the PicoSPM was used in combination with tips of the type NCH Pointprobes from ScienTec, France (resonant frequency and spring constant in the range of 280–
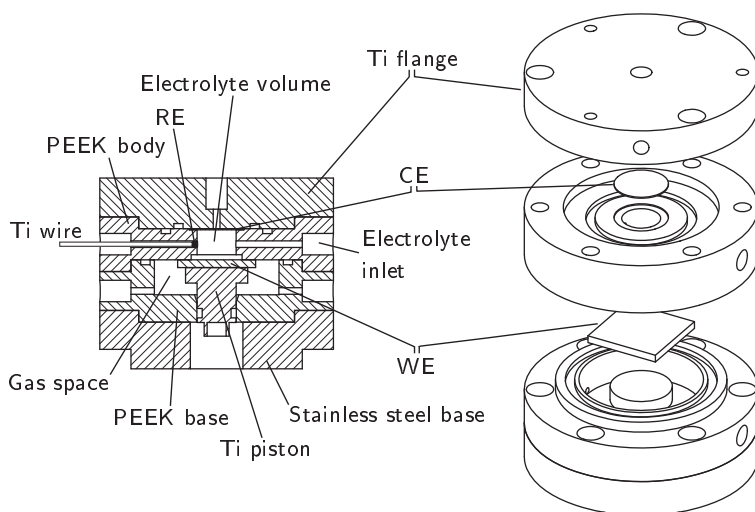
Figure 8.4.: Electrochemical cell developed for the electrochemical treatment of flat, monolithic working electrodes such as HOPG in non-aqueous electrolytes.

365 kHz and 25–50 N m^{-1}, respectively). For contact mode AFM, Microlevers type D (resonant frequency of 15 kHz and spring constant of 0.03 N m^{-1}) from Park Scientific Instruments were used in conjunction with the Autoprobe CP, while CSC38/Al BS tips from Mikromash, Estonia, (type B, resonant frequency 7–14 kHz and spring constant 0.01–0.08 N m^{-1}) were used with the PicoSPM.

8.3. X-ray scattering

8.3.1. Background

X-rays are electromagnetic radiation with wavelengths (and hence photon energies) between those of γ and ultraviolet (UV) rays, typically in the range 0.5–2.5 Å (about 2.5–0.5 keV). The production or of X-rays is achieved by a rapid acceleration or deceleration of charged particles, usually electrons. Conventional X-ray tubes consist of two electrodes: a heated tungsten filament, serving as an electron source, and a metal target (anode). A voltage of several 10^5 V is applied between the two,

causing electrons from the filament to accelerate towards the anode and strike at very high velocities (approximately 1/3 of the speed of light). Most of the kinetic energy of the electrons is converted to heat, with less than 1 % being transformed to X-rays due to deceleration of the electrons. The energy spectrum of the emitted X-rays consists of a continuous spectrum (bremsstrahlung), arising from different deceleration behaviors of individual electrons and dependent on the X-ray tube voltage, and a line spectrum characteristic of the anode material. The latter arises due to well-defined electronic transitions within the anode which become relevant when the incident electrons transfer a sufficient fraction of their kinetic energy to the bound electrons. In terms of atomic orbitals, an electron may thus be knocked out of the K shell and the corresponding vacancy immediately filled by a higher energy electron from an outer shell, causing the emission of a photon with an energy corresponding to this electronic transition. If the electronic transition occurs from the L to the K shell, the radiation is termed K_α. For an $M \rightarrow K$ transition, K_β radiation is emitted, although the emission of K_α radiation is more likely. More details may be found in Cullity's book on X-ray diffraction [293].

Another method to produce X-rays is by means of a synchrotron, which is a circular accelerator in which electrons move at highly relativistic velocities in a circular orbit [294]. The corresponding emitted radiation is termed synchrotron radiation. Briefly, electrons emitted from an electron gun are linearly accelerated and injected into the storage ring, in which bending magnets provide for the circular orbit of the electrons. In the case of full energy injection [294], the linearly accelerated electrons are first injected into a booster synchrotron in which the electrons are accelerated up to their final kinetic energy along a circular orbit.

Within the storage ring, acceleration of the electrons and compensation for lost energy due to the emission of synchrotron radiation is provided by radiofrequency cavities which consist of oscillating electromagnetic fields. In order to produce synchrotron radiation needed at the experimental stations, radiation sources such as bending magnets or insertion devices such as undulators and wigglers are required. The latter two are constituted by an assembly of dipole magnets which cause a

local deflection of the electrons. Undulators differ from wigglers in that the former produce a periodic magnetic field along the orbital path of the electrons, hence leading to a more monochromatic radiation [294]. However, in order to obtain the desired final monochromatic radiation, it is necessary to introduce X-ray mirrors and monochromators prior to the actual measurement. Finally, the scattered X-rays (see below) are recorded via suitable detector equipment.

When X-rays, regardless of their source, encounter any form of matter, they are only partly transmitted. Neglecting electronic transitions within the sample, the ratio of the linear absorption coefficient μ to the sample density ρ is a material characteristic and is approximately proportional to $\lambda^3 Z^3$, where λ is the X-ray wavelength and Z is the atomic number of the sample [293]. Thus, X-ray absorption is more pronounced in heavier elements. Also, shorter wavelength X-rays tend to be highly penetrating and are therefore termed hard, while longer wavelength X-rays are more easily absorbed and described as soft.

Absorbed X-rays, for the most part, result in electronic transitions and photoemission (Section 8.7). However, a fraction of absorbed X-rays is said to be scattered [293] due to the interaction of the oscillating electric field of the X-ray beam with the electrons in the sample. The resulting in-phase oscillating motion of the electrons results in the emission of an electromagnetic wave which has the same wavelength and frequency as the incident X-rays. These scattered X-rays are therefore said to be coherent with the incident X-rays. Incoherent X-rays are produced by the inelastic collision of an incident photon with an electron, known as the Compton effect—however, the according Compton modified radiation has a different wavelength and unrelated phase with respect to the incident radiation, and therefore does not contribute to diffraction (Section 8.3.2).

The essential information content of an X-ray scattering experiment is the intensity of the scattered X-ray beam as a function of the scattering angle 2θ (Figure 8.5). It has become common practice to differentiate between wide-angle X-ray scattering (WAXS), or X-ray diffraction (XRD), and small-angle X-ray scattering (SAXS). Although the fundamental interaction between X-rays and matter is of course identical in both cases, the experimental requirements and data analysis may be

quite different. For this reason, the two cases are presented separately in the following.
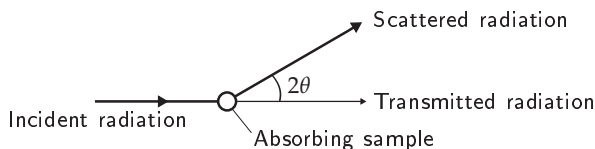
Figure 8.5.: Definition of the scattering angle 2θ during scattering of incident radiation.

8.3.2. Wide-angle X-ray scattering

Consider a wavefront of X-rays with wavelength λ impinging on a crystalline lattice as depicted in Figure 8.6. As discussed in the previous section, a part of the X-rays will be coherently scattered in all directions through interaction with the electrons in the lattice. Interference of the scattered X-rays causes a modification of the amplitude of the scattered wavefront. Under certain conditions, this interference is purely constructive, leading to a considerable reinforcement of the scattered X-rays called diffraction.

The conditions for XRD may be derived by considering the scattering of an incident wavefront from two adjacent lattice planes as shown in Figure 8.6. Completely constructive interference is only given when the scattered rays are entirely in phase, i.e. when the difference in optical path length $|LMN|$ is a whole number multiple k of λ. This diffraction condition is conveniently formulated in terms of the Bragg law [293],

$$2d \sin \theta = k\lambda \tag{8.1}$$

in which d is the distance between adjacent lattice planes. Thus, diffraction only occurs in the presence of a strictly periodic arrangement of scattering centers and only for well-defined angles of incidence θ. Of course, scattering at all other angles also takes place, but the intensity of those rays is much weaker than the intensity of the scattered rays which fulfill the Bragg law. Due to the similarity of diffraction at the so-called Bragg angles and the phenomenon of reflection of light from a planar
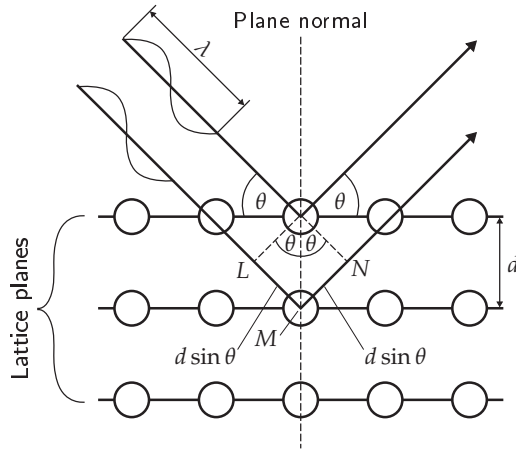
Figure 8.6.: Schematic diffraction of X-rays from a crystalline lattice.

surface, it has become common practice [293] to refer to diffracted X-rays as reflected X-rays. Diffraction for $k = 1, 2, \ldots$ is referred to as first-order diffraction, second-order diffraction and so on.

Considering incident Cu K_α radiation with $\lambda = 1.54\,\text{Å}$, the distance between adjacent graphene sheets in graphite ($d_{002} = 3.35\,\text{Å}$) is observed at $2\theta = 26.6\,°$ and is termed the $0\,0\,2$ reflection in accord with the Miller indices of the corresponding planes in the unit cell of hexagonal graphite (see Figure 4.11). Smaller periodic spacings are observed at correspondingly larger scattering angles. Therefore, the investigation of lattice spacings using XRD typically involves scattering angles above 5–$10\,°$, and is therefore also referred to as WAXS.

Due to the finite size of crystallites, destructive interference is never complete at incident angles which are close to the Bragg angle given by Equation (8.1). This results in a broadening of the diffraction curve in which the intensity of the scattered rays is plotted against the scattering angle 2θ, which is more pronounced for smaller crystals which contain fewer adjacent lattice planes [293]. The crystallite size t in direction of the reflecting planes is related to the shape of the diffraction curve by the Scherrer formula [293],

$$t = \frac{K\,\lambda}{B\,\cos\theta} \tag{8.2}$$

where B is the FWHM of the diffraction peak (expressed as an angular width, in radians, in terms of 2θ) and θ is the corresponding Bragg angle. K is a shape factor which is close to 0.9 for three-dimensional lattices ($h\,k\,l$ reflections) [293] and 1.84 for a two-dimensional lattice ($h\,k$ reflections) [295].

In the present work, XRD was used in situ to investigate changes in the lattice spacings of carbonaceous electrodes in EDLCs. The experiments were performed at the Materials Science (X04SA) Powder beamline [296] at the Swiss Light Source (SLS) using monochromatic synchrotron radiation with an energy of 17.5 keV (corresponding to $\lambda = 0.708$ Å) and the Mythen multi-channel microstrip detector [297]. The XRD measurements were carried out in transmission mode using an automatic sample changer [298, 299] which enabled the acquisition of a large number of successive diffractograms without the need for manual intervention.

Two types of electrochemical cells were used: a flexible pouch cell (Figure 8.7) and a hard-cased cell (Figure 8.8) which was developed in the context of the present work.

The pouch cell was entirely assembled in an argon-filled glovebox with less than 5 ppm O_2 after thorough drying of all cell components apart from the cell bag at 120 °C during 24 hours at less than 10^3 Pa. An activated carbon cloth (ACC-568-15 from American Kynol, USA) served as the counter electrode, from which a central hole was punched out in order to avoid contributions to WAXS. The cloth was pasted onto an expanded aluminum current collector (Dexmet, USA) using a conductive slurry consisting of 10 wt% graphite (TIMREX® KS44 from TIMCAL, Switzerland) in a 5 wt% sodium CMC solution. SFG44/PVDF (Section 6.1.2) was rolled onto an aluminum current collector and used as the working electrode. Four layers of unbound glass fiber separator (GF/G3 from Whatman International, England) were placed in between the counter and working electrode. This separator was found to have no significant contributions to the WAXS of the pouch cell. After hot sealing of the cell, the electrolyte solution was filled into the pouch cell through a poly(ethylene) (PE) tube with a syringe. After removal of excess electrolyte from the cell, this tube was also hot sealed.
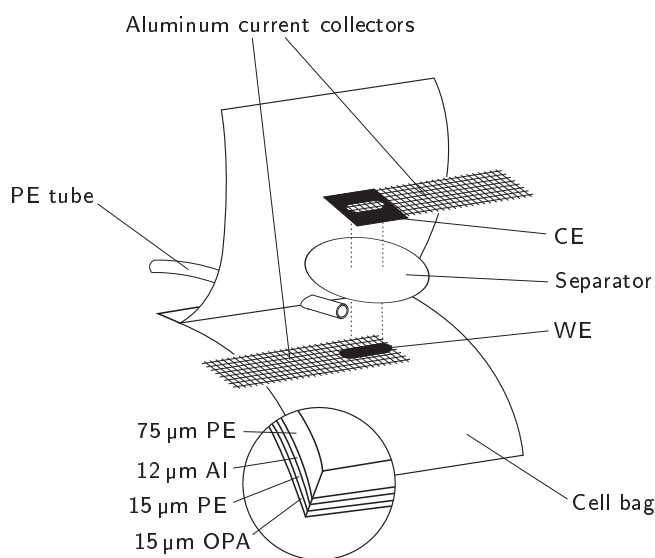
Figure 8.7.: Pouch cell for in situ XRD measurements [300]. The size of the pouch is $70 \times 70\,\text{mm}^2$. PE and OPA represent poly(ethylene) and oriented polyamide layers.

In contrast to the pouch cell, the hard-cased cell shown in Figure 8.8 enabled measurements of large amounts of loose powder in the absence of binder, imparted a compressive pressure on the electrode stack and featured less contributions to WAXS due to the cell material itself. The latter advantage is demonstrated in Figure 8.9, in which the diffractograms of SFG44/PVDF electrodes in the two cell designs are compared. Note that, due to the restricted opening angle of the conical flange of the hard-cased cell, the maximum scattering angle 2θ was limited to about 30–40 ° depending on the cell geometry. In the present work, this angular range was more than sufficient for the study of the main WAXS features of graphite.

The hard-cased cell was assembled according to the procedure outlined in Section 7.1. Glass fiber separators (GF/G3 from Whatman International, England, or EUJ from Hollingsworth & Vose, England) were used. The counter electrode consisted of MM204, a PTFE-bound activated carbon with a significant mesoporosity which is identical in composition and structure to the activated carbon MM192 described
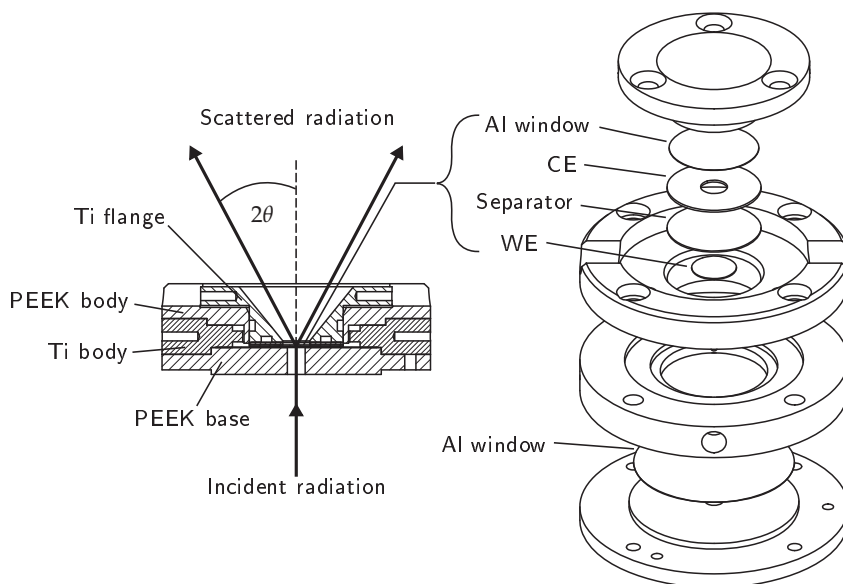
Figure 8.8.: Hard-cased cell for in situ XRD measurements. The aluminum windows and titanium parts serve as current collectors for the working and counter electrode, respectively.

in [288]. X-ray windows of aluminum (300 µm thickness) or titanium (50 µm thickness) were used to hermetically seal the cell, function as current collectors and provide an internal standard for the diffraction peaks.

For both pouch and hard-cased cells, the working electrode potential was controlled against the potential of the counter electrode using a battery cycler (CCCC from Astrol Electronics, Switzerland). The potential of the counter electrode was considered to be pinned due to its large capacitance relative to the working electrode. At the potential of maximum charging of the working electrode, the potential of the counter electrode was estimated to shift by 160 mV at most.

In situ diffractograms were collected within 30 s per acquisition, and per measurement a total of two acquisitions was performed at two detector positions differing by $\Delta(2\theta) = 0.5\,°$ in order to compensate for blind spots on the detector.
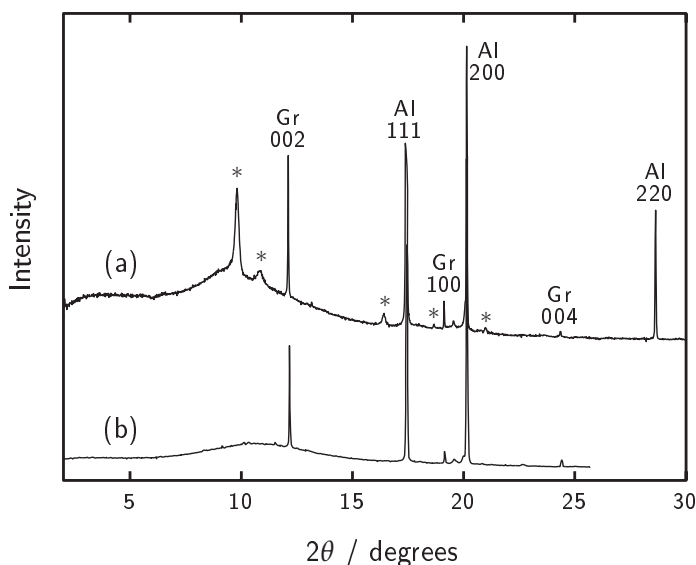
Figure 8.9.: Comparison of in situ diffractograms recorded at the MS Powder beamline ($\lambda = 0.708\,\text{Å}$) of the SLS for (a) a pouch cell and (b) a hard-cased cell, each containing SFG44/PVDF as working electrode. The patterns are offset along the y-axis for clarity. Gr and Al denote diffraction peaks due to the graphitic working electrode and aluminum, respectively, with the corresponding Laue symbols also being given. Significant contributions from other cell components are marked by $*$.

Finally, ex situ measurements were performed on a selection of as-received powders using a conventional X-ray diffractometer (D500 from Siemens, Germany) using Ni-filtered Cu K_α radiation and slit widths of $0.3\,\text{mm}$ ($0.05\,\text{mm}$ for the receiving slit). The tube voltage and current were $40\,\text{kV}$ and $40\,\text{mA}$, respectively.

8.3.3. Small-angle X-ray scattering

Considering a typical length scale of $2\,\text{nm}$ for the microporosity in activated carbons, scattering maxima are expected at 2θ values in the order of $2\,°$ for Cu K_α radiation ($\lambda = 1.54\,\text{Å}$) via the Bragg law. Such small scattering angles usually involve particular experimental requirements, such as a large sample–detector distance, to be measured accu-

rately. Also, strictly periodic arrangements such as those found in a crystalline lattice are not expected for the porosity of carbons, meaning that the conditions for diffraction as discussed in the previous section can not be met in this case. In the following, the principle treatment of SAXS from disordered, porous carbons will be outlined. For general introductions to SAXS, particularly with regard to systems of dilute scattering centers, the textbooks by Guinier and Fournet [301], Glatter and Kratky [302] or Feigin and Svergun [303] are recommended.

Debye and Bueche [304] introduced the concept of the correlation function which will be briefly outlined in the following. In X-ray scattering from an inhomogeneous solid, the average electron density is n_{Av} onto which local variations, η, are superimposed. For two points A and B separated by a distance r, the product $\eta_A \eta_B$ will depend on the value of r. With the boundary condition $\eta_A \eta_B = \eta^2$ for $r = 0$, one can write

$$\langle \eta_A \eta_B \rangle_{Av} = \gamma(r) \langle \eta^2 \rangle_{Av} \tag{8.3}$$

where $\langle \eta_A \eta_B \rangle_{Av}$ is the average product of the electron density difference between all point pairs and for all distances in the solid, and $\langle \eta^2 \rangle_{Av}$ is the average value of η^2 for the entire solid. $\gamma(r)$ is the so-called correlation function, which is dimensionless and drops from 1 to 0 with increasing r, thus describing the average extension of the inhomogeneities. Debye, Anderson and Brumberger [305] showed that the correlation function of a randomly distributed two-phase system is given by

$$\gamma(r) = \exp(-r/a) \tag{8.4}$$

In (8.4), the parameter a is the so-called Debye correlation length which may be taken as a measure for the spatial extension of charge density inhomogeneities. Based on the classical theory of X-ray scattering [306], the intensity i of the scattered X-rays is generally given by [301, 302, 305]

$$
\begin{aligned}
i &= \iint I_e(s) \langle \eta_A \eta_B \rangle_{Av} \exp(iks \cdot r) \, d\Omega_A d\Omega_B \tag{8.5} \\
&= I_e(s) \langle \eta^2 \rangle_{Av} V \int \gamma(r) \exp(iks \cdot r) \, d\Omega \tag{8.6}
\end{aligned}
$$

where V is the illuminated volume, $k = 2\pi/\lambda$ and s is the scattering vector with the absolute value $|s| = s = 2\sin\theta$. The integration is performed over volume elements $d\Omega$ of the solid. $I_e(s)$ is the scattering intensity of a single electron as given by the Thomsen formula [302]. For a completely isotropic solid in which the properties do not depend on the direction of r, (8.6) can be rewritten as [302, 305, 306]

$$i = 4\pi \langle \eta^2 \rangle_{Av} \, I_e(q) \, V \int_0^\infty \gamma(r) r^2 \frac{\sin(qr)}{qr} \, dr \qquad (8.7)$$

with the momentum transfer $q = ks = 4\pi \sin\theta/\lambda$, which essentially describes the direction of the (elastically) scattered waves. Substitution of (8.4) into (8.7) and subsequent integration gives [305]

$$i = \frac{K \Delta n_e^2 \, a^4}{(1 + q^2 a^2)^2} \qquad (8.8)$$

with the constant

$$K = \frac{8\pi \, S \, I_e(q)}{4c(1 - c)} \qquad (8.9)$$

in which S is the total interfacial area in the two-phase system and c the volume fraction of one of the phases. It is worth noting that I_e depends on the primary beam intensity and sample–detector distance and that, at small angles, I_e is practically independent of q [302, 305]. $\Delta n_e^2 = \langle \eta^2 \rangle_{Av}$ is the electron density contrast between the two phases. In Equation (8.8), the electron density within each phase is assumed to be constant, and the boundary between the phases infinitely sharp [305]. It is also worth noting that the absolute electron densities of the two phases do not enter into Equation 8.8, and that it is therefore not possible to attribute the scattering to one particular phase (also known as the reciprocity principle of Babinet in optics) [302, 307].

Equation (8.8) provides the basis for the interpretation of SAXS data obtained from porous carbons in the present work. It states that the scattered intensity is proportional to the total interfacial area, including the interfaces located within closed or narrow porosity which is not accessible by gas. Further, the scattered intensity is proportional to the square of the electron density contrast between the two phases and depends on the length scale of the inhomogeneities which is represented by the correlation length a.

Kalliat et al. [308] investigated the microporosity of coals by SAXS and based their analysis on the above formalism. These authors considered that the total scattered intensity could be expressed as the sum of contributions from pore modes characterized by distinct correlation lengths, an approach which was later also adopted by several other authors [309–312] and notably by Stevens and Dahn [313, 314] in their in situ studies on the electrochemical insertion of lithium and sodium into hard carbons.

For a system containing a bimodal distribution of porosity, with one mode centered on a sufficiently large length scale so that $q^2a^2 \gg 1$, representing macroporosity or the packing of powder grains, and another on a much smaller length scale, representing microporosity, the total scattering intensity may be written as the sum of these two contributions, each of them given by (8.8),

$$i = \frac{A}{q^4} + \frac{B\,a^4}{\left(1 + q^2a^2\right)^2} \qquad (8.10)$$

with the terms A and B being characteristic for the large and small pore mode, respectively:

$$A \quad \propto \quad \frac{\Delta n_{e,A}^2\,S_A}{c_A\,(1 - c_A)} \qquad (8.11)$$

$$B \quad \propto \quad \frac{\Delta n_{e,B}^2\,S_B}{c_B\,(1 - c_B)} \qquad (8.12)$$

Attention needs to be directed towards the exponent of q in the first term of (8.10), which is 4 in this case. Gibaud et al. [310] pointed out the effect of so-called slit smearing due to finite beam height and sample size on the q-exponent as a function of q itself. For slit-collimated systems with infinite slit height, the observed exponent of q is 3, while for ideal pin-hole systems the exponent of 4 is recovered [301, 315–317]. The exponent may, in fact, take any value between 3 and 4 depending on the range of q and the maximum distance between scattering points in the sample [310].

As a consequence, for an infinite slit height or incident X-ray beam with large cross-section, (8.10) should be rewritten as [317]

$$i = \frac{A}{q^3} + \frac{B\,a^3}{(1 + q^2 a^2)^{3/2}} \tag{8.13}$$

More generally, the exponent of q for each pore mode may be represented by n_1 and n_2, respectively:

$$i = \frac{A}{q^{n_1}} + \frac{B\,a^{n_2}}{(1 + q^2 a^2)^{n_2/2}} \tag{8.14}$$

The exponent n_1 in (8.14) was used as an additional fitting parameter in the work by Stevens and Dahn [313, 314] and Laudisio et al. [312], while both studies set $n_2 = 4$. In the present work, both n_1 and n_2 were fitted according to (8.14) with an upper limit of 4 defined for each parameter.

Apart from the slit smearing effect mentioned above, deviations of the q-exponent n from the value of 4 may also have physical origins. Based on the concept of fractal dimensions, Bale and Schmidt [318] derived an expression in which $n = 6 - D$, with $2 \leq D \leq 3$ representing the fractal dimension of the interface. For $D = 2$, the interface is perfectly smooth and flat, while the excess $D - 2$ is a measure of how quickly similar interfacial features repeat themselves upon progressive magnification of the interface [319, 320]. This interpretation has been applied to SAXS studies of porous carbons numerous times in the scientific literature (a review of some of these investigations has been given in reference [321]).

However, such rough interfaces with fractal characteristics appear improbable in light of the smooth nature of graphene sheets which are thought to bound the porosity in carbons (see Section 4.5). In fact, Ruland [322] has criticized the interpretation of SAXS data from carbons in terms of fractals and emphasized that the assumptions of constant electron density within the phases and an infinitely sharp boundary between them are too idealistic. In fact, due to a fluctuation of the interlayer spacing between roughly parallel graphene sheets in non-graphitic carbons, the electron density in this direction also fluctuates and adds a scattering term $i_{\mathrm{fl}} \propto 1/q^2$ to (8.10). Upon graphitization, the i_{fl} term gradually diminishes due to an improvement in stacking order of the graphene sheets [323] and the apparent q-exponent approaches 4

as in (8.10). As a consequence, Perret and Ruland [315, 323, 324] concluded that the electron density transition between the two phases is in fact very sharp, there are no fractal structures present and the one-dimensional fluctuations of electron density perpendicular to graphene layers are the reason for deviations from the q-exponent of 4.

In agreement with the latter view, Equation 8.14 was used to fit scattering data in the present work and the deviation of the exponent n from the theoretical value of 4 interpreted as fluctuations in the interlayer distance between graphene sheets due to imperfect stacking order.

In situ SAXS measurements were performed on YP17 at the cSAXS beamline of the SLS using synchrotron radiation with $\lambda = 0.708\,\text{Å}$ and the PILATUS 2M detector (the PILATUS 1M detector has been described in [325]). The sample–detector distance was calibrated by means of the $0\,0\,1$ diffraction peak of a silver behenate [326] reference sample ($d_{0\,0\,1} = 58.380\,\text{Å}$). The electrochemical cells used were of the type shown in Figure 8.8, and a battery cycler (CCCC) from Astrol Electronics, Switzerland, was used for the potiontiostatic control. The working electrode was polarized with respect to the oversized counter electrode in steps of 500 mV and held at this potential until the current decay was negligible.

The slit smearing effect described above was considered to be unimportant in these measurements due to the highly focused incident X-ray beam. Assuming a circular cross-section of 300 μm, the smearing effect was estimated [301, 310] to become important at q values below $6 \cdot 10^{-4}\,\text{Å}$, which was a range not studied in the present work.

After radial summation of the two-dimensional pixel data, plots of the scattered intensity against q were fitted with Equation (8.14) using a non-linear least squares routine in MATLAB™.

8.4. Nitrogen gas adsorption

Gas adsorption techniques are widely used for assessing the porosity of solid samples, and have become a standard characterization tool for the determination of adsorption capacity and pore dimensions of activated carbons. The measured quantity in these experiments is always the amount of gas adsorbed within the sample under certain conditions,

and the derivation of pore size distributions or specific surface areas is a matter of interpretation of the adsorption data, as critically reviewed by Marsh [327].

In the context of EDLCs, the surface area determined by gas adsorption is often (e.g. [101, 102, 245, 328, 329]) taken as a measure for the interfacial area which can be accessed by the electrolyte. However, it is clear that the interactions responsible for gas adsorption and electrochemical double layer charging are fundamentally different, and therefore caution should be exercised when predicting the effective electrode/electrolyte interfacial area from gas adsorption measurements. This point will be reiterated later in the present work (Chapter 11). In any case, it is important to bear in mind that gas adsorption techniques provide a measure for the amount of porosity which is accessible by the probe gas, with all further conclusions drawn being subject to certain assumptions which should be clearly stated.

For an introduction to the determination of porosity and surface area using gas adsorption, the textbook by Gregg and Sing [330] is recommended. In the present work, nitrogen was used exclusively as the adsorbate, which undergoes only non-specific adsorption (i.e. only dispersive and repulsive forces are active) on graphene-based carbons by physisorption. In gas adsorption measurements, the adsorbed volume of gas is measured as a function of its partial pressure at a constant temperature. In the following, the procedures used in this work to interpret gas adsorption data obtained via such isotherms will be outlined.

According to the Brunauer, Deming, Deming and Teller (BDDT) classification [331], the majority of physisorption isotherms may be classified as one of five types (Figure 8.10). The relevant isotherms in the present work are the frequently encountered Type I, II and IV isotherms and the corresponding composite isotherms. In the following, the characteristic features and information content of these isotherms is discussed.

The Type I isotherm is characteristic for strictly microporous materials in which practically the entire adsorption capacity is utilized already at low partial pressures, followed by a saturation plateau. The shape of such an isotherm is reproduced well by the Langmuir isotherm [330],
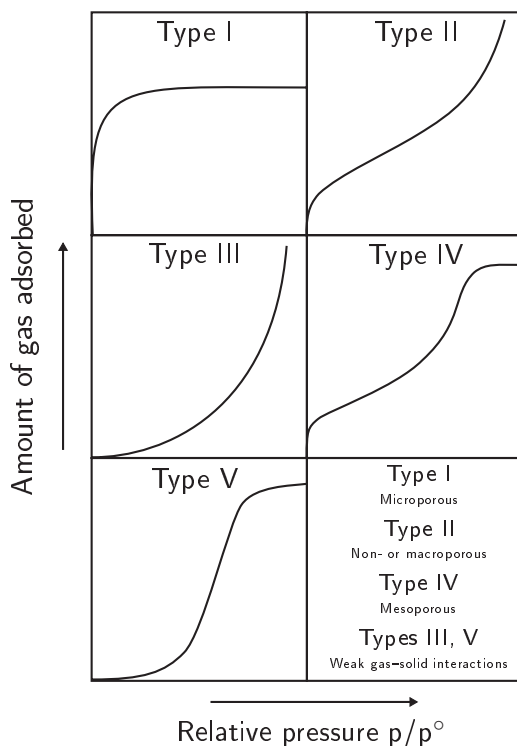
Figure 8.10.: Classification of adsorption isotherms. Adapted from [330, 331].

$$\frac{n}{n_{\mathrm{m}}} = \frac{c(p/p^\circ)}{1 + c(p/p^\circ)} \qquad (8.15)$$

where n is the number of mols of adsorbed gas, n_{m} is the number of mols adsorbed upon complete surface coverage with one monolayer, and p/p° is the relative pressure of the adsorbate (p° is the saturation vapor pressure). c is a constant which depends, among others, on the evaporation and condensation rate of the adsorbate.

In terms of the Langmuir equation (8.15), which was originally formulated to describe the monolayer coverage of non-porous, open surfaces, the plateau of Type I isotherms was interpreted as a consequence of the confined volume within micropores being unable to accommodate more than a monolayer. However, it has since been established that adsorption in micropores occurs via a volume filling mechanism [330,

332] due to the overlapping potentials of opposing pore walls (Figure 8.11).

In order to account for this volume filling of micropores, the Dubinin-Radushkevich (DR) equation [332–334] assumes a Gaussian distribution of pore sizes and a dependence of the filling degree on the characteristic energy of adsorption E_0 of the vapor as follows:

$$\frac{W}{W_0} = \exp\left[-\left(\frac{A}{\beta E_0}\right)^2\right] \tag{8.16}$$

where W_0 is the total volume of the microporous system and W is the filled volume at p/p^0. A is the molar work of adsorption, given by $A = RT\ln(p^0/p)$ and β is the adsorbate affinity coefficient ($\beta = 1$ for benzene, which was chosen as reference adsorbate). A more general form of (8.16) is the Dubinin-Astakhov (DA) equation [204, 332, 335],

$$\frac{W}{W_0} = \exp\left[-\left(\frac{A}{\beta E_0}\right)^n\right] \tag{8.17}$$

in which the exponent n is a measure for the width of the adsorption energy distribution. For $n = 2$, the DA and DR equations are
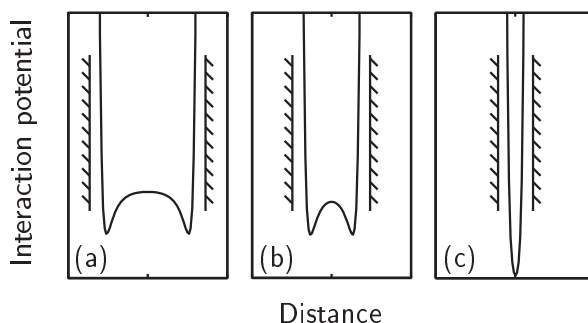
Figure 8.11.: Enhancement of interaction potential of a slit-shaped micropore due to the overlapping potentials of opposing pore walls with progressively smaller separation distance for (a), (b) and (c), respectively. The potential distribution is based on the superposition of two identical Lennard-Jones [330] potentials given by $U(r) = -A/r^6 + B/r^{12}$, where r is the separation distance and A and B are constants (see also Section 8.2 for a brief description of the attractive and repulsive components).

equivalent. For heterogeneous pore size distributions, the DA equation usually provides a better fitting of experimental data.

Thus, through non-linear curve fitting of adsorption data at low partial pressures, E_0 can be determined via Equations (8.16) or (8.17). From their study of molecular sieve carbons, Dubinin and Stoeckli [335] showed that the characteristic pore width, w, is inversely proportional to E_0 and can be estimated by

$$w\,(\mathrm{nm}) = 26\,(\mathrm{kJ\,nm\,mol^{-1}})/E_0\,(\mathrm{kJ\,mol^{-1}}) \tag{8.18}$$

The variation of the numeric factor in (8.18) for pore widths of 0.45–2 nm is 10–15 % [204].

More recently, the advancement of molecular modeling of adsorption phenomena has led to detailed descriptions of the pore structure from adsorption isotherms [336, 337]. For a given adsorbate–adsorbent system, the theoretical isotherms of individual pores are derived from fundamental gas–gas and gas–solid interactions. The ensemble of isotherms is termed the kernel, and is computed using non-local density functional theory (NLDFT) [336]. The adsorption data of an entire experimental isotherm, $N_{\mathrm{exp}}(p/p^0)$, is fitted as the sum of the adsorption isotherms of individual pores in terms of a generalized adsorption isotherm:

$$N_{\mathrm{exp}}(p/p^0) = \int_{w_{\mathrm{min}}}^{w_{\mathrm{max}}} N_{\mathrm{S}}(p/p^0, w)\,f(w)\,\mathrm{d}w \tag{8.19}$$

where N_{S} is the isotherm of a single pore of width w, $f(w)$ is the pore size distribution and w_{min} and w_{max} represent the minimum and maximum pore widths needed to fit the data. Thus, the NLDFT approach can in principle be used to fit any type of isotherm.

Type II isotherms are typical for non-porous or macroporous solids. Here, the Langmuir equation (8.15) fails to describe the adsorption behavior due to the adsorption of multiple layers of adsorbate. Brunauer, Emmet and Teller [338] extended the Langmuir mechanism by assuming that, in all adsorption layers beyond the monolayer, the heat of adsorption is equal to the heat of condensation and the rates of evaporation and condensation are identical to each other, while different conditions were assumed for the monolayer itself. The adsorption is

thus unrestricted perpendicular to the sample surface, which can account for the steep rise of the adsorption isotherm upon approaching the saturation vapor pressure.

Named after its creators, the so-called BET equation is frequently written in the following two equivalent forms [330, 338]:

$$\frac{n}{n_\mathrm{m}} = \frac{C\,(p/p^\circ)}{(1 - p/p^\circ)(1 + (C - 1)\,p/p^\circ)} \tag{8.20}$$

$$\frac{p/p^\circ}{n(1 - p/p^\circ)} = \frac{1}{n_\mathrm{m}C} + \frac{C - 1}{n_\mathrm{m}C}\frac{p}{p^\circ} \tag{8.21}$$

where C is the BET constant, which depends on the heat of adsorption of the monolayer and the heat of condensation of the probe gas. According to (8.21), a plot of $\frac{p/p^\circ}{n(1-p/p^\circ)}$ against p/p° then straightforwardly yields values for C and n_m. From the area occupied by a single adsorbed gas molecule (16.2 Å^2 for N_2 [330]), the so-called BET surface area of the sample can be readily calculated from n_m.

In practice, the BET equation has been extremely successful in describing Type II and also Type IV isotherms [330]. In fact, it is perhaps the most widespread method for the evaluation of gas adsorption data and has also been applied to the analysis of microporous samples, often providing satisfactory agreement with the other more dedicated micropore evaluation techniques described above. Since the so-called BET surface areas can be extracted from all kinds of isotherms, they provide a convenient yardstick for comparative purposes. However, for BET plots based on Equation (8.21) which do not exhibit straight lines over the entire range of p/p° (and this is usually the case), it is essential that the precise range is given from which the BET surface area is derived.

It is worth to dwell on the application of the BET method to the analysis of microporous samples for a moment. Due to the enhanced adsorption in micropores (Figure 8.11), the BET C constant is particularly large. Since micropore adsorption takes place at very low relative pressures, $p/p^\circ \to 0$, the BET equation (8.20) resembles the Langmuir equation (8.15). In fact, the Langmuir equation can be derived directly from the BET equation for restricted adsorption capacity [330]. This explains why the BET equation has to some extent been successful in describing microporous solids. However, the region of linearity

of Equation (8.21) is significantly shortened and shifted towards lower relative pressures [330]. This must be borne in mind when evaluating Type I isotherms or composite isotherms which contain a microporous fraction via the BET method, and the resulting surface area must not be considered a "true" surface area [327] but rather as a convenient index for comparing adsorption capacities.

Finally, the effect of mesopores (Type IV isotherms) on gas adsorption is addressed. It is characteristic for mesoporous systems to exhibit a hysteresis loop in which the amount of adsorbed gas is higher during desorption than during adsorption, as indicated in Figure 8.12. The reason for this hysteresis is attributed to the capillary condensation of the adsorbate gas within mesopores, and the particular shape of the hysteresis loop can provide information about the shapes of the pores in which capillary condensation takes place.

The reason for the condensation of the adsorbate gas below its saturation vapor pressure p° can be understood on basis of the Kelvin equation [330],

$$\ln \frac{p}{p^\circ} = -\frac{\gamma V_\mathrm{L}}{RT} \left(\frac{1}{r_1} + \frac{1}{r_2} \right) \tag{8.22}$$

where γ and V_L are the surface tension and molar volume of the adsorbate gas, while r_1 and r_2 are characteristic radii of the liquid meniscus
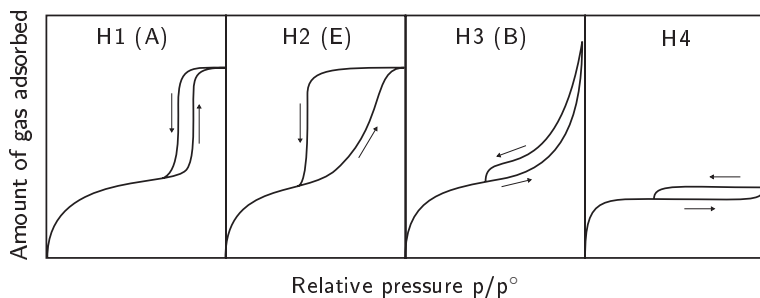
Figure 8.12.: Types of hysteresis loops associated with the presence of mesopores according to IUPAC [339]. The classification of de Boer is given in parentheses [330]. The mesopores between spheroidal particles and within open-ended cylindrical channels tend to exibit H1 behavior, while slit-shaped mesopores are often associated with the H3 and H4 types. Adapted from [330].

within the pore. In (8.22), positive radii indicate a concave meniscus (contact angle $< 90\,°$). For a cylindrical pore, the meniscus has a hemispherical shape, and thus $r_1 = r_2$. From the Kelvin equation, it is clear that the capillary condensation of a vapor to a liquid occurs at a pressure p which is lower[1] than the saturation pressure $p^{°}$.

In capillary condensation, the contact angle between the liquid adsorbate and the adsorbent is usually assumed to be zero (perfect wetting) [330], which is of course an oversimplistic description but has proven extremely convenient in practice. The capillary condensation and adsorption/desorption hysteresis for two characteristic cases may now be discussed by means of the Kelvin equation—that within an infinitely long cylindrical pore of radius r'_{cyl} and that within a slit-shaped pore between two perfectly parallel plates separated by a distance d'_{slit}. Starting from the empty pores, adsorption in each case will result in the formation of an adsorbed film of thickness t, so that the effective inner radius of the pore (the Kelvin radius) for the cylindrical pore is given by $r_{\text{cyl}} = r'_{\text{cyl}} - t$ and the effective pore width of the slit pore by $d_{\text{slit}} = d'_{\text{slit}} - 2t$.

In the case of the cylindrical pore, the characteristic radii of the liquid meniscus are $r_1 = r_{\text{cyl}}$ and $r_2 \to \infty$, so that capillary condensation takes place at

$$\left(\frac{p}{p^{°}} \right)_{\text{ads,cyl}} = \exp \left(-\frac{\gamma V_{\text{L}}}{RT} \frac{1}{r_{\text{cyl}}} \right) \tag{8.23}$$

while, during desorption, the meniscus of the liquid within the filled cylindrical pore is hemispherical in shape with characteristic radii $r_1 = r_2 = r_{\text{cyl}}$, leading to capillary evaporation at

$$\left(\frac{p}{p^{°}} \right)_{\text{des,cyl}} = \exp \left(-\frac{\gamma V_{\text{L}}}{RT} \frac{2}{r_{\text{cyl}}} \right) \tag{8.24}$$

Equations (8.23) and (8.24) provide a qualitative basis for understanding why capillary condensation and capillary evaporation occur at different relative pressures for cylindrical mesopores. The expected shape of the isotherm is therefore of the Type H1 given in Figure 8.12.

---

[1] For a convex meniscus, the characteristic radii enter as negative values in Equation (8.22), and correspondingly $p > p^{°}$.

For the ideal slit-shaped mesopore, the characteristic radii of the liquid meniscus upon adsorption are both infinite and hence no capillary condensation takes place below the saturation vapor pressure. Instead, the pore is filled by multilayer adsorption until the two opposing adsorption films meet and the pore is full of adsorbate. For a sufficiently large pore (greater than ca. 2 nm [330]), the state of the adsorbate is indistinguishable from that of the liquid and the meniscus is cylindrical in shape with the characteristic radii $r_1 = d_{\text{slit}}/2$ and $r_2 \rightarrow \infty$. Upon desorption, capillary evaporation from the slit-shaped mesopore thus takes place at

$$\left(\frac{p}{p^\circ} \right)_{\text{des,slit}} = \exp \left(-\frac{\gamma V_{\text{L}}}{RT} \frac{2}{d_{\text{slit}}} \right) \tag{8.25}$$

with the corresponding isotherm hysteresis resembling Type H3 (B) or Type H4 in Figure 8.12.

Assuming a certain pore shape, the mesopore size distribution can be derived using a variety of theoretical approaches [330]. In the present work, the approach by Barrett, Joyner and Halenda (BJH) [340] was applied. Briefly, the model assumes a stepwise desorption process for which an average Kelvin radius r_{K} can be calculated from the Kelvin equation for a relative pressure decrease $\Delta p/p^\circ$ for each pair of successive measurement points of the desorption branch. Then, assuming open-ended cylindrical mesopores and a successive decrease of the adsorbate layer thickness t upon desorption, the pore radius $r = r_{\text{K}} + t$ can be calculated for a given relative pressure p/p°. The necessary $t(p/p^0)$ values may be taken from de Boer's master curve [341].

In the present work, nitrogen adsorption and desorption experiments were conducted at 77 K using an Autosorb-1 from Quantachrome Instruments, USA. Prior to the measurement, the samples were dried at 300 °C for at least 12 hours or, in some cases (Chapter 14), at 150 °C for at least 24 hours, always combined with a vacuum better than 1 Pa. Data evaluation based on the BET, DA/DR, NLDFT and BJH methods described above was carried out using the AS1WIN software provided by Quantachrome Instruments. For the NLDFT calculations, the N_2 on carbon kernel implemented in the AS1WIN software was used assuming a mixed slit/cylindrical pore shape, for which the best isotherm fitting results were obtained.

8.5. Raman spectroscopy

8.5.1. Background

Raman spectroscopy relies upon the phenomenon of Raman scattering, which is the inelastic scattering of photons by matter. In this process, vibrational modes of the irradiated sample participate in scattering, leading to a change in the frequency of the scattered photons with respect to the incoming photons. The much more frequent elastic scattering of photons is called Rayleigh scattering, in which the scattered photons have the same frequency as the incoming photons. Hence, inelastically scattered photons carry information about the vibrational properties of the sample, which are highly sensitive to the structural arrangement of atoms without the necessity for long-range order.

In this section, an outline of the application of Raman spectroscopy to the study of sp^2 hybridized carbonaceous materials will be given. For a general introduction to Raman spectroscopy, the text by Ferraro, Nakamoto and Brown is recommended [342].

In solids, the Raman effect may be depicted schematically as in Figure 8.13. It is assumed that the incident radiation interacts with the vibrational system through the intermediary of the electrons in the sample [343]. In Figure 8.13a, a first-order Raman scattering process is illustrated in which a single phonon is emitted. In second-order Raman scattering processes, two phonons are emitted as shown in Figure 8.13b. In the case of first-order Raman scattering, three virtual electronic transitions occur. First, the incident photon with energy $\hbar\omega_{ph}$ is absorbed, creating an electron-hole pair. Second, an optic phonon of energy $\hbar\omega_{vib}$ is created via scattering with the electron. Third, a photon of energy $\hbar(\omega_{ph} - \omega_{vib})$ is emitted through electron-hole recombination.

The emission of a phonon as shown in Figure 8.13a is also referred to as Stokes scattering. In the case of excited vibrational states already being present in the sample, phonons may also be destroyed via interaction with electrons, which is referred to as anti-Stokes scattering. In the latter case, the emitted photon has a higher energy than the incident photon. However, since the number of occupied vibrational ground states is greater than the number of occupied vibrationally excited states at room temperature, Stokes scattering is far more frequent
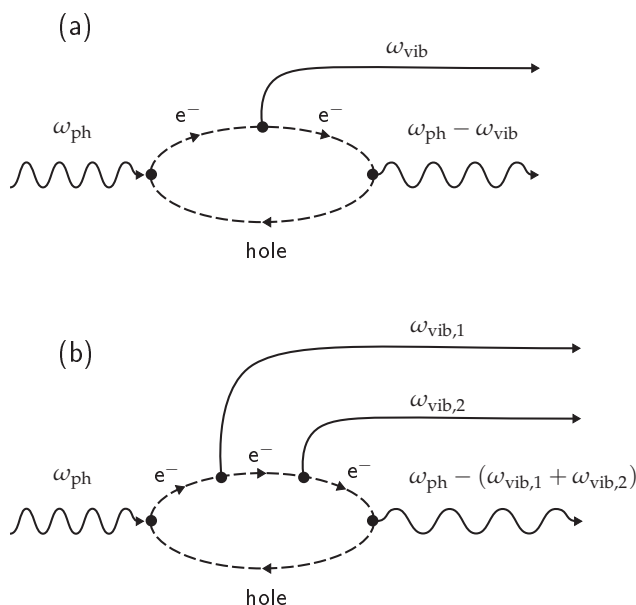
Figure 8.13.: (a) First-order Raman scattering process involving an incident photon with frequency ω_{ph}, the generation of an electron-hole pair, generation of a phonon of frequency ω_{vib} and emission of a photon with frequency $(\omega_{ph} - \omega_{vib})$. (b) Second-order Raman scattering process involving the generation of two phonons with frequencies $\omega_{vib,1}$ and $\omega_{vib,2}$. Adapted from [343].

than anti-Stokes scattering. Therefore, exclusively the Stokes components of Raman scattered light were investigated in this work.

In order for a certain vibrational mode to be involved in Raman scattering, there must be a change in polarizability during the vibration [342]. The polarizability describes how easily an electric dipole moment is induced by the fluctuating electric field of the incident radiation. Hence, not all vibrational modes necessarily result in Raman scattering and are thus accessible by Raman spectroscopy.

Raman scattering from sp^2 hybridized carbon is resonantly enhanced due to the excitation of electrons in real electronic transitions between the π and π^* bands. In graphene, there are two atoms per unit cell, giving rise to six phonon dispersion relations which are plotted in Figure 8.14 for the first Brillouin zone. There are three modes which pass

through zero, called acoustic modes, and three modes which remain at high frequencies throughout the Brillouin zone, corresponding to optical modes. The only Raman-active modes of graphene according to group theory [342] are the degenerate LO (longitudinal optical) and iTO (in-plane transverse optical) modes near the Γ point [344, 345], which have E_{2g} symmetry as shown in Figure 8.15a.

The phonon modes drawn in Figure 8.15a give rise to the so-called G band (G for graphite) at a Raman shift of about $1580\,\mathrm{cm}^{-1}$. Despite the misleading nomenclatures of this band, it is in fact present in all kinds of sp^2 hybridized carbons, including linear hydrocarbon chains [349]. The position of the G band depends on the stiffness of the phonon mode and is therefore independent of the energy of the incoming photons (i.e. the laser wavelength) for graphitic carbon. However, it is found to depend on the laser wavelength for disordered carbons which are characterized by small sp^2 clusters [350]. This dispersive behavior of the G band in disordered carbons is due to the distribution of cluster sizes and hence band structures and phonon modes, which does not
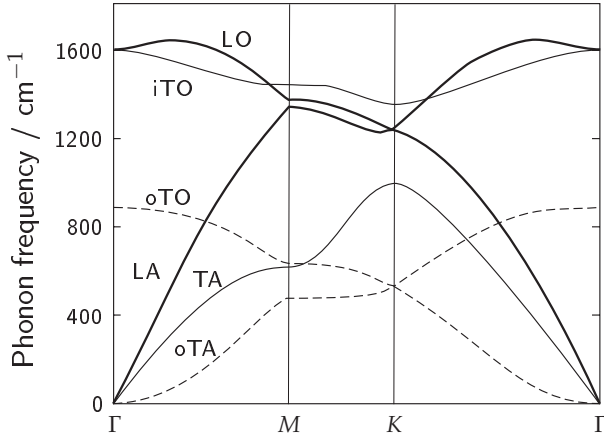
Figure 8.14.: Phonon dispersion of graphene within the first Brillouin zone. A and O designate acoustic and optical branches, respectively, while L and T denominate longitudinal and transverse modes. The prefixes i and o stand for in-plane and out-of-plane vibrations. When no prefix is given, an in-plane phonon mode is implicit. Adapted from [344, 346].
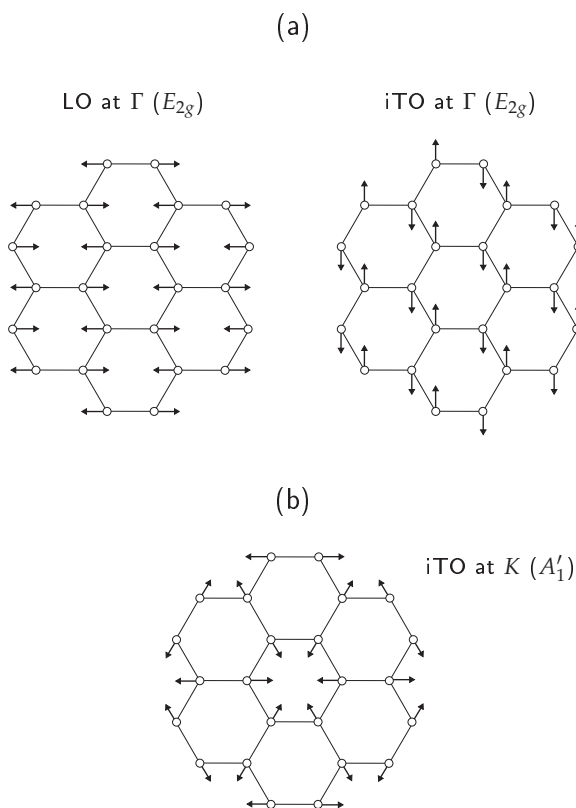
Figure 8.15.: Phonon modes giving rise to (a) the G band and (b) the D band in sp^2 hybridized carbons. The symmetries of the vibrations are given in parantheses. Adapted from [347, 348].

occur in nanocrystalline graphite [350]. Depending on the laser energy, those sp^2 clusters with matching $\pi \rightarrow \pi^*$ transition energies and their corresponding phonon modes will be selectively sampled due to the resonance enhancement.

The appearance of other bands in experimental first-order Raman spectra (i.e. at Raman shifts below about $1620\,\mathrm{cm}^{-1}$) can be correlated with the scattering of electrons by defects, as was first shown by Tuinstra and Koenig in 1970 [351] for small crystallites of graphite. In their case, the edges of the crystallites constituted the defects, giving rise to the so-called D band (D for defect- or disorder-induced [345])

at 1355 cm^{-1} in their study. However, the nature of the defects may be quite general, as shown by the appearance of the D band upon boron-doping or electrochemical oxidation of HOPG [352].

In contrast to the G band, the D band position depends on the laser wavelength for all sp^2 hybridized carbons [352–354]. On these grounds, Thomsen and Reich [355] established that the D band originates from a double resonance process due to the approximately linear dispersion of the π and π^* bands at the *K* point of the Brillouin zone. The double resonance process for graphene is depicted schematically in Figure 8.16. Normal resonant Raman scattering is shown in Figure 8.16a, in which the excited electron is scattered inelastically under emission of a phonon with wavevector *q* before recombination and photon emission. In order for electron–hole recombination to take place, the scattered *k* + *q* state should not differ from *k* by more than two times the photon wavevector. Since the latter is usually very small compared to the size of the Brillouin zone, *q* $\approx$ 0 in order to conserve energy and crystal momentum [53, 166]. The corresponding phonon modes are called zone-center or Γ point phonon modes.

Of course, excited electrons are also scattered by other phonons with *q* $\neq$ 0 as shown in Figure 8.16b. The resonant transition to another real
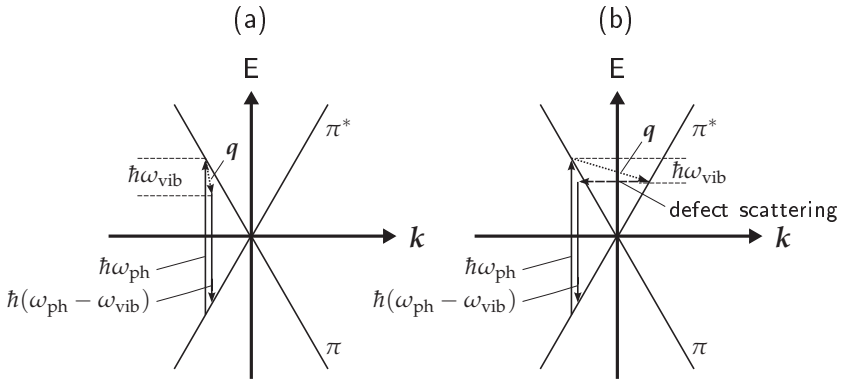
Figure 8.16.: Electronic band dispersion of graphene near the *K* point of the Brillouin zone. (a) Resonance Raman scattering with the emission of one phonon of wavevector *q* $\approx$ 0, and (b) double resonance Raman scattering with a phonon of wavevector *q* and elastic scattering by a defect. Adapted from [344, 345].

electronic state will be selectively enhanced, thus resulting in a double resonance process. For Raman activity, however, linear momentum must be conserved by elastic scattering of the electron back to its initial k value prior to recombination and photon emission. Hence, due to this double resonance process and the presence of defects which act as scattering centers, phonon modes other than those with E_{2g} symmetry may also become Raman active. As larger laser energies selectively enhance phonons with larger q, the double resonance mechanism also explains the dependence of the D band position on the laser wavelength [345].

Reich and Thomsen [345] showed that the electron-phonon scattering during the double resonance process may either be an inter- or an intravalley process as depicted in Figure 8.17. Due to a change in the selection rules for Raman activity during double resonance scattering [345], the emitted phonon must be either of A_1 symmetry close to the K point for the intervalley process in Figure 8.17a or of B_1 symmetry near the Γ point for the intravalley process in Figure 8.17b.

Thus, it could be shown [345, 346, 356] that the D band of sp^2 hybridized carbons arises due to the iTO phonon mode close to the K point with symmetry A_1' (Figure 8.15b) through an intervalley double resonance process (Figure 8.17a) involving elastic scattering of elec-
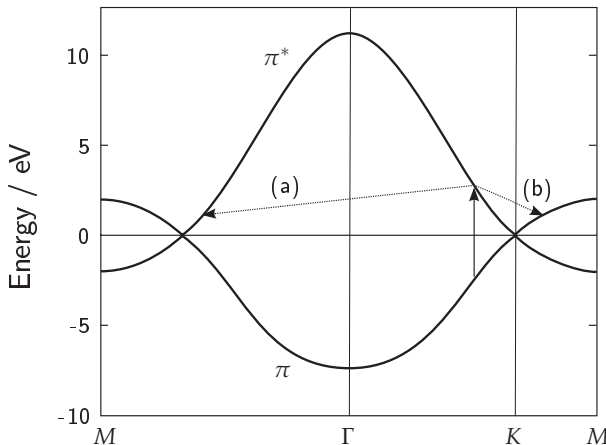
Figure 8.17.: Double resonance scattering within the first Brillouin zone of graphene for (a) inter-valley and (b) intra-valley scattering of an electron by a phonon. Adapted from [345].

trons by defects. The other disorder-induced mode which is Raman active through double resonance arises from the LO branch near the Γ point and corresponds to the intravalley scattering process shown in Figure 8.17b, appearing as a band at $1620\,\mathrm{cm}^{-1}$ (for a laser wavelength of 514.5 nm) and denominated as the D′ [344] or G′ [345] band.

Due to the high symmetry of the A_1' mode, it is only observable in ring structures. In fact, the D band is strictly associated with the presence of sixfold aromatic rings [349], as opposed to the G band which is characteristic for all kinds of sp^2 hybridized carbon structures. It is worth noting that the Raman spectra of polyaromatic hydrocarbons consisting of small domains of sp^2 hybridized, aromatic clusters share the same features [348, 356, 357] as those outlined above for disordered graphene.

The precise nature of the information content of the D band has been disputed since Tuinstra and Koenig first used the ratio of the G and D band intensities to estimate the crystallite size L_a (see Section 4.4) of graphite [351]. Since not only the position, but also the intensity of the D band depends on the laser wavelength as well as on the presence of defects other than the crystallite edges, the estimation of crystallite size via Raman spectroscopy should be generalized with caution. In particular, by comparison of crystallite sizes obtained via XRD and Raman spectroscopy, the assessment of L_a via the G to D band ratio has been shown to be prone to grave errors for domains smaller than about 2 nm [117, 358]. A possible explanation for this is that aromatic ring structures tend to open with decreasing cluster size, thus decreasing the D band intensity without affecting the G band [349].

Recently, the information content of Raman spectra regarding the nature of disorder in graphene-based carbons was discussed by Pimenta et al. [344]. It was shown that the D band contribution is strong from the armchair edge and weak from the zigzag edge of graphene. Information regarding the number of graphene sheets stacked in parallel was found by analyzing the overtone of the D band, situated at Raman shifts of 2500–$2800\,\mathrm{cm}^{-1}$ and called G′ [344] or 2D [359] band. This band is a second-order feature resulting from the two-phonon scattering process involving two iTO phonon modes which also give rise to the D band, but is present regardless of disorder due to the conservation

of momentum in the two-phonon process without the need for elastic scattering from defects. The shape of the overtone of the D band in fact enables differentiation between single, bi- and multilayer graphene due to changes in the electronic band structure upon stacking [344, 359, 360].

It should be mentioned that the phonon dispersion of graphene is characterized by a strong coupling of electronic bands with the phonon modes which give rise to the G and D bands at the Γ and K points of the Brillouin zone, respectively. In general, atomic vibrations are always partially screened by electrons to some extent [361]. However, phonons with a wavevector q which can scatter electrons from a K to a K' point in the Brillouin zone experience a particularly strong electron-phonon coupling, leading to a pronounced softening of these phonon modes which is referred to as a Kohn anomaly [346, 361]. Such Kohn anomalies occur for graphene [362] and SWCNTs [361], but also for graphite [361] due to the closely related electronic and vibronic structures. The presence of significant electron-phonon-coupling in these materials is important for the interpretation of their behavior during electrostatic doping [363–366].

In the context of the present work, Raman spectroscopy was used in order to obtain information about the bonding arrangement of sp^2 hybridized carbons which lack long-range order, such as the activated carbons preferentially used in EDLCs, and information about the defect density. Due to the resonance enhancement of Raman scattering in these samples, the Raman spectrum is also affected by the electronic properties of the carbon. As described in the next section, Raman spectroscopy was used to study the above phenomena in situ .

8.5.2. Methodology

Raman spectra were collected using a Labram series Raman microscope (HORIBA Jobin Yvon, France) equipped with a HeNe laser ($\lambda_{\text{laser}} = 623.8\,\text{nm}$ and $E_{\text{laser}} = 1.96\,\text{eV}$). The instrument enables a direct selection of the region of interest through illumination of the sample with white light by transmission and visualization on a television screen. During the measurement, the backscattered laser light passes through a notch filter to remove the elastically scattered fraction (the Rayleigh line) and through the confocal hole and slit aperture before reaching

the grating spectrograph. The grating spectrograph disperses the scattered light according to its different wavelengths before it impinges on a charge-coupled device (CCD) photodetector.

In situ Raman spectra were acquired by means of an electrochemical cell which was developed in-house [194] and is depicted in Figure 8.18. YP17/PTFE was used as counter and quasi-reference electrode in a three-electrode configuration with a glass-fiber separator (EUJ116 from
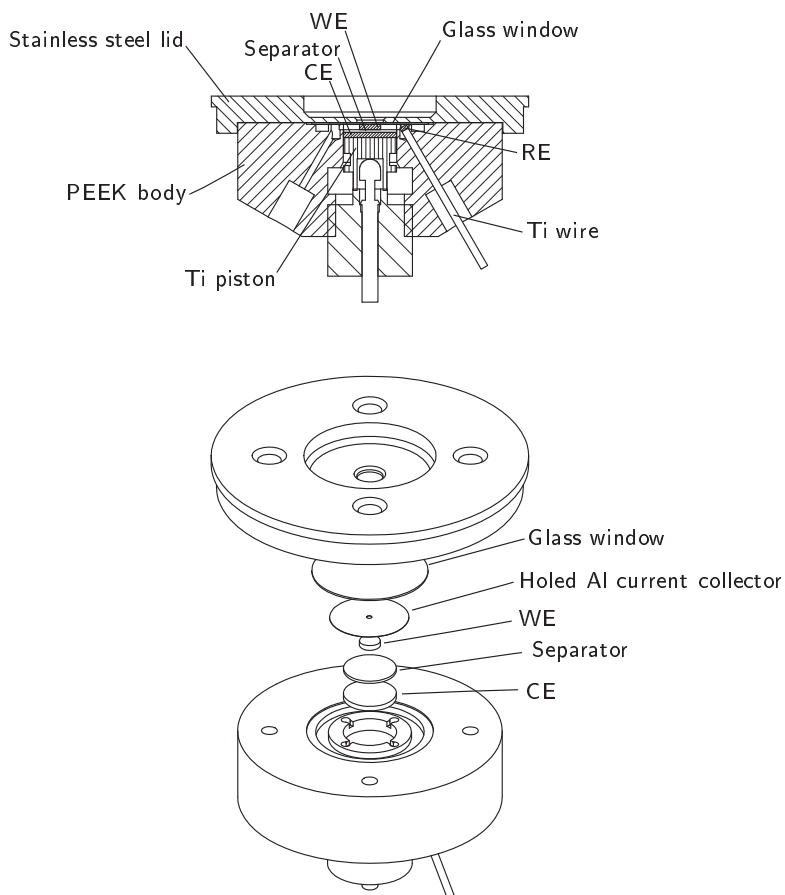
Figure 8.18.: Cross-section (top) and partial assembly (bottom) of the electrochemical cell used for in situ Raman spectroscopy. The working electrode was contacted via the Al current collector by inserting Al or Ti wires into the cell (not shown).

Hollingsworth & Vose, UK) placed between the counter and working electrode. An aluminum foil (thickness 15 µm) was used as the current collector for the working electrode.

All materials were investigated as powders without any additives or binder. Electrical contact between the aluminum current collector and the powder working electrode was achieved by compressing the electrode arrangement with a spring-loaded screw. The cell components were dried and assembled according to the procedures given in Section 7.1, whereby the final hermetical sealing was achieved by means of a glass window (thickness 300 µm) and EPDM O-rings.

The Raman spectra were collected by focusing the laser through the glass window and a hole in the aluminum current collector onto the working electrode. Electrochemical cycling was performed using the battery tester described in Section 7.4. Unless mentioned otherwise, all spectra were obtained through an objective with 80-fold magnification and an incident laser power close to 10 mW. The spot diameter of the laser impinging on the sample surface was in the order of 1 µm. The Raman spectra were collected with a resolution of $1\,cm^{-1}$ and calibrated against the phonon mode of Si at $520\,cm^{-1}$ prior to each measurement. The confocal hole and slit were set to 300 µm and 200 µm, respectively. The measurement time for a single in situ Raman spectrum was 60 s for YP17, 30 s for SFG44 and 10 s for SWCNTs. Fitting of the obtained Raman spectra was performed with the LabSpec 4.08 software supplied by HORIBA Jobin-Yvon.

8.6. Scanning electron microscopy

In SEM, an electron beam is focused down to a diameter in the order of 1 nm onto a sample surface using electromagnetic lenses [367]. By rastering this spot across the sample surface and simultaneously detecting the emitted electrons, an image of the sample topography is obtained with a depth of focus considerably superior to optical microscopy due to the fact that the incident electrons travel very close to the optical axis [367]. Further, these electrons have an energy corresponding to the accelerating voltage of the electron gun, typically less than 30 keV. Upon impinging on the sample surface, the incident electrons undergo elastic

(through interaction with the atomic nuclei of the sample) and inelastic (through interaction with the bound electrons in the sample) scattering [367]. Through the loss of kinetic energy of the primary electrons via inelastic scattering, elastic collision events and thus larger scattering angles become more probable, giving rise to the characteristic pear-shaped interaction volume shown in Figure 8.19. This volume describes the sample space in which the incident primary electrons are brought to rest (causing electrostatic charging in the case of insulators), and is larger for higher accelerating voltages and samples consisting of lighter elements. While SEM is, in principle, a non-destructive analytical technique, organic samples in particular may be damaged over time due to heating during beam exposure.

The emission of X-rays during inelastic scattering of electrons in matter was discussed in Section 8.3. Electrons emitted due to the characteristic radiation are called Auger electrons and have well-defined maximum kinetic energies which depend only on the elemental composition of the sample.

Through inelastic scattering of primary electrons, sufficient energy may also be directly imparted upon the bound electrons to cause their emission from the sample. The escape depth of these secondary electrons is usually less than 2 nm [367] and depends on their kinetic en-
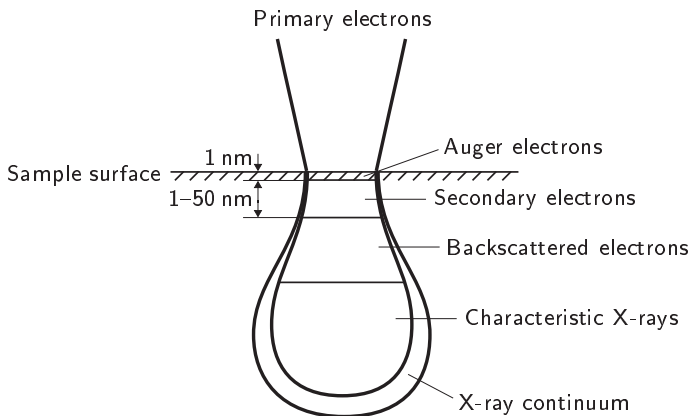
Figure 8.19.: Interaction volume of incident primary electrons and escape depth of emitted species in SEM.

ergy. Per definition, all emitted electrons with kinetic energies less than 50 eV are referred to as secondary electrons, while all electrons which are emitted from the sample with higher kinetic energies are attributed to backscattered primary electrons.

The number of backscattered electrons increases notably with the atomic number of the scattering nuclei due to the higher probability of elastic scattering. In contrast, the number of secondary electrons emitted from the sample is approximately constant for atomic numbers greater than 15 and tends towards zero for lighter elements. Therefore, in secondary electron imaging, light elements tend to appear darker due to the lower secondary electron yield. In the present work, no use was made of backscattered electrons for image generation. The number of secondary electrons generated within the escape depth increases with decreasing accelerating voltage and at oblique angles of incidence due to the lower penetration depth of primary electrons in both cases. The latter is responsible for the excellent visualization of topography in SEM.

In the present work, a Supra 55 VP scanning electron microscope (Carl Zeiss NTS, Germany) equipped with a Schottky-type field emission gun was used for SEM imaging. The gun and system vacuum were better than $9 \cdot 10^{-7}$ Pa and 10^{-4} Pa, respectively. Accelerating voltages in the range of 1–3 kV were used and secondary electron detection was performed using an in-lens detector.

8.7. X-ray photoelectron spectroscopy

XPS or its synonymous description, electron spectroscopy for chemical analysis (ESCA), relies on the photoelectric effect [368] which involves the ejection of electrons from a sample upon irradiation with photons of sufficiently high energy. In this respect, the previous discussions on the interaction of X-rays with matter (Section 8.3) and the emission of electrons (Section 8.6) are of relevance. XPS is widely used to determine the elemental composition of the surface region of a sample and obtain information about the chemical state of the element [369]. The principles of the technique will be briefly outlined in the following.

In XPS, the incident photons are generated by an X-ray source and are characterized by the energy $\hbar\omega$. In a certain fraction of scattering events of these photons with bound electrons, the entire energy of one photon may be transferred to a bound electron. If this event occurs within the escape depth of the electron (typically less than 5 nm in XPS), the latter is expelled from the sample surface as a photoelectron with a maximum kinetic energy given by Einstein's equation:

$$E_{\text{kin}} = -E_{\text{B}} + \hbar\omega \tag{8.26}$$

where E_{B} is the binding energy of the electron prior to photoionization. Experimentally, ultra-high vacuum (UHV) is required to ensure sufficient mean free path lengths of the photoelectrons prior to detection. Photoelectrons of a certain kinetic energy (typically > 100 eV in XPS) are discriminated by an analyzer through the application of a suitable voltage before being counted by a channeltron or multichannel array detector.

Due to the discretization of the electronic binding energies of the so-called core electrons, which are strongly bound to the atomic nucleus, the kinetic energy distribution of the photoelectrons features sharp maxima. The energy diagram relevant for the determination of the binding energy is schematically depicted in Figure 8.20. The measured kinetic energy, E'_{kin}, is related to the binding energy E_{B} by

$$E_{\text{B}} = \hbar\omega - E'_{\text{kin}} - \Phi' \tag{8.27}$$

where Φ' is the work function of the spectrophotometer.

Since the core electrons, as opposed to the valence electrons, are not involved in interatomic bonding, their binding energy is almost independent of the bonding environment. Hence, the binding energy of aliphatic carbon is almost identical to that of aromatic carbon or that of carbon in $C-H$ groups ($E_{\text{B}} \approx 284.6$ eV for $\hbar\omega = 1253.6$ eV). However, for bonding with more electronegative elements such as N, O and F, the decrease in electron density in the vicinity of the carbon atom results in an increase of the corresponding binding energy. This chemical shift enables the analysis of the bonding environment of specific elements using XPS.
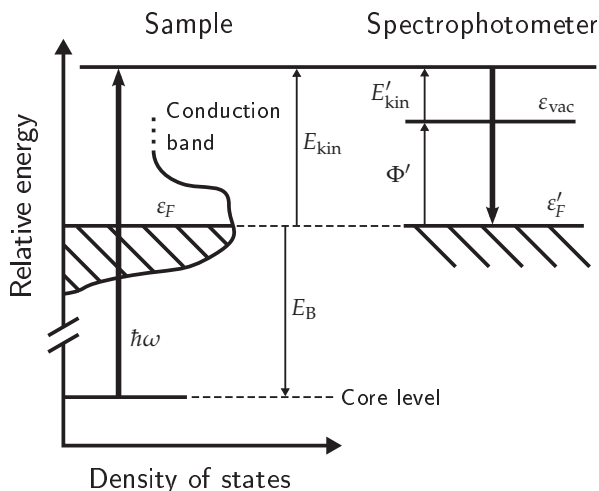
Figure 8.20.: Determination of the binding energy E_B of core electrons in XPS for a metallic sample with the Fermi energy ε_F. ε_{vac} is the vacuum level and ε'_F is the Fermi level of the spectrophotometer. It is assumed that electrical contact between sample and spectrophotometer is established, the respective Fermi levels thus being equilibrated.

In the present work, XPS analysis was performed using an ESCALAB 220iXL (formerly Vacuum Generators, now Thermo Electron, USA) using either Mg K_α ($\hbar\omega = 1253.6$ eV) or Al K_α ($\hbar\omega = 1486.6$ eV) radiation. The resulting binding energies were compared with entries listed in the database maintained by the National Institute of Standards and Technology (NIST) of the United States Department of Commerce [370].

8.8. Electrode resistivity measurements

From Ohm's law, the current density j (in A m^{-2}) through a material is directly proportional to the strength of the applied electric field $\mathcal{E}$ (in V m^{-1}):

$$j = \sigma \mathcal{E} \tag{8.28}$$

where σ is the specific conductivity in S,m^{-1}. For a given charge carrier density n, with the charge $|q|$ assigned to each charge carrier, $j = n|q|v$ where v is the drift velocity of the charge carriers (in m s^{-1}). One can

now define a mobility μ of the charge carriers given by $\mu = v/\mathcal{E}$ (in $m^2(Vs)^{-1}$) and write

$$\sigma = n|q|\mu \qquad (8.29)$$

A measurement of the steady-state conductivity σ (or the resistivity $\rho = 1/\sigma$) thus provides a measure of the density of charge carriers and their mobility. With regard to carbonaceous electrodes in EDLCs, this is of particular interest since the charge carrier density n is expected to change with the position of the Fermi level within the electronic density of states (Section 4.2). Significant changes in the resistance of activated carbon upon electrochemical charging in various electrolytes were reported by Kastening et al. [371, 372], Hahn et al. [108] and Pollak et al. [107, 373].

For a given sample geometry, the absolute resistance R can be readily measured using standard two- or four-point direct current (DC) techniques according to $R = U/I$. A sketch of the electrochemical cell used in the present work to measure R in situ is given in Figure 8.21. The working electrode was pressed into a concave cavity and contacted with four gold or platinum wires. These wires served as current collectors during electrochemical charging and as contacts during four-point probe resistance measurements. Two separator layers (EUJ116 from Hollingsworth & Vose, UK) and the oversized counter electrode (YP17/PTFE) were stacked on top of the working electrode, with the reference electrode (YP17/PTFE) placed close to the working electrode. The electrode/separator sandwich was compressed by means of a spring-loaded piston, whereby the applied force F was successively increased until no further change in the resistance was measured.

The detailed measurement routine has been described in previous work [108]. Briefly, the working electrode was held at a certain potential using a potentiostat (model 273 from EG & G Princeton Applied Research, USA) for a sufficiently long time to allow the charging current to drop to almost zero. In the subsequent open circuit step, a direct current was applied for the four-point probe measurement using a multimeter (model 34401A from Hewlett-Packard, USA). A waiting time of 10 s prior to the measurement of the voltage drop across the sample was
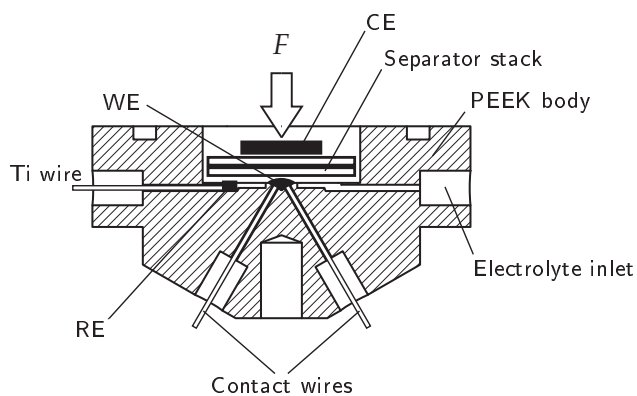
Figure 8.21.: Electrochemical cell used to measure resistance changes in situ .

found to be sufficient to achieve a constant current distribution within the electrode as there was no further change in the measured resistance over time.

Due to the uncertainty in the sample geometry, no absolute resistivities are given in the present work. Instead, the measured resistances were normalized with respect to the maximum resistance value.

Part III.

Results and discussion

Chapter 9.

Characterization of electrodes and electrolytes

9.1. Motivation

This chapter summarizes the physicochemical characterization of the electrode materials investigated in the present work, with a particular emphasis on the activated carbon YP17. A more detailed knowledge of the chemical composition and structural properties beyond the information provided by the manufacturer is indispensable for the subsequent investigation and interpretation of electrochemical charge storage mechanisms and aging phenomena.

Besides chemical (XPS) and structural (Raman spectroscopy, WAXS and N_2 adsorption) characterization, the electrochemical characterization of YP17/PTFE in $1\,M\,Et_4NBF_4$ in AN and in PC using impedance spectroscopy and cyclic voltammetry is presented in the following. The main findings and conclusions of these investigations are summarized at the end of this chapter in Section 9.3.

9.2. Results and Discussion

9.2.1. Chemical analysis via XPS

The chemical analysis of HOPG, YP17 and SWCNTs via XPS is summarized in Table 9.1. No elements other than carbon were detected in the case of HOPG. For YP17, an oxygen content $(7.3 \pm 1.5)\,at\%$ was found by analyzing different positions on an as-received powder sample, indicating the presence of oxygen-containing functional groups. Assuming that all of this oxygen is bonded to the activated carbon framework, there is approximately one oxygen-containing moiety per three contiguous sixfold aromatic rings.

In the bound YP17/PTFE electrode, the binder contributed around 20 at% of fluorine. The C:F mass ratio was only about 2:1, although according to the binder concentration in the electrode (Section 6.1.1) a ratio above 9:1 was expected. A possible reason for this significant discrepancy could be a preferential accumulation of PTFE at the electrode surface during the electrode rolling process. The increased O:C ratio of YP17/PTFE with respect to the unbound powder could be the result of the oxidative conditions employed during the electrode fabrication process (Section 6.1.1). Apart from carbon, oxygen and fluorine, no further elements and notably no impurities such as alkali metals from the precursor material were detected by XPS.

In the SWCNT sample, oxygen moieties were also detected. Oxygen-containing species may be located at tube ends, along tube walls or bonded to carbonaceous and metallic impurities. Traces of non-carbonaceous impurities (less than 6 at%) were detected, probably in the form of catalyst remnants from the fabrication process.

To obtain an estimate of the purity of the electrolytes used in the present work, the solid residues remaining after gentle evaporation of the respective solvent in air were analyzed via XPS (Table 9.2). Other than oxygen, no foreign species were detected. The atomic ratios de-

Table 9.1.: Elemental composition of some carbonaceous electrode materials used in the present work. Where available, the mean composition and standard deviation are given for multiple measurements of the same sample type.

Sample	C	O	F	others
HOPG	100 %	–	–	–
YP17	(92.7 ± 1.5) at%	(7.3 ± 1.5) at%	–	–
	(90.5 ± 1.5) wt%	(9.5 ± 2.0) wt%	–	–
YP17/PTFE	70.5 at%	8.6 at%	20.9 at%	–
	61.3 wt%	9.97 wt%	28.8 wt%	–
SWCNTs	87.2 at%	7.1 at%	–	5.7[a] at%

[a] Includes B, Al and Fe.

viated slightly from the expected stoichiometric ratios (B:N = 1.2–1.3 instead of 1, F:B = 3.6 instead of 4).

Table 9.2.: Elemental composition (in at%) of electrolytes after evaporation of the solvent.

Electrolyte	B	C	F	N	O
$1\,M\,Et_4NBF_4/AN$	6.72	62.0	24.0	5.74	1.50
$1\,M\,Et_4NBF_4/PC$	6.22	62.8	22.1	4.97	3.88

9.2.2. Water content

The water content of the electrolytes used in the present work was determined by coulometric Karl Fischer titration (684 KF Coulometer from Metrohm using HYDRANAL® from Sigma-Aldrich as anolyte and catholyte). For $1\,M\,Et_4NBF_4$ in AN and in PC, the water content was determined to be 20–35 ppm in both cases.

In order to assess the amount of adsorbed moisture present in YP17, anhydrous AN was used as an extracting agent and the water content of the liquid phase determined via Karl Fischer titration after an extraction time of three days. A similar approach was followed by Strebkova et al. [374] using different extractants to measure the moisture content of sawdust.

0.45 g of YP17 powder were immersed in 7 g of anhydrous AN inside an argon-filled glovebox and kept in closed bottles for the duration of the extraction. A similar amount of AN without YP17 was stored under identical conditions as a reference sample. From the analysis of the water content of the liquid phase after the extraction, the water content of YP17 could be estimated (Table 9.3).

Although the efficacy of the above method regarding the detection of strongly adsorbed water is uncertain, the results in Table 9.3 suggest that approximately 90 % of the initial water content of YP17 may be removed by the drying process employed in the present work. It is worth noting that the water contribution of dried YP17 is roughly ten times higher than that of the electrolyte solutions per unit mass.

Table 9.3.: Moisture content of YP17 as estimated by a single three-day extraction with anhydrous AN.

Sample	Water content / ppm
as-received YP17	4299
dried YP17[a]	434
reference extractant	40

[a] Dried at 120 °C and 10^3 Pa for 24 hours.

The presence of relatively high amounts of water even after the drying procedure may be ascribed to the strong bonding of water within microporous channels, which has been observed by transmission electron microscopy of the interior of MWCNTs [375]. Under these conditions of spatial confinement, water is predicted to have an icelike mobility with a high degree of hydrogen bonding [376].

9.2.3. Raman spectroscopy

The Raman spectra of all carbonaceous materials investigated in the present work are summarized in Figure 9.1 along with the corresponding band labeling. For HOPG (Figure 9.1a), in which the defect concentration is very low and the degree of crystallinity is high, the only first-order feature observed clearly was the G band at 1580 cm^{-1}. The D band was not observed due to the fact that $q \neq 0$ for the phonon mode associated with this band as discussed in Section 8.5. However, the overtone of the D band, 2D, can be seen in the second-order spectrum near 2680 cm^{-1} due to momentum conservation in the two-phonon scattering process. The presence of two overlapping features within the 2D band is typical for the three-dimensional crystalline order in well-stacked graphite [344].

The transition from monolithic HOPG to microcrystalline SFG44 (Figure 9.1b) leads to the appearance of the D band at ca. 1330 cm^{-1}. In this case, the Raman scattering process involves inelastic one-phonon scattering and elastic scattering from crystallite edges or other defects (Section 8.5) to satisfy momentum conservation.
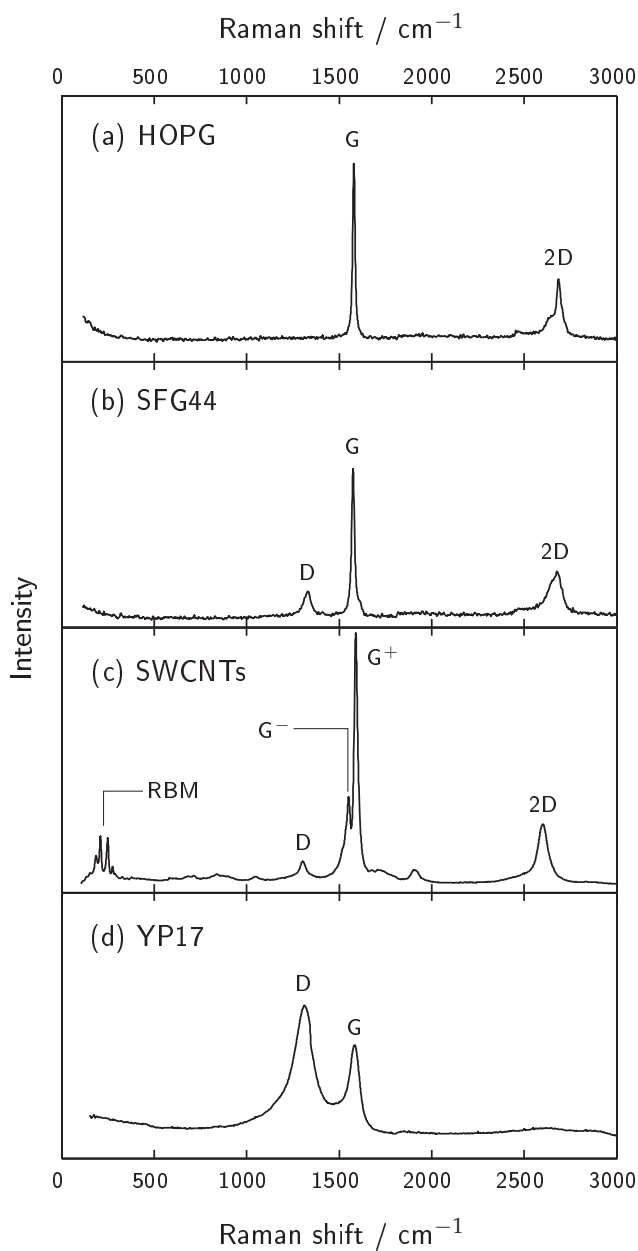
Figure 9.1.: First- and second-order Raman spectra of (a) HOPG, (b) SFG44, (c) a SWCNT mat, and (d) YP17. All spectra were recorded with a laser energy of 1.96 eV using an accumulation time of 60 s except for the SWCNTs (1 s).

The resonance enhancement of the Raman intensity in SWCNTs (Figure 9.1c) enabled the measurement of Raman spectra with high signal-to-noise ratios using very short acquisition times. Besides the D and G bands, some additional peaks can be identified in the Raman spectrum which have been discussed by Dresselhaus et al. [166] and Jorio et al. [170]. At very low Raman shifts, the radial breathing modes (RBMs) characteristic for SWCNTs were observed. The RBM is a bond-stretching out-of-plane phonon mode in which all carbon atoms move coherently in the radial direction. The frequency of this phonon mode is directly related to the nanotube diameter, as will be discussed in more detail in the context of the in situ Raman study of SWCNTs presented in Section 10.3. It should be noted that the Raman spectrum represents the phonon modes of those SWCNTs whose electronic structure matches the incident photon energy and thus favors a resonance enhancement.

In addition, the G band was seen to consist of multiple features and could be approximated by a high-frequency G^+ (1592 cm^{-1}) and a low-frequency G^- band (1555 cm^{-1}). Both are attributed to the same E_{2g} in-plane vibrational mode as in graphite, but the anisotropic properties of C$-$C bonds along the tube axis compared to the circumferential direction result in different characteristic frequencies depending on the bond orientation.

Finally, the Raman spectrum of YP17 (Figure 9.1d) differs from the above spectra in a few important respects. The D band at 1313 cm^{-1} exhibited a higher intensity than the G band at 1585 cm^{-1}, as is often observed for activated or amorphous carbons [377, 378]. For this particular sample, the ratio of the peak intensities I_D/I_G was 1.33, while the ratio of the peak areas (approximated by a fitting of the D and G bands by two Lorentzian functions) was 2.71. The ratio of the peak widths, FWHM$_D$ / FWHM$_G$, was 2.29. According to the combined Raman and XRD studies on a large variety of carbons by Cuesta et al. [117], these ratios correspond to L_a values in the range of 2–7 nm. The value of this L_a parameter, however, should not be taken as a measure of crystallite size as is the case for nanocrystalline graphites, but rather as a characteristic length scale for disorder (Section 8.5).

An important structural difference between YP17 and the other carbonaceous materials analyzed in Figure 9.1 is the absence of the second-order 2D feature for YP17. The lack of distinct second-order features has been reported previously [378] for disordered carbons, but has sometimes been mistaken as a sign for a lack of three-dimensional ordering. However, Raman measurements on single graphene sheets have revealed a well-defined, single-peak 2D feature [344, 359]. In fact, turbostratic graphite exhibits a very similar 2D band [344, 379] due to the misorientation of graphene layers with respect to each other. Hence, there is a fundamental difference in the structure of nanocrystalline turbostratic graphite and activated carbon which is clearly expressed by the lack of the 2D feature in case of the latter.

The lack of the 2D band for YP17 must therefore be interpreted in terms of bond length and angle disorder on the atomic scale as is the case for amorphous carbons [360], with roughly in-plane assemblies of distorted sixfold rings and rings of other orders. Such a bonding arrangement may be expected to lead to a distribution of phonon modes, which explains the significant widening of Raman bands upon increasing disorder [380]. As a further result of this distribution of phonon modes, two-phonon processes involving equal phonon momenta become highly unlikely, thus providing an explanation for the missing 2D band in activated carbons such as YP17.

9.2.4. WAXS of YP17

The WAXS pattern of as-received YP17 powder is shown in Figure 9.2. As an internal reference for the position of diffraction maxima, $10\,\text{wt}\%$ of silicon powder (-325 mesh, Sigma-Aldrich) were mixed into the powder. Generally, in comparison with graphite, the WAXS of non-graphitic carbons exhibits only weak and diffuse $00l$ and hk reflections [199, 381]. In Figure 9.2, YP17 exhibits two scattering maxima which appear near the expected 002 and $100/101$ reflections of graphite. Correspondingly, these features are denominated the 002 band, which originates due to interlayer scattering from approximately parallel graphene sheets, and the 10 band, which arises due to intralayer scattering [382]. In non-graphitic carbons, there are no hkl reflections due to the lack of three-dimensional ordering [199, 382].
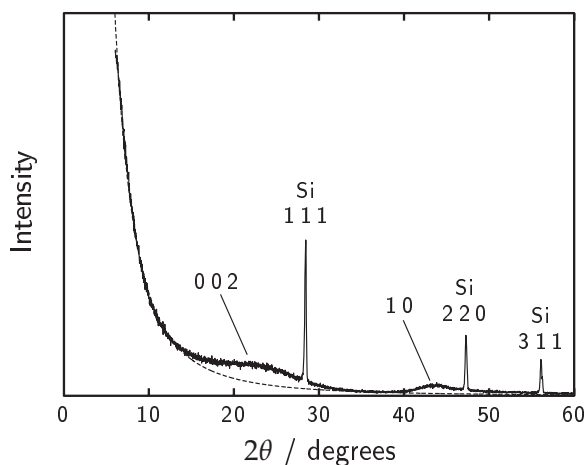
Figure 9.2.: XRD pattern of YP17 with an internal Si reference. The dashed line denotes the background which was empirically fitted by a power law of the type $y = a\,x^b$ and subtracted from the diffraction data. Structural parameters were obtained from the background-subtracted diffraction curve. The data was recorded with Cu K_α radiation ($\lambda = 1.54\,\text{Å}$).

At scattering angles below about $20\,^\circ$, the small-angle scattering contribution of YP17 due to its microporosity becomes dominant. The positions and FWHM of the WAXS maxima were obtained from the WAXS curve after subtraction of the small-angle scattering from the raw data. Following the conventional nomenclature for graphite, the d_{002} spacing as well as the L_c and L_a parameters were estimated from the Bragg (8.1) and Scherrer (8.2) equations, respectively. The corresponding values are summarized in Table 9.4. The average separation distance between graphene sheets, d_{002}, was calculated to be 3.9 Å, while the spatial extent of order perpendicular to the graphene sheets, L_c, was 7.6 Å. As a measure for the length scale of in-plane ordering, L_a, a value of 3.9 nm was obtained.

Thus, for YP17, it can be concluded that the ordered domains which give rise to WAXS maxima consist of at most three roughly parallel graphene sheets with no preferential mutual orientation. These sheets extend over a distance of 3.9 nm, corresponding to about 15 contiguous sixfold aromatic rings. It is worth noting that these values agree well

Table 9.4.: Structural parameters for YP17 extracted from the XRD pattern shown in Figure 9.2.

d_{002} / nm	0.39
L_c / nm	0.76
L_a / nm	3.9

with those of other non-graphitic carbons [117, 382–384], despite the simplistic and direct application of the Bragg and Scherrer equations which only strictly relate to crystalline materials. For sake of completeness, more refined WAXS fitting procedures [382–385] are mentioned here, even though it was not deemed necessary to implement them in the present work.

9.2.5. Porosity of YP17 and SWCNTs

The presence of pronounced small-angle scattering in YP17 already indicates a pronounced microporosity. While the SAXS measurements of YP17 are discussed in the context of the corresponding in situ experimental series in Chapter 12, the N_2 adsorption data obtained from YP17 will be summarized in the following and compared with that of SWCNTs.

The adsorption and desorption isotherms of YP17 and SWCNTs are shown in Figure 9.3. Both materials exhibited significant N_2 adsorption capacities in the range of 600–800 $cm^3 g^{-1}$. The adsorption isotherm of YP17 is a Type I isotherm according to the BDDT classification, exhibiting a strong uptake at very low relative pressures and a Langmuir-type saturation with increasing relative pressures. The slight hysteresis observed during desorption is indicative of mesoporosity with predominantly slit-shaped morphology. The SWCNTs investigated in the present work exhibited a composite Type II/IV isotherm with a significant hysteresis loop characteristic of concave pore shapes.

The BET plot of YP17 (Figure 9.4a) exhibited an excellent fit in the relative pressure range of 0.008–0.12, resulting in a BET surface area of 1683 $m^2 g^{-1}$. Also, a significant linear regime was observed in the DR plot (Figure 9.4b), giving a micropore volume of 0.55 $cm^3 g^{-1}$ for
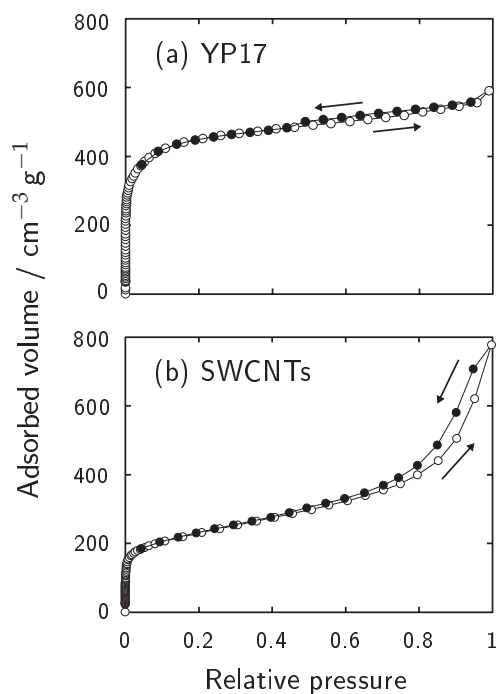
Figure 9.3.: N_2 adsorption (○) and desorption (●) isotherms of (a) YP17 powder and (b) part of a SWCNT mat. The solid lines are guides to the eye.

YP17. Equally good fits were obtained with SWCNTs and all other samples studied in the present work. The porosity data obtained for YP17, YP17/PTFE and SWCNTs is compiled in Table 9.5.
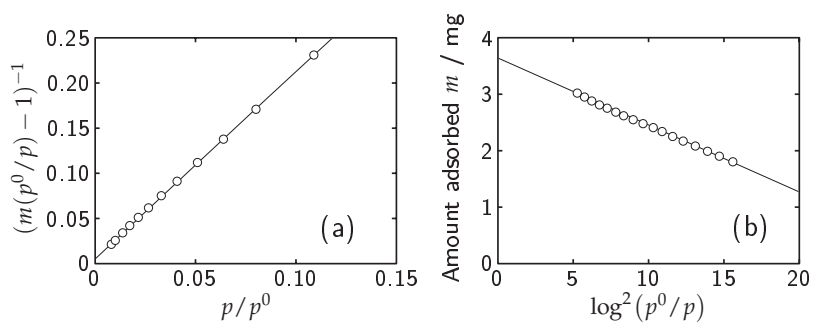
Figure 9.4.: (a) BET and (b) DR plots for YP17. m is the mass of adsorbed gas.

Table 9.5.: Porosity and surface area of YP17 and SWCNTs.

	YP17	YP17/PTFE	SWCNTs
BET area / $m^2 g^{-1}$	1683	1466	816
NLDFT total area / $m^2 g^{-1}$	1705	1503	986
NLDFT total pore volume / $cm^3 g^{-1}$	0.85	0.71	1.10
NLDFT micropore area / $m^2 g^{-1}$	1460	1291	564
NLDFT micropore volume / $cm^3 g^{-1}$	0.57	0.50	0.16
DA micropore area / $m^2 g^{-1}$	1549	1467	641
DA micropore volume / $cm^3 g^{-1}$	0.55	0.50	0.23
BJH mesopore volume[a] / $cm^3 g^{-1}$	0.24	0.20	0.89

[a] Evaluated from the desorption branch.

The isotherm fitting via NLDFT reproduced the adsorption data very well at high relative pressures, with slight deviations noticeable at low relative pressures (Figure 9.5). Based on the NLDFT analysis of YP17 (Table 9.5), 67 % of the total pore volume and 86 % of the total surface area is located in micropores. In SWCNTs, the mesoporous character is much more dominant, with 85 % of the total pore volume being accounted for by meso- or macropores. The accessible microporosity in the SWCNT sample, however, still accounts for 57 % of its total surface area.

From Table 9.5, it can also be seen that the specific surface areas and pore volumes of YP17/PTFE are systematically about 10 % smaller than those of unbound YP17. Thus, the PTFE binder may be considered to increase the sample mass while contributing negligibly towards the surface area. Apart from the augmented mass, the binder does not appear to affect the porosity or accessible surface area of YP17.

Based on the NLDFT and DA methods, the micropore size distributions in Figure 9.6a and b were obtained for YP17. Clearly, the vast majority of the pore volume and thus surface area is found within pore widths of 2 nm or smaller. According to the BJH pore size distribution in Figure 9.6c, there are virtually no mesopores larger than 10 nm.

Considering the specific surface area of $2630 \, m^2 g^{-1}$ for a single sheet of graphene, the total surface area of around $1700 \, m^2 g^{-1}$ for YP17 (Table 9.5) implies that almost each carbon atom in YP17 is a surface atom.
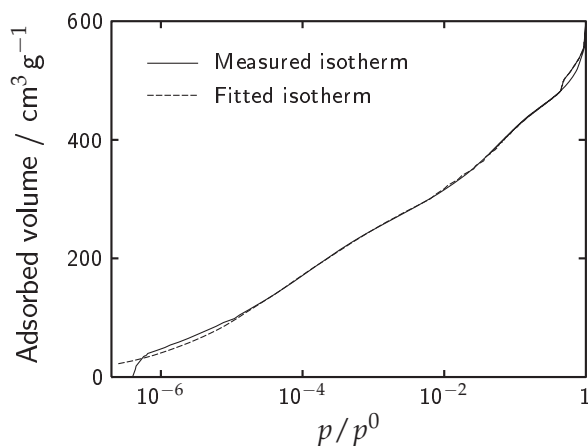
Figure 9.5.: Comparison of the measured isotherm (solid line) with the isotherm fitted by NLDFT (dashed line) using a mixed slit/cylindrical pore model for YP17. Note the logarithmic pressure scale.

On average, the surface area accessible by the probe gas corresponds to the specific surface area of 1–2 stacked graphene sheets.

The theoretical specific surface area of a lone SWCNT is half of a graphene sheet, i.e. $1315 \, \text{m}^2 \, \text{g}^{-1}$. The accessible surface area measured in the present work is only 75 % of this value according to Table 9.5. The lower specific surface area can not be explained solely on the basis of non-porous impurites, as the respective mass fractions (Table 9.1) are too low. In view of the bundled structure of the SWCNT sample, it appears as though only the exterior bundle surface is accessible by the probe gas.

According to Peigney et al. [164], the specific surface area observed in the present work is consistent with close-packed bundles made up of approximately six SWCNTs in which only the exterior surface is accessible. It cannot be entirely ruled out that some of the SWCNTs might be open-ended [156, 164], but it appears as though the interior of the majority of SWCNTs can be considered inaccessible to gas on the basis of the above results. The observed microporosity of the SWCNTs may primarily arise from the grooves on the outer surface of SWCNT bundles, but possibly also from loosely packed bundles in which the interstitial channels are accessible or from defects in the tube walls [133, 386].
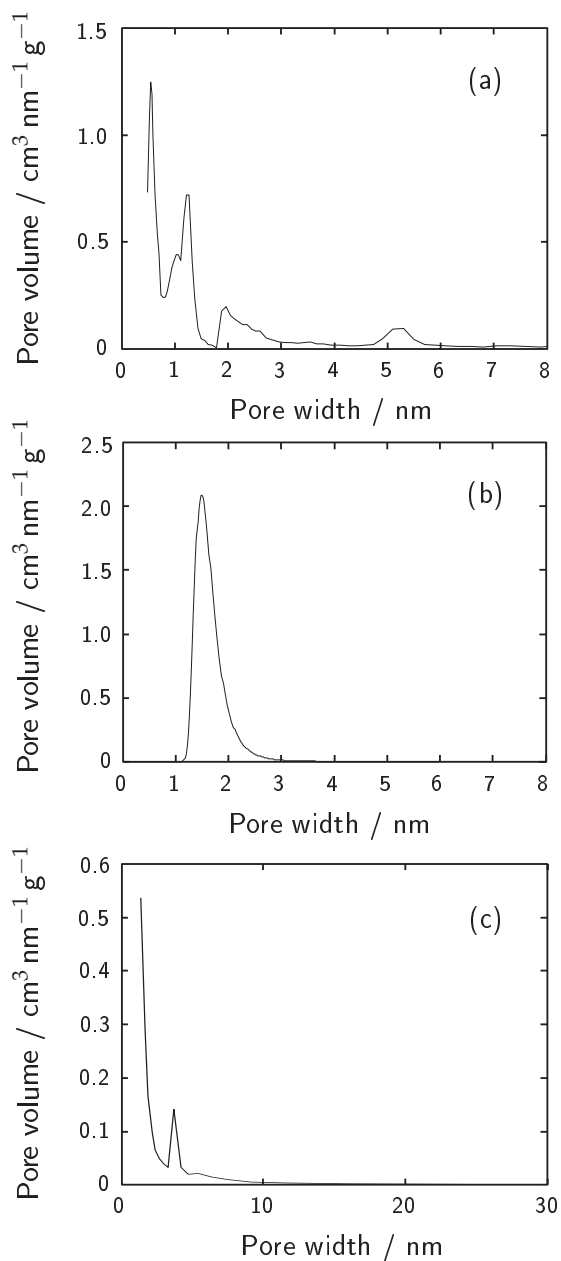
Figure 9.6.: Pore size distributions of YP17 according to the (a) NLDFT (assuming a mixed slit/cylindrical pore model), (b) DA (n = 2.4), and (c) BJH methods. Note the different pore size scale for (c).

9.2.6. Electrochemical characterization of YP17 in EDLC electrolytes

Stability of activated carbon as a quasi-reference electrode

As discussed in Section 7.2, the use of an ideally polarizable electrode such as activated carbon as a reference electrode is uncommon in electrochemical investigations and requires some justification. On one hand, the contamination introduced by placing activated carbon into a non-aqueous electrolyte is usually less than when using a QRE of the first or second kind, since no foreign ionic species are added to the test solution. In fact, by using the same material as working, counter and reference electrode, any contamination due to the QRE can be considered negligible compared to the other two usually much larger electrodes.

In order to assess the stability of the potential of YP17/PTFE over time, CVs of AN- and PC-based EDLC electrolytes containing 2 mM Fc were recorded against a YP17/PTFE QRE. A conversion to the com-
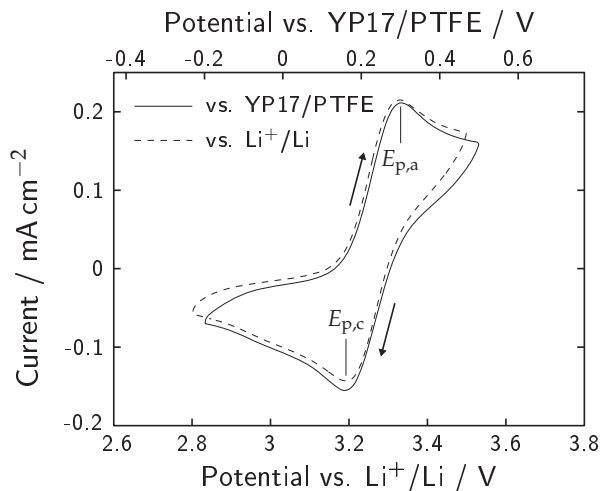
Figure 9.7.: CVs of a solution of 1 M LiClO$_4$ and 2 mM Fc in PC against YP17/PTFE and Li$^+$/Li. The working and counter electrodes consisted of platinum and the sweep rate used was 50 mV s^{-1}. The half-wave potential $E_{1/2}$ was determined from $E_{p,c} + \Delta E/2$, where $\Delta E = E_{p,a} - E_{p,c}$.

monly used Li^+/Li potential scale [387] was achieved by performing the same experiments in 1 M $LiClO_4$/PC by alternating between metallic lithium and YP17/PTFE as reference electrode. From Figure 9.7, the immersion potential of YP17/PTFE was found to be close to +3 V with respect to Li^+/Li.

The stability of the potential of YP17/PTFE was evaluated by determining the half-wave potential, $E_{1/2}$, of the Fc^+/Fc redox system against this potential over time (Figure 9.8). Over a test period of about one week, a drift of the immersion potential in the order of +20 mV was measured in either electrolyte. Under the assumption of a linear drift in time, the initial potentials of the YP17/PTFE QREs were (-202 ± 2) mV and (-213 ± 2) mV vs. Fc^+/Fc for 1 M Et_4NBF_4 in AN and in PC, respectively, while the potential drifts were determined to be $(+3 \pm 1)$ mV per day in either case. Compared to the timescale and potential ranges of the electrochemical experiments typically conducted in the present work, this drift may safely be considered as negligible.

From Table 9.6, it can be seen that $E_{1/2}$ of the Fc^+/Fc redox system is similar in the different solvents and supporting electrolytes investigated here. Duschek and Gutmann [388] and Gritzner [389] found that $E_{1/2}$
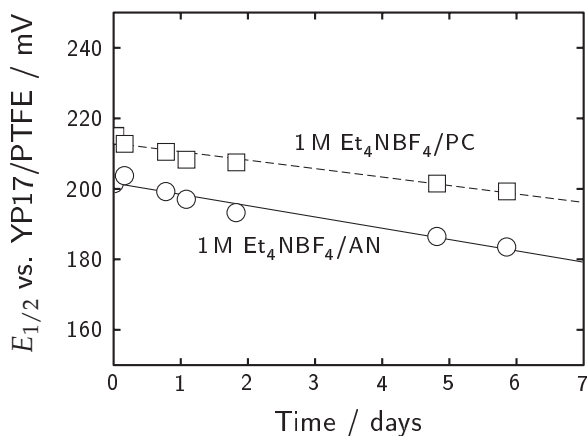
Figure 9.8.: Change in position of the half-wave potential $E_{1/2}$ of the Fc^+/Fc redox system against YP17/PTFE over time. The solid and dashed lines correspond to linear fits of the data for 1 M Et_4NBF_4 in AN and in PC, respectively.

of Fc^+/Fc is practically invariable in a wide range of solvents, including AN and PC. Therefore, it is now possible to convert electrode potentials referred to YP17/PTFE to other frequently employed reference systems. In particular, the conversion to the Li^+/Li potential scale is presented in Table 9.6. The potential of the Li^+/Li electrode measured in the present work, -3.26 V vs. Fc^+/Fc in 1 M $LiClO_4/PC$, converts to -2.89 V vs. saturated calomel electrode (SCE) [388] and -2.65 V vs. SHE [60], which is 140 mV more positive than the literature value of the Li^+/Li electrode in PC [390]. This uncertainty should be borne in mind when comparing potentials quoted in the present work to other published reference potential scales.

According to the above findings, the use of YP17/PTFE as a QRE in EDLC electrolytes may thus be considered valid on the grounds of its stability and interconversion with other potential scales. For convenience and simplicity, all single electrode potentials in the present work are therefore implicitly quoted against YP17/PTFE without further specification.

Table 9.6.: Immersion potential of YP17/PTFE against the half-wave potential $E_{1/2}$ of the Fc^+/Fc reference redox system in 1 M solutions of different electrolytes and interconversion with the Li^+/Li potential scale.

Potential / V	Et_4NBF_4/AN	Et_4NBF_4/PC	$LiClO_4/PC$
vs. Fc^+/Fc	-0.202	-0.213	-0.229
vs. Li^+/Li	+3.00	+3.05	+3.03

Electrochemical characterization of YP17 in EDLC electrolytes

The impedance spectra of YP17/PTFE in the AN- and PC-based electrolyte solutions are compared in Figures 9.9 and 9.10. In both electrolytes, the Nyquist plot approached a vertical line at low frequencies and exhibited an approximately 45° slope at high frequencies. The impedance response is thus typical for double layer charging of highly porous electrodes as discussed in Sections 3.5 and 7.5.

At high frequencies, the impedance is governed by the electrolyte solution outside of the pores. As expected, the AN-based electrolyte
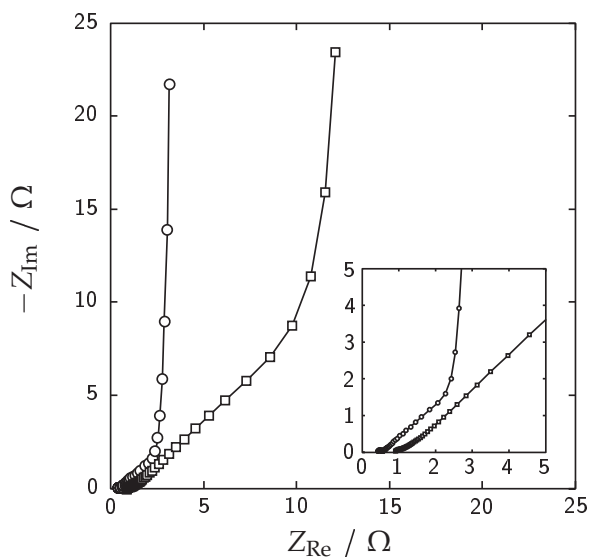
Figure 9.9.: Nyquist plots for symmetric two-electrode cells consisting of YP17/PTFE in 1 M Et$_4$NBF$_4$ in AN (○) and in PC (□) in the frequency range between 100 kHz and 10 mHz. A paper-based separator of 25 μm thickness was used. The inset is an enlargement of the high frequency region. The geometric electrode area was 1.1 cm^2 and the thickness of each electrode was (500 ± 10) μm. The total active electrode mass was 37.2 mg for the AN-based solution and 38.5 mg for the PC-based solution.

exhibited a lower ESR in this region. At 100 kHz, the ESR of the PC-based electrolyte was twice as high as that of the AN-based electrolyte. From literature values regarding the conductivities of these electrolytes (Table 3.3), even a fourfold higher resistance of the PC-based electrolyte could be expected.

In fact, the difference in the ESRs of the two electrolytes was much more pronounced at low frequencies due to a significantly higher EDR of the PC-based electrolyte within the porous structure of the electrode. From Figure 9.9, the EDR of the PC-based electrolyte was about four times higher as that of the AN-based electrolyte. The difference in EDR implies that the pore conductivity is sensitive to the type of solvent used. In this context, PC appears to hinder the ionic mobility more than AN, a result which has previously also been obtained by Lust et
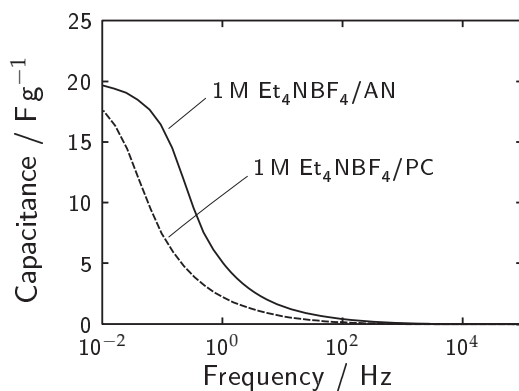
Figure 9.10.: Bode plot for the same cells as in Figure 9.9. The capacitance of the full cell is normalized to the total active mass of both electrodes.

al. using impedance spectroscopy [391]. Obvious explanations for this include the larger size of the PC molecule and the higher viscosity of PC (Table 3.3), whereby these two properties are linked to each other. The slower charging kinetics of the porous electrodes in the PC-based electrolyte are also clearly visible in Figure 9.10, where the capacitance is plotted as a function of frequency.

Three-electrode cyclic voltammetry of YP17/PTFE was performed against YP17/PTFE QREs in separate experiments for the negative and positive potential ranges in both electrolytes (Figures 9.11, 9.12, 9.13 and 9.14). In these experiments, the potential sweeps were carried out at different rates and the potential window was successively opened to larger values.

The corresponding CVs of YP17/PTFE in $1\,M\,Et_4NBF_4/AN$ are plotted in Figure 9.11 for a sweep rate of $1\,mV\,s^{-1}$ and Figure 9.12 for a sweep rate of $10\,mV\,s^{-1}$. During reversible capacitive charging at $1\,mV\,s^{-1}$, the differential capacitances were found to be $124\,F\,g^{-1}$ at -1.5 V and $147\,F\,g^{-1}$ at +1 V. At 0 V, the capacitance was $72\,F\,g^{-1}$.

Notable deviations from reversible charging occurred at about -2 V and +1.2 V at $1\,mV\,s^{-1}$, where significant irreversible reductive and oxidative currents were observed. At the sweep rate of $10\,mV\,s^{-1}$ following these irreversible processes, the negative electrode retained its capacitive behavior to a large extent, while the positive electrode ex-
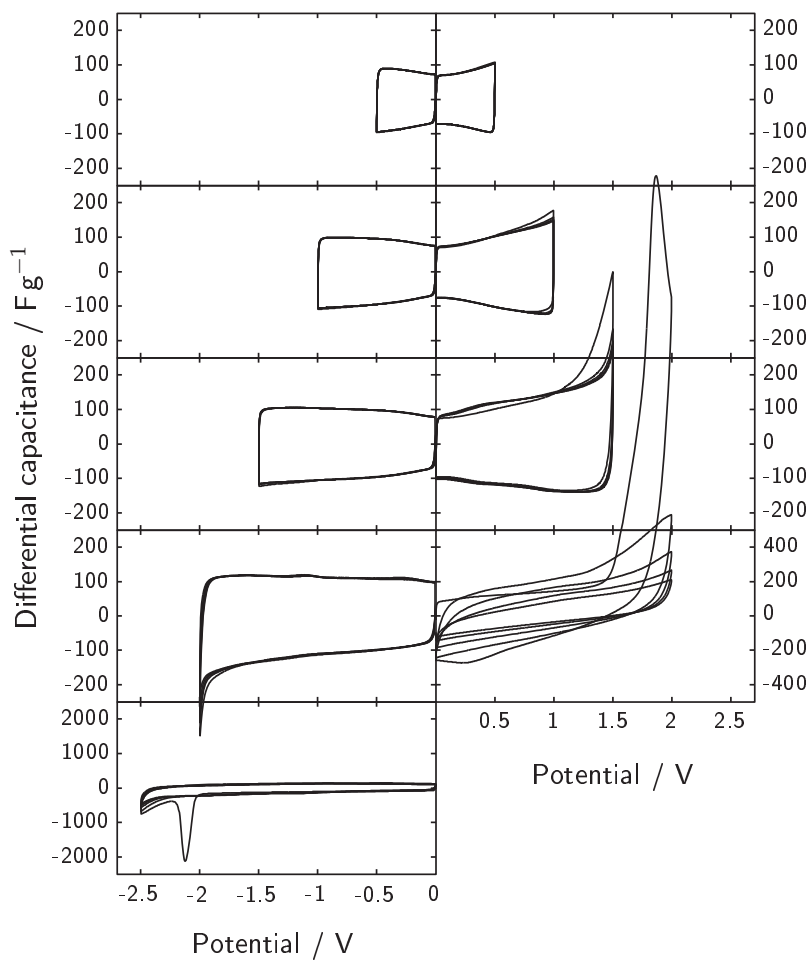
Figure 9.11.: Three-electrode CVs of YP17/PTFE in $1\,M\,Et_4NBF_4/AN$ at a sweep rate of $1\,mV\,s^{-1}$ in successively larger potential windows. Five cycles were performed for each potential window. The negative and positive potential ranges were recorded in separate experiments and the differential capacitance refers to the active working electrode mass. The electrode diameter was 13 mm in both cases, and the electrode thicknesses were 114 μm (negative potentials) and 100 μm (positive potentials). Note the different capacitance scales for the largest negative and positive potential windows.
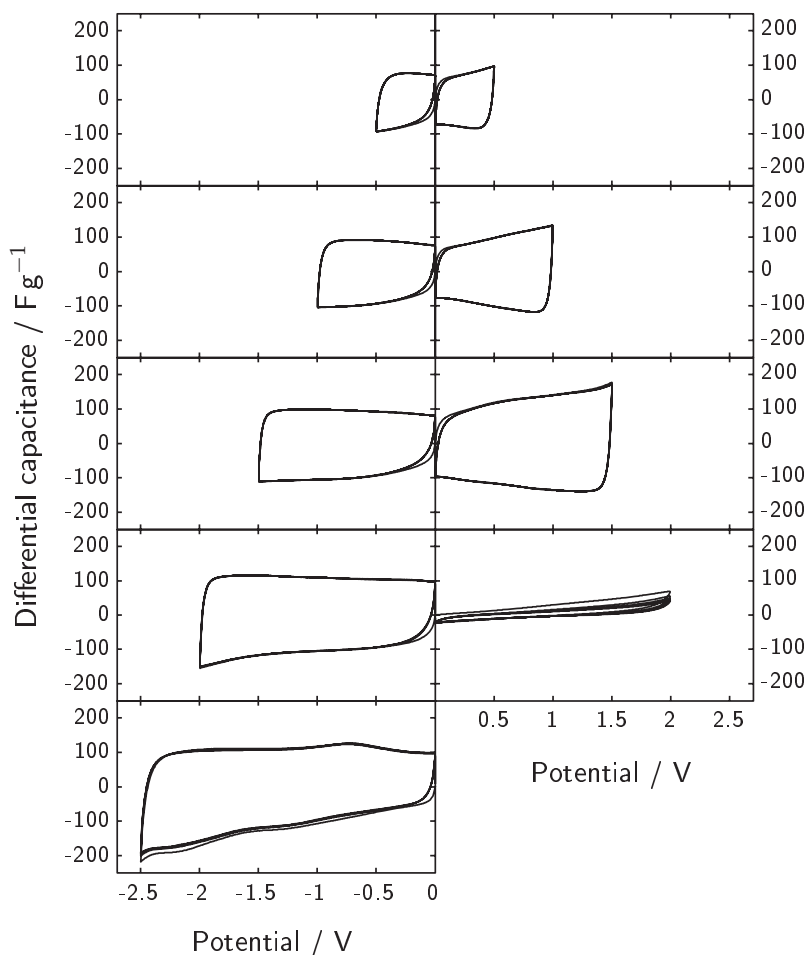
Figure 9.12.: Three-electrode CVs of YP17/PTFE in $1\,\mathrm{M}$ $\mathrm{Et_4NBF_4}$/AN at a sweep
rate of $10\,\mathrm{mV\,s^{-1}}$. Five CVs were performed in the same potential
window after the corresponding CVs at $1\,\mathrm{mV\,s^{-1}}$ (Figure 9.11).

hibited a significant loss of double layer capacitance (Figure 9.12). It
is noted that the pronounced reduction peak just below -2 V was ab-
sent in binder-free electrodes, and was thus attributed to the reductive
carbonization of PTFE by defluorination [392].

Upon examination of the CVs in the reversible potential window
ranges, an increase in the (reversible) capacitance with increasing elec-
trode potential excursion can be noticed. The potential of minimum
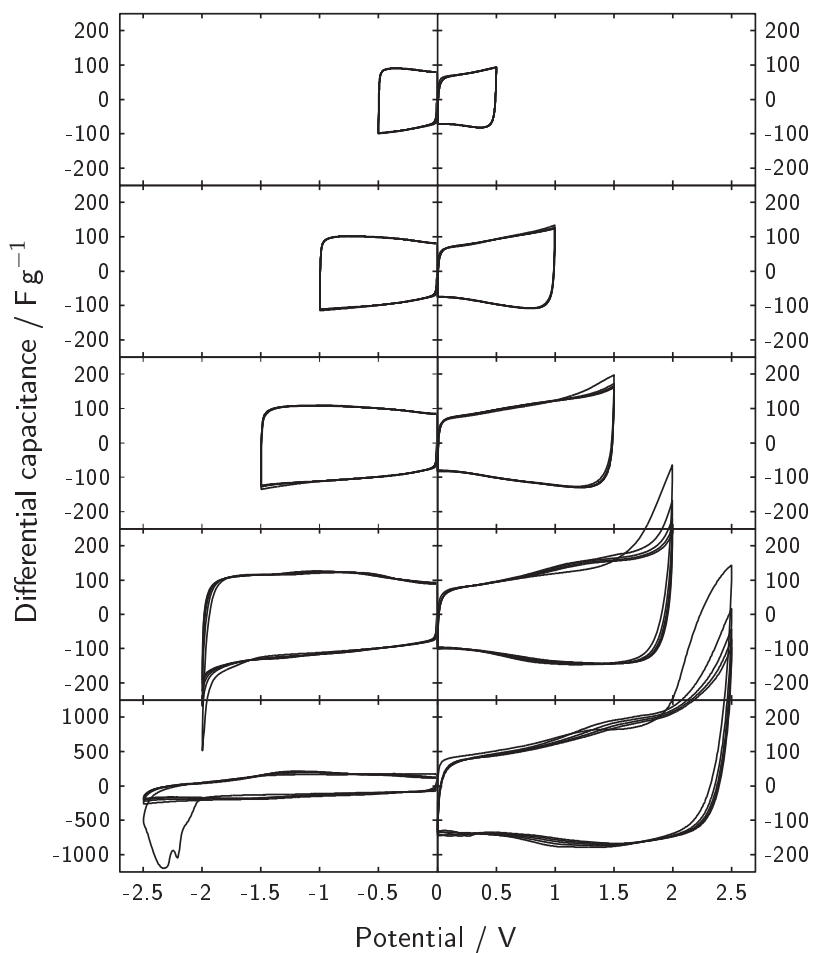
Figure 9.13.: Three-electrode CVs of YP17/PTFE in $1\,M$ Et_4NBF_4/PC at a sweep rate of $1\,mVs^{-1}$ in successively larger potential windows. Five cycles were performed for each potential window. The negative and positive potential ranges were recorded in separate experiments and the differential capacitance refers to the active working electrode mass. The electrode diameter was $13\,mm$ in both cases, and the electrode thicknesses were $123\,\mu m$ (negative potentials) and $130\,\mu m$ (positive potentials). Note the different scale for the largest negative potential window.
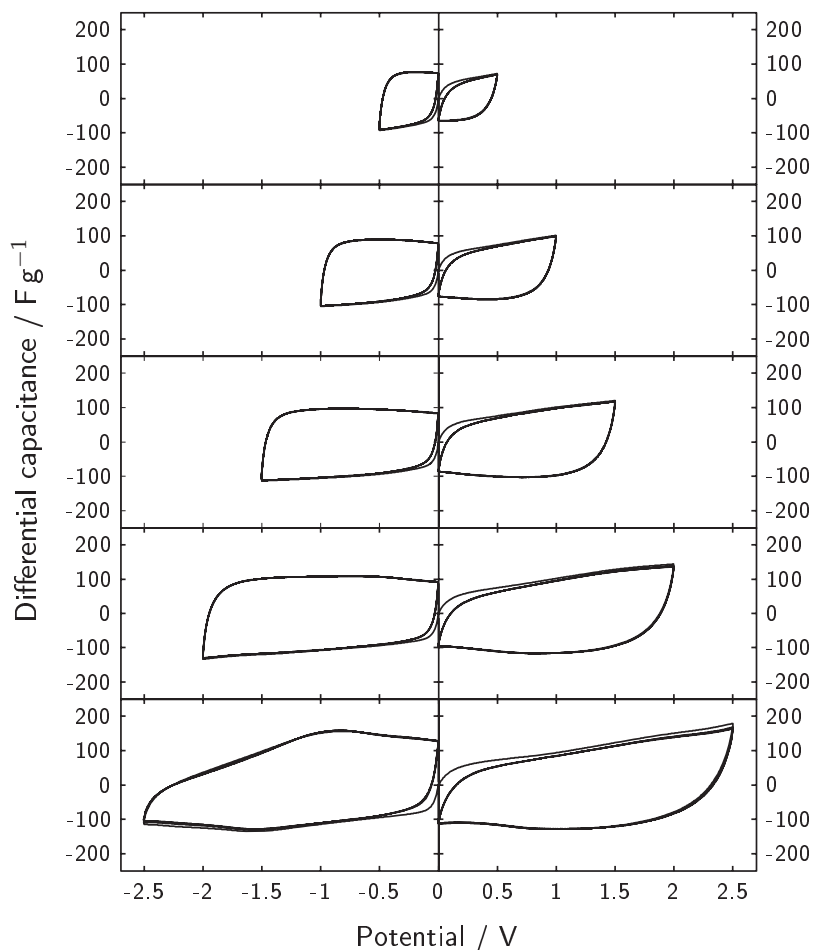
Figure 9.14.: Three-electrode CVs of YP17/PTFE in $1\,\text{M}$ Et_4NBF_4/PC at a sweep rate of $10\,\text{mV}\,\text{s}^{-1}$. Five CVs were performed in the same potential window after the corresponding CV at $1\,\text{mV}\,\text{s}^{-1}$ (Figure 9.13).

capacitance was close to the immersion potential, which may be taken as a measure for the pzc of ideally polarizable, high surface area electrodes as discussed by Tobias and Soffer [240]. Salitra et al. [104] therefore proposed that polarization to potentials remote of the pzc results in electroadsorption of ions within the pores of activated carbon, the interaction between pore wall and ion being enhanced when the pore size matches the ion size in analogy to the enhanced inter-
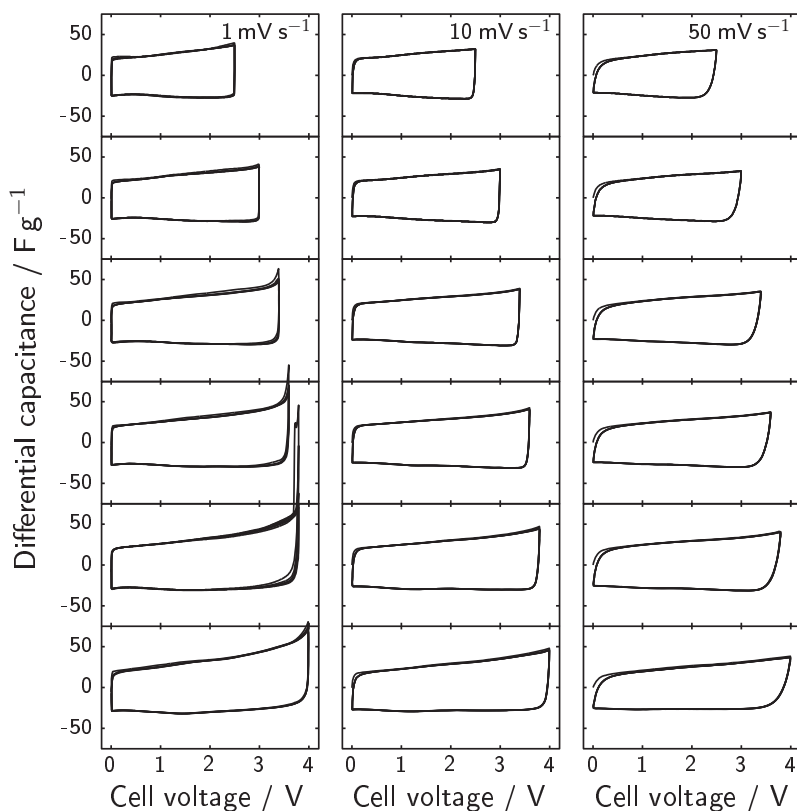
Figure 9.15.: Two-electrode CVs of YP17/PTFE in $1\,M$ Et_4NBF_4/AN at different sweep rates and successively larger voltage windows. The differential capacitance refers to the total active electrode mass. The electrodes were $170\,\mu m$ thick each and separated by a glass-fiber separator.

action potential during the adsorption of gases in micropores (Figure 8.11 on page 135). However, a minimum in differential capacitance is also observed for HOPG electrodes [393], which has been explained by Gerischer et al. [66, 70] in terms of the dependence of the space charge capacitance on the electrode potential (Section 3.3.2). This line of argument led Hahn et al. [108] to adopt the interpretation of the capacitance minimum of activated carbons in EDLC electrolytes in terms of the limiting space charge capacitance of the electrode due to the minimum number of available electronic charge carriers at this poten-
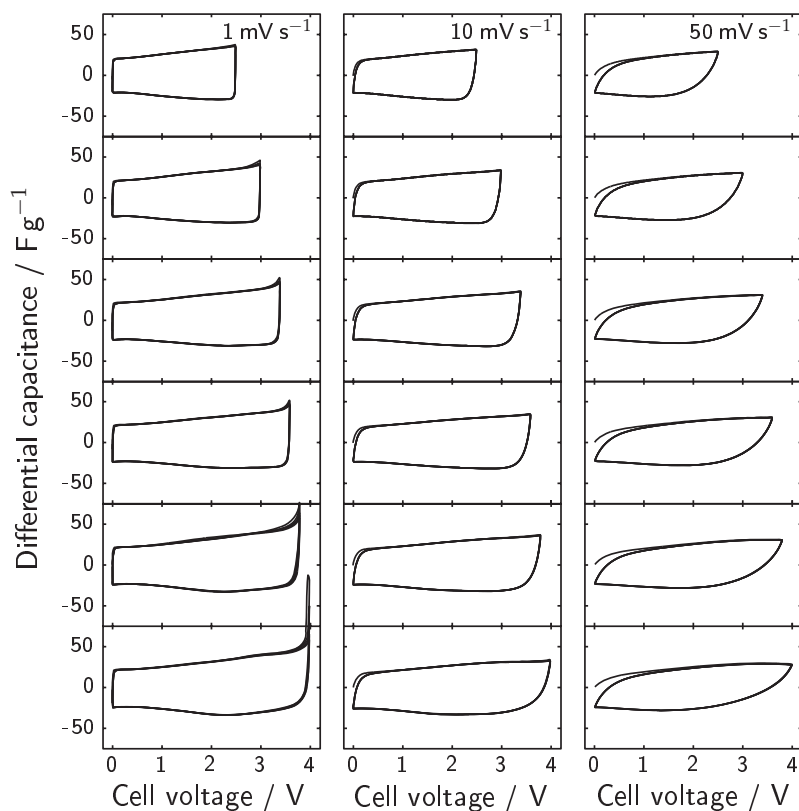
Figure 9.16.: Two-electrode CVs of YP17/PTFE in $1\,M$ Et$_4$NBF$_4$/PC. Identical conditions were employed as described for Figure 9.15.

tial. The effect of the electronic structure on the charging of the electrochemical double layer will be discussed in more detail in Chapter 10.

Further, it can be seen that the capacitance tends be higher at positive potentials with respect to the corresponding negative potential window (Figure 9.11). If the space charge capacitance of the electrode is considered to be limiting, this observation implies that the electronic density of states increases more steeply in the valence (π) band compared to the conduction (π^*) band. On the basis of the electronic structure of an ideal graphene sheet (Section 4.2), such an asymmetry is not expected. However, the presence of in-plane disorder (evidence for which was obtained by Raman spectroscopy, Figure 9.1) in the form of odd-numbered

rings or heteroatoms may alter the density of states [116, 121]. If, on the other hand, the Helmholtz capacitance were limiting, the higher capacitance at positive potentials could be explained by a closer distance of approach of BF_4^- to the electrode surface compared to Et_4N^+. This aspect will also be discussed in some more detail in the context of electrochemical doping in Chapter 10.

Analogous three-electrode cycling experiments were carried out in 1 M solutions of Et_4NBF_4 in PC and are summarized in Figures 9.13 and 9.14. The increased electrolyte resistance when using PC as a solvent instead of AN is clear when comparing the transient current response upon changing the sweep direction (Figures 9.14 and 9.12). In the region of capacitive charging, the minimum capacitance was found to be $83 \, \mathrm{F \, g^{-1}}$ while the maximum capacitances were $125 \, \mathrm{F \, g^{-1}}$ at -1.5 V and $+134 \, \mathrm{F \, g^{-1}}$ at +1 V.

While the capacitive behavior in the PC-based electrolyte is, in general, very similar to that observed in the AN-based electrolyte, some differences can be noted, particularly in the extended potential windows.

In the negative potential range, a significant irreversible current set in at around -2 V at a sweep rate of $1 \, \mathrm{mV \, s^{-1}}$ (Figure 9.13). In the positive range, irreversible oxidative processes became significant at potentials above +1.5 V (at $1 \, \mathrm{mV \, s^{-1}}$), which is higher than the corresponding case in the AN-based electrolyte (Figure 9.11). Also, even upon potential cycling to +2.5 V, the irreversible charge loss in the PC-based electrolyte was significantly less than in the AN-based electrolyte at +2 V.

During subsequent CVs at $10 \, \mathrm{mV \, s^{-1}}$ for the positive potential range in the PC-based electrolyte, the capacitive properties of YP17/PTFE were retained even up to +2.5 V. This stands in pronounced contrast to the case of the AN-based electrolyte discussed above. On the other hand, the negative electrode cycled to -2.5 V in the PC-based electrolyte exhibited a decrease in capacitance upon subsequent polarization to beyond -1.5 V. The corresponding CVs shown on the bottom left in Figure 9.14 are indicative of either electrolyte starvation, in which there are not enough ions present to balance the electronic charge on the electrode, or ion sieving, in which the effective pore size has been reduced and, accordingly, the number of ions which can be accommo-

dated within the pores has decreased. Considering that the reduction process which occurred prior to this effect (Figure 9.13, bottom left) was only observed in the first cycle and no such ion sieving was observed for the AN-based electrolyte despite a significantly higher amount of irreversible charge consumption, the latter explanation appears more plausible. Further investigations into the nature of the irreversible current peaks as well as the performance loss of single electrodes due to elevated voltages for both the AN- and PC-based electrolytes are presented in Chapter 14.

Full cells were constructed with symmetric YP17/PTFE electrodes and tested by recording two-electrode CVs at different sweep rates, thus approximating the charge/discharge behavior of technical EDLC devices. A YP17/PTFE QRE was used to monitor the individual electrode potentials during these experiments. The results for $1\,M\,Et_4NBF_4$ in AN and in PC are shown in Figures 9.15 and 9.16, respectively. The potential excursions of the individual electrodes during the full cell cycling are compiled in Figure 9.17.
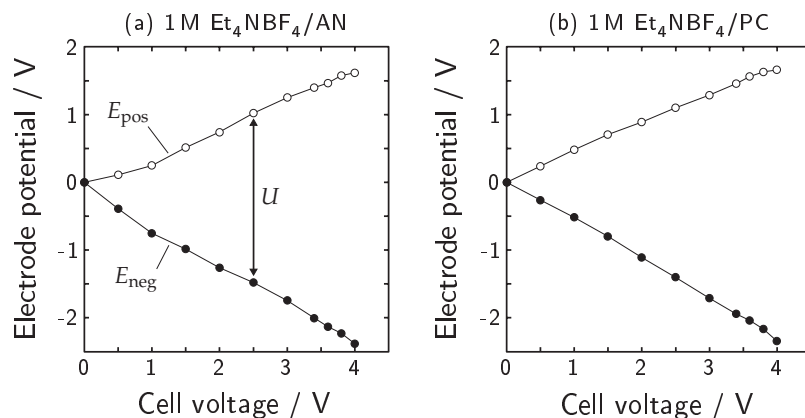
Figure 9.17.: Maximum potential excursions of the positive (E_{pos}) and negative (E_{neg}) YP17/PTFE electrodes for symmetric cells cycled to different maximum voltages in $1\,M\,Et_4NBF_4$ in AN (a) and in PC (b). The values were obtained from the experiments shown in Figures 9.15 and 9.16 by measuring the electrode potentials during cycling. The potential excursions were found not to change by more than ca. 10 mV during the five cycles performed in each voltage window.

The increased capacitance of the full cell upon charging reflects the capacitance minima of the positive and negative electrode at their immersion potentials. For both electrolytes, it is worth noting that no catastrophic failure or significant modification of the shape of the CVs occurred even when the full cell was cycled in the voltage range between 0 V and 4 V, i.e. significantly above the nominal voltage of commercial EDLCs.

Just below a cell voltage of 3.8 V, the full cell CV in the AN-based electrolyte exhibited a sharp, irreversible current spike at $1\,\mathrm{mV\,s^{-1}}$ which occurred only in the first cycle. The different potential excursions of the two identical electrodes is due to the different specific capacitance values exhibited in the negative and potential ranges as discussed above. At a cell voltage of 3.8 V, the negative electrode reached a potential of -2.23 while the positive electrode reached +1.57 V (Figure 9.17a). At these electrode potentials, significant irreversible charge losses are expected for both electrodes according to the three-electrode CVs (Figure 9.11).

A similar irreversible current spike was also observed for full cell cycling in the PC-based electrode just below 4 V. In this case, the electrode potentials were -2.34 V and +1.66 V, respectively, and the corresponding three-electrode measurements (Figure 9.13) suggest that irreversible charge losses occur primarily the negative electrode under these conditions.

However, for both electrolytes, it is worth reiterating that the full cell still exhibited highly capacitive behavior, particularly at higher sweep rates, for the limited number of cycles up to 4 V which were conducted in the present study. The study of the aging of full cells is presented in Chapter 14, and will demonstrate that the stability of EDLC systems at elevated voltages must be assessed over longer time periods in order to draw practically relevant conclusions.

9.3. Conclusions

A chemical, physical and electrochemical characterization of YP17 and a comparison of some of its properties with other carbonaceous electrodes was carried out and discussed in this chapter.

YP17 was found to contain no heteroatomic impurities detectable via XPS apart from oxygen. The absence of cationic impurities is presumed to be advantageous, since these have been proposed to be an important cause for the self-discharge of biomass-derived carbons in EDLCs (Section 5.2.2). Oxygen-containing functional groups, however, are relatively abundant, with approximately one oxygen-containing moiety observed per 12–13 carbon atoms.

Through the drying process employed in the present work, about 90 % of water was estimated to be removed from YP17. However, the measured water content of about 400 ppm for YP17 clearly exceeds that of the electrolyte solution (less than 35 ppm). Considering that, in all electrochemical experiments performed in the present work, an excess of electrolyte was used, it may be estimated that the two contributions towards the total water content of the system are approximately equal.

The disordered, highly porous structure of YP17 was probed by Raman spectroscopy, WAXS and nitrogen adsorption. The results suggest a significant in-plane disorder due to a distribution of bond lengths and angles. The most ordered domains consist of up to three parallel, misoriented graphene sheets extending over an in-plane distance of about 4 nm. The inner surface area of YP17 is considerable, with the equivalent specific surface of 1–2 graphene sheets being fully accessible by gas, indicating that virtually every carbon atom is a surface atom. The fraction of surface area contained within micropores (< 2 nm) is 0.86 of the total surface area determined by NLDFT (about $1700 \, \text{m}^2 \, \text{g}^{-1}$).

The quality of the SWCNTs used in this work was verified by XPS and Raman spectroscopy. An oxygen content similar to that of YP17 was found, as well as less than 6 at% of other non-carbonaceous impurities. The SWCNTs exhibited clear RBM features, indicative of single-tube phonon modes, and a multi-peak G band feature due to the highly anistropic nature of $C-C$ bonds within single tubes. The high specific surface area of the SWCNTs ($986 \, \text{m}^2 \, \text{g}^{-1}$ via NLDFT) contains a significant contribution from mesopores (about 43 %) due to the low extent of bundling, which was estimated to be in the order of six SWCNTs per bundle.

YP17/PTFE was found to serve as a convenient and stable QRE in the electrolytes employed in the present work, possibly also represent-

ing a suitable QRE for a range of other electrolyte solutions. Through the electrochemical investigation of YP17/PTFE in EDLC electrolytes consisting of $1\,M$ Et_4NBF_4 in AN and in PC, it was found that the AN-based electrolyte has a significantly higher performance than the PC-based electrolyte in terms of transient response, particularly due to the higher pore conductivity (EDR) of the former, suggesting that the solvent molecules actively participate in the migration and diffusion processes of the electrolyte within micropores.

From the cyclic voltammetric study of YP17/PTFE in the AN- and the PC-based electrolytes, reversible differential capacitances between $72\,F\,g^{-1}$ and $147\,F\,g^{-1}$ were found for the single electrodes depending on the electrode potential. No catastrophic performance loss of the full cells was evident during the first few cycles and successive voltage window opening up to even $4\,V$. At the initial and slowest sweep rate, $1\,mV\,s^{-1}$, a first irreversible charge consumption occurred just below $3.8\,V$ and $4\,V$ for the AN- and PC-based electrolytes, respectively. From the potential excursions of the single electrodes measured in these experiments and comparison with the corresponding three-electrode CVs, it may be concluded that both the negative and the positive electrode contribute to the observed irreversible charge losses at $3.8\,V$ in the AN-based electrolyte, while for the PC-based electrolyte predominantly the negative electrode was found to be involved in irreversible charge consumption.

Chapter 10.

Electrochemical doping of SWCNTs and YP17 in EDLCs

10.1. Motivation

EDLCs based on activated carbon electrodes and non-aqueous electrolytes rely on the charging of the electrochemical double layer for energy storage and its fast charge and discharge for high power capability (Chapter 3). Upon charging, the injection of electrons or holes into the electronic band structure of the electrodes is compensated on the electrolyte side by the accumulation of the corresponding counterions within the electrochemical double layer. Ideally, no electron transfer occurs across the electrode/electrolyte interface, which implies that charge storage is exclusively electrostatic and only takes place within the electrochemical double layer.

Thus, the charging of an EDLC essentially corresponds to a simultaneous electrochemical doping of the negative and the positive electrode. Considering that the activated carbon electrodes consist of an sp^2 hybridized, π electron conducting carbon framework (Chapter 4), two different solid-state phenomena are expected to occur upon doping:

- the injection of charge leads to a change in the number of mobile electronic charge carriers, and

- this change in electron density results in a variation of the $C-C$ bond length.

Both of these effects are of considerable fundamental and practical interest for EDLCs since the number of mobile electronic charge carriers directly affects the space charge capacitance of the carbon electrode, which is considered to be the overall limiting capacitance for the entire

EDLC (Section 3.3.2). Also, cyclic dimensional changes undergone by the activated carbon electrodes during charge/discharge processes have been suggested to be a possible fatigue mechanism which contributes to electrode aging in EDLCs (Section 5.2.2). Ideally, both charge transfer and bond length changes should be fully reversible in order to enable efficient charge storage and avoid aging of the electrode material in EDLCs.

While the macroscopic expansion of carbonaceous electrodes will be treated in more detail in Chapter 11, the present chapter aims to elucidate the effects of electrostatic doping due to charge injection into the electrodes. In this context, Raman spectroscopy and conductivity measurements pose two attractive techniques for investigating both of the phenomena listed above. Since Raman scattering from carbons is always a resonant process [350] involving electronic transitions between the π (valence) and π^* (conduction) bands, the resonant Raman intensity depends on the position of the Fermi level within the DOS. Further, changes in bond length are expected to be accompanied by frequency shifts of Raman-active bands as the corresponding vibrational modes soften or stiffen [394].

Therefore, the electrochemical doping of carbonaceous electrodes in an EDLC electrolyte, $1\,M\,Et_4NBF_4$ in AN, was studied by in situ Raman microscopy (Section 8.5) and in situ resistance measurements (Section 8.8). Among the various types of microporous carbons investigated for use in EDLCs, SWCNTs (Section 6.1.4) are probably the most well-defined and have been studied in terms of doping behavior both theoretically [366, 395, 396] and experimentally [397]. Thus, SWCNTs can be considered a convenient model system in which the effects of electrochemical doping in EDLC electrolytes may be studied.

In the following sections, a comparison of the electrochemical doping behavior of SWCNTs and YP17 in $1\,M\,Et_4NBF_4/AN$ is given. The electrochemical performance of these two materials is compared in Section 10.2, followed by a presentation of the in situ Raman spectroscopy results in Section 10.3. Finally, Section 10.4 compares the in situ resistance measurements of the two materials. The findings of this chapter are summarized in Section 10.5.

10.2. Comparison of electrochemical performance

10.2.1. Background

In the following, the electrochemical performance of SWCNTs in $1\,M$ Et_4NBF_4/AN is compared to that of YP17/PTFE. Prior to studying the electrochemical doping of SWCNTs as a model system in more detail using in situ techniques, it should first be verified that the corresponding electrochemical behavior is essentially capacitive and similar to that of classical EDLC electrodes. Further, it is worth noting that SWCNTs have been proposed as a promising technical electrode material in EDLCs by many groups [176, 398–404], mainly due to the following arguments:

- a large fraction of the surface area is expected to be easily accessible to the electrolyte,

- the specific power should be higher than for conventional activated carbons, and

- the carbon atoms of SWCNTs should be less electrochemically active than in activated carbon.

In view of the materials characterization presented in Chapter 9, the first point should be viewed critically as the accessible surface area of SWCNTs depends on the extent of bundling and whether or not the interstitial porosity within bundles is accessible to the electrolyte.

The second point is based on the premise of parallel pathways of electronic conductance along the nanotubes and ionic conductance along the pores of low tortuosity between the nanotubes. In comparison, the intertwined network of solid phase and porosity in YP17 is essentially isotropic and results in a high tortuosity on the nanometer scale.

The third argument in favor of SWCNTs for EDLCs is based on the notion that the surface in contact with the electrolyte solution has predominantly graphene basal plane character, thus being less electrochemically active than carbons containing a significant fraction of edge plane sites [405]. Hence, it might be anticipated that using SWCNTs instead of activated carbon will provide fewer active sites due to the low concentration of tube ends when compared to the concentrations

of sites with edge plane character in activated carbons, thus potentially reducing the rate of electrolyte degradation for SWCNT-based EDLCs at high voltages.

However, the demonstration of the above advantages of SWCNTs compared to activated carbon as electrode material based on a direct comparison has yet to be presented for a commercial device. In the following, the suitability of SWCNTs both as a model system for the investigation of electrochemical doping in EDLCs and as a potential technical electrode material for commercial EDLCs will be evaluated on the basis of cyclic voltammetry and impedance spectroscopy.

10.2.2. Results

The three-electrode CVs of YP17/PTFE and SWCNTs in $1\,M\,Et_4NBF_4$ in AN are presented in Figure 10.1. Both materials exhibited high gravimetric capacitances as expected from the large specific surface areas. For YP17/PTFE, the capacitance is normalized to the active mass alone (i.e. excluding 10 wt% due to the PTFE binder), while the capacitance is normalized to the entire electrode mass for the SWCNTs.

From Figure 10.1, it is clear that the gravimetric capacitance of the YP17/PTFE electrode is higher than that of the SWCNT electrode in
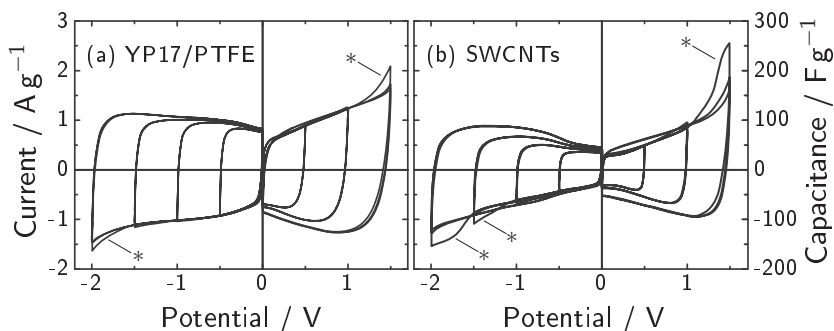
Figure 10.1.: Three-electrode CVs of (a) YP17/PTFE and (b) a SWCNT mat in $1\,M\,Et_4NBF_4$ in AN at a sweep rate of $10\,mV\,s^{-1}$ during potential window opening. Three cycles were performed in each potential window, the first cycles for certain potential windows being marked with an asterisk (∗). The negative and positive potential ranges were investigated in separate experiments.

both the negative and positive potential ranges, particularly at low polarizations. As was already observed in the systematic electrochemical characterization of YP17 in Section 9.2.6, the gravimetric capacitance tends to be lower at electrode potentials near 0 V. This effect appears to be particularly pronounced for SWCNTs (Figure 10.1b).

Some irreversible charge loss was observed for both materials during the first cycle of certain potential windows, which in a first approximation can be associated with the reduction and oxidation of impurities on the electrodes or in the electrolyte.

The CVs measured in symmetric two-electrode configurations are plotted in Figure 10.2. For both materials, the capacitance of the full cell was lowest in the discharged state, thus reflecting the behavior of the single electrodes. The full cell gravimetric capacitances based on the total active mass of both electrodes varied between 9 and $32\,\mathrm{F\,g^{-1}}$ for YP17/PTFE and between 7 and $20\,\mathrm{F\,g^{-1}}$ for the SWCNT cell during charging from 0 to 2.5 V.

Electrochemical impedance spectra were collected from the same full cells and are presented in the Nyquist plot in Figure 10.3. The impedance spectra of both materials display the expected shape for double layer charging of porous electrodes (Sections 3.5 and 7.5), consisting of a high frequency region with a slope close to $45\,^\circ$ and a low frequency region in which an ideal capacitive behavior is approached. The crossover between these two domains occurred at 5 Hz for the SWCNT cell
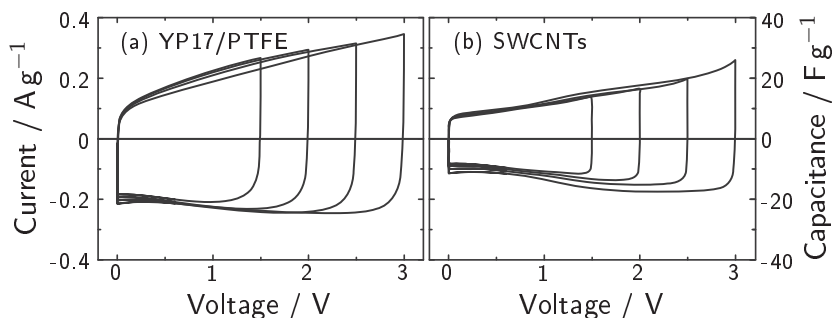
Figure 10.2.: Two-electrode CVs of (a) YP17/PTFE and (b) a SWCNT mat in 1 M Et$_4$NBF$_4$ in AN at a sweep rate of $10\,\mathrm{mV\,s^{-1}}$ during voltage window opening. Only the fifth cycle is shown for each voltage window.

and at 1 Hz for the YP17/PTFE cell, respectively. At high frequencies, an indication of a small semi-circle in the Nyquist plot was seen for the YP17/PTFE cell (Figure 10.3b), which is tentatively attributed to a higher contact resistance (Section 7.5) between electrode and current collector for YP17/PTFE when compared to the SWCNT mat.

The frequency dependent capacitance of both materials is plotted in Figure 10.4. In the high-frequency limit, virtually no capacitance is obtained due to charging of the external surface area only. At progressively lower frequencies, charging of the internal electrode porosity occurs. While the capacitance of YP17/PTFE is clearly superior at low frequencies, the SWCNT cell exhibits higher values at frequencies above ca. 2 Hz.
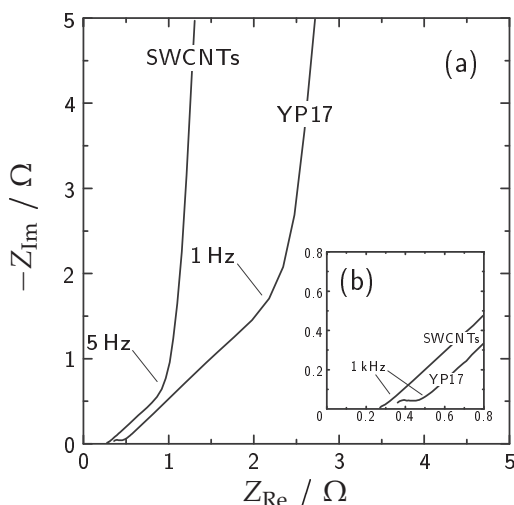
Figure 10.3.: (a) Nyquist plot of the electrochemical impedance of YP17/PTFE and SWCNT full cells at 0 V. The inset (b) shows an enlarged view of the high frequency region. Each measurement was performed on a symmetric electrode pair with a thickness of 140 μm per electrode in the frequency range between 100 kHz and 10 mHz. The geometric area of the electrodes was 0.785 cm^2 in both cases and the total electrode masses were 12.7 mg for the SWCNTs and 13.9 mg for YP17/PTFE (including binder). A paper separator of 25 μm thickness was used in both cases.
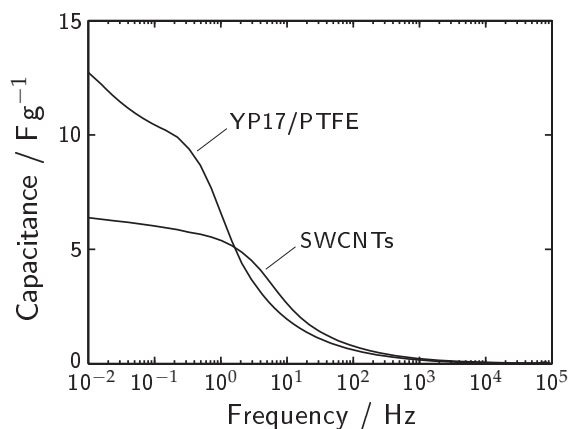
Figure 10.4.: Bode plot of the same cells as in Figure 10.3.

10.2.3. Discussion

The SWCNTs studied in the present work exhibited similar capacitive charging behavior to YP17 during cyclic voltammetry (Figures 10.1 and 10.2), whereby the gravimetric capacitance of the SWCNTs is clearly lower than that of YP17 at low levels of charging.

From EIS of the full cells at $0\,\mathrm{V}$ prior to any electrochemical cycling (Figure 10.3), the capacitance $(-2\pi f\, Z_{\mathrm{Im}})^{-1}$ was determined to be $25.5\,\mathrm{F\,g^{-1}}$ (SWCNTs) and $57\,\mathrm{F\,g^{-1}}$ (YP17) on the single electrode level at a frequency f of $10\,\mathrm{mHz}$. Normalizing these gravimetric capacitances to the respective total NLDFT surface areas (Table 9.5) results in specific capacitances of $2.6\,\mathrm{\mu F\,cm^{-2}}$ for the SWCNTs and $3.3\,\mathrm{\mu F\,cm^{-2}}$ for YP17, which agrees well with previously measured values for the basal plane of graphite [66, 393] and for activated carbon [108]. The slightly higher specific capacitance of YP17 probably arises from a higher concentration of graphene edges and other defects in this material, both of which contribute to a higher DOS. Further, regardless of defects, the space charge capacitance limitation is expected to be more pronounced in SWCNTs due to the presence of semi-conducting SWCNTs, as will be discussed in more detail in the context of the in situ Raman spectroscopy study presented in Section 10.3.

The Nyquist plots of YP17 and the SWCNTs (Figure 10.3) differ notably in the high frequency region with $45\,^\circ$ slope which can be at-

tributed to the electrolyte resistance within pores (the EDR). The EDR of the SWCNT cell is only 40 % of the corresponding value of the YP17/PTFE cell at equal electrode thicknesses and similar densities (about $0.6 \, \mathrm{g \, cm^{-3}}$ for both electrode types). Also, the frequency at which the impedance response approaches that of an ideal capacitor is 5 Hz for the SWCNT cell and 1 Hz for the YP17/PTFE cell, indicating a shorter characteristic time constant for SWCNTs compared to YP17.

According to the discussions in Sections 3.5 and 7.5, the observed differences in the impedance behavior imply both a higher electrolyte conductivity within pores and a larger effective pore diameter of the SWCNT electrodes compared to YP17/PTFE. This result suggests that the porous structure of the SWCNT mat is more suitable for fast electrolyte transport, which may be attributed to the pronounced mesoporosity of this electrode with respect to YP17 and the associated readily accessible volume between SWCNT bundles, while for YP17 the significant tortuosity on the micropore scale presents a greater hindrance for the migration and diffusion of ions.

Thus, in comparison to YP17/PTFE, electrodes of equal thickness exhibit a higher power capability when using SWCNTs even without the need for a parallel alignment of bundles [177, 406] or direct growth on current collectors. However, due to the higher gravimetric capacitance of YP17 compared to the SWCNTs used in this work, thinner electrodes of equal capacitance may be obtained with the former, thus resulting in similar power density and characteristic time constant, respectively.

Finally, the practical relevance of SWCNTs as a potential electrode material in commercial EDLCs is addressed. In terms of accessible surface area, no advantage may be identified for SWCNTs over conventional activated carbons, as the theoretical specific surface area of a lone SWCNT with capped ends ($1315 \, \mathrm{m^2 \, g^{-1}}$) is less than that of YP17, for instance (Table 9.5). Further, the bundling of SWCNTs reduces the effective surface area measured by gas adsorption. Thus, the question immediately arises whether double layer formation occurs only on the external bundle surface or also within the bundles. For instance, Stoll et al. [407] studied SWCNTs in seven different aqueous electrolytes and obtained single electrode capacitances of 31–$39 \, \mathrm{F \, g^{-1}}$. From this, these authors inferred that only the external surface area of

bundles was used for charge storage. Similarly, Barisci et al. [408, 409] concluded for several aqueous and non-aqueous electrolytes that no ion insertion into the interstitial porosity between SWCNTs within bundles takes place upon electrochemical charging, with the possible exception of Li^+ insertion when using $1\,M\;LiClO_4/AN$ as the electrolyte. On the other hand, electrolyte insertion into SWCNT bundles was reported by Sumanasekera et al. [410] ($18\,M\;H_2SO_4$) and Claye et al. [411] ($1\,M\;KCN$ in Et_4B/tetrahydrofuran or $1\,M\;LiPF_6$ in ethylene carbonate/dimethyl carbonate). In the present work, the specific capacitance prior to any electrochemical polarization was found to be $2.6\,\mu F\,cm^{-2}$, which appears to agree with a utilization of the external bundle surface area only. However, evidence for a change in the effective interfacial area as a function of electrode potential will be presented in Chapter 11.

The full cell capacitance of $20\,F\,g^{-1}$ at $2.5\,V$ obtained for SWCNTs in the present work compares well with the full cell capacitance reported by Futaba et al. for SWCNTs grown using a water-assisted CVD process [177, 406], which was also $20\,F\,g^{-1}$ in the voltage range 0–$2.5\,V$ using $1\,M\;Et_4NBF_4$ in PC as electrolyte. It should be emphasized that a wide range of gravimetric capacitances has been reported for SWCNTs in different electrolytes in the past. Experiments using $LiClO_4$ in AN or in PC resulted in single electrode capacitances between $12\,F\,g^{-1}$ [412] and $45\,F\,g^{-1}$ [176]. Results from experiments in KOH include single electrode capacitances between $20\,F\,g^{-1}$ [412] and $180\,F\,g^{-1}$ [400]. Possible reasons for the wide spread in reported specific capacitance values include differences in the SWCNT defect concentration, purity and bundle size, the investigated potential window, the type of electrolyte and the charge/discharge rate.

Regarding the higher power capability predicted for SWCNTs compared to activated carbon, a lower resistance and thus higher specific power of SWCNTs compared to YP17 was indeed observed in the frequency range studied in the present work via EIS. However, as discussed above, normalizing the resistance to the capacitance results in approximately equal values for SWCNTs and YP17, implying that electrodes with equal performance per unit mass may be readily obtained simply by varying the electrode thickness. Therefore, no practical ad-

vantage in terms of power capability may be ascribed to the SWCNTs studied in the present work.

The third argument concerning an improved electrolyte stability with SWCNTs as electrode material could not be verified in this work. From the three-electrode cycling experiments (Figure 10.1), higher irreversible charge losses were observed for SWCNTs compared to YP17 within a given potential window. Therefore, from the limited investigations performed in this respect, no enhanced electrolyte stability when using SWCNT electrodes could be attested. Regarding the amount of metallic impurities remaining in the SWCNT sample (see Table 9.1), however, it is fair to state that this particular sample may not be optimized in terms of electrochemical inertness, and that definitive conclusions regarding the electrochemical stability of SWCNT-based EDLCs may not be drawn at present.

To summarize the discussion regarding the practical relevance of SWCNTs as EDLC electrodes, it should be pointed out that the published values for specific capacitance, energy and power of SWCNTs are at best similar to those of activated carbons currently employed in EDLCs. Also, on the basis of the above investigations, no intrinsic practical advantage of the SWCNTs currently available on a commercial basis over conventional activated carbons such YP17 can be identified at present, and the widespread claims stating otherwise should be critically examined. Nonetheless, as the dominant charge storage mechanism appears to be strictly electrostatic and thus similar to that of activated carbons in EDLCs, a significant value may be attributed to SWCNTs for fundamental studies related to EDLCs, as will be shown in the next sections and in Chapter 11.

10.3. In situ Raman microscopy

10.3.1. Electrochemical doping of SWCNTs

Background

The effect of electron and hole injection on the Raman spectrum of SWCNTs was first reported by Rao et al. [413] in the context of chemical vapor-phase doping. The electrochemical doping of SWCNTs studied

by in situ Raman spectroscopy was described later in several studies employing aqueous [407, 410, 414–421] and non-aqueous [364, 411, 422–426] electrolyte solutions. A review of the spectroelectrochemistry of carbon nanostructures, including SWCNTs, has been given by Kavan and Dunsch [397].

Earlier work on the doping of sp^2 hybridized, π electron conducting carbon established that C$-$C bonds contract upon hole injection and dilate upon electron injection [394, 427–429]. In their work on GICs, Chan et al. [394] demonstrated that the combination of charge transfer and bond length change leads to a stiffening of the E_{2g} mode in the case of hole injection and a softening of this mode upon electron injection, causing respective blueshifts (upshifts) and redshifts (downshifts) of the G band in the Raman spectrum.

Later, in situ Raman studies [364, 407, 410, 414, 416–418, 420, 422–424] confirmed that hole doping also leads to upshifts of the main G band frequency in electrochemically doped SWCNTs, indicating a contraction of C$-$C bonds in agreement with the expectations. The upshift of Raman bands has even been suggested to be a direct measure of charge transfer to the SWCNT electrode [407, 410, 420]. However, upon electron doping of SWCNTs, this framework of discussion seems to be inadequate. Although the expected downshift of the G band upon electron doping has been reported in some studies [411, 414, 422], other experiments report upshifts [364, 417, 423], no shifts [417, 418] and even non-monotonous shifts of varying sign [364, 411, 430] as a function of doping level. This sensitivity of the doping-induced Raman band shifts on the experimental conditions implies that the bond length change arguments established for GICs are not sufficient for explaining the observed behavior of SWCNTs upon doping.

In recent years, important advances have been made towards understanding the Raman band shifts of SWCNTs upon doping. Lazzeri and Mauri [431] extended the semi-empirical approach of Pietronero and Strässler [427] for the description of GICs to include non-adiabatic effects, notably Kohn anomalies, in order to describe the G band shift of a single graphene sheet upon doping. In doing so, it was found that G band upshifts for both hole *and* electron doping are expected, with electron doping levels in excess of ca. $3.5 \cdot 10^{13}$ e per cm^{-2} then

leading to a subsequent downshift of the G band [431]. Das et al. [363] have recently provided experimental evidence for these trends in doped graphene and have also shown [366] that upshifts of the main G band feature occur in metallic and semi-conducting SWCNTs upon doping as well.

In a different approach, Margine et al. [396] showed that the specific chirality of a SWCNT is critical in predicting bond length changes upon doping, as the conduction band may have bonding or anti-bonding character depending on the orientation of the bonds with respect to the nanotube axis. Anisotropies in SWCNT bond length changes depending on chirality and doping level have also been discussed by Gartstein et al. [395].

Thus, the observed shift of the G band, which in SWCNTs is a multi-peak feature reflecting $C-C$ bonds with different orientations, depends on the phonon mode which causes the G band feature, the chirality of the SWCNTs which are selectively sampled by the resonance Raman experiment and finally on the actual doping level itself.

From the above discussion, it can be stated that the G band shifts in SWCNTs are related to charge transfer and bond length changes in a subtle manner which may vary considerably depending on the experimental conditions. However, other information may also be extracted from the Raman spectrum of SWCNTs. The RBMs at low Raman shifts are directly related to the SWCNT diameter and immediate environment [166, 170].

Further, a sensitive response to the doping level is also exhibited by the Raman intensity. Since, for SWCNTs, the high experimental Raman intensity arises due to resonance enhancement via electronic transitions, the immediate cause for the loss of Raman intensity is attributed to the bleaching of vHs upon both electron and hole doping [397]. In other words, the Raman intensity is indicative of the position of the Fermi level within the DOS and the corresponding changes in electron transition probability during doping.

The above concepts will be applied to the in situ Raman spectroscopy results obtained in the present work, which are presented in the following.

Results

Selected features of the in situ Raman spectrum of a SWCNT mat are shown in Figure 10.5. Upon wetting of the SWCNTs with the electrolyte solution (1 M Et_4NBF_4 in AN), no modifications in the Raman features were noticed apart from slight changes in the relative intensities of the Raman bands. The four most prominent RBMs, which depend strongly on the nanotube diameter, were found at $198\,cm^{-1}$, $221\,cm^{-1}$, $260\,cm^{-1}$ and $286\,cm^{-1}$ and labeled 1–4 as indicated in Figure 10.5. The D band was located at $1312\,cm^{-1}$ while the G^- and G^+ features were detected at $1555\,cm^{-1}$ and $1592\,cm^{-1}$, respectively.

The vibrational modes which give rise to the RBM and G band features are also indicated in Figure 10.5, whereby the RBM bands result from the breathing motion of SWCNTs in the radial direction while the G^- and G^+ bands arise due to in-plane vibrations with components parallel and perpendicular to the SWCNT axis. According to the study of optical phonons in SWCNTs by Piscanec et al. [432], the G^- and G^+ bands are attributable to the TO and LO mode, respectively, for
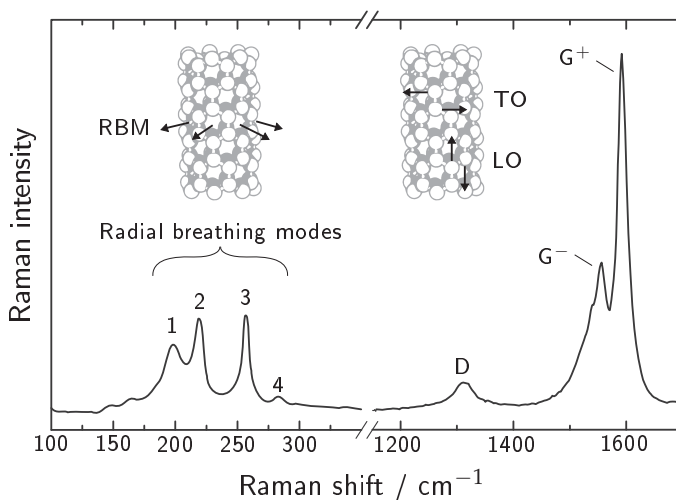
Figure 10.5.: Raman spectrum of the SWCNT mat prior to electrochemical doping. The vibrational modes relevant for the most pronounced features are the radial breathing mode (RBM) as well as the longitudinal optical (LO) and transverse optical (TO) modes.

semi-conducting SWCNTs. However, due to a strong electron–phonon coupling of the LO mode in metallic SWCNTs, this vibration is significantly softened and the associated band strongly downshifted [432]. Thus, in metallic SWCNTs, the assignment of the G band features is the opposite of semi-conducting SWCNTs.

The dependence of the RBM frequency ω_{RBM} (in cm^{-1}) on the diameter d_t (in nm) of the SWCNT is often expressed in terms of the general equation [166, 170]:

$$\omega_{RBM} = \frac{A}{d_t} + B \qquad (10.1)$$

where A (in $nm\,cm^{-1}$) and B (in cm^{-1}) are experimentally determined parameters which vary depending on the nanotube environment. For debundled HiPco SWCNTs dispersed in an aqueous solution using the surfactant sodium dodecyl sulfate (SDS), (A, B) pairs of (214.4, 18.7) [433], (223, 10) [172], (218, 17) [172] and (223.5, 12.5) [434] have been reported. For SWCNT bundles in air, (234, 10) [166, 170] has been given.

Regardless which of the above values is used, tube diameters of 1.2, 1.1, 0.9 and 0.8 nm may be allocated to the RBM bands 1–4 in the present work, respectively, accurate to within 0.1 nm. Both theoretical [170] and experimental [175] Kataura plots indicate that the bands 1 and 2 are thus resonantly enhanced via the E_{11}^M transition and are assigned to metallic SWCNTs, while bands 3 and 4 arise due to E_{22}^S transitions of semi-conducting SWCNTs. This RBM band assignment is summarized in Table 10.1.

In certain cases, an assignment of specific (n, m) indices is possible by comparing the RBM band positions with tabulated values [172, 397, 425,

Table 10.1.: Assignment of RBM bands in the Raman spectra of SWCNTs in the present work using a laser energy of 1.96 eV.

Band label	Tube diameter / nm	Resonant electronic transition
1	1.2 ± 0.1	E_{11}^M
2	1.1 ± 0.1	E_{11}^M
3	0.9 ± 0.1	E_{22}^S
4	0.8 ± 0.1	E_{22}^S

433–435]. However, in the present work, this specific assignment is not performed due to the uncertainty concerning the chemical environment of individual SWCNTs and extent of bundling during electrochemical charging, as will be shown later.

The positions and intensities of individual spectral features were quantified by approximating the band shapes using Lorentzian fits (Figure 10.6). The amplitude was chosen as a measure for the band intensity rather than the peak area since the former is less sensitive to discrepancies in the peak shape.

The four most prominent RBM features were fitted with one Lorentz function each while the G mode features could be approximated well by a total of three Lorentzians. Including a Breit-Wigner-Fano (BWF) feature to fit the G^- band did not change the position and intensity of the Lorentzian fit for the G^+ band notably, which was the primary G band feature of interest in this work. Also, since no significant BWF broadening of the G^- band was observed, as is usually the case when the resonance Raman scattering is dominated by metallic SWCNTs [166], the exclusively Lorentzian fitting may be deemed appropriate. Dur-
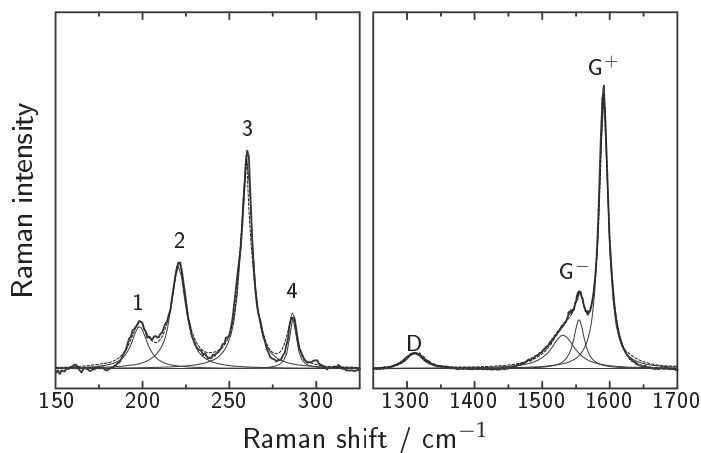
Figure 10.6.: Fitting of the most prominent Raman features of the SWCNT electrode with Lorentzian lineshapes. The baseline-corrected data is plotted in bold, while the individual Lorentzian fits are represented by thin solid lines and the sum of these fits is displayed as a dashed line.

ing electrochemical doping, it was found that the G^+ band experienced significant broadening, which worsened the quality of the fit but still reflected the changes in band position and amplitude well. A single Lorentzian was used to represent the D band, which is not strictly valid due to the fact that disorder-induced bands are caused by double resonance processes (Section 8.5) which result in inhomogeneous line broadening [166, 355]. Regarding variations in position and amplitude of the D band, however, the approximation was sufficiently accurate.

The cyclic voltammogram obtained during the in situ measurement is shown in Figure 10.7. Raman spectra were acquired every 60 s during cycling, whereby initially the RBM region was investigated during three anodic and three cathodic cycles, respectively, followed by the higher frequency region spanning the D and G bands during three subsequent anodic and cathodic cycles.

Following the first anodic cycle, the only change observed in the RBM region at 0 V was a drop in the intensities of the RBM bands (Figure 10.8). From the in situ Raman spectra (Figure 10.9), the Raman intensity decreased strongly upon both positive and negative polarization. Upon positive polarization, the positions of the RBM bands labeled 1 and 2 as well as the D and G^+ bands shifted towards higher
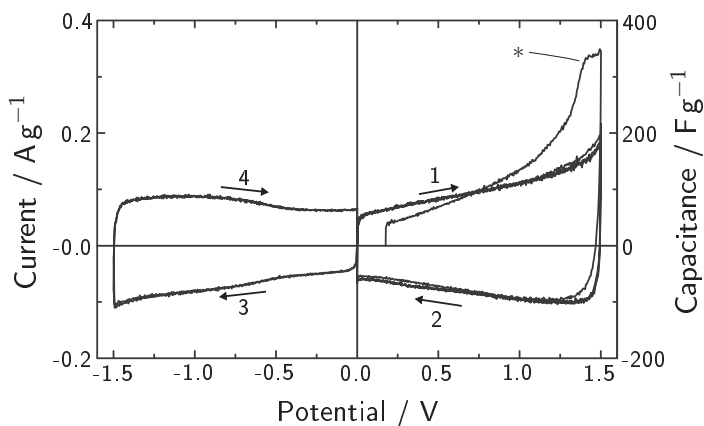
Figure 10.7.: CV of SWCNTs in 1 M Et_4NBF_4/AN at $1\,mV\,s^{-1}$ during the in situ Raman spectroscopy experiment. The numbers indicate the measurement sequence, while the first cycle is denoted by an asterisk (∗). The total electrode mass was 0.5 mg.

frequencies. Upon negative polarization, the RBM features 1 and 2 exhibited a similar behavior, while the D and G bands did not appear to undergo any significant shift upon doping. The changes were both reversible and reproducible within the investigated potential windows.

Through the Lorentzian fitting procedure (Figure 10.6), the band positions and intensities were evaluated as a function of the SWCNT electrode potential. For the RBM bands, the corresponding results are summarized in Figure 10.10. The bands 1 and 2, which were attributed to metallic SWCNTs, exhibited pronounced upshifts during doping regardless of the sign of the applied charge (Figure 10.10, top) and a significant intensity attenuation (Figure 10.10, bottom). The bands 3 and 4, which were allocated to semi-conducting SWCNTs, were not observed to shift markedly in position over a wide potential range. Also, the intensity profiles of these two bands featured plateaus instead of immediate attenuation as was the case for bands 1 and 2. For all of the bands, the intensity maximum was centered at an electrode potential close to -150 mV. The FWHM values of the intensity–potential profiles were found to be approximately 0.8 V (band 1), 1.2 V (band 2), 1.5 V (band 3) and 1.4 V (band 4).

The variation of the D and G^+ band positions and intensities with the electrode potential is plotted in Figure 10.11. The Raman shifts
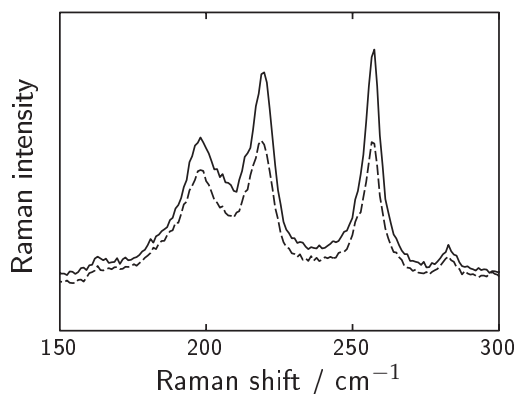
Figure 10.8.: RBM bands of the SWCNT electrode prior to electrochemical cycling (solid line) and following the first anodic cycle (dashed line) at 0 V.
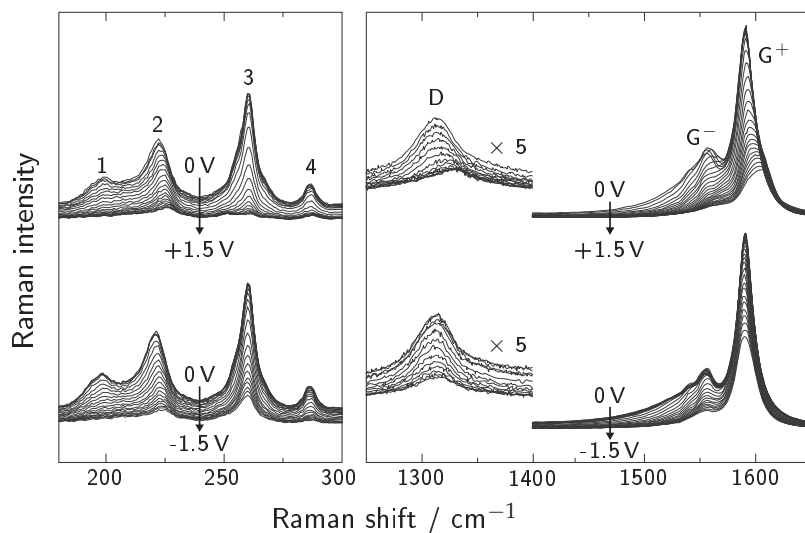
Figure 10.9.: In situ Raman spectra obtained during the forward scan of the third anodic and cathodic cycle of the CVs shown in Figure 10.7.

were displaced notably towards higher wavenumbers for both bands upon positive polarization, but varied significantly less during negative polarization. The band intensities, however, decreased similarly regardless of the sign of the applied potential. Upon positive polarization, the G^+ intensity displayed a kink close to +350 mV (Figure 10.11, bottom), above which the intensity attenuation occurred more rapidly. This potential matched the onset of significant upshifting of the G^+ band (Figure 10.11, top) in the positive potential range. Upon negative polarization, the G^+ band first exhibited a small downshift followed by an upshift of similar magnitude, resulting in no net displacement of the band at maximum negative charging. The D band exhibited similar behavior as that described above for the G^+ band, although both the band shift and the intensity attenuation occurred more smoothly and continuously during polarization.

Discussion

Before discussing the changes observed for the different Raman bands, it is important to emphasize that the acquisition of Raman spectra us-
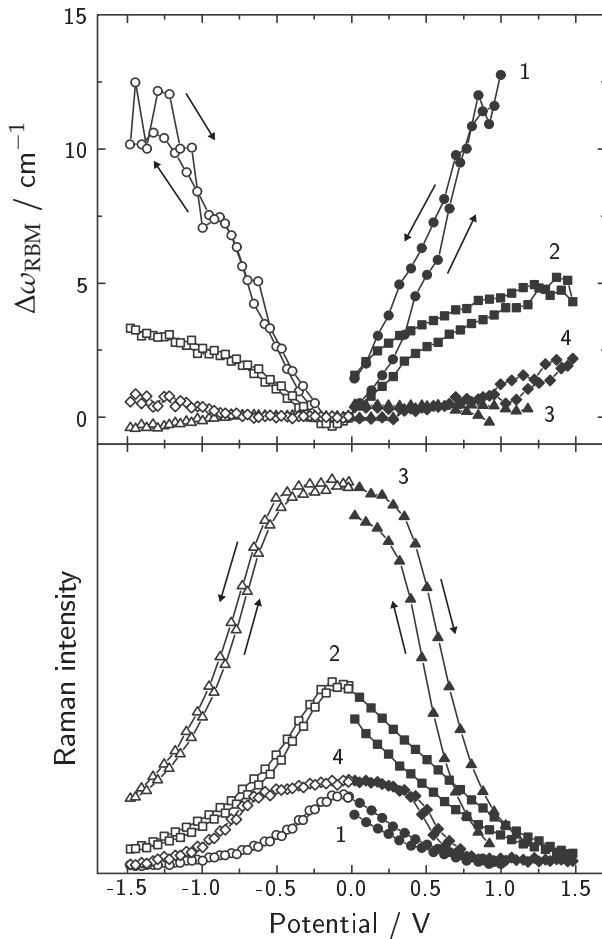
Figure 10.10.: Changes in band positions (top) and intensities (bottom) of the RBM features 1–4 during the third anodic and cathodic cycle shown in Figure 10.7. Filled symbols denote data obtained from positive polarization while open symbols represent data from negative polarization. Data points have been omitted where the Raman intensity became too weak to enable a satisfactory fitting.

ing a single laser wavelength selectively discriminates those SWCNTs in which the electronic transitions between the vHs are close to E_{laser}. This direct consequence of the resonance Raman effect is illustrated schematically for a metallic and a semi-conducting SWCNT in Figure 10.12. The energy scale is given against the half-filling energy ε_{hf}, which may be
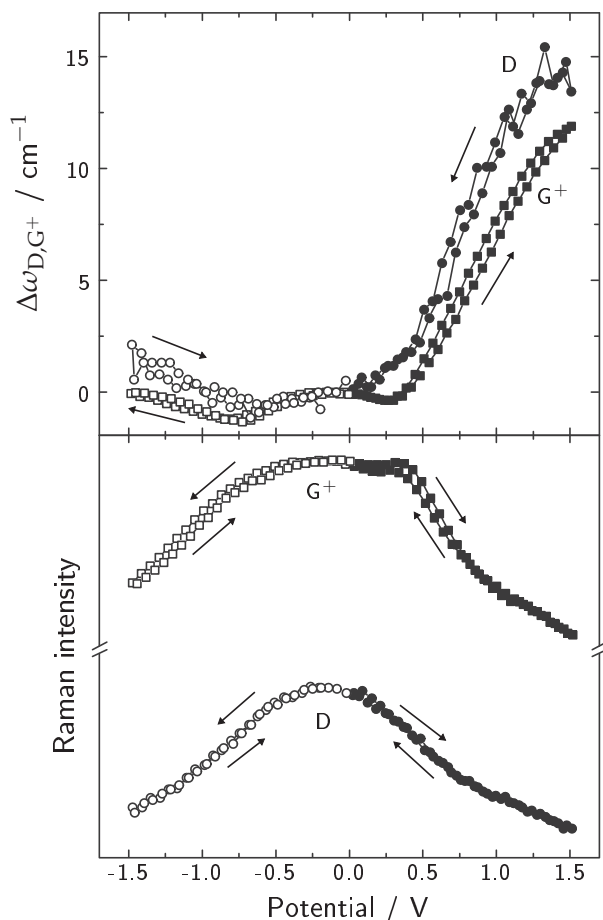
Figure 10.11.: Changes in the D and G^+ band positions (top) and intensities (bottom). Filled symbols denote data obtained from positive polarizations while open symbols represent data from negative polarization.

defined as the energy at which all π orbitals are filled and all π^* orbitals are empty, yielding exactly one occupied π orbital per C atom [436]. In the example given in Figure 10.12, the metallic and the semi-conducting SWCNT are in resonance with the exciting laser via the electronic transitions E_{11}^M and E_{22}^S, respectively. It is worth noting that a matching of the E_{11}^S transition of semi-conducting SWCNTs with the HeNe laser used in the current work would require tube diameters in the order

of 0.4 nm [166, 170], which is significantly less than the typical diameters present in SWCNT samples produced by the HiPco method [437]. Therefore, it is fair to assume that all semi-conducting SWCNTs sampled in the present Raman study were resonantly enhanced via the E_{22}^S transition.

Hence, despite the fact that HiPco SWCNT samples are known to consist of nanotubes with evenly distributed chiralities [433], a single laser wavelength probes the sub-population of SWCNTs which fulfills the resonance condition $E_{ii}^{M,S} = E_{\text{laser}}$. From the SWCNT diameters determined in Table 10.1 and comparison with theoretical and experimental Kataura plots [166, 170, 434, 435], it can therefore be concluded that the SWCNTs which contribute to the Raman spectra in the present work have interband transition energies of $E_{11}^M \approx E_{22}^S \approx 1.96 \pm 0.1$ eV due to the resonance condition [172]. From the same Kataura plots, the
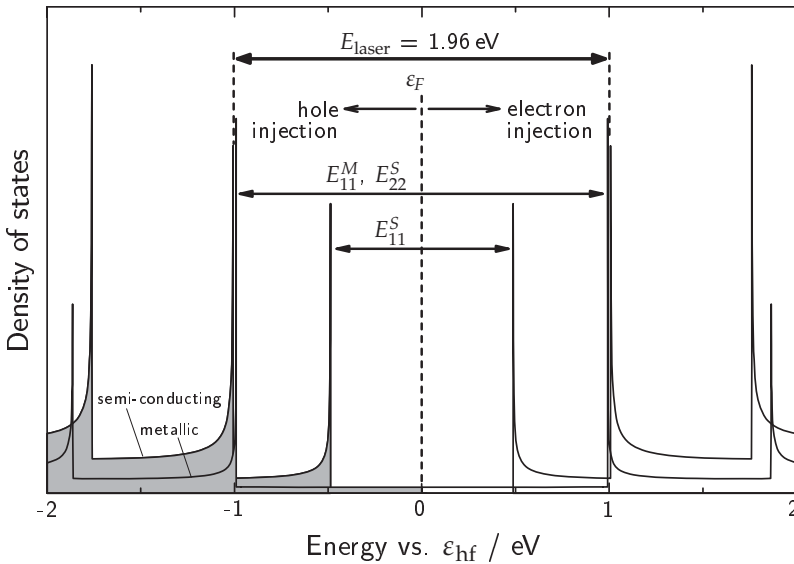
Figure 10.12.: Electronic DOS of the π and π^* bands of a metallic and a semi-conducting SWCNT. The Fermi level is denoted by ε_F while the half-filling energy is ε_{hf}. The occupied states are represented by the shaded areas under the DOS. E_{ii} is the energy spacing between the ith vHs on either side of ε_{hf} while the superscripts S and M denote whether this spacing belongs to a semi-conducting or a metallic SWCNT.

band gaps of the semi-conducting SWCNTs (RBM bands 3 and 4), E_{11}^S, can be estimated to be close to 1.1 ± 0.1 eV [166, 170, 172, 434].

Changes in RBM intensities

Upon electron and hole doping, the intensities of all RBM bands were found to drop in an ambipolar way (Figure 10.10). Such behavior has already been reported in the past [397] and is attributed to a decrease in the resonance Raman effect due to bleaching of electronic transitions as the Fermi level is shifted through the vHs in the DOS. The position of maximum intensity for all bands was found to lie close to -150 mV. Since the resonance Raman intensity is maximum when the Fermi level ε_F is equal to ε_{hf}, it may be concluded that this is the case at a potential of $E_{hf} = -150$ mV in the present investigation.

In order for bleaching of electronic transitions between vHs to occur, an injection of charge (either holes or electrons) into the SWCNT DOS is required. Electroneutrality requires that the corresponding ionic counter-charge is accumulated near the SWCNT surface. During electrochemical doping, this is achieved via a charging of the electrochemical double layer. In the past, the different bleaching responses for RBM peaks centered at different Raman shifts were associated with the different SWCNT diameters, and it was stated that larger SWCNTs (lower RBM frequencies) lose intensity more easily than smaller SWCNTs (higher RBM frequencies) due to a better accessibility of the larger interstitial porosity in bundles consisting of the former [424]. Larger pores were thought to offer easier access to the dopant species and thus facilitate charge injection into the SWCNT DOS. However, this concept has since been challenged and revised with arguments based solely upon the rigid band model, in which ε_F is equilibrated throughout the electrode and shifted through the DOS during doping [425, 438]. Since the vHs in larger SWCNTs are closer together than in smaller SWCNTs [166, 170], the resonance Raman intensities of the former tend to be attenuated more readily.

The attenuation of the RBM band intensities in the present investigation (Figure 10.10) was found to be markedly different for metallic and semi-conducting SWCNTs. It is therefore suggested that the shape of the DOS is of primary importance in explaining this observation. As

the metallic SWCNTs (bands 1 and 2) have a non-vanishing DOS, charge injection into the SWCNTs is achieved even at small ε_F shifts, causing a gradual loss of Raman intensity [416, 438]. For the semi-conducting SWCNTs (bands 3 and 4), charge injection only becomes possible when ε_F is shifted into the first vHs of the valence or the conduction band. According to the previous estimation of E_{11}^S, these vHs are situated at approximately $\pm 0.55\,\text{eV}$ with respect to ε_{hf}. The corresponding Raman intensities were observed to be attenuated at roughly $\pm 0.5\,\text{V}$ vs. E_{hf} and drop to half of their maximum value close to about $\pm 0.7\,\text{V}$ vs. E_{hf}, which appears to agree well with the expected positions of the vHs considering that a large fraction of the potential drop across the double layer occurs within the semi-conducting SWCNTs in form of a Fermi level shift due to the low DOS at potentials near E_{hf} [436].

In a recent study, Paolucci et al. [439] determined the redox potentials of different debundled SWCNTs in solution and found the energetic gap between the reduction and oxidation potential to be greater than the optical gap by up to 40 %. This was attributed to excitonic effects [440, 441] in SWCNTs, i.e. the Coulomb interaction between excited electrons and the corresponding holes, which effectively lowers the optical gap with respect to the electronic band gap. Strictly speaking, this implies that the resonance Raman intensity arises due to excitonic transitions and not interband electronic transitions as depicted in Figure 10.12. As the optical band gap is probed by the exciting laser energy and the electronic band gap determines the band filling (i.e. Raman intensity attenuation) during electrochemical doping, a comparison of the two allows an estimation of the exciton binding energy [439, 442–444]. In the present work, a quantitative determination of the electronic band gap is difficult due to the rather gradual attenuation of the Raman intensity (Figure 10.10). Yet, it is interesting to note that the FWHM values of the Raman intensity vs. potential curves in Figure 10.10 agree well with the corresponding electronic band gaps presented by Paolucci et al. for debundled SWCNTs [439].

It might be expected that the first vHs of the metallic or the second vHs of the semi-conducting SWCNTs at around $\pm 1\,\text{eV}$ vs. ε_{hf} could be reached in the present experiments. However, there appears to be no indication hereof in the RBM intensity profiles (Figure 10.10). Possibly,

the resonance Raman intensity is already reduced to such an extent that further changes are difficult to detect, or that the potential drop across the electrolyte side of the double layer becomes significant and thus renders the rigid band approximation less suitable [436].

Changes in RBM frequencies

Similar to the two types of RBM intensity behavior upon electrochemical charging, there appear to be two different ways in which the RBM peak positions change during polarization (Figure 10.10). For bands 1 and 2 (metallic SWCNTs), considerable upshifts were found upon both electron and hole doping. On the other hand, bands 3 and 4 (semi-conducting SWCNTs) did not exhibit any significant change in position over a wide potential range.

A stiffening of the radial breathing phonon modes may be due to two immediate causes, namely a collective stiffening of the C−C bonds or a change in the empirical constants A and B in Equation (10.1) during doping, the latter of which signifies a change in the chemical environment of the SWCNTs.

Further, it has been shown [172, 173] that tube–tube interactions within bundles cause a redshift of $E_{ii}^{M,S}$ (i.e. a decrease in the electronic transition energies between vHs) when compared to isolated nanotubes, regardless of metallic or semi-conducting character. Hence, a change in SWCNT environment can also lead to a modification in the $E_{ii}^{M,S}$ spacings. In fact, in going from bundled to debundled SWCNTs, the $E_{ii}^{M,S}$ spacings can increase by up to 0.2 eV [172, 173]. This increase in the transition energies is of importance as it may change the type of SWCNTs which are in resonance with the laser energy. More specifically, SWCNTs with smaller diameters (larger $E_{ii}^{M,S}$ transitions) than those previously in resonance will tend to move into resonance with the laser upon debundling. The fact that the same laser energy excites different diameter SWCNTs in bundled and debundled samples leads to an *apparent* upshift of the RBM band which may be in the order of 6–20 cm^{-1} [173], similar to the values observed in the present work. Actually, the possibility of shifting resonance windows might also explain why no evidence for the bleaching of E_{11}^M or E_{22}^S was found.

In the present work, it is suggested that the upshifts of RBM bands 1 and 2 are not primarily due to C−C bond stiffening as a consequence of charge injection, as the evolution of the D and G$^+$ bands do not support the notion of pronounced bond stiffening upon electron injection (Figure 10.11). Also, Margine et al. [396] have predicted that electron injection always leads to a dilatation in the off-axis bonds, which seems to contradict an upshift of RBM features in this doping regime. This conclusion stands in contrast to the work of Stoll et al. [407], who attributed the electrochemically induced upshift in RBM peak position to the stiffening of C−C bonds. However, due to the use of an aqueous electrolyte solution, these authors were limited to the region of positive polarization only and could not observe the behavior of the RBM bands upon electron doping.

Having excluded bond stiffening as the reason for the observed upshifts of the RBM features 1 and 2, cyclic changes in the chemical environment upon doping and undoping may be proposed as a viable explanation. Since the number of SWCNTs per bundle was estimated to be very low (only about six on average, Section 9.3), most SWCNTs may be considered to be in contact with the electrolyte solution. In addition, an infiltration of ions into interstitial porosity within bundles is possible, and evidence for this charging mechanism is presented in Chapter 11.

In any case, the accumulation of counter-ions within the electrochemical double layer upon SWCNT doping changes the environment of these SWCNTs, introducing electrostatic tube–electrolyte interactions which may be expected to be stronger than the weak tube–tube interactions. Such a modification would lead to an increase in the interaction parameter B in Equation (10.1) and a corresponding upshift of the RBM frequency. In addition, if the extent of SWCNT bundling is modified due to the insertion of ions into the interstitial porosity, the effect of blueshifting of $E_{ii}^{M,S}$ transitions could cause smaller SWCNTs to move into resonance, thus possibly contributing an additional *apparent* upshift of these RBM bands. The difference in the absolute values for the upshifts of bands 1 and 2 indicate that either the DOS is greater for the SWCNT associated with band 1 and/or the apparent upshift contribution is greater for this band.

The effect of double layer charging should be minimal at the pzc, which in this case may be set equal to E_{hf}. Hence, the above effects should be least pronounced at this potential, which is in agreement with the results obtained in the present work. It should be noted that a modification of the SWCNT environment has also been suggested by Kavan et al. [425] to explain upshifts of RBM bands in their in situ study on chirality-resolved SWCNTs. Further, Rafailov et al. [445, 446] have recently also proposed a partial debundling of SWCNTs using in situ Raman spectroscopy in aqueous electrochemical systems, describing this mechanism as intercalative doping. However, these authors observed a downshift of an RBM band, in apparent contradiction to the results of the present work and those reported by Kavan et al. [425]. It remains to be clarified whether this is solely due to different tube–electrolyte interactions or due to different mechanisms of electrochemical doping.

It is worth noting that Pénicaud et al. [447] have demonstrated a debundling of SWCNTs in solution after reduction with alkali metals. This technique was also used by Paolucci et al. [439] in their electrochemical study of HiPco SWCNTs. In those cases, debundling was achieved by generating a charged interface between SWCNTs and their environment. There is a strong analogy to the present work, in which electron doping (reduction) and hole doping (oxidation) both lead to charging of the electrode/electrolyte interface, thus indicating that varying degrees of bundling may be obtainable by this technique.

Comparing the RBM features before and after the first anodic cycle (Figure 10.8), a loss in intensity can be seen. The fact that this intensity drop is not uniform across the entire spectrum is an indication that a modification of the resonance enhancement of individual SWCNTs has taken place. Although no changes in the peak positions could be noticed, the modifications in peak intensities indicate changes in the positions of the vHs within the DOS, which could be attributed to the partial debundling effect discussed above.

Finally, the RBM bands 3 and 4 are addressed. These bands did not shift in position over a wide potential range (Figure 10.10), which may be attributed to the semi-conducting character of the SWCNTs associated with these bands. As discussed above in context of the RBM intensity variations, the semi-conducting SWCNTs can only be doped when

the Fermi level is shifted beyond the band gap, which was estimated to occur at ± 0.5 V vs. E_{hf}. Before reaching these potentials, no charge can be applied to the semi-conducting SWCNTs, and thus the electrostatic interaction between the SWCNTs and the surrounding electrolyte is not expected to change significantly. Even beyond these potentials, the total amount of charge applied to a semi-conducting SWCNT is expected to be less than for a metallic SWCNT at the same potential, which could explain the small upshift of band 4 compared to bands 1 and 2 (Figure 10.10).

It should be noted that the fitting of the RBM bands at high polarizations is complicated by the drastic reduction of the resonance Raman intensity (Figure 10.9). Thus, the data points obtained at the most extreme potentials for the semi-conducting SWCNTs are very sensitive to the fitting routine. This should be considered when comparing data from different sources.

Changes in D and G$^+$ band intensity

Following the arguments presented above for variations in the RBM band intensities, the intensity decrease of the D and G$^+$ bands (Figure 10.11) may also be attributed to a bleaching of the electronic transitions between vHs due to electron and hole injection, respectively, which leads to a decrease in the resonance Raman effect.

The loss of intensity is continuous for both bands except for the G$^+$ band in the positive potential range, where a kink close to +0.5 V vs. E_{hf} was observed. This potential coincides with the onset of intensity loss of the RBM bands 3 and 4 (Figure 10.10). Therefore, the abrupt loss of intensity for the G$^+$ feature could be due to bleaching of the E_{11}^S transition. However, a similar behavior of the G$^+$ band is not observed for electron injection, where the intensity loss is gradual and continuous. This asymmetry in the Raman intensity attenuation is not clear and requires further work.

On the other hand, the intensity of the D band is smoothly attenuated upon both hole and electron doping. Such behavior is expected when metallic SWCNTs make a significant contribution to the D band or if defects associated with the D band locally induce allowed electronic states within the band gap of semi-conducting SWCNTs.

Changes in D and G$^+$ band frequency

The changes in peak positions of the D and G$^+$ bands are qualitatively similar to one another and are characterized by strong upshifts of $15\,\mathrm{cm}^{-1}$ and $12\,\mathrm{cm}^{-1}$, respectively, in the positive potential range and only small variations in the negative potential range.

In contrast to the RBM frequencies, the frequency of the G$^+$ band is practically independent of the environment and thus insensitive towards changes in the SWCNT surroundings [173]. Shifts of the G$^+$ band position can therefore be related directly to charge transfer effects and changes in bond stiffness.

It is possible to relate the G$^+$ band shifts to the doping level (Figure 10.13) in order to compare the results obtained in the present work with published data from other sources. However, it should be noted that the change in the G$^+$ band is specific for those SWCNTs in resonance with E_{laser}, while the doping level is derived from the total amount of charge applied to the SWCNT electrode (i.e. the entire mixture of all metallic and semi-conducting SWCNTs). Due to the large distribution of $E_{\mathrm{ii}}^{M,S}$ transitions in such an electrode, electrochemical doping is achieved in a continuous manner. In the present experiments, the amount of charge applied to individual SWCNTs can therefore not easily be specified without a detailed knowledge of the chirality distribution and according DOS of all SWCNTs in the electrode.

Based on ab initio calculations, Das et al. [366] predicted G$^+$ band upshifts of $5\,\mathrm{cm}^{-1}$ for doping levels of ± 0.005 electrons per carbon atom. The G$^+$ band shifts observed in the present work are much lower at comparable doping levels, but the extent of doping of the semi-conducting SWCNTs in resonance with E_{laser} is expected to be only a small fraction of the overall doping level determined for the mixture of metallic and semi-conducting SWCNTs. In fact, doping of the semi-conducting SWCNTs was estimated to begin at around $\pm 0.5\,\mathrm{V}$ vs. E_{hf}, and the charge applied before reaching these potentials is therefore not strictly associated with the semi-conducting SWCNTs. The charge applied after exceeding these potentials contributes in part to the doping of the semi-conducting SWCNTs, and indeed upshifts of the G$^+$ band were observed when exceeding approximately $\pm 0.5\,\mathrm{V}$ vs. E_{hf} (Figure 10.13).
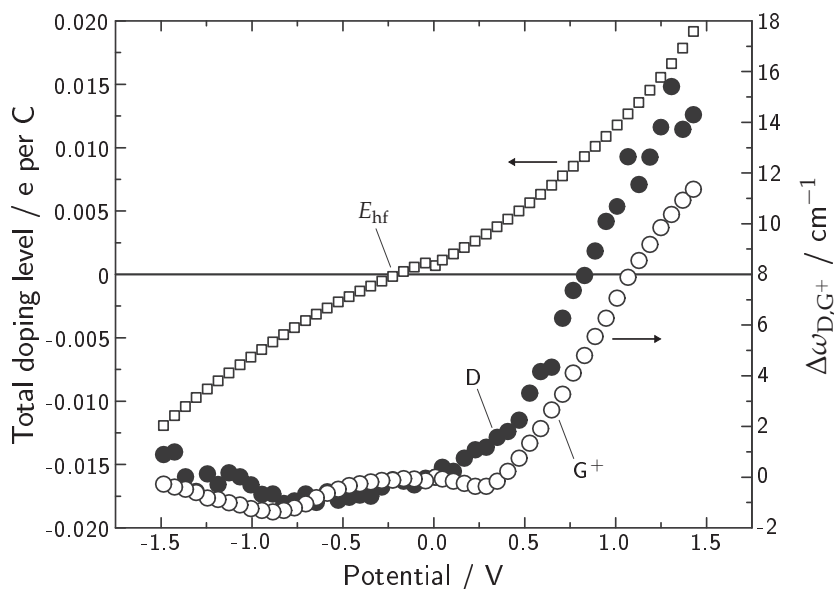
Figure 10.13.: Doping level ($\square$) and change in D band ($\bullet$) and G^+ band ($\circ$) positions of SWCNTs as a function of the electrode potential in $1\,M\;Et_4NBF_4/AN$.

The change of the G^+ band position within this potential interval is not well understood. A contribution from metallic SWCNTs can probably be excluded as the G^+ band of metallic SWCNTs has been assigned to the circumferential (TO) phonon mode (Figure 10.5) which is not predicted to change significantly in frequency upon doping [365, 366]. Kalbac et al. [364] have recently shown similar results in their in situ Raman investigation of electrochemically doped SWCNTs. In their work, the G^+ band was found to first downshift by a few cm^{-1} before upshifting considerably upon electron and hole doping. However, their Raman spectra were found to be dominated by metallic SWCNTs, for which the TO phonon mode (and hence the G^+ band) should not change in frequency upon doping as mentioned above. The authors concluded that the assignment of the TO phonon mode to the G^+ band in metallic SWCNTs and also the assignment of the LO phonon mode to the G^+ band in semi-conducting SWCNTs cannot account for the doping-induced changes of the G^+ band position. They attributed the initial

downshifts of the G^+ band position to the removal of a Kohn anomaly which occurs due to strong electron–phonon coupling in the undoped state and is predicted for the LO mode of metallic SWCNTs [365, 366]. However, the observation of initial downshifts of the G^+ band in the present work questions this interpretation, as Kohn anomalies do not occur in semi-conducting SWCNTs [365, 366, 432]. Further, the frequency minima of the LO mode of metallic SWCNTs during doping are expected to occur at doping levels close to ± 0.001 electrons per carbon atom [365], which is not in accord with the data from the present work.

The asymmetry of the G^+ band shifts upon electron and hole doping was also observed by Kalbac et al. [364]. As SWCNTs with different chiralities may exhibit different G^+ band shifts upon electron doping, possibly even with varying sign [395, 396], the net displacement of the G^+ band will depend on the contributions of each SWCNT in resonance with E_{laser}. However, according to the previous discussions, the determination of specific (n, m) indices is complicated by the fact that the extent of bundling and influence of the chemical environment is not precisely known in the present experiments. Also, these factors are likely to change during charging, which may even cause SWCNTs with different chiralities to contribute to the Raman spectra at different potentials. Further, it is not yet clear how the chemical and steric properties of the ions which balance the charge on the SWCNTs influence the phonon mode frequencies. Considering the host of arguments presented above, it appears that further studies are needed to fully understand the variation of the G^+ band position of both metallic and semi-conducting SWCNTs upon electrochemical doping.

Finally, it is noted that the position of the D band does not pass through distinct minima upon hole or electron doping (Figure 10.13). The upshift of the D band agrees qualitatively with the stiffening of the $C-C$ bonds which are associated with the G^+ band due to charge transfer. Also, no onset potential of abrupt band shifts are noticed. These findings are thus in line with the smooth attenuation of the D band intensity during doping, which implies that doping of the structural features associated with the D band is achieved continuously over the entire potential range investigated in this work.

10.3.2. Electrochemical doping of YP17

Background

Given the considerable efforts of various research groups towards improving the understanding of the electrochemical doping of SWCNTs using Raman spectroscopy, it is appealing to apply this technique to activated carbon in view of the apparent similarities in electrochemical charge storage of the two materials in EDLCs. At present, almost no reports concerning such investigations are available in the scientific literature.

Bonhomme et al. [448] used in situ Raman spectroscopy to study carbon cloth electrodes in 1 M Et_4NBF_4/PC. Their investigation focused on the electrolyte contribution to the Raman spectra, which allowed these authors to quantify bulk electrolyte concentrations in the macroscopic space between the positive and negative electrode during charging. Modifications of the D and G band positions, although mentioned, were not treated in detail. These parameters are pertinent to the doping of carbon electrodes and of primary interest in the present work.

Recently, Hardwick et al. [195] reported on the electrochemical doping of an activated carbon (Picactif from PICA, France) in 1 M Et_4NBF_4 in AN using the same experimental setup as in the present work. Shifts in the D and G band positions were tentatively explained by considering the activated carbon to be composed of nanocrystalline domains joined by cross-linking chains as in the Franklin model (Section 4.5). Although the validity of this structural model may be subject to doubt, the concept of distinct contributions of different structural domains to the Raman spectrum of activated carbon actually forms a suitable framework for the discussion of the results obtained in the present work, which are presented in the following.

Results

Electrochemical charging of YP17 in 1 M Et_4NBF_4/AN was achieved by cyclic voltammetry in various potentials windows (Figure 10.14). During the CVs, Raman spectra were collected approximately every 120 s from at least two different locations on the electrode separated by several tens of micrometers. The changes observed were found to be sim-

ilar for different points in all experiments. Separate experiments were performed in which YP17 was polarized to extreme negative or positive potentials during spectrum acquisition using a constant potential sweep rate of $1\,\mathrm{mV\,s^{-1}}$.

The variations in the Raman spectrum of YP17 during polarization were relatively modest and most noticeable in the extended potential range (Figure 10.15). Upon negative polarization, both the D and G bands weakened in intensity and broadened considerably, while the G band downshifted. The latter observation implies a softening of the E_{2g} phonon mode (i.e. bond lengthening) during electron injection. During positive polarization, a similar intensity weakening and band broadening occurred, while in this case the most pronounced shift was undergone by the D band towards higher frequencies, corresponding to a stiffening of the A_1' phonon mode (i.e. bond contraction) during hole injection. The G band position was relatively constant until potentials above ca. $1\,\mathrm{V}$ were reached, above which a slight upshift of this band was observed. However, as can be seen in Figure 10.15b, a drastic increase in the background intensity occurred at high positive poten-
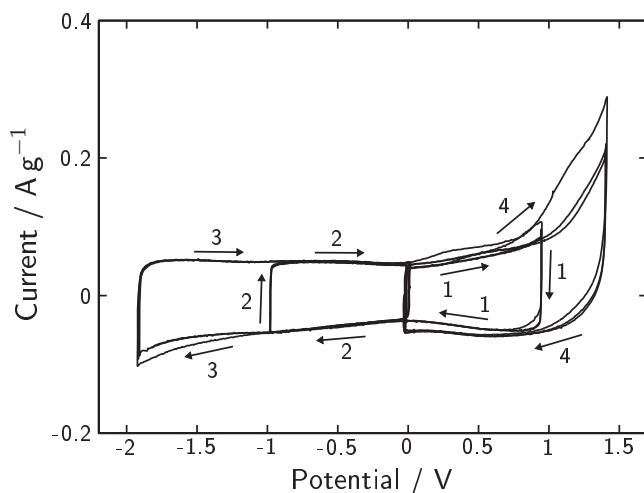
Figure 10.14.: CV of YP17 in $1\,\mathrm{M}$ Et$_4$NBF$_4$/AN during the in situ Raman measurement. The numbers indicate the measurement sequence, whereby three cycles were performed in each potential range. The sweep rate was $0.5\,\mathrm{mV\,s^{-1}}$.

tials which ultimately led to a saturation of the detector and prevented further resolution of the bands.

The total integrated Raman intensity in the spectral range of 1000–1800 cm^{-1} is plotted in Figure 10.16 for a wide potential range. The dramatic rise in intensity at potentials above about +1.3 V is evident from this plot. Also, an intensity maximum can be seen close to 0 V, similar to the results for the SWCNT Raman bands discussed in the previous section.

Quantification of the spectral changes was performed by evaluating the maximum intensities of the D and G bands and the corresponding frequencies after subtraction of a linear background. Further, the FWHM of each spectral feature was estimated by simply noting the
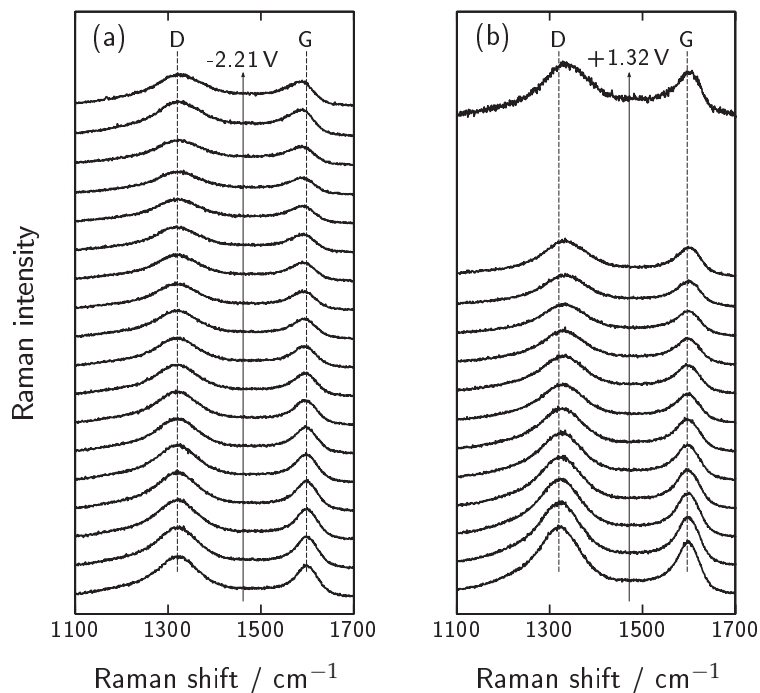
Figure 10.15.: In situ Raman spectra of YP17 in 1 M Et$_4$NBF$_4$/AN during excursions from 0 V to extreme negative (a) and positive (b) potentials. The spectra are offset along the y-axis for clarity, and the quoted values are single electrode potentials.
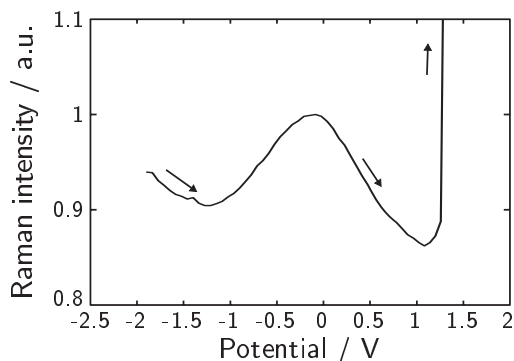
Figure 10.16.: Integrated Raman intensity of YP17 in $1\,M\,Et_4NBF_4/AN$ as a function of the electrode potential.

width of the raw data curve at half of the peak intensity (after background subtraction). No attempts were made to fit the spectra by multiple components [449, 450] which could arise from small polycyclic aromatic hydrocarbon clusters [357]. The corresponding changes in the D and G band parameters are summarized in Figure 10.17.

In the narrow potential range between -1 V and +1 V, the changes in band positions (Figure 10.17a and b, left) were very reversible. At +1 V, the D band upshifted by about $6\,cm^{-1}$ while no change in the G band position was noticed with respect to 0 V. At -1 V, the D band position remained invariant while the G band downshifted by $6\,cm^{-1}$. The ratio of the band amplitudes and FWHM (Figure 10.17c, left) were practically constant in this potential range, indicating that the broadening and intensity decrease occurred to the same extent for each band.

For the extended potential range between -2.3 V and +1.3 V, the D band shift in the positive range amounted to ca. $+16\,cm^{-1}$. Interestingly, an upshift of the D band was also observed below about -1.6 V, exhibiting a noticeable hysteresis during the back scan (Figure 10.17a, right). At -2.3 V, the total downshift of the G band was ca. $20\,cm^{-1}$. The ratio of the band FWHM remained constant over the entire potential range, while the D/G amplitude ratio appeared to drop slightly at high polarizations of either sign (Figure 10.17c, right).
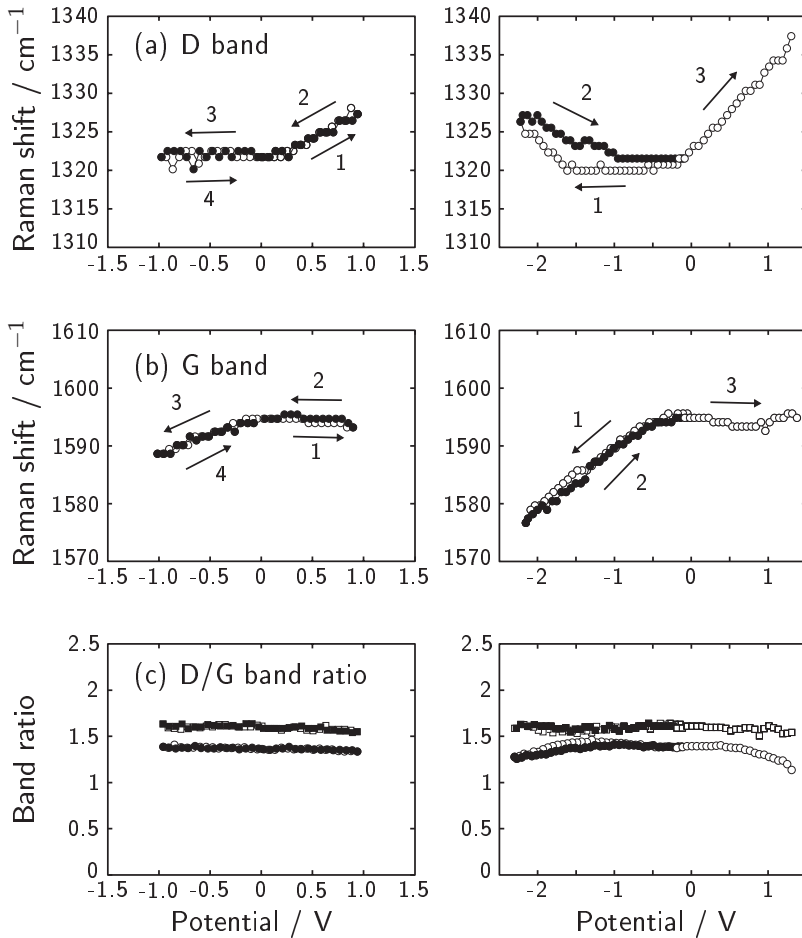
Figure 10.17.: Positions of the (a) D band and (b) G band of YP17 as a function of the electrode potential. In the narrow potential range (left), all data points were collected from the third anodic and cathodic cycles, respectively, while the first cycle was used for the extended potential windows (right). The measurement sequence is indicated by arrows, whereby open symbols denote potential sweeps away from 0 V and solid symbols represent the corresponding back scans. The corresponding D/G band intensity ratios are given in (c) with respect to both the amplitudes (○) and the FWHM (□).

Discussion

The fundamental differences between the spectral changes of YP17 during electrochemical doping and those of SWCNTs are intriguing, as they imply that no straightforward analogy can be made between the current theoretical understanding of electronic and vibrational properties of graphene or SWCNTs and those of activated carbon during doping. It should be noted that the results presented here are in excellent agreement with those reported by Bonhomme et al. [448] and Hardwick et al. [195], suggesting that the observed behavior could be representative for activated carbons in general.

Beginning the discussion by considering the changes in Raman intensity (Figure 10.16), two explanations may be brought forward to explain the nearly symmetric attenuation towards either side of 0 V. Bonhomme et al. [448] suggested that the increased conductivity of activated carbon during doping results in a decreased laser penetration depth and, thus, in a decreased intensity of the scattered light. Considering the resonance enhancement of the Raman signal, which was shown to dominate the intensity attenuation in the case of SWCNTs, a decrease in the Raman intensity of activated carbon during doping may also be attributed to the bleaching of $\pi \rightarrow \pi^*$ interband transitions. Since both mechanisms involve injection of charge into the DOS, they cannot be easily deconvoluted, and it is likely that both contribute to the observed intensity attenuation during doping.

An increase in the Raman intensity of YP17 was observed at the most extreme potentials (Figure 10.16), which was essentially due to an increase in the background scattering. An intense background signal is generally attributed to fluorescence [342]. Since, in this case, the background modification is potential-dependent, generation of fluorescent species at the extreme potentials could be a possible explanation for the observed intensity evolution. Particularly, in the positive range above ca. +1.3 V, the background intensity increased irreversibly and by more than one order of magnitude.

The FWHM of Raman bands serves as an indication for the spread in the corresponding phonon modes. Thus, the width of the G band is often taken as a measure of disorder [451], which in the absence of heteroatoms is given by varying bond lengths and edge sites. Similarly,

the width of the D band may be considered to represent the distribution of bond lengths in ring structures. The broadening of both bands during electrochemical doping (Figure 10.15) may thus be considered to represent an increased spread in the bond length distribution.

In order to understand this increasing disorder upon doping, it is useful to briefly address the electronic properties of activated carbon. The structure of amorphous and activated carbons has been found to consist of finite-sized π bonded clusters [116] with a hopping mechanism between these clusters [372, 452] accounting for the macroscopic conductivity[1]. The doping levels of carbonaceous electrodes in EDLCs typically lie in the range of up to 0.02 electrons per carbon atom. Considering the small cluster sizes, a maximum doping level of one elementary charge per 50 carbon atoms indicates that electrochemically doped activated carbon in EDLCs may consist of a mixture of doped and undoped localized domains. Since the doping of π bonded carbon clusters results in bond length changes, the increased linewidths upon doping may thus possibly arise from an increased spread in the distribution of bond lengths due to heterogeneous doping.

Turning now to the variations in the band positions, the most striking fact is that the shifts of the D and G bands are dissimilar and apparently unrelated to each other (Figure 10.17a and b). This stands in immediate contrast to the results discussed above for SWCNTs. In the latter case, it was implicitly assumed that the G and D bands originate from phonon modes involving the same C−C bonds of the nanotubes. Then, a change in bond stiffness would, in a first approximation, affect both bands in the same way, as was indeed observed.

For YP17, the phonon modes associated with the D and G bands are affected differently through electrochemical doping, thus strongly suggesting that each band is dominated by different structural features. As described previously (Section 8.5), both bands are associated with sp^2 hybridized carbon, but only the D band reflects the presence of sixfold aromatic rings [349]. This is due to the fact that the origin of the D band is the totally symmetric A'_1 phonon mode [356, 357], which

---

[1]The electronic conductivity of amorphous and activated carbon has been found to increase with temperature as a consequence of hopping between localized states [372, 453].

implies that linear sp^2 chains as well as five- or sevenfold rings do not contribute to the D band.

Thus, the D band may be traced back to structural features containing essentially sixfold aromatic rings, similar to graphene. The D band upshifts in either potential range correspond to a stiffening of the C−C bonds upon both electron and hole injection, which is in fact also predicted for the doping of graphene [431]. Thus, the behavior of the D-band during electrochemical doping can be explained by the doping of localized, graphene-like clusters.

On the other hand, the G band exhibits a different behavior, namely a pronounced downshift in the negative potential range and only slight upshifts at extreme positive potentials (Figure 10.17b). Therefore, it must be concluded that the main G band contributions arise from structural features other than those considered for the D band.

In Figure 10.18, a hypothetical polycyclic molecular fragment of activated carbon is considered which incorporates a distribution of bond lengths, separate π bonded clusters and differently sized rings. The
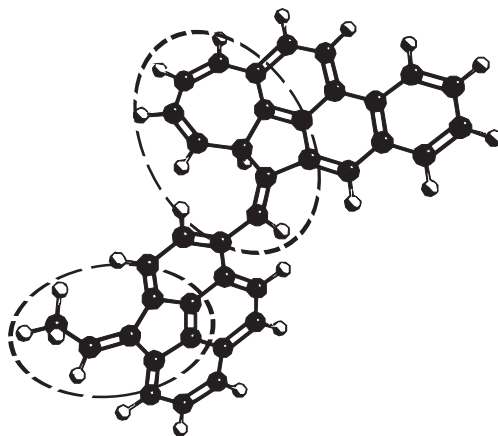
Figure 10.18.: Schematic fragment of activated carbon inspired by the molecular structures proposed by Ferrari and Robertson [451] for amorphous carbon and by Marsh and Rodríguez-Reinoso [142] for coal. Heteroatoms other than hydrogen have been omitted for clarity. The circled features mark deviations from the idealized graphene structure.

circled features in Figure 10.18 are of considerable importance to the electronic properties of activated carbon, as clusters with an odd number of π states or containing non-cyclic carbon atoms have an increased DOS near the Fermi level [116, 453]. This modification of the DOS may be expected to have two consequences relevant for the current discussion. First, doping is preferentially enabled in clusters containing a greater fraction of these structural imperfections. Second, the deformation of the Fermi surface is likely to reduce the electron–phonon coupling which is maximal in graphene and metallic SWCNTs [361, 431].

Since smaller clusters tend towards ring opening and may therefore be expected to contain a greater fraction of disorder [349], the effect of Kohn anomalies due to strong electron–phonon coupling may be expected to be small in these clusters. As a result, the doping of such clusters could be described well within the adiabatic Born-Oppenheimer approximation, which leads to the prediction of a softening of the E_{2g} phonon mode (G band downshift) for electron injection and a stiffening of this mode (G band upshift) for hole injection [431], as observed in the present work (Figure 10.17b). It is worth noting that these trends agree with the classical description of doping in graphite intercalation compounds [394, 427].

A self-consistent interpretation of the changes in the Raman spectrum of activated carbon during electrochemical doping may thus be proposed as follows. Activated carbon consists of islands of π bonded clusters. Those clusters which contain a significant amount of odd-numbered rings or non-cyclic carbon contribute weakly to the D band but strongly to the G band. Upon weak electron doping, the charge tends to be localized in these clusters, possibly due to an enhanced DOS as a consequence of the disorder present, leading to softening of the phonon modes within these clusters and a downshift of the G band. At higher levels of electron doping, also the more ordered clusters containing a significant fraction of sixfold aromatic rings, which resemble small graphene-like fragments and therefore contribute strongly to the D band, undergo doping, leading to a stiffening of these phonon modes due to reduced electron–phonon coupling and an upshift of the D band. In the positive potential range, the disordered clusters do not appear to contribute significantly towards charge storage, as no pro-

nounced frequency change of the G mode was observed. Instead, a significant stiffening of the phonon mode of the graphene-like clusters was noted, indicating that hole doping predominantly takes place within these structural units.

While the above explanations remain tentative and need to be validated, they provide an attractive means of interpreting the electrochemical doping of activated carbon in EDLCs while taking into account the differences between the structure of such carbons and that of model carbonaceous electrodes such as SWCNTs.

10.4. In situ resistance measurements

10.4.1. Background

The interest in the electronic resistance of the electrode material in EDLCs in the present work is not due to the corresponding ohmic losses during current flow, which are dominated by the electrolyte, but rather due to the influence of the charge carrier density on the space charge capacitance of the electrode. According to Hahn et al. [108], the space charge capacitance is actually the smallest capacitive term in the electrochemical double layer and thus limiting for the entire EDLC device.

After Equation (8.29), the conductivity of a material is directly proportional to the charge carrier density n and the mobility of the carriers, μ. Considering relative changes in the electrode resistance R during doping and assuming that the mobility remains constant, the relative change in the charge carrier density is simply given by

$$\frac{n}{n_0} = \frac{R_0}{R} \tag{10.2}$$

where n_0 and R_0 are the charge carrier density and resistance at any convenient reference point. The assumption of a constant mobility μ may be partially justified by the fact that electrochemical doping is expected to lead to relatively small bond length changes (less than 0.1 % for 0.02 electrons per carbon atom [412]), a low number of electroadsorbed ions per carbon atom which could act as scattering centers [454, 455] (one electroadsorbed ion per 50 carbon atoms at the

aforementioned doping level), and no significant changes in the macro-scopic conduction paths [452].

Resistance measurements of SWCNTs and YP17/PTFE were carried out in $1\,M\,Et_4NBF_4/AN$ and are described in the following.

10.4.2. Results

The variation of the electrode resistance within a narrow potential win-dow is shown in Figure 10.19. The observed trends were found to be very reversible within this potential range. For both SWCNTs (Fig-ure 10.19a) and YP17 (Figure 10.19b), the maximum resistance was mea-sured close to 0 V. Upon polarization, the resistance of both materials decreased significantly regardless of the polarity of the applied poten-tial, the drop in resistance being more pronounced for the SWCNTs.

In an extended potential range (Figure 10.20), most of the resistance decrease of the SWCNT electrode was found to occur within $\pm 0.5\,V$ of the resistance maximum (Figure 10.20a). The resistance drop in this potential range corresponded to about 90 %, with further polarization only causing relatively modest resistance decreases of a few percent. In comparison, the resistance of YP17 dropped relatively steadily in the potential range between approximately -2 V and +1 V (Figure 10.20b).

A notable asymmetry of the resistance decrease was observed for YP17 as a function of the sign of the applied charge (Figure 10.20b).
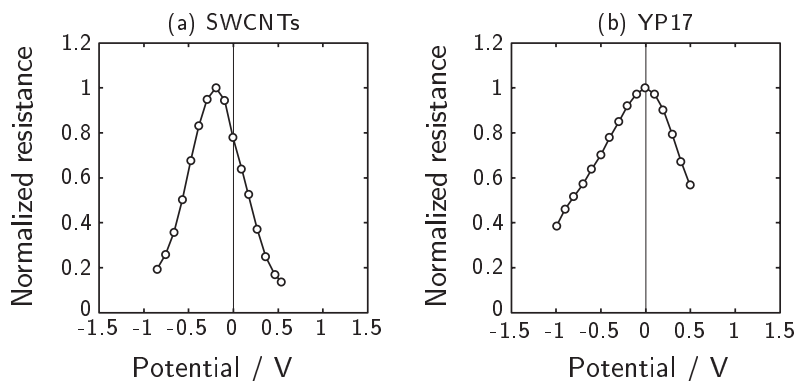
Figure 10.19.: In situ resistance measurements of SWCNTs (a) and YP17/PTFE (b) in $1\,M\,Et_4NBF_4/AN$ within a limited potential window.
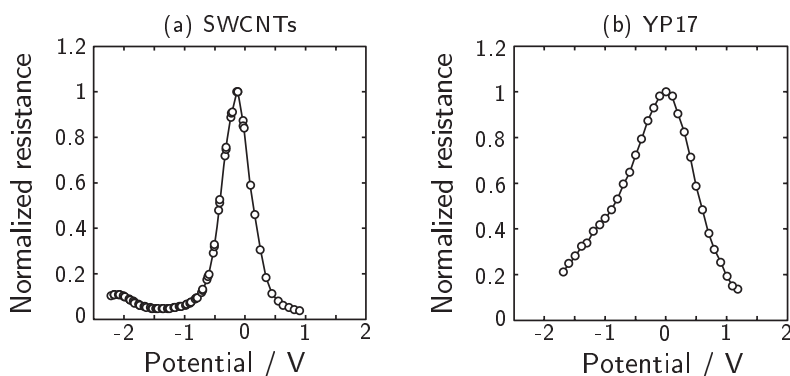
Figure 10.20.: In situ resistance measurements of SWCNTs (a) and YP17/PTFE (b) in 1 M Et_4NBF_4/AN within an extended potential window.

For electron doping (negative polarization), the drop in resistance was always significantly less pronounced than for hole doping (positive polarization). At +1 V, the resistance was 19 % of its initial (maximum) value, while at -1 V the resistance was still 43 % of the initial value. For SWCNTs, the resistance attenuation was found to be much more symmetrical (reduced to about 5 % at both -1 V and +1 V with respect to the potential of maximum resistance).

10.4.3. Discussion

The in situ measurements of electrode resistance substantiate an increased charge carrier density due to electrochemical doping in both the positive and the negative potential ranges. In contrast to YP17, the DOS of individual SWCNTs feature sharp vHs at well-defined energy levels which depend on the SWCNT diameter and chirality (Figure 10.12). However, due to the presence of a wide distribution of different types of SWCNTs in entangled networks such as those investigated in the present study [456], these single-tube characteristics cannot be resolved. In this respect, the present results are similar to those obtained by Kimizuka et al. [457] for SWCNT electrodes produced by a water-assisted CVD process [406]. The fact that the drop in resistance was more pronounced for the SWCNTs than for YP17 implies that the

DOS of the former increases more steeply upon electron and hole doping, respectively, than for the latter.

For the SWCNTs, the pronounced resistance drop within a relatively narrow potential window is in agreement with the presence of semiconducting SWCNTs with vanishing DOS at low Fermi level shifts, which do not contribute to charge storage at low polarizations at all. The maximum resistance should be at the potential E_{hf} at which the Fermi level is equal to the half-filling energy ε_{hf} introduced previously in this chapter (Figure 10.12). Indeed, the position of E_{hf} near -0.15 V is in good agreement with the findings of the Raman study presented earlier. With increasing polarization, the Fermi level is shifted across the vHs of the valence (hole doping) or conduction (electron doping) band of progressively smaller SWCNTs until, finally, all SWCNTs exhibit a non-vanishing DOS at the Fermi level and contribute to charge storage. From the results of the present study, this may be estimated to be the case at potentials beyond ca. ± 0.5 V vs. E_{hf} as more than 90 % of the resistance decrease occurs within this potential range.

According to Equation (10.2), a drop of the SWCNT electrode resistance to 5 % of its maximum value upon polarization to ± 1 V vs. E_{hf} corresponds to an increase by a factor of 20 in the charge carrier density n. Considering that the space charge capacitance scales with $\sqrt{n}$ for semi-conducting and metallic electrodes (Section 3.3), this results in a predicted increase of capacitance by a factor of ca. 4.5 at these potentials. This value is slightly higher than the increase in differential capacitance observed in the CVs in Figure 10.1b, but indicates that an increase in the space charge capacitance due to an augmented charge carrier concentration can easily account for the observed increase in capacitance of SWCNTs.

For YP17, the asymmetry in resistance loss during electron and hole doping is of particular interest, since it implies an asymmetric DOS with respect to the Fermi level. More specifically, the results of the present study indicate a higher DOS for the valence (π) band than for the conduction (π^*) band, resulting in a higher charge carrier density during hole doping. Similar findings were presented by Hahn et al. [108] using a proprietary PTFE-bound activated carbon. In this context, the different contributions of electronically distinct clusters to the in situ Raman

spectra discussed in the previous section may be hypothesized to cause this asymmetry in the DOS of activated carbon.

At +1 V, the resistance of YP17 drops to 19 % of its maximum value, corresponding to an increase in the charge carrier density by a factor of 5.3 and an increase in the space charge capacitance by a factor of 2.3. The corresponding values at -1 V are a residual resistance of 43 %, a charge carrier density increase by 2.3 and a space charge capacitance increase by 1.5. From the electrochemical characterization of YP17 in 1 M Et_4NBF_4/AN (Section 9.2.6), the increase in the differential capacitance with respect to the minimum capacitance at 0 V was 2.0 (at +1 V) and 1.5 (at -1 V), respectively. The good match between the increase in capacitance and that of the charge carrier density supports the notion that the overall capacitance is indeed limited by the space charge capacitance.

Thus, for YP17, the enhanced capacitance of the positive electrode with respect to the negative electrode may be ascribed solely to the difference in charge carrier densities in the respective potential ranges. The influence of the variable capacitance of the Helmholtz layer due to a smaller effective radius of the anion compared to the cation appears to be secondary.

10.5. Conclusions

The electrochemical doping of the activated carbon YP17 was compared with a SWCNT model electrode in 1 M Et_4NBF_4/AN in terms of performance in EDLCs, changes in Raman scattering and electrode resistance.

It was found that the SWCNT electrode exhibited a very low capacitance at low doping levels, while its capacitance approached that of YP17 for higher doping levels. The low initial capacitance of the SWCNTs was due to the fact that semi-conducting SWCNTs do not contribute to charge storage at all at low polarizations, as was shown by in situ Raman spectroscopy and in situ resistance measurements.

Using impedance spectroscopy, the intrinsic porosity of the entangled network of SWCNT bundles was found to provide pores of larger effective size and higher electrolyte conductivity compared to YP17, resulting in an advantage of SWCNTs in terms of gravimetric capacitance

at higher frequencies for a given electrode thickness. However, due to the higher gravimetric capacitance of YP17 at lower frequencies, similar power characteristics may be obtained simply by varying the electrode thickness. Thus, no practical advantage of SWCNTs over conventional activated carbons as EDLC electrode material could be identified.

Nonetheless, the study of SWCNTs provided insights into the mechanisms of electrochemical doping of graphene-based electrodes. Using in situ Raman spectroscopy, changes in the electrostatic interaction between charged SWCNTs and ions within the electrochemical double layer could be monitored via the frequencies of the RBM features which are unique to SWCNTs. Further, by following the position of the G^+ band, a contraction of C$-$C bonds in the axial direction was found during hole doping, while virtually no changes in the axial phonon mode stiffness were observed during electron doping of semiconducting SWCNTs. Given the complex interplay of SWCNT chirality, specificity of the Raman experiment with respect to the SWCNT DOS and the dependence of the latter on bundling and the chemical environment, no definitive explanations regarding the asymmetric C$-$C bond length changes upon electron and hole doping can be proposed at present. Experiments using different laser energies or studies on individual, chirality-resolved SWCNTs could help to improve the understanding of these phenomena.

Intriguingly, the Raman response of YP17 during electrochemical doping exhibited some fundamental differences to that of SWCNTs. The simplistic picture of activated carbon being composed exclusively of graphene-like fragments can not account for the observed behavior. Instead, a heterogeneous assembly of π bonded clusters with separate contributions to the D and G band must be inferred to provide a consistent explanation for the observed trends. Based in this hypothesis, hole doping primarily results in charge injection into graphene-like fragments, while electron doping primarily occurs in clusters in which non-symmetric phonon modes predominate, for instance through the presence of sp^2 chains or odd-numbered rings.

The asymmetry in electron and hole doping in YP17 was further underlined through in situ resistance measurements, which pointed towards a higher DOS of the conduction band and thus to a higher charge

carrier density during hole doping. As a consequence, the higher capacitance of the positive electrode compared to the negative electrode in EDLCs can be explained by the electronic properties of activated carbon. Considering the hypothesis developed on the basis of the Raman scattering experiments, it is appealing to attribute this asymmetry to the presence of different clusters in activated carbon with distinct structural and electronic properties.

Clearly, these findings warrant further efforts to establish the influence of electronically heterogeneous domains on the capacitance limits of EDLC electrodes. The use of model systems such as SWCNTs with well-defined bonding arrangements can assist in this respect. However, even in the latter case there is still controversy remaining in the scientific community regarding the precise mechanisms of electrochemical doping, with the prospect of further developments in the coming years.

Chapter 11.

Dimensional changes of carbon electrodes during electrochemical charging

11.1. Motivation

In the first studies on the cyclic expansion and contraction of activated carbon in EDLCs upon charging [190, 288], different hypotheses regarding the cause and influence of these dimensional changes were brought forward.

Regarding the origin of the cyclic expansion, three possible explanations [190] were identified:

- modification of the $C-C$ bond length due to charge injection,

- decreasing surface tension of the electrode due to charging of the electrochemical double layer, and

- intercalation of ions into the interlayer spacing between parallel graphene sheets.

The first expansion mechanism listed above has been proposed as the basis for electrochemical actuators consisting of carbon nanotubes [412, 458]. For more details regarding the changes in bond length due to electrochemical doping, the discussions in Chapter 10 are referred to.

The second possible expansion mechanism involves a change in interfacial surface tension of the electrode due to charging of the electrochemical double layer remote from the pzc, which is a well-studied phenomenon for the dropping mercury electrode [60, 63] and has also been reported for different carbons in neutral aqueous solutions [282, 459].

At the levels of charging typically encountered in EDLC electrodes (up to ca. 0.02 elementary charges per carbon atom), the changes in both $C-C$ bond length and surface tension are expected to be very small, namely less than 0.1 % for either effect [412, 459].

Finally, the first point is a well-known phenomenon in GICs, with reviews of this broad field notably given by Ebert [181], Hérold [182], Dresselhaus and Dresselhaus [183] and Solin [184]. The electrochemical intercalation of both cations and anions into graphite has been studied extensively, with reviews given by Besenhard and Fritz [460] and Noel and Santhanam [461], eventually leading to the development of the commercially successful Li-ion battery in which the intercalation of Li$^+$ into graphite is the mechanism of charge storage for the negative electrode [186, 188].

It is well established that ion intercalation can lead to a significant expansion of the graphite lattice perpendicular to the graphene sheets of more than 100 % [183]. In Li-ion batteries, an irreversible expansion (exfoliation) of graphite electrodes, usually due to solvent cointercalation and decomposition, is an important failure mechanism [462] which requires an intricate interfacial chemistry in order to prevent rapid performance loss [97–99].

In terms of Franklin's model for non-graphitic carbons (Section 4.5), domains consisting of parallel graphene sheets may be thought to offer intercalation sites also in EDLC electrodes. In this case, the intercalation of ions could be either beneficial, in terms of an additional charge storage contribution, or detrimental due to an exfoliation of these domains. An enhanced charge storage contribution due to ion intercalation in non-porous carbonaceous electrodes for EDLCs has in fact been suggested by Takeuchi, Okamura et al. [463–466]. Therefore, it is of considerable interest to clarify whether or not ion intercalation occurs in conventional activated carbons such as YP17.

On the basis of the above motivation, the importance of a detailed knowledge about the cause and effect of the dimensional changes of activated carbon electrodes in EDLCs is evident. In the present work, the expansion of three different carbonaceous electrodes (SFG44, YP17 and SWCNTs) was quantified via in situ dilatometry in $1\,\mathrm{M}$ Et$_4$NBF$_4$/AN as a function of the electrode potential (Section 11.2). Further, in situ WAXS experiments were carried out in order to study changes in the lattice spacings of a graphitic (SFG44) and an activated carbon (YP17) electrode (Section 11.3). First results are also presented for a graphite-oxide (GO) derived electrode material with an expanded interlayer sep-

aration distance compared to graphite (Section 11.4). A summary of the key findings of these investigations is given in Section 11.5.

11.2. Electrochemical dilatometry

11.2.1. Charging of graphite

The graphite powder SFG44 cycled in $1\,M$ Et_4NBF_4/AN exhibited a negligible double layer capacitance (Figure 11.1, top) over a wide potential range due to its low specific surface area ($5\,m^2\,g^{-1}$). Reversible charging currents were observed at potentials below -2.1 V and above +1.6 V, coinciding with maximum reversible electrode height changes of 6 % and 8 %, respectively (Figure 11.1, bottom). Upon discharge, a shrinkage of the electrode was observed which tended to be more pronounced than the previous expansion for both potential ranges, indicative of a compaction of the electrode during cycling.

11.2.2. Charging of SWCNTs

The height changes of SWCNT mats were measured during cyclic voltammetry in $1\,M$ Et_4NBF_4/AN. In Figure 11.2, the results of two separate experiments are summarized in which the initial range of potential cycling was negative (Figure 11.2a) or positive (Figure 11.2b), respectively.

For both experiments, a striking observation was the pronounced initial expansion during the very first charging step, regardless of the sign of the applied charge. For an initial negative polarization, this irreversible height change was 9.5 % (Figure 11.2a), while a value of 6 % was found for an initial positive polarization (Figure 11.2b).

Following this initial irreversible expansion, the SWCNT electrodes exhibited cyclic dimensional changes in phase with the applied polarization which is conveniently visualized by examining the evolution of the electrode height as a function of the applied potential profile over time (Figures 11.3 and 11.4).

While the magnitude of the electrode expansion was found to depend on the cycling history, maximum reversible height changes in the order
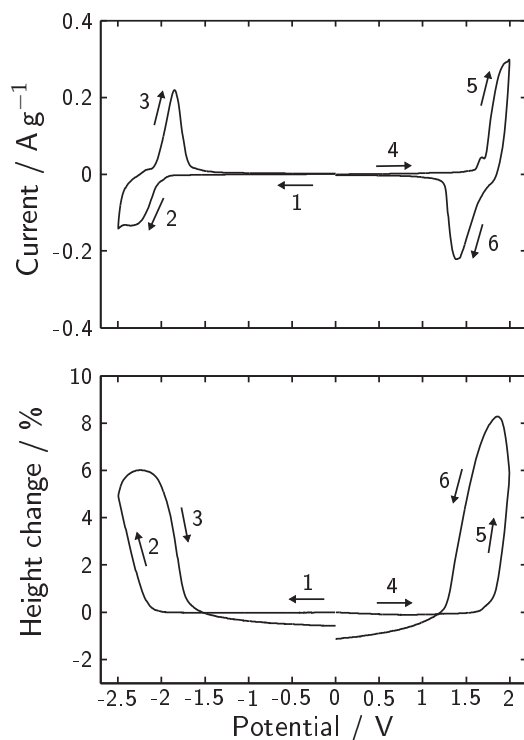
Figure 11.1.: CV of SFG44 in $1\,M\ Et_4NBF_4/AN$ (top) and the concomitant relative height change (bottom). The numbers indicate the measurement sequence. For clarity, only the third cycle in each potential range is shown, and the corresponding relative height changes are normalized to the electrode height at the beginning of each cycle. The sweep rate was $1\,mV\,s^{-1}$.

of 2.7 % during negative polarization and 1.3 % during positive polarization were found in the potential range between -1.5 V and +1.5 V (Figure 11.3).

These experiments are the first of their kind reported for SWCNTs in EDLC electrolytes, and the observed electrochemically induced irreversible expansions thus represent important insights into the charging mechanism of SWCNTs. Certain carbonaceous electrodes have been found to exhibit a qualitatively similar but much less pronounced irreversible expansion behavior in the first electrochemical charging cycle [262].
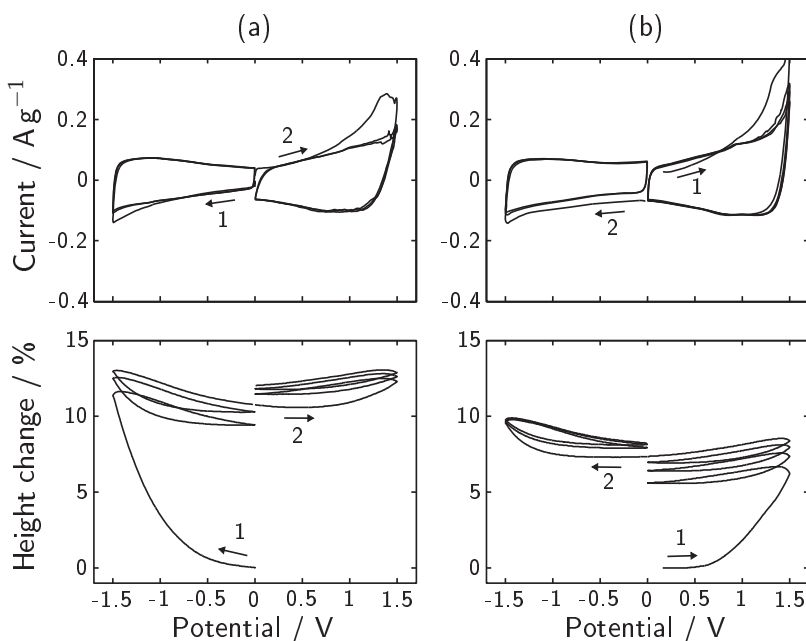
Figure 11.2.: CVs (top) and corresponding relative height changes (bottom) of SWCNT electrodes in $1\,M\ Et_4NBF_4/AN$ at a sweep rate of $1\,mV\,s^{-1}$ for cycling commenced in the negative (a) and positive (b) potential ranges.

In order to elucidate the mechanism of the irreversible electrode expansion in the first charging cycle, the capacitance and frequency response of SWCNT electrodes before and after one charge/discharge cycle were evaluated by cyclic voltammetry (Figure 11.5) and EIS (Figure 11.6).

From the CVs performed in a narrow range around $0\,V$, it is clear that the cycling to extended potential windows results in an enhanced capacitance, regardless of whether the polarization occurred in the negative (Figure 11.5a) or positive (Figure 11.5b) potential range. Depending on the cycling history and potential, the observed capacitance enhancement was significant, being up to $+60\,\%$ in the CVs shown in Figure 11.5.

Impedance spectroscopy revealed a similar capacitance enhancement in the case of a full cell consisting of two symmetric SWCNT electrodes.

Figure 11.3.: Electrode height change (top) and potential (bottom) as a function of time for the CV shown in Figure 11.2a.
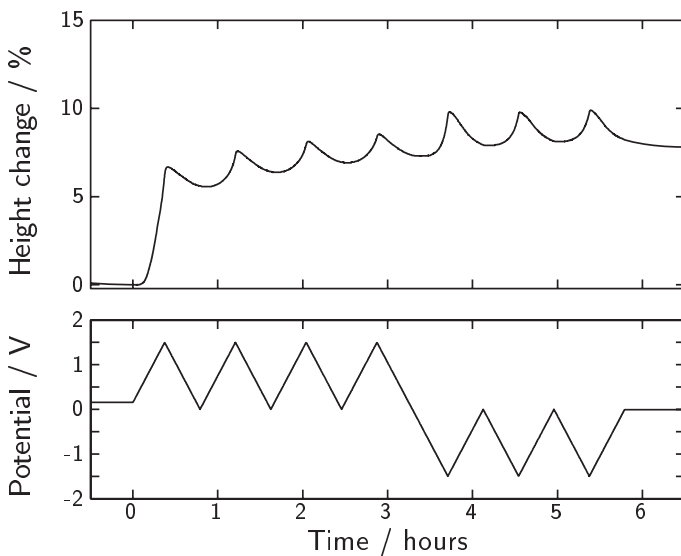
Figure 11.4.: Electrode height change (top) and potential (bottom) as a function of time for the CV shown in Figure 11.2b.
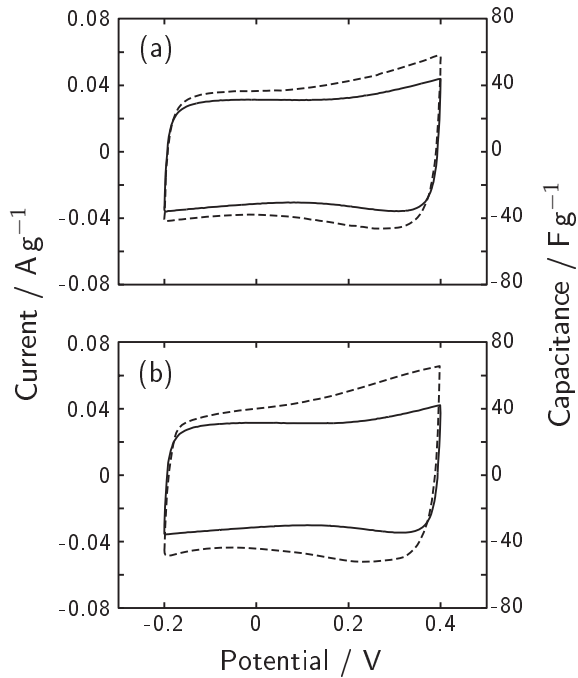
Figure 11.5.: Three-electrode CVs of SWCNTs in 1 M Et$_4$NBF$_4$/AN before (solid line) and after (dashed line) potential excursions to (a) -2.5 V and (b) +2 V. The sweep rate was 1 mV s^{-1}.
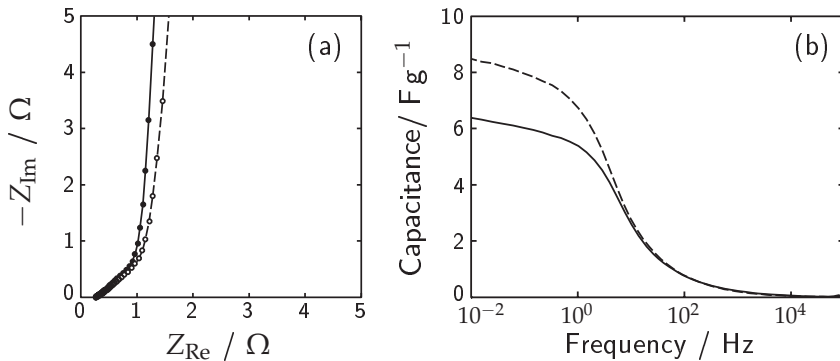
Figure 11.6.: Nyquist (a) and Bode (b) plots of a symmetric SWCNT full cell in 1 M Et$_4$NBF$_4$/AN before (solid line) and after (dashed line) five cycles between 0 V and 3 V. The experimental conditions were identical to those used in Figure 10.3.

In Figure 11.6, the impedance response of this cell is shown in the fully discharged state before and after polarization to 3 V. Following the electrochemical polarization, the distributed resistance described by the 45 ° region at high frequencies was elongated (Figure 11.6a), and the crossover from this regime to purely capacitive charging shifted to slightly lower frequencies.

The capacitance enhancement was found to occur exclusively at lower frequencies (Figure 11.6b). Thus, the increase in the characteristic time constant of the SWCNT cell can be explained by the increase in the distributed capacitance within pores. A slight increase in ESR at all frequencies was found, although this change was negligible compared to the capacitance increase, indicating that the electrolyte pore conductivity was not altered considerably by the electrochemical polarization.

11.2.3. Charging of YP17

The electrode height changes of YP17/PTFE in 1 M Et_4NBF_4/AN are presented in Figure 11.7 along with the according CV in the potential range between -1.5 V and +1.5 V. In contrast to the case for graphite and SWCNTs, the height changes hardly exhibited any irreversible character apart from a slight electrode compaction of 0.25 % upon changing the polarity of the electrode.

The evolution of the electrode height over time is shown in Figure 11.8. The similarity to the cyclic reversible expansion of the SWCNT electrode (Figure 11.3) is worth noting, although the magnitude of the height changes were smaller for YP17. The maximum reversible height changes were found to be 1.3 % and 0.5 % in the negative and positive potential ranges, respectively.

11.2.4. Discussion

The potential-dependent height changes of the three investigated electrode materials exhibited notable differences which will be discussed in the following.

For the graphite SFG44 (Figure 11.1), no electrode expansion during double layer charging was observed over a wide potential range. In this case, the onset of charging implies the intercalation of ions into
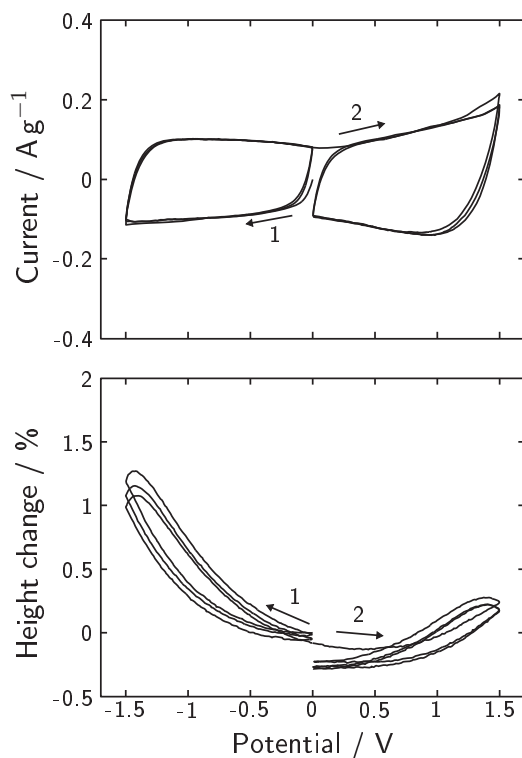
Figure 11.7.: CVs of YP17/PTFE in 1 M Et_4NBF_4/AN (top) and the simultaneous electrode height change (bottom). The numbers indicate the measurement sequence, whereby three cycles were performed in both the negative and positive potential ranges, respectively. The sweep rate was $1\,mV\,s^{-1}$.

the bulk graphite lattice, namely Et_4N^+ in the negative potential range and BF_4^- in the positive potential range. Both of these ions are larger than the d_{002} interlayer spacing of graphite (Table 11.1). Thus, the accommodation of ions within graphite clearly requires a widening of the interlayer distance, which explains the macroscopic expansion during charge storage in this case.

It is convenient to normalize the measured height changes to the amount of applied charge for all materials (Figure 11.9). The fact that the observed macroscopic expansion is ambipolar for all materials but of different magnitude depending on the polarity is a strong indication
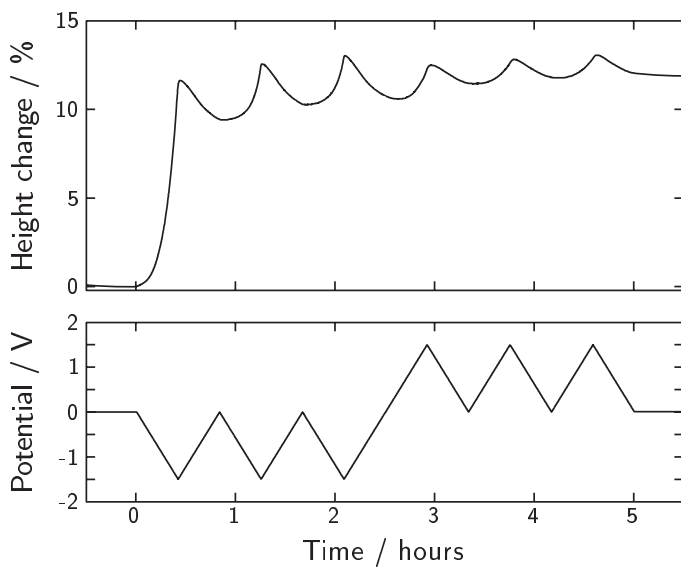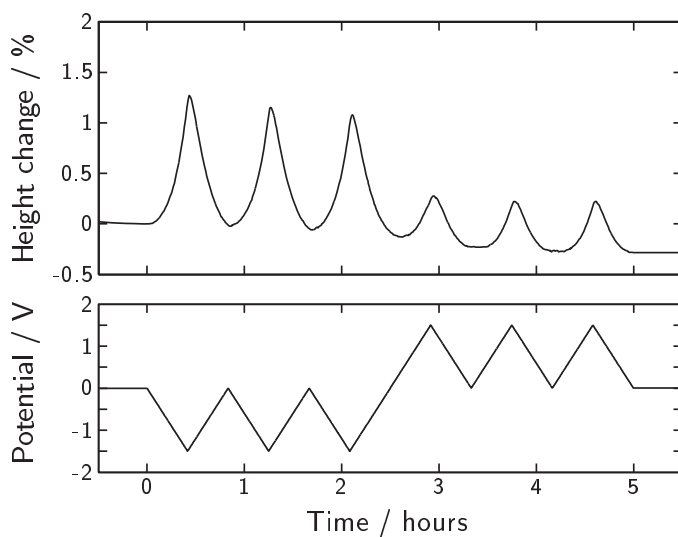
Figure 11.8.: Electrode height change (top) and potential (bottom) as a function of time for the CV shown in Figure 11.7.

that changes in bond length and surface tension due to doping are not the dominant contributions to the dimensional changes.

Still dwelling on the discussion of the graphite electrode, the application of an absolute charge of $50\,\mathrm{C\,g^{-1}}$ results in a height change of +4.6 % for negative charging ($\mathrm{Et_4N^+}$ intercalation) and +3.5 % for positive charging ($\mathrm{BF_4^-}$ intercalation). The relatively good match of the

Table 11.1.: Volumina and diameters of $\mathrm{Et_4N^+}$, $\mathrm{BF_4^-}$, AN and PC estimated according to the Connolly solvent excluded volume (ChemBio3D™, probe radius 1.4 Å). To be compared with the interlayer spacing of graphite, $d_{002} = 3.35\,\text{Å}$.

Ion	Volume / Å^3	Diameter[a] / Å
$\mathrm{Et_4N^+}$	163	6.78
$\mathrm{BF_4^-}$	41.4	4.29
AN	37.5	4.15
PC	77.8	5.30

[a] Assuming strictly spherical ion shapes.
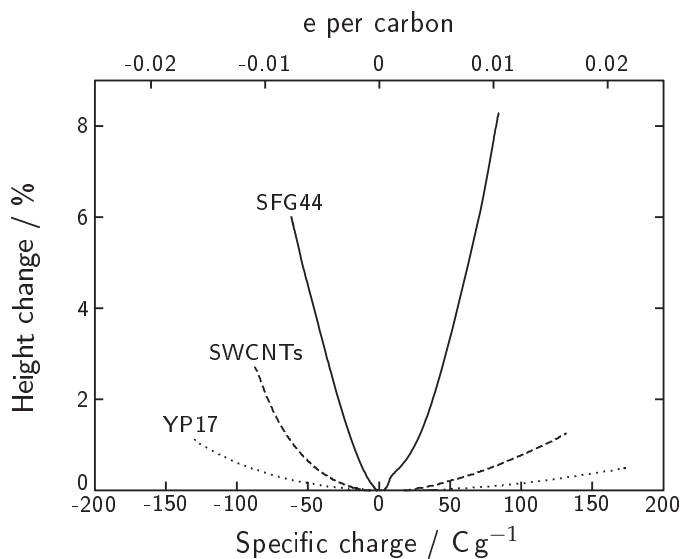
Figure 11.9.: Electrode height change per unit applied charge for SFG44 powder, a SWCNT mat and YP17/PTFE. The data was extracted from the third charging cycle for both the negative and positive potential range.

cathodic to anodic expansion ratio (1.3) with that of the respective ion diameters (1.5, from Table 11.1) is likely to be coincidental due to the possible influence of solvent cointercalation and staging on the dimensional changes. In fact, Hahn et al. [190] reported a contrary result for a different graphite (TIMREX® KS44 from TIMCAL), namely a more pronounced expansion upon positive charging, which was interpreted as being due to solvent (AN) cointercalation. The complementation of the dilatometry results by in situ XRD measurements, presented in the next section, will address this issue in more detail and provide additional insight into the mechanism of ion intercalation into graphitic electrodes in EDLC electrolytes.

For the SWCNT electrode, the macroscopic expansion stands in contrast to the C−C bond stiffening measured by Raman spectroscopy (Chapter 10). In addition, due to the absence of parallel graphene sheets in this material, ion intercalation in the classical sense can not be the cause for the measured height changes. Ion accumulation on the external surface of SWCNT bundles during charging is not expected

to result in macroscopic dimensional changes due to the considerable void space between bundles. In addition, the pronounced irreversible expansion in the first charging cycle can not be explained simply by a charging of the external bundle surface.

Hence, in order to account for both the initial irreversible expansion and the subsequent cyclic height changes, an expansion of SWCNT bundles in the radial direction must take place during which ions are accumulated within the bundles. Thus, after immersion of the SWCNT electrode in the electrolyte solution, predominantly the external bundle area is thought to be involved in double layer formation, and this area is expected to be close to the NLDFT surface area determined via gas adsorption. This is in agreement with the measured specific capacitance of the SWCNTs prior to the first charge/discharge cycle (ca. $3\,\mu\mathrm{F\,cm^{-2}}$), which is close to that of the basal plane of graphite (Chapter 10). During the very first charging cycle, irrespective of the sign of the applied charge, the large measured expansion indicates an infiltration of the bundles with ions, with the additional spatial requirements forcing the loosely bound SWCNTs apart. Correspondingly, the effective interfacial area is now expected to be the sum of the external and internal bundle surface areas. Indeed, higher capacitances were observed after the first electrochemical charge/discharge cycle. The corresponding impedance response (Figure 11.6) demonstrated that the capacitance enhancement was obtained exclusively at low frequencies and therefore at slow charging sites which are likely to be located within bundles as opposed to between bundles.

It may be debated whether the ion insertion sites are provided by the inner core of SWCNTs or by the interstitial void space between neighboring SWCNTs within a bundle. There are a few arguments which speak against the insertion of ions into individual SWCNTs. The typical SWCNT diameter is relatively large (ca. 1 nm) compared to the ion size (Table 11.1), rendering an interpretation of the pronounced irreversible expansion difficult. Further, if the macroscopic expansion was to be accounted for solely by the radial expansion of individual SWCNTs, a significant lengthening of C−C bonds would be expected, which appears contradictory to the results of the in situ Raman study (Chapter 10). Therefore, for the present work, it is concluded that the irreversible

expansion and corresponding increased capacitance and modified impedance response are due to an infiltration of ions into the interstitial porosity of SWCNT bundles, resulting in a partial debundling. The irreversible nature of this debundling implies that the internal double layer, once formed, remains intact even during subsequent discharge, which differs from GICs in which the interlayer distance is usually reestablished following deintercalation. Thus, the cyclic expansion and contraction of the SWCNTs during cycling may then be thought to consist of the accumulation and expulsion of ions, respectively, upon charging and discharging the electrochemical double layer within bundles.

Noting that the capacitance enhancement for the full cell at $0\,V$ due to the proposed electrolyte infiltration process is in the order of $30\,\%$ (Figure 11.6), a straightforward extrapolation to the effective interfacial area between electrode and electrolyte implies an increase from $986\,m^2\,g^{-1}$ (the NLDFT surface area of the dry electrode, Table 9.5) to $1282\,m^2\,g^{-1}$, which approaches the specific surface area of one side of a single SWCNT ($1315\,m^2\,g^{-1}$) and thus supports the notion of double layer formation at individual SWCNTs within bundles.

Similar conclusions regarding the electrochemical ion insertion into the interstitial porosity of SWCNT bundles were drawn by Claye et al. [467] using a Li-based electrolyte solution. Shimoda et al. [468] even proposed that ion insertion into individual SWCNTs occurred after pretreating the nanotubes via a combination of strong acid etching and ultrasonication, which led to a significant shortening of the SWCNTs, the opening of tube ends and the introduction of sidewall defects.

For both SWCNTs and YP17, the magnitude of expansion clearly depends on the polarity (Figure 11.9), i.e. on the type of ion added to the double layer. For activated carbon, this behavior has been reported previously [190, 288]. In contrast to SWCNTs, YP17 was found to contain small ordered domains consisting of 2–3 parallel graphene sheets (Chapter 9), thus giving rise to the possibility of ion intercalation into these domains. However, the observation of dimensional changes in SWCNTs under identical conditions suggests that the presence of crystalline intercalation sites is not a necessary prerequisite for electrode expansion during charging. In fact, the presence of narrow microporosity in SWCNT bundles within which an electrochemical double layer can

be formed appears to be sufficient to explain the expansion in this material.

Therefore, the charging of the electrochemical double layer within micropores, which approach the dimensions of the ions present in the electrolyte, seems to be a satisfactory frame of discussion in which the expansion of activated carbon may also be understood. The macroscopic expansion of activated carbon electrodes in EDLCs may thus be explained by the steric requirements of the ions accumulated in micropores to counter the electronic charge on the carbon.

The fact that the relative reversible height change of the SWCNT mat was several times larger than that of YP17/PTFE (Figure 11.9) can be explained in part by the significant anisotropy of the SWCNT mat (see Figure 6.1 on page 99) and, tentatively, by the more rigid framework of YP17/PTFE.

The more pronounced height change during the application of negative charge to the electrode indicates that the effective size of the cation (Et_4N^+) is larger than that of the anion (BF_4^-) for both SWCNTs and YP17. A comparison between the height changes of SWCNTs and YP17 in either potential range (Figure 11.10) reveals that the ratio between cathodic to anodic height change lies between 3 and 4 for both materials over a wide range of applied charge. Similar results were obtained previously by Hahn et al. [190], providing a cathodic/anodic expansion ratio of 2.7. Notably, this ratio differs significantly from that of the graphite SFG44 (1.3, see above), again pointing towards different ion insertion mechanisms.

Possible explanations for the apparent discrepancy in the effective relative spatial requirements of the ions compared to their diameters may be based on an underestimation of the effective cation size or an overestimation of the effective anion size within pores. Different extents of solvation of the ions within micropores [103] may be at the origin of this discrepancy, but beyond the scope of the present discussion. Another possible explanation is that ion insertion contributes less to charge storage, and thus less to the macroscopic expansion, in the positive compared to the negative potential range. Further work is needed to clarify the origin of the high ratio of cathodic to anodic ex-

pansion and whether this is a common characteristic of all microporous carbons.
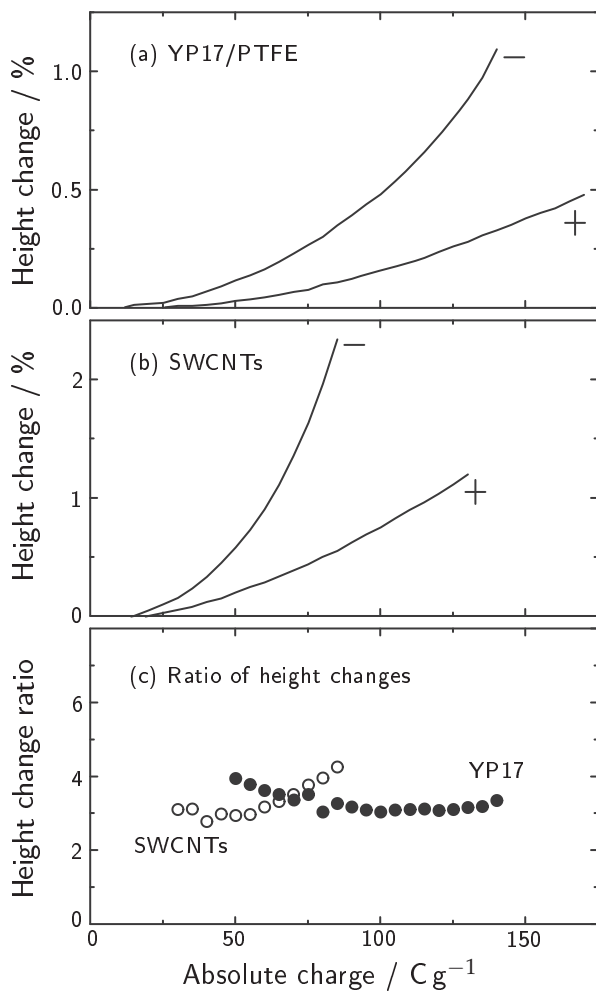
Figure 11.10.: Comparison of height changes in the cathodic ($-$) and anodic ($+$) potential ranges for (a) YP17/PTFE and (b) a SWCNT mat as well as (c) the ratio of cathodic ($-$) to anodic ($+$) height change. Data was taken from the third cathodic and anodic charging cycles in $1\,M\ Et_4NBF_4/AN$, while data points below the resolution limit of the dilatometer were omitted from the figure.

11.3. In situ WAXS

11.3.1. In situ XRD of ion intercalation into graphite

The electrochemical intercalation of BF_4^- into graphite has been reported previously by different authors based on a variety of methods [469–471]. The principle experimental technique in these studies has been cyclic voltammetry, in some cases complemented by other analytical techniques such as thermogravimetry (TG) and differential thermal analysis (DTA) [470] or XRD [470, 471].

For the electrochemical intercalation of R_4N^+ into graphite, investigations have been presented by Besenhard and Fritz (R = Me) [472] based on cyclic voltammetry, Santhanam and Noel (R = Bu) [470] using cyclic voltammetry, TG, DTA and XRD, and more recently by Campana et al. (R = Et) [273] using in situ AFM.

Investigations on the intercalation of both Et_4N^+ and BF_4^- from AN- and PC-based electrolytes into graphite have been carried out by Hahn et al. [190, 288] using electrochemical dilatometry as well as by Hardwick et al. [194] by means of in situ Raman microscopy. So far, however, no in situ XRD data has been available to assess the structural changes undergone by graphitic electrodes upon intercalation in the commonly employed AN- and PC-based EDLC electrolytes. An XRD study of the ion intercalation into SFG44 from 1 M solutions of Et_4NBF_4 in AN and in PC using synchrotron radiation is presented in the following.

Results

The CVs obtained during the in situ XRD measurements are plotted in Figure 11.11 for both the AN- and the PC-based electrolyte solutions. In separate experiments, SFG44 was cycled to -2.7 V and -3 V as well as to +2.2 V and +2.5 V against the oversized activated carbon counter electrode. The electrochemical behavior is similar for both electrolytes, with pronounced current increases observed near -2 V and +1.7 V for both electrolyte solutions. The charging of the counter electrode by approximately 100 mV can be seen clearly during the back scan of the second cycle in each case, causing shifts in the current maxima as expected.
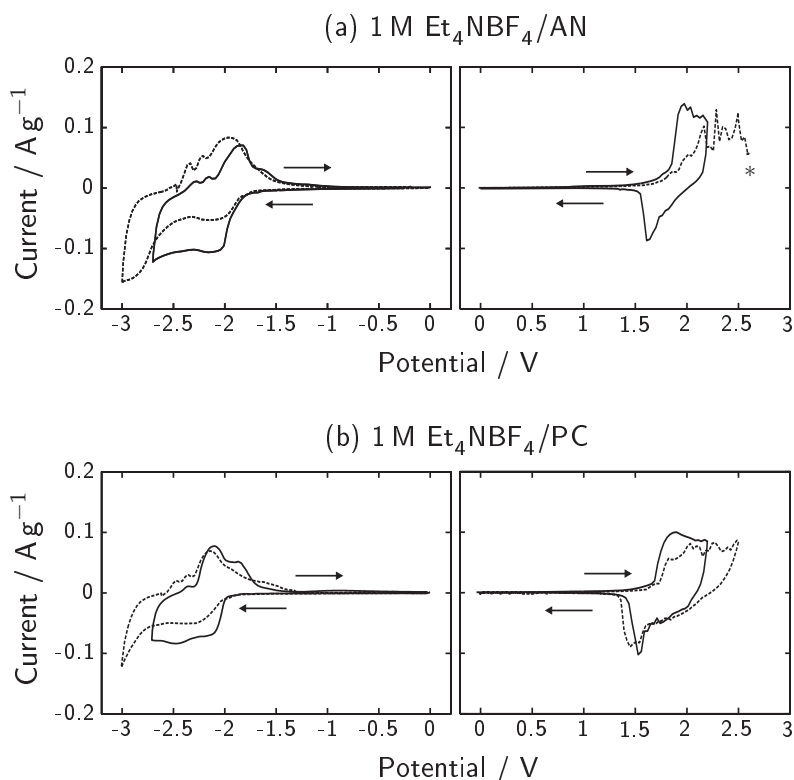
Figure 11.11.: CVs of SFG44 in (a) $1\,M\ Et_4NBF_4/AN$ and (b) $1\,M\ Et_4NBF_4/PC$ during the in situ XRD measurements. The first cycle (solid line) was followed by a second cycle (dashed line) in an extended potential window. The sweep rate was $0.3\,mV\,s^{-1}$. The back scan of the anodic cycle in (a) is not shown due to difficulties with the in situ cell (marked by $*$).

The CDEs were determined for each cycle shown in Figure 11.11 and are listed in Table 11.2. The values obtained indicate that the CDEs are generally higher in PC than in AN under the present experimental conditions. The intercalation of BF_4^- in the PC-based electrolyte appears to be particularly efficient, which agrees with the data presented by Santhanam and Noel [470].

XRD patterns were recorded during the CVs approximately every 5 minutes. The results are shown in Figures 11.12 and 11.13 for the AN- and PC-based electrolyte, respectively. The diffractograms are plotted

Table 11.2.: Charge–discharge efficiencies of the intercalation of Et_4N^+ and BF_4^- into SFG44 during the in situ XRD experiments.

Solvent	Potential range	Cycle	Charge[a] / $Ah\,kg^{-1}$	Efficiency[b]
AN	negative	1	88	0.35
		2	93	0.48
AN	positive	1	49	0.39
		2	63	–
PC	negative	1	51	0.59
		2	67	0.58
PC	positive	1	47	0.65
		2	57	0.67

[a] From the forward scan direction of each respective cycle.
[b] Ratio of discharge capacity to charge capacity.

against $q = 4\pi \sin\theta / \lambda$ in order to obtain a wavelength-independent representation. Missing XRD patterns are due to short interruptions in the X-ray beam at the synchrotron source.

Similar changes were observed for either electrolyte depending on the polarity. In the positive potential range (Figures 11.12b and 11.13b), a new reflection appeared at low q values upon intercalation, while at the same time a splitting of the 002 diffraction peak was observed. The extent of splitting differed for each electrolyte. In the AN-based electrolyte, additional reflections were observed close to $q = 1.4\,\text{Å}^{-1}$ and near the original 004 reflection. The 100 peak broadened during intercalation and shifted slightly towards higher q, indicating a decrease of the in-plane C−C bond length. Upon deintercalation, the new reflections disappeared almost completely, while the 002 diffraction peak returned at its original position.

Compared to the AN-based electrolyte, the most notable differences in the in situ XRD patterns for the PC-based electrolyte are the absence of the reflection near $q = 1.4\,\text{Å}^{-1}$ and the significantly lower intensity of the reflection near $q = 2\,\text{Å}^{-1}$ during intercalation. Also, the splitting of the 002 reflection is strongly asymmetric in the PC-based electrolyte.
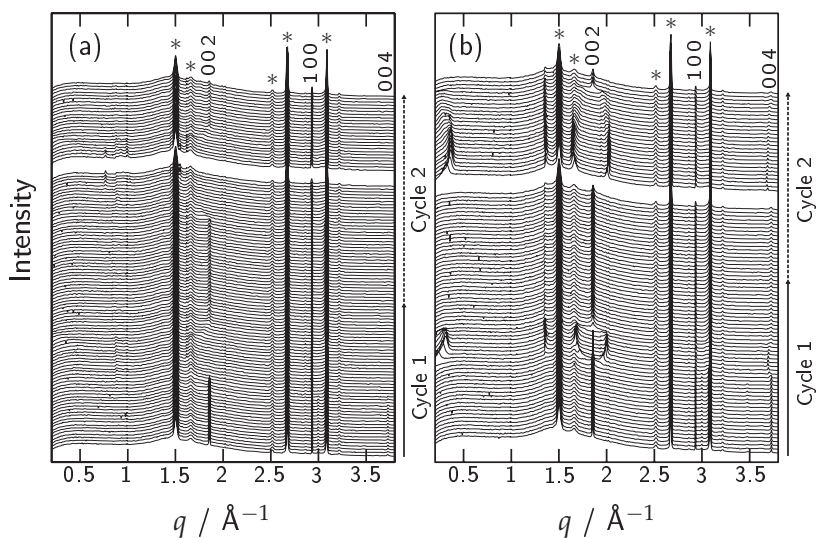
Figure 11.12.: In situ XRD patterns during cycling of SFG44 in $1\,M\,Et_4NBF_4/AN$ for the (a) negative and (b) positive potential ranges. Contributions from the pouch cell are denominated by an asterisk ($*$), while the reflections of SFG44 are labeled by their respective Laue symbols.

The changes in the XRD patterns during negative cycling were far less pronounced (Figures 11.12a and 11.13a). The most prominent effect was the disappearance of the $0\,0\,2$ diffraction peak during intercalation and its reappearance following deintercalation. Its intensity was significantly reduced after the intercalation/deintercalation process. There is a faint indication of a shift of the $0\,0\,2$ reflection towards lower q during intercalation and a shift back to its original position upon deintercalation, as well as slight signs of the appearance of WAXS maxima at low q during intercalation. However, these features are too weak to warrant further interpretation at this point.

Contrary to the positive potential range, the $1\,0\,0$ reflection moved to slightly lower q values during intercalation, indicating an increase in the in-plane $C-C$ bond length. This observation agrees with the theory of bond length changes of graphite during charging, in which a negative charging of the graphite lattice results in a lengthening of the $C-C$ bonds while a shortening is predicted during positive charging
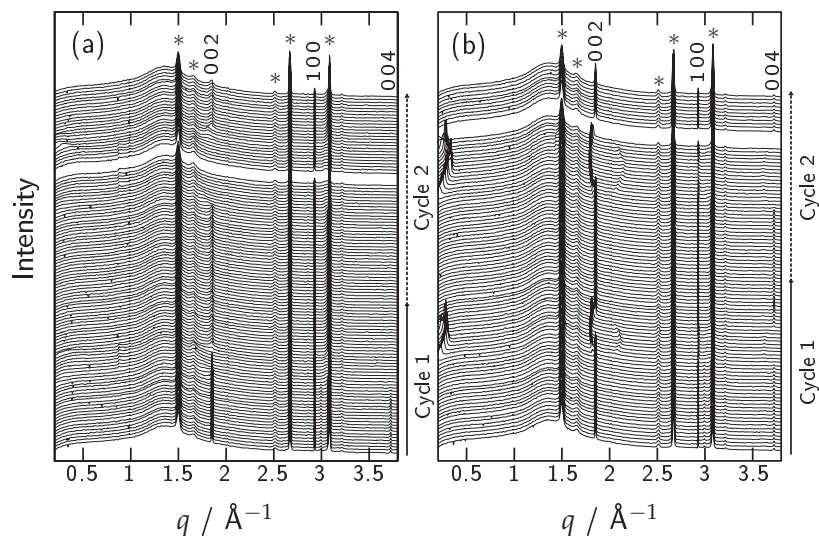
Figure 11.13.: In situ XRD patterns during cycling of SFG44 in $1\,M$ Et_4NBF_4/PC for the (a) negative and (b) positive potential ranges. Contributions from the pouch cell are denominated by an asterisk ($*$), while the reflections of SFG44 are labeled by their respective Laue symbols.

(Chapter 10). The fact that both the intensity and peak shape of the $1\,0\,0$ reflection did not vary significantly during both negative and positive polarization indicates that the in-plane ordering of the graphite lattice was not significantly affected by intercalation.

The attenuation of the $0\,0\,2$ diffraction peak of graphite during polarization is plotted in Figure 11.14. As expected, the original periodicity along the c-axis is disrupted near -2 V and near +1.8 V, which agrees well with the charging of the graphite electrode at these potentials. This indicates that the insertion of ions into the graphite lattice contributes directly to the first current rise in the CVs shown in Figure 11.11.

Further, the relative peak intensity of the $0\,0\,2$ reflection can be used as a measure of stability of the graphite lattice during the intercalation/deintercalation process as shown in Figure 11.15. For each potential range, the initial $0\,0\,2$ reflection is plotted along with the reflection after completion of the first and second electrochemical cycle, respectively. A decrease in the intensity and an increase in the FWHM of
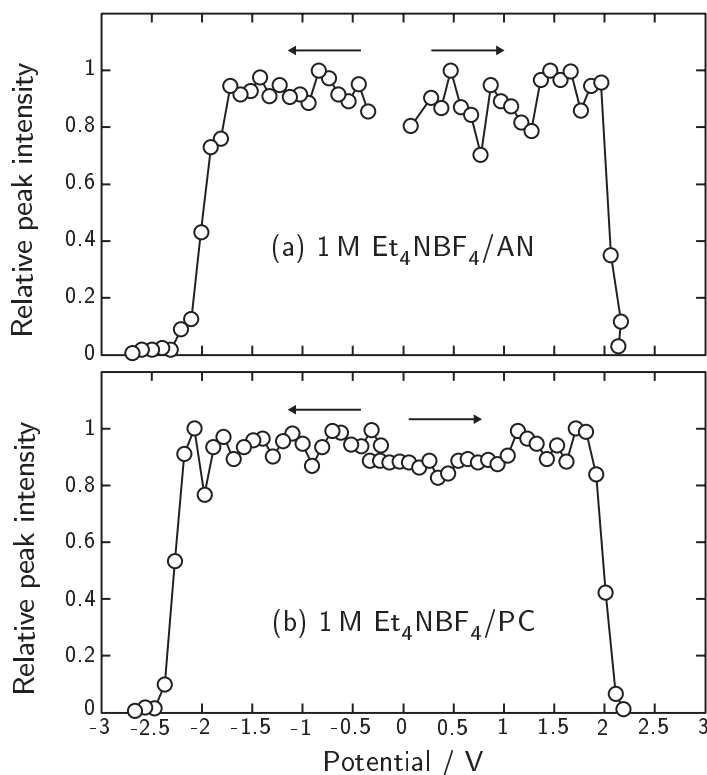
Figure 11.14.: Loss of peak intensity for the 002 reflection of SFG44 in (a) $1\,M$ Et_4NBF_4/AN and (b) $1\,M$ Et_4NBF_4/PC as a function of potential.

the 002 reflection indicates a loss of translational symmetry along the *c*-axis, i.e. in the direction perpendicular to the graphene sheets. Thus, the ion insertion and deinsertion process appeared to have a destructive effect on the crystallinity of the graphite electrode, particularly during the first cycle in the negative potential range investigated here.

After cycling in the positive potential range, the loss of crystallinity appeared to be less pronounced (Figure 11.15). This is particularly true for BF_4^- intercalation in the PC-based electrolyte, which had no noticeable effect on the 002 reflection following the first electrochemical cycle.
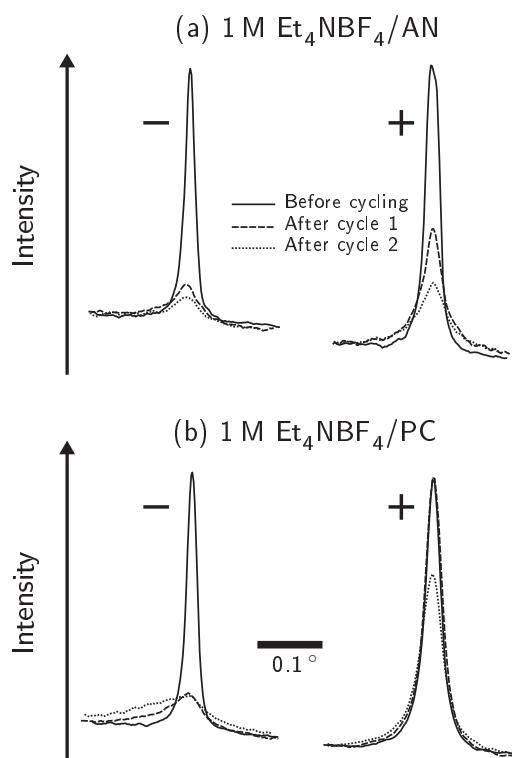
Figure 11.15.: Comparison of the 002 reflections before and after the first and second intercalation cycles using $1\,M\,Et_4NBF_4$ in AN (a) and in PC (b) for the negative ($-$) and positive ($+$) potential ranges. The 2θ position was $12.12\,^\circ$ in each case, corresponding to $q = 1.87\,\text{Å}^{-1}$.

Discussion

In situ XRD complements the data obtained from the CVs by provid-ing structural information about the graphite electrode during elec-trochemical cycling. Cyclic voltammetry alone does not easily allow distinguishing between different modes of charge transfer such as ion intercalation and electrolyte decomposition. While the relatively low efficiencies observed in the present work (Table 11.2) suggest that the latter also contributes to the CVs, the disappearance of the 002 reflec-tion clearly proves that ion insertion between graphene sheets occurs

in the very first current rise during cycling in both the positive and negative potential ranges.

While intercalation was shown to take place for both cations and anions, the XRD patterns suggest that staged GICs were only formed during the intercalation of BF_4^-. The staging phenomenon is schematically depicted in Figure 11.16, in which the intercalated species tend to form contiguous islands while maximizing the separation distance to other intercalated layers [182, 183]. The driving force for maximizing the interlayer distance depends on the balance between intra- and interlayer interactions [473], which can be modeled by elastic strain mediation [474, 475] or by electronic charges, e.g. using a series of capacitive components to represent the charge centers of the intercalated ions [476].

The repeat distance perpendicular to the graphene sheets is given by d_i, resulting in the appearance of $00l$ diffraction peaks in the case of well-ordered GICs. Given such an ordering, the stage index n can be determined, which is defined as the number of graphene sheets separating each intercalated layer. The repeat distance d_i can be expressed in terms of the stage index n and the thickness of the intercalated layers, d_1, by the following equation:
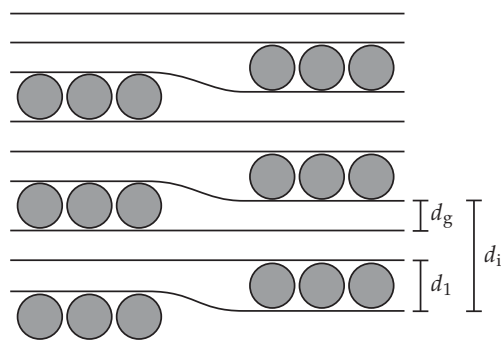
Figure 11.16.: Schematic staging model in a GIC for a stage index $n = 3$. The presence of pleated layers according to the Daumes-Hérold domain model [182, 183] is indicated. The nomenclature for the interlayer distances follows the nomenclature recommended by IU-PAC [477].

$$d_i = d_1 + (n-1)\, d_g \tag{11.1}$$

where d_g is the interlayer spacing between the graphene sheets. To a good approximation, d_g is equal to d_{002} in the pristine graphite structure [182]. d_1 is also often referred to as the sandwich thickness or gallery height. The d-spacings corresponding to the $00l$ reflections of the GIC are then given by

$$d_{00k} = \frac{1}{k}\left[d_1 + (n-1)\, d_g\right] \tag{11.2}$$

where k is the order of the reflection. From the absence of pronounced $00l$ reflections for the intercalation of Et_4N^+, it may be concluded that no well-defined staging occurred for this ion under the cycling conditions employed in the present work.

For BF_4^- intercalation, however, it is possible to compare the XRD data with the theoretical diffraction peak positions. The latter can be determined from Equation (11.2) for a given stage index provided d_1 is known. Billaud et al. [478] presented a value of $d_1 = 7.9\,\text{Å}$ for intercalated BF_4^-. However, in their work, chemical analysis revealed that cointercalation of the solvent, in this case nitromethane, had also taken place. It is possible that the intercalation of BF_4^- alone results in a smaller sandwich thickness d_1. Studies on the intercalation of PF_6^- have dealt with similar difficulties, with a variety of values reported for d_1 including 4.5 Å [479], 8 Å [480] and 11 Å [481].

Due to this uncertainty of the true thickness d_1, the theoretical diffraction peak positions are calculated for the two most probable situations in the following. In the first case, d_1 is taken as 5.2 Å which has been suggested for the intercalation of naked BF_4^- [470, 479] and is close to the diameter of the lone ion (Table 11.1). In the second case, d_1 has been taken as 7.9 Å based on the results of Billaud et al. [478], thus accounting for a possible increase in the sandwich thickness due to solvent cointercalation.

The positions of the corresponding $00l$ reflections of the GICs for $n = 1\ldots5$ are given in Figure 11.17. In each case, the 001 reflection of the GIC appears at low q values which were accessible in the present work. Two important differences between the two cases presented in

Figure 11.17 should be emphasized. First, the two reflections which re-place the original 002 peak on either side change their index from $00n$ and $00(n+1)$ to $00(n+1)$ and $00(n+2)$ in going from the smaller to the larger sandwich thickness. Second, the splitting of the 002 peak is more asymmetric for the larger d_1 value.

The apparent splitting of the 002 diffraction peak during intercala-tion proceeding via progressively lower stage indices n is plotted in
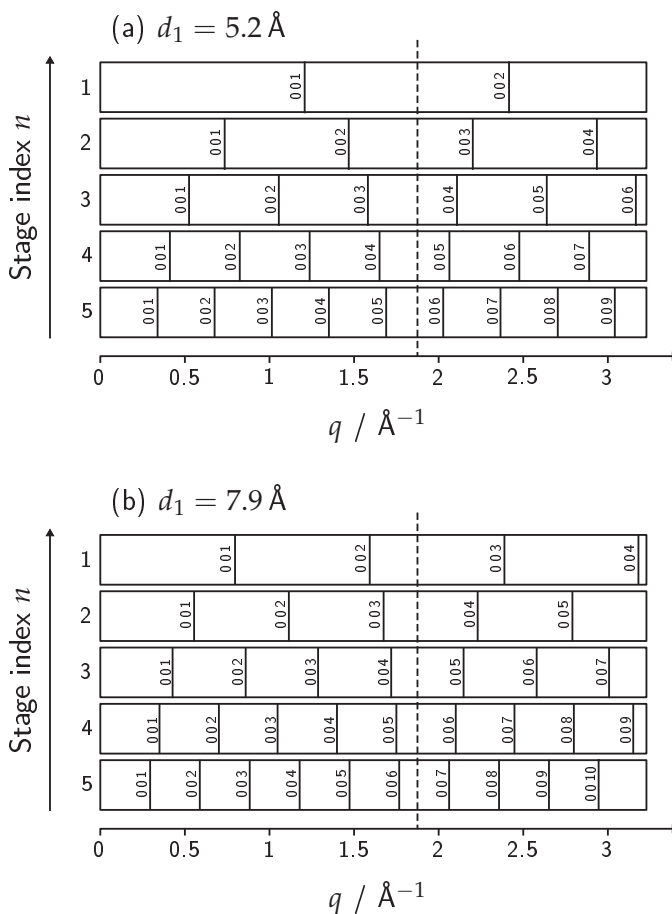
Figure 11.17.: Calculated positions of XRD peaks of pure stages in BF_4^- inter-calated GICs for (a) $d_1 = 5.2\,\text{Å}$ and (b) $d_1 = 7.9\,\text{Å}$. The dashed line indicates the position of the 002 reflection of pure graphite ($q = 1.87\,\text{Å}^{-1}$).

Figure 11.18 for the two cases, thus underlining the above statement regarding the splitting symmetry.
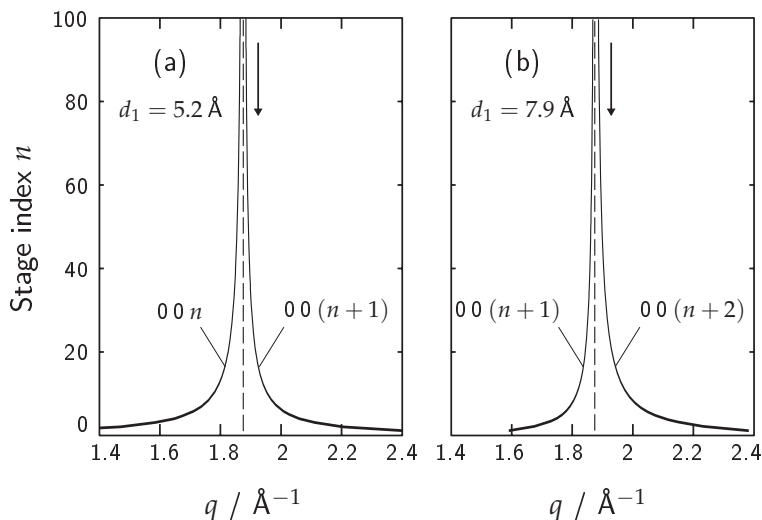
Figure 11.18.: Replacement of the 002 reflection of graphite (dashed line) with neighboring reflections of the staged GIC for progressively lower stage indices. Calculated based on the formation of pure staged compounds for (a) $d_1 = 5.2\,\text{Å}$ and (b) $d_1 = 7.9\,\text{Å}$.

The diffraction peak of the GIC located at the lowest q is always the 001 reflection. The corresponding d-spacing is equal to d_i. In Figures 11.12b and 11.13b, the reflection observed below $q = 0.5\,\text{Å}^{-1}$ in both electrolytes can therefore be identified as the 001 reflection of the respective BF_4^- GIC. From the symmetry of the splitting of the original 002 reflection of graphite, it appears as though anodic intercalation in the AN-based electrolyte (Figure 11.12b) corresponds to the case of a low sandwich thickness d_1 (Figure 11.17a). In this case, the diffraction peaks which replace the 002 reflection of graphite on either side are the $00n$ and $00(n+1)$ reflections of the GIC. Thus, an average stage index n may be estimated by considering the following equation:

$$n \, d_{00n} \ = \ (n+1) \, d_{00\,(n+1)}$$

$$n \ = \ \frac{d_{00\,(n+1)}}{d_{00n} - d_{00\,(n+1)}} \tag{11.3}$$

For BF_4^- intercalation from PC, the XRD patterns (Figure 11.13b) suggest a larger d_1 spacing corresponding more to Figure 11.17b. In this case, n can be estimated by

$$(n+1) \, d_{00n+1} \ = \ (n+2) \, d_{00\,(n+2)}$$

$$n \ = \ \frac{2 d_{00\,(n+2)} - d_{00\,(n+1)}}{d_{00\,(n+1)} - d_{00\,(n+2)}} \tag{11.4}$$

The fact that the apparent sandwich thickness d_1 depends on the type of solvent used strongly suggests solvent cointercalation. While the determination of n based on the two peaks in the vicinity of the original $0\,0\,2$ reflection is convenient, caution should be exercised as to which of the two equations above is applied. A general rule may be simply derived from Equation (11.2) by setting $d_{00k} = d_{002}$ in order to determine which $0\,0\,k_{gr}$ reflection of the GIC replaces the original $0\,0\,2$ reflection. It follows that

$$k_{gr} = n - 1 + x \tag{11.5}$$

where $x = d_1 / d_{002}$ is the ratio of the sandwich thickness to the graphite interlayer spacing. Thus, for $1 < x < 2$, the $0\,0\,n$ and $0\,0\,(n+1)$ reflection of the GIC are nearest to the $0\,0\,2$ reflection of graphite, while for $2 < x < 3$ it is the $0\,0\,(n+1)$ and $0\,0\,(n+2)$ reflections, and so on.

The average stage index n was calculated for BF_4^- intercalation in both solvents using Equations (11.3) and (11.4) for AN and PC, respectively. In both cases, minimum stage indices between 4 and 5 were obtained (Figure 11.19). The realization of similar stages is in agreement with the similar amounts of charge applied to the graphite electrode reversibly in both electrolytes (Table 11.2).

The stage indices were used in combination with the repeat distance d_i determined from the respective $0\,0\,1$ reflection of the BF_4^- GIC in order to calculate the sandwich thickness d_1 from Equation (11.1). For
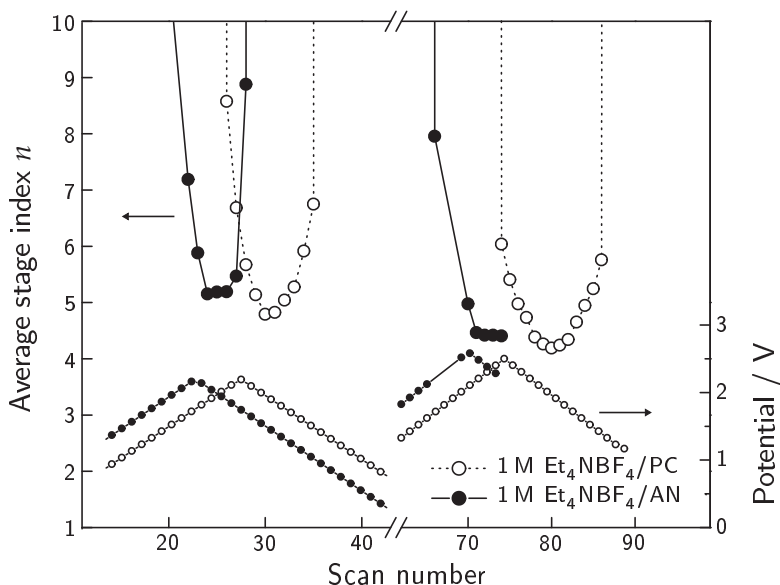
Figure 11.19.: Average stage index n for the intercalation of BF_4^- into SFG44 from the AN- and PC-based electrolyte solutions.

the AN-based electrolyte, d_1 was determined to be $5 \pm 0.3\,\text{Å}$ during intercalation while a value of $8 \pm 2\,\text{Å}$ was found during intercalation in the PC-based electrolyte.

For homogeneous staging, the relative height change h/h_0 of a single graphite crystallite during intercalation may easily be calculated by

$$\frac{h}{h_0} = \frac{d_i}{n\, d_{002}} = \frac{d_1 + (n-1)\, d_{002}}{n\, d_{002}} \tag{11.6}$$

Taking the d_1 values from above and a stage index of $n = 5$, height changes of 8–12 % and 16–40 % are estimated for BF_4^- intercalation into graphite from the AN- and the PC-based electrolyte, respectively. These values correspond roughly to those obtained by in situ dilatometry measurements under similar conditions (compare with Figure 11.9 and references [190, 288]).

The results strongly indicate that BF_4^- undergoes intercalation in the solvated state in the PC-based electrolyte. The question immediately arises whether solvent cointercalation also takes place in the AN-based electrolyte. In the latter case, it is possible that d_1 is dominated by the

larger size of BF_4^- compared to the smaller AN molecule ($41.4\,\text{Å}^3$ vs. $37.5\,\text{Å}^3$, Table 11.1), whereby the latter can also orientate itself favorably due to its linear structure. A molecule of PC, however, is significantly larger ($77.8\,\text{Å}^3$) than BF_4^- and may therefore be expected to influence d_1 upon cointercalation.

Considering that the expansion of graphite due to BF_4^- intercalation (and solvent cointercalation) was found to be greater in PC than in AN, it is perhaps unexpected that the crystallinity of the graphite lattice is less affected due to cycling in PC (Figure 11.15). Also, the CDEs during the first two anodic cycles in the PC-based electrolyte were the highest of the systems investigated here. Apparently, a larger expansion of the graphite lattice does not necessarily imply a more severe degradation of its structure.

A possible explanation for the increased degradation of the graphite lattice upon anodic cycling in AN might therefore be associated with the higher fraction of irreversible faradaic charge transfer associated with cycling in this electrolyte. Such faradaic losses can be ascribed to electrolyte decomposition or ion trapping within the graphitic structure, both of which could have a detrimental effect on the *c*-axis periodicity of graphite. Electrolyte decomposition within the graphite lattice would imply that AN also coinserts into graphite during BF_4^- intercalation, but with a lower anodic stability than cointercalated PC. Evidence for the lower anodic stability of AN was also observed in the context of the electrochemical characterization of YP17 (Chapter 9).

From the changes in the $0\,0\,2$ reflection, it was found that the graphite structure appeared to degrade markedly in both AN and in PC during cathodic cycling (Figure 11.15). Due to its significantly lower charge density, Et_4N^+ is likely to be less solvated than BF_4^-, if at all [72]. Santhanam and Noel [470] suggested that Bu_4N^+ intercalates into graphite without the cointercalation of solvent molecules (e.g. PC) due to the intrinsic hydrophobicity of this cation. Yet, the type of solvent used in the present work had a pronounced influence on the CDE of Et_4N^+ intercalation, again suggesting that electrolyte decomposition within the graphite lattice may have occurred.

11.3.2. In situ WAXS of YP17

Results

Compared to graphite, YP17 only featured very weak and diffuse wide-angle scattering due to the lack of structural periodicity. In fact, it was observed that the scattering contribution due to the electrolyte solution was larger than the scattering features associated with YP17 itself (Figure 11.20).

Obviously, this presented a significant complication during the in situ WAXS measurements. Repetition of wetting experiments of the type shown in Figure 11.20 using SFG44 as working electrode confirmed that the change in WAXS pattern was not due to a structural change of the activated carbon itself or its porosity during wetting, but rather due to scattering from the bulk electrolyte solution. It is well known that electrolyte solutions exhibit scattering maxima due to short-range order within the solvation shell, with XRD often being capable of resolving the first solvation shell of ions [482–484]. However, no systematic studies in this respect were performed in the present work.

Upon wetting of YP17 in either electrolyte, the intensity at low q due to small-angle scattering was significantly reduced. This may be explained by a filling of the porosity with the electrolyte solution, which reduces the electron density contrast between solid and void fractions
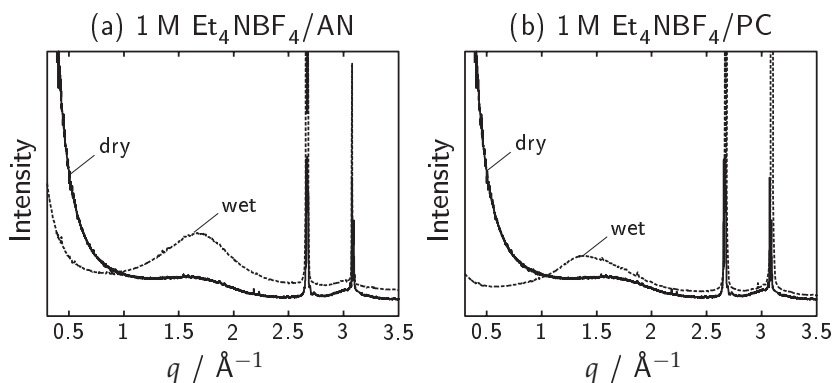
Figure 11.20.: Effect of the electrolyte solution on the WAXS of YP17 in (a) 1 M Et_4NBF_4/AN and (b) 1 M Et_4NBF_4/PC. The two XRD peaks at higher q arise due to the aluminum windows of the in situ cell.

of the carbon. From the curves in Figure 11.20, the intensity reduction is more pronounced for the PC-based electrolyte, which might be expected due to its higher gravimetric and thus higher electron density compared to the AN-based electrolyte.

In situ WAXS measurements were performed on YP17 in the negative and positive potential ranges under a variety of conditions. In all cases, the changes in the WAXS patterns were found to be very small even at extreme potentials. Representative data is summarized in Figure 11.21 for the AN-based electrolyte and in Figure 11.22 for the PC-based electrolyte. Extremely faint but reversible intensity variations around the main region of scattering from the overlapping diffuse 0 0 2 band of YP17 and the electrolyte scattering maximum were observed in both cases during polarization to -2.5 V and +2 V, respectively.

Discussion

Due to the dominant electrolyte scattering contribution, no definitive conclusions can be drawn regarding structural changes of YP17 based on the WAXS experiments in the present work. However, at the lowest q values accessible in these experiments, it was found that the intensity of the small-angle scattering varied in a more pronounced fashion than the WAXS features shown in Figures 11.21 and 11.22. This observation implies that changes in the scattering behavior may take place on length scale of the porosity of activated carbon, which was not accessible at a sufficiently high resolution during the WAXS experiments. This initiated further experiments dedicated to SAXS, which are reported in Chapter 12.

While ion insertion between parallel graphene sheets in YP17 cannot be ruled out, there are a number of arguments which suggest that this contribution to charge storage and dimensional changes is small compared to the pore insertion mechanism postulated previously in this chapter.

First, the fraction of graphene sheets stacked in parallel is estimated to be very small compared to the number of single graphene sheets and other structural units which are bounded by microporosity. This statement is based on the accessible surface area for nitrogen adsorption (Table 9.5) and the diffuse WAXS pattern of YP17. In their studies on
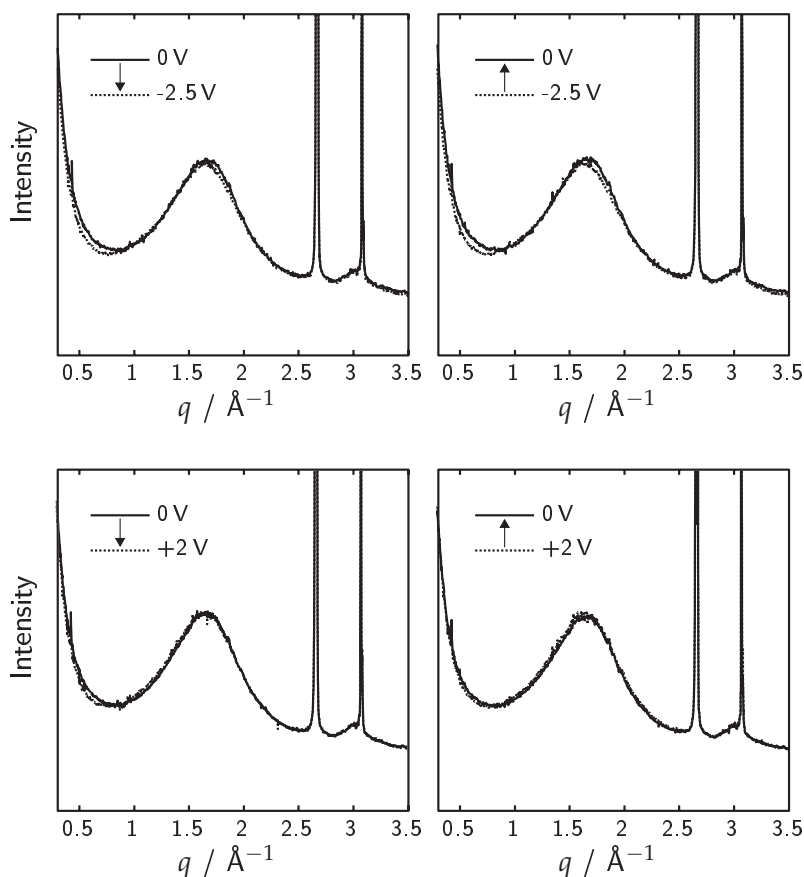
Figure 11.21.: WAXS patterns of YP17 in $1\,M$ Et_4NBF_4/AN before, during and after extreme negative (top) and positive (bottom) potentials.

various hard carbons, Liu et al. [485] arrived at a similar conclusion, leading to the development of the house of cards or falling cards model for hard carbons [485–487].

In addition, the absence of hkl reflections for YP17 indicate that the graphene sheets arranged in parallel are misoriented with respect to each other. It has been shown by Zheng et al. [488, 489] that Li^+ intercalation between parallel graphene sheets with a turbostratic alignment is significantly hindered, and the corresponding interlayer spacings have been described as blocked galleries. Essentially, this is due to the fact that Li GICs feature a well-defined stacking sequence of the graphene
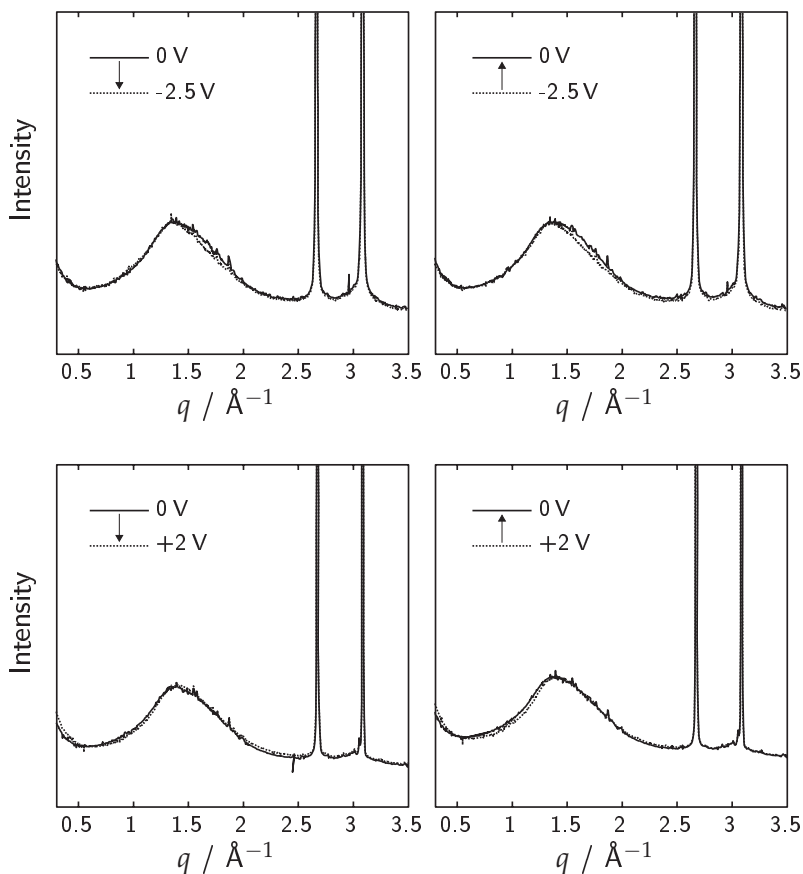
Figure 11.22.: WAXS patterns in $1\,\mathrm{M}$ Et_4NBF_4/PC before, during and after extreme negative (top) and positive (bottom) potentials of YP17.

layers, whereas turbostratic graphene sheets can be considered to be pinned to a certain extent by defects [488, 489]. It is likely, however, that turbostratic disorder of stacked graphene sheets hinders the intercalation of other ions, also. Therefore, there are strong arguments that the intercalation of ions into the interlayer spacing of parallel graphene sheets is not a mechanism which contributes significantly to charge storage or structural degradation in activated carbons such as YP17.

11.4. Effect of graphene sheet spacing

The fact that the formation of GICs via electrochemical intercalation depends on the electrode potential has long been established. From the point of view of charge storage, this class of materials represents a limiting case in which charge storage is either practically zero (due to the very low interfacial area between the non-porous electrode and electrolyte) or very high (due to the utilization of the electrode bulk) depending on the potential range.

For activated carbons in EDLCs, it is generally assumed that the charge storage is governed by charge accumulation within the electrochemical double layer, with the interfacial area between electrode and electrolyte being invariant during polarization. In fact, the pore size distributions determined by gas adsorption techniques and comparisons with the theoretical dimensions of solvated or unsolvated ions are often used to discuss ion accessibility (e.g. [81, 103, 329, 490, 491]).

However, there is a priori no reason to assume that the interfacial area between electrode and electrolyte is independent of the electrode potential. In fact, severe errors in interpretation may be made on this premise. An extreme example serves to illustrate this point. The integral capacitance of SFG44 in the potential window between $0\,V$ and $-2.5\,V$ is in the order of $35\,F\,g^{-1}$ (obtained from the data presented in Figure 11.1). Normalized to the BET surface area of SFG44, an enormous specific capacitance of $700\,\mu F\,cm^{-2}$ is obtained. Similarly, a petroleum coke based carbon material developed by Takeuchi, Okamura et al. [463–466] exhibited a BET surface area significantly below $100\,m^2\,g^{-1}$, but delivered capacitances comparable to conventional high surface area activated carbons. Takeuchi et al. [464] presented some evidence that the cell voltage at which capacitance enhancement of their essentially non-porous electrode materials occurred depended on the d_{002} spacing.

Clearly, the error made in the calculation of specific capacitances from highly porous electrodes with a rigid framework is not as drastic as for the above non-porous materials. However, the results presented so far in this chapter demonstrate that SWCNTs and activated carbons undergo measurable macroscopic dimensional changes. For the former,

a capacitance enhancement of 30 % following a widening of the potential window was found, with evidence pointing towards electrolyte infiltration into previously inaccessible void space. The analogy to the interpretation of the capacitance enhancement of carbon blacks by Kim et al. [492] upon electrochemical polarization is worth pointing out.

In this section, first results are presented regarding the influence of interlayer spacing between parallel graphene sheets on the potential-dependent charge storage capability. The motivation behind these experiments was based on the concept of facilitating ion insertion by increasing the distance between graphene sheets. Starting from graphite with a separation distance of 3.35 Å and extending the above discussion to slit-shaped pores of widths in the order of 10 Å, it is conceivable that the occupation of intermediate length scales by ions depends on the electrode potential in a continuous manner.

The material used to investigate the effect of the graphene sheet separation distance in the present work was provided by Tommy Kaspar (ETH Zurich). Briefly, a graphitic starting material (natural graphite powder, Alfa Aesar) was chemically oxidized in a concentrated mixture of HNO_3 and $NaClO_3$, resulting in the formation of a non-conductive GO [493] with a characteristic interlayer spacing close to 5.9 Å in the dry state. Due to a loss of well-defined stacking order during this process, the interlayer spacing of GO and its derivatives is denominated d_{001} in the following. In a subsequent step, d_{001} was gradually reduced via a controlled thermal reduction, enabling to obtain conductive materials with d_{001} values in the range of about 3.4 Å to 5 Å. The samples produced by the above method were used as working electrodes without the addition of binder.

This technique of electrode preparation bears significant promise for systematic investigations regarding the influence of the interlayer distance on the electrochemical performance of carbonaceous electrodes. This is demonstrated in the following by presenting a selection of initial results.

Results

A GO-derived material with an interlayer spacing of 4.5 Å (GO45) was investigated in $1\,M$ Et_4NBF_4/AN via electrochemical dilatometry in the

negative potential range and in situ XRD in both the negative and positive potential ranges.

From electrochemical dilatometry, the current rise during the initial potentiometric cycle (Figure 11.23, top) occurred near -0.7 V, significantly earlier than for crystalline graphite (ca. -2 V, see Figure 11.1). At the same time, the charging of the material marked the onset of a considerable height increase by up to almost 60 %. The irreversible height change following this initial cycle was in the order of 20 %.

The subsequent CVs suggested markedly slow charging and discharging kinetics, with reversible expansions in the order of 30 % occurring during cycling. These apparently large dimensional changes
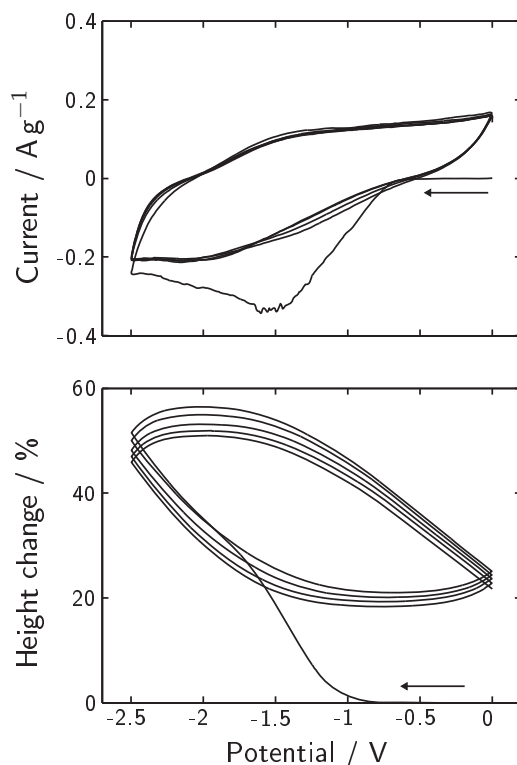
Figure 11.23.: CVs (top) and concomitant height change (bottom) of GO45 in 1 M Et_4NBF_4/AN during five cycles between 0 V and -2.5 V. The sweep rate was $1\,mV\,s^{-1}$ and the initial electrode height was $150\,\mu m$.

are put into perspective when related to the amount of charge applied to the electrode (Figure 11.24). Thus, the expansion of the electrode is actually less per unit charge than for SFG44, and the pronounced expansion observed for GO45 can thus be explained by the considerably higher capacity in a given potential window when compared to SFG44.

The CVs recorded during the in situ XRD measurements are summarized in Figure 11.25. The potential of intercalation onset upon negative polarization agrees well with the value deduced from electrochemical dilatometry, although the shape of the subsequent CV implies faster charging and discharging kinetics than observed during the dilatometry measurement. Reasons for this discrepancy may include different electrode thicknesses and compression or a smearing of the electrode potential due to the two-electrode setup used for the in situ XRD experiments.
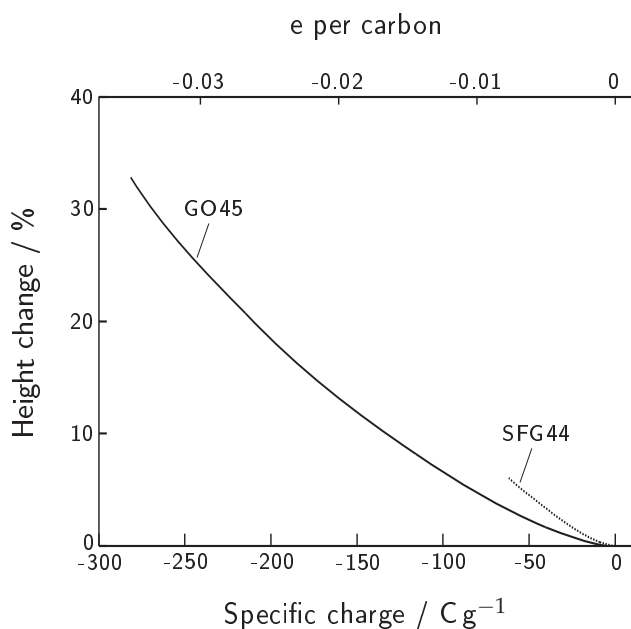
Figure 11.24.: Height change of the material investigated in Figure 11.23 as a function of the applied charge for the forward scan of the third cycle. For comparison, the expansion of SFG44 from Figure 11.9 is shown.

271
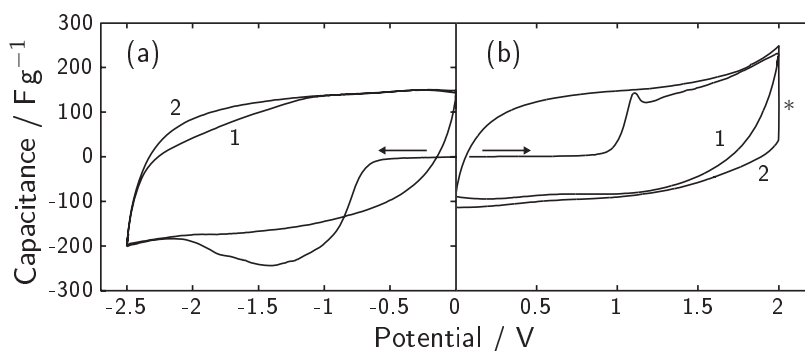
Figure 11.25.: CVs recorded during in situ XRD experiments on GO45 in 1 M Et$_4$NBF$_4$/AN at sweep rates of 1 mV s-1 (a) and 0.5 mV s^{-1} (b). The numbers indicate the measurement sequence in each experiment. A potential holding period was introduced at ∗.

In the positive range, a potential of ca. +1 V for the onset of significant charging was observed (Figure 11.25) compared to +1.7 V for SFG44 (Figure 11.1). The in situ XRD patterns recorded during the first potentiometric cycles in either potential range are shown in Figure 11.26. The 0 0 1 peak of GO45 was located at $q = 1.4$ Å^{-1}, corresponding to the interplanar distance of 4.5 Å. Compared to the diffractograms of SFG44 in the previous section, the lower intensity and larger FWHM of the 0 0 1 reflection in the present case implies a significantly lower periodicity in the *c*-axis direction. A strong scattering maximum near the expected 1 0 0 and 1 0 1 reflections of graphite was observed, and is labeled 1 0 x in Figure 11.26. The associated in-plane periodicity can thus be stated to exhibit long-range order. The absence of *h k l* reflections at higher *q* implies a misorientation of parallel graphene sheets with respect to each other in a turbostratic manner.

The rapid loss of intensity for the 0 0 1 reflection upon polarization in either potential range confirms that the initial charging currents observed in the CVs are due to the intercalation of electrolyte species into the electrode bulk. The appearance of broad scattering maxima at low *q* (Figure 11.26) suggest that a periodic structure was formed during intercalation. It was not possible to unambiguously identify the presence of pure staged phases in this case, but the development of these diffuse
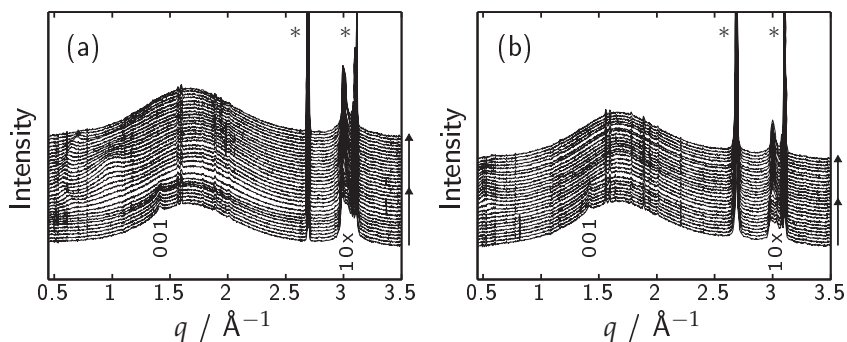
Figure 11.26.: XRD patterns of GO45 recorded during the first cycle of the CVs in Figure 11.25 in the negative (a) and positive (b) potential ranges. The reflections originating from GO45 are labeled with the corresponding Laue symbols while the diffraction peaks of the aluminum windows of the in situ cell are marked by an asterisk ($*$).

maxima indicate that the intercalated layers tend to arrange themselves at certain characteristic intervals.

It is interesting to note that the most pronounced indications for staging were found during Et_4N^+ intercalation into GO45, whereas for SFG44 this was precisely the case for which no well-ordered staging was observed.

Discussion

Despite the need for further studies on GO-derived electrode materials in order to improve the understanding of their electrochemical behavior in non-aqueous electrolytes, a number of important points can be made on the basis of the limited study presented here. In the context of the previous results discussed in this chapter, the behavior of GO-derived electrodes highlights the influence of the carbonaceous structure on the potential-dependent insertion of ions into confined spaces.

The potential onsets for the intercalation of ions were significantly modified with respect to crystalline graphite, which may be attributed to the wider interlayer spacing between the graphene sheets in the sample investigated here. The facilitation of ion access to the bulk results in a greater charge storage capability for a given potential window. As a consequence, the height change of the electrode is larger during po-

tentiometric cycling. However, normalized to the amount of charge applied to the electrode, the expansion of the GO-derived material was found to be less than that of the microcrystalline graphite powder SFGG. Assuming that the effective size of the intercalated ions is the same for both materials, the different expansions may be understood on a qualitative basis by considering that the larger interlayer spacing of the GO-based electrode ($d_{001} = 4.49\,\text{Å}$) expands less than that of SFG44 ($d_{002} = 3.35\,\text{Å}$) in order to accommodate the intercalated species. However, it is also possible that the sizes of the intercalated ions vary in the two cases, as the in situ XRD patterns indicate differences in the intercalation mechanisms.

In addition, past studies have indicated that turbostratic disorder can hinder or even suppress the intercalation of ions (see the discussion starting on page 265). Evidently, this is not the case for the GO-derived material studied here. Apparently, the wider separation distance between graphene sheets alleviates the restrictions imposed by turbostratic disorder. Clearly, more work is needed to elucidate the particular mechanisms of ion intercalation into expanded graphite structures.

11.5. Conclusions

During the polarization of carbons in EDLC electrolytes, dimensional changes of the electrodes occur depending on the electrode potential and on the carbon structure, indicating deviations from the idealized concept of double layer charging during which the porous electrode is pictured as a strictly rigid, electronically conducting framework.

More specifically, it was found that all electrode materials studied in this chapter—SFG44, SWCNTs, YP17 and GO45—exhibited more or less pronounced dimensional changes during charging.

For SFG44, the expansion during charging can be unambiguously assigned to the intercalation of electrolyte species into the bulk graphite lattice. Notably, it was found that the intercalation of BF_4^- above ca. $+1.8\,\text{V}$ results in the formation of staged compounds with simultaneous cointercalation of the solvent. Et_4N^+ was also shown to intercalate into graphite at sufficiently negative potentials, below ca. $-2\,\text{V}$,

whereby no clear indication of staging could be observed by in situ XRD. After only one or two intercalation/deintercalation cycles, the periodicity of SFG44 perpendicular to the graphene sheets was severely disrupted, presumably due to the decomposition of intercalated electrolyte species, while the in-plane periodicity was not significantly affected. The lowest amount of structural degradation was found for the PC-based electrolyte in the positive potential range, for which the coulombic efficiency of the intercalation process was also observed to be highest in the present work, presumably due to the improved anodic stability of PC compared to AN.

While the expansion and thus intercalation of ions into the graphite lattice required relatively large polarizations, it was found that both SWCNTs and YP17 expanded practically immediately upon polarization. Evidence for the loosening of SWCNT bundles due to the insertion of ions into the interstitial porosity was presented, which was shown to result in a capacitance enhancement as a consequence of the increased interfacial area between electrode and electrolyte. Besides an irreversible expansion during the initial ion infiltration into the SWCNT bundles, cyclic dimensional changes were also found during charge/discharge due to the accumulation and expulsion of ions in and out of the electrochemical double layer within bundles.

The potential-dependent reversible expansion of YP17 was very similar to that of the SWCNTs. Due to the very diffuse WAXS of activated carbon and the overlapping scattering contribution from the electrolyte solution, no conclusive results concerning the insertion of ions into interlayer spacings between neighboring graphene sheets could be obtained in the present work. However, it is very likely that the dimensional changes of YP17 are dominated by the same phenomenon as described for the SWCNTs above, namely an exchange of ions within micropores during double layer charging and discharging along with the corresponding fluctuating steric requirements. Given the dominance of such a pore expansion mechanism, it appears unlikely that ion intercalation between stacked graphene sheets contributes significantly to charge storage or structural degradation in YP17. Since YP17 exhibits a distribution of micropore widths at dimensions approaching those of the electrolyte species, it is conceivable that successively

smaller pore widths are filled at increasing polarizations. Such ion insertion processes differ notably from intercalation in that the former is characterized by a relatively broad distribution of site energies, while the latter is relevant for isoenergetic sites such as those found within well-ordered graphite crystallites.

Initial experiments on electrodes derived from GO demonstrated that a widening of the interlayer distance between graphene sheets facilitates the insertion of ions. However, even with an interlayer spacing (4.5 Å) larger than that of YP17 (3.9 Å), intercalation did not take place at potentials in the region of expansion of YP17. This supports the notion that the expansion of YP17 is dominated by the accumulation of ions within micropores during charging rather than the intercalation of ions between parallel graphene sheets.

Chapter 12.

In situ small-angle X-ray scattering of activated carbon

12.1. Motivation

In Chapter 11, it was proposed that the most pronounced structural changes of YP17 during electrochemical charging in EDLCs occur on the length scale of the microporosity rather than due to changes on the level of interatomic spacings or stacked graphene sheets.

An analysis of the porosity of activated carbon in situ is possible by SAXS (Section 8.3.3). For a disordered porous solid with a bimodal pore size distribution, the scattered intensity i depends on the scattering parameter $q = 4\pi \sin\theta/\lambda$ according to

$$i = \frac{A}{q^{n_1}} + \frac{B\, a^{n_2}}{(1 + q^2 a^2)^{n_2/2}} \tag{8.14}$$

where a is the Debye correlation length, which is a measure for the mean spacing between interfaces, while n_1 and n_2 are the scattering exponents which describe the fluctuation of electron density within phases for each pore mode.

Each of the coefficients A and B describes the scattering intensity on a different length scale, whereby A is relevant for the scattering from large length scales (e.g. macropores) and B is valid for short length scales (e.g. micropores). Considering a constant porosity, both coefficients are directly proportional to the square of the electron density contrast, Δn_e^2, and the interfacial area, S, so that

$$A, B \propto \Delta n_{e,A,B}^2\, S_{A,B} \tag{8.11}$$

Clearly, changes in the parameters A, B and a during electrochemical charging are of significant interest. On one hand, changes in the

electrolyte composition (electron density contrast) within micropores should be reflected in B. Also, the possibility to detect modifications of the characteristic spacing between interfaces, a, is of relevance for the hypothesis brought forward in the previous chapter concerning ion insertion into micropores.

In this chapter, it is shown that the interpretation of the in situ SAXS results obtained for YP17 in the present work is not straightforward. Nonetheless, this approach to detecting changes in the porous structure of EDLCs during electrochemical charging is novel in the field of EDLC research and represents an interesting research tool for further investigations. The most important findings and results relevant for the present work are summarized in the following.

12.2. Results and discussion

The small-angle scattering curves of YP17 and $1\,M$ solutions of Et_4NBF_4 in AN and in PC were measured separately in sealed glass capillaries in order to quantify the scattering contribution of each component (Figure 12.1).

A significant SAXS of YP17 was observed over a wide q range, while the scattering contribution of the two electrolyte solutions was found to be negligible for $q \leq 0.3\,\text{Å}^{-1}$. At larger q values, the data presented in
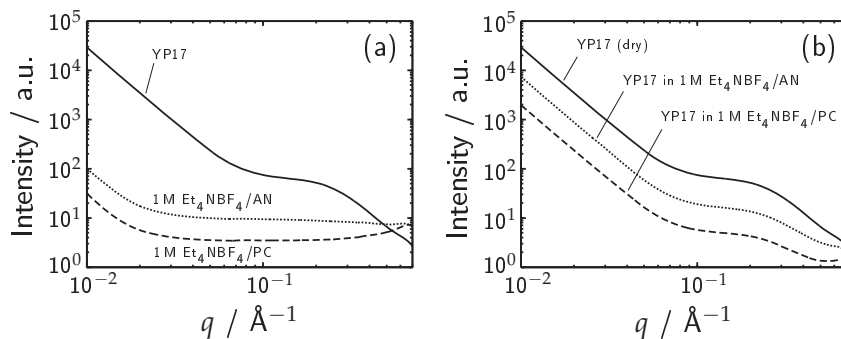
Figure 12.1.: SAXS curves of different samples analyzed in sealed glass capillaries. (a) Separate measurements of dry YP17 and the AN- and PC-based electrolytes, (b) YP17 in the dry state and wetted with the two electrolyte solutions.

Figure 12.1 indicates a significant contribution of the electrolyte which eventually exceeds the scattering from the carbon. It was found that the immersion of YP17 in the electrolytes (Figure 12.1b) resulted in an attenuation of the scattering signal due to the increased absorption of the electrolyte solution without affecting the shape of the scattering curve for $q \leq 0.3\,\text{Å}^{-1}$. At higher q, the scattering was affected significantly by the electrolyte scattering. This finding is in accord with the significant electrolyte scattering contribution observed during the WAXS experiments in Section 11.3.2.

An example of data fitting by means of Equation 8.14 is shown in Figure 12.2 for dry YP17. The parameter n_2 was limited to a maximum value of 4. The quality of the overall fit was acceptable considering that the measured data spans several orders of magnitude and a simple bimodal size distribution of scattering centers was assumed. The fitting parameters are summarized in Table 12.1 for dry and wetted YP17.

For the coefficients A and B, only relative values are given here since the scattering intensity was not measured in absolute units, which would require a precise knowledge of the illuminated sample volume. However, from the results in Table 12.1, it can be seen that B was always at least two orders of magnitude greater than A, indicative of the
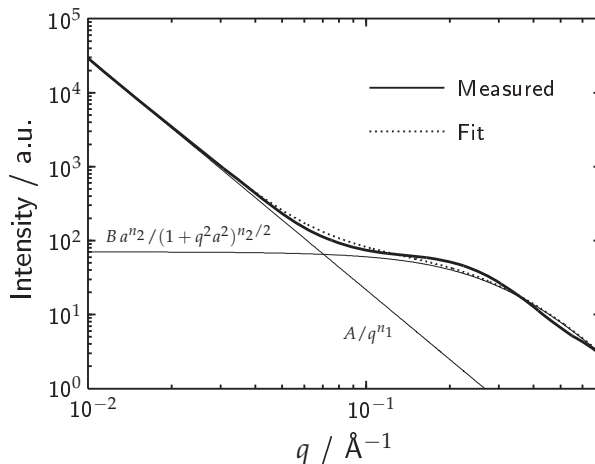
Figure 12.2.: Curve fitting (dotted line) of experimental data (solid line) obtained from dry YP17. Separate contributions of the two terms in Equation (8.14) are indicated.

Table 12.1.: Fitting parameters for the measurements shown in Figure 12.1 using Equation (8.14) in combination with a non-linear least squares fitting routine in MATLAB™. The fitting error was less than 10 % for all values based on the 95 % confidence bounds of the fit. All data series were fitted for $q < 0.37\,\text{Å}^{-1}$. The values in brackets indicate fitting results for which n_1, n_2 and a were fixed at the values obtained for dry YP17.

Parameter	YP17 dry	YP17 1 M Et$_4$NBF$_4$/AN	YP17 1 M Et$_4$NBF$_4$/PC
A / a.u.	$1.6 \cdot 10^{-2}$	$4.3 \cdot 10^{-3}$ ($3.9 \cdot 10^{-3}$)	$1.3 \cdot 10^{-3}$ ($1.0 \cdot 10^{-3}$)
B / a.u.	1.5	1.2 (0.4)	0.57 (0.13)
a / Å	2.6	1.9 (2.6)	1.7 (2.6)
n_1	3.1	3.1 (3.1)	3.1 (3.1)
n_2	4.0	4.0 (4.0)	4.0 (4.0)

large value of S_B compared to S_A. Further, the values for A and B were roughly 3–4 as high in the AN- compared to the PC-based solution. Presumably, this reflects the lower attenuation of scattered intensity by the lower density electrolyte solution (compare with Figure 12.1).

It should be noted that the Debye correlation length a was found to depend on the presence of electrolyte (Table 12.1). In both electrolyte solutions, a decrease in the correlation length was observed. Thus, the fitting parameters obtained for wetted YP17 must not be considered representative of the carbonaceous phase alone. Rather, the results describe scattering properties which result from the combination of carbon and electrolyte. Similar values for the correlation length a have also been reported previously for hard carbons [310, 313, 486]. The radius of gyration R_g [301] of a spherical scatterer is obtained from a by $R_g = \sqrt{6}\,a$ [310], resulting in R_g values of 4–6 Å in the present work.

The scattering exponents n_1 and n_2 were found to be virtually independent of the presence of electrolyte, suggesting that the electron density fluctuations in the solid phase are not affected by wetting with the electrolyte solutions. The scattering exponent n_1 was 3.1 for both electrolytes, the deviation from 4 indicating electron density fluctuations within either the carbonaceous phase or the solution phase on a

length scale much larger than the microporosity. Scattering from YP17 particles (diameter 3–20 μm) could be at the origin of these fluctuations, since the electron density within the grains is far from constant.

For SAXS measurements on YP17 using the in situ cells, the fitting parameters A and B decreased due to enhanced absorption and the resulting loss of scattered intensity. Further, the scattering exponent n_1 was found to increase to 3.4–3.6, presumably due to additional scattering contributions from other cell components such as the glass fiber separator.

YP17 powder was polarized in the negative and positive potential ranges in separate in situ cells for both electrolyte solutions by applying potential steps of ± 0.5 V between 0 V and -2.5 V or +2 V and allowing the charging current to decay to a negligible value prior to recording the SAXS data. The experimental data and corresponding fits obtained in 1 M Et_4NBF_4/AN are summarized in Figure 12.3. The most pronounced change observed in either potential range was the drop in scattered intensity during charging. A slight recovery of intensity was recorded during discharge, but an overall irreversible intensity loss was maintained after one full charge/discharge cycle.

Similar behavior was noted in the PC-based electrolyte (Figure 12.4), in which the intensity loss during charging was only partially recovered following discharge. In either electrolyte, no pronounced changes in the SAXS curves could be discerned apart from the mentioned intensity variation.

A more detailed assessment of the data was performed by fitting the SAXS data at each potential using Equation (8.14). In order to reduce the number of fitting parameters, the exponents n_1 and n_2 were determined at 0 V and kept constant for subsequent fits. This approach is justified under the assumption that the electron density fluctuations within phases are not significantly modified during charging and that the shape of the scattering centers does not change. For these conditions, the evolution of the fitted coefficients during the first charge/discharge cycle in the negative and positive potential ranges is summarized in Figures 12.5 and 12.6.

Before engaging in a detailed interpretation of the variations exhibited by the fitting coefficients during polarization, it should be noted
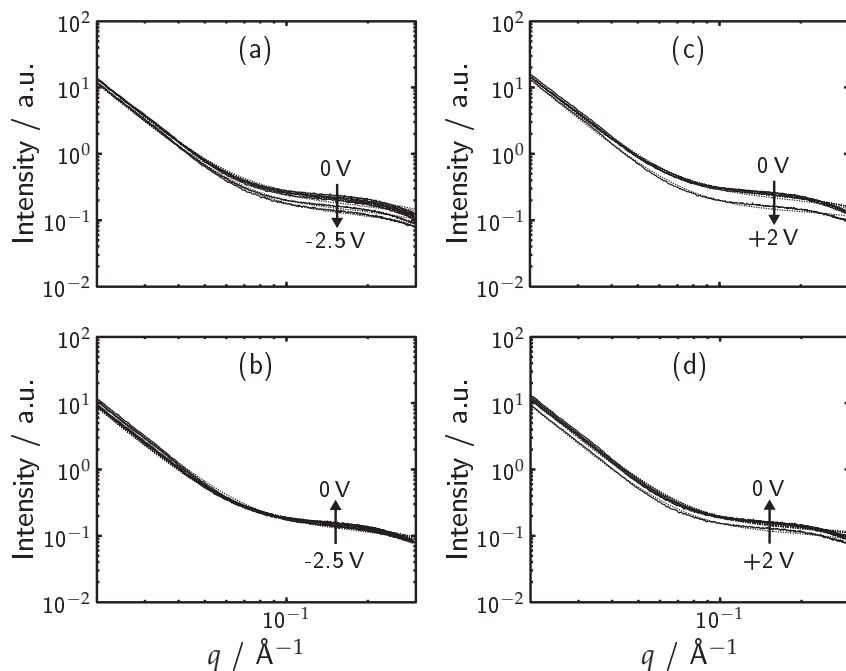
Figure 12.3.: In situ SAXS curves during polarization of YP17 in 1 M Et$_4$NBF$_4$/AN for the negative (a, b) and positive (c, d) potential ranges. Both the experimental data (solid lines) and corresponding fits (dotted lines) are shown.

that the changes observed were usually very small and often within the uncertainty of the fit. This observation attests a certain robustness of the structure of YP17 during electrochemical charging. However, a few other useful conclusions can be drawn. In both the AN- and PC-based electrolyte, the parameter A was reduced during the charge/discharge experiment, thus explaining the observed intensity loss of the SAXS curves during polarization. According to Equation (8.11), such a variation implies either a loss of interfacial area on the macropore scale within the illuminated sample volume or a change in electron density within the particles and/or the electrolyte solution. The loss of interfacial area would require the elimination of porosity by fusing of the carbon, which appears unlikely. Thus, changes in A can probably be attributed to changes in the electron density of either phase.
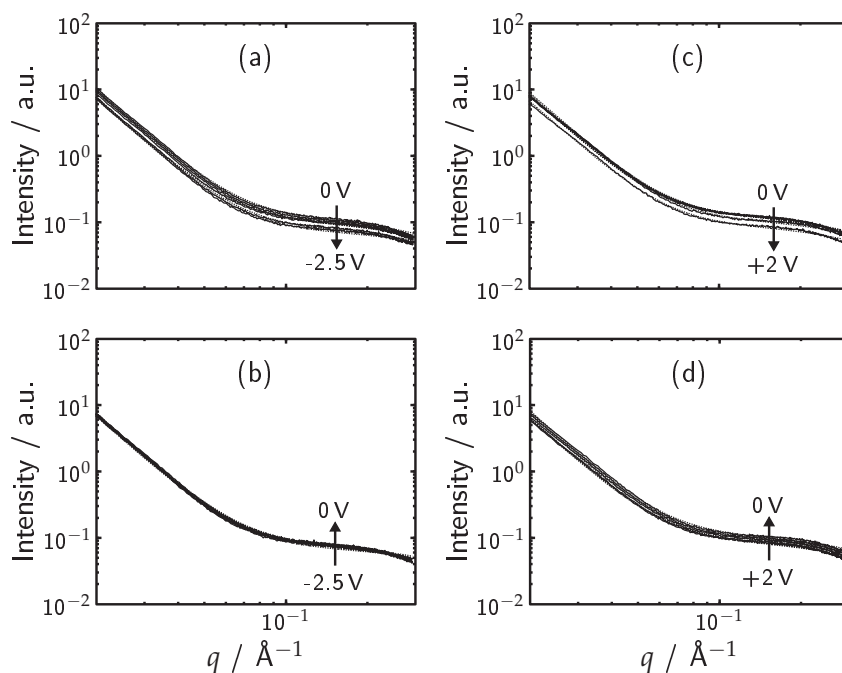
Figure 12.4.: In situ SAXS curves during polarization of YP17 in 1 M Et$_4$NBF$_4$/PC for the negative (a, b) and positive (c, d) potential ranges. Both the experimental data (solid lines) and corresponding fits (dotted lines) are shown.

A similar interpretation may be brought forward concerning variations of the parameter *B* during polarization. A marked increase in *B* was observed upon charging of YP17 in 1 M Et$_4$NBF$_4$/AN to beyond +1.5 V (Figure 12.5), indicative of pronounced changes in the electron density contrast on the length scale of microporosity. Simultaneously, the correlation length *a* dropped notably. Even though it should be borne in mind that these results represent single measurements, it is interesting to note that the AN-based system at potentials above +1.5 V proved the least stable of all investigated systems in the present work (Section 9.2.6). Therefore, it is tempting to ascribe the changes in the fitting coefficients at +2 V in the AN-based electrolyte to significant electron density variations within micropores as a consequence of chemical changes such as the formation of degradation products. It is worth
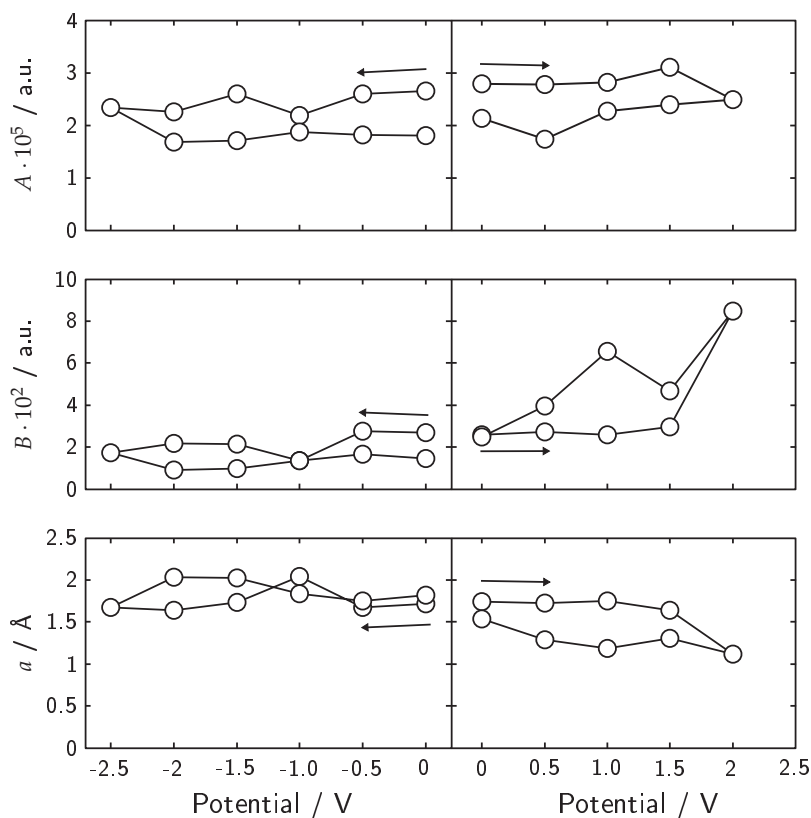
Figure 12.5.: Evolution of the fitting coefficients as a function of the electrode potential of YP17 in 1 M Et$_4$NBF$_4$/AN.

pointing out that a similar hypothesis was proposed based on the pronounced increase in Raman intensity at these potentials (Figure 10.16). The variations of the parameters a and B at +2 V in 1 M Et$_4$NBF$_4$/AN imply that the postulated chemical changes directly affect the microporosity of YP17, which may be expected have an important influence on the electrochemical performance and thus explain the capacitance loss of YP17 upon polarization in this potential range (Section 9.2.6).

In the PC-based electrolyte solution, variations in B and a were most pronounced in the negative potential range (Figure 12.6), indicating a qualitative difference to the above case in AN. During the electrochemical characterization of YP17 in 1 M Et$_4$NBF$_4$/PC (Section 9.2.6), it was
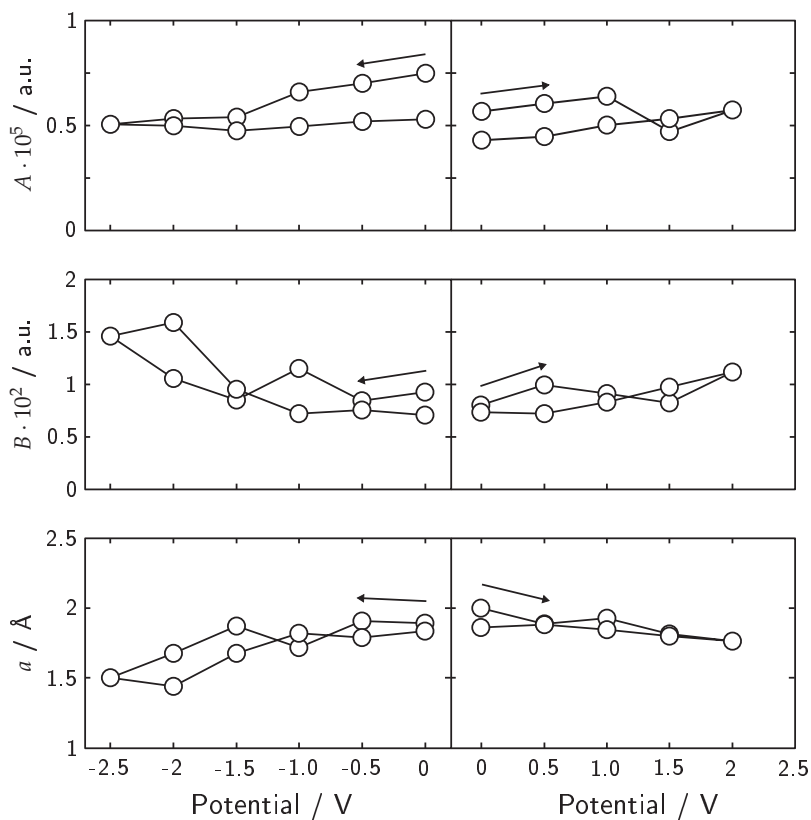
Figure 12.6.: Evolution of the fitting coefficients as a function of the electrode potential of YP17 in $1\,M\ Et_4NBF_4/PC$.

found that the capacitive behavior was modified notably upon polarization to -2 V and below. The SAXS results presented here offer indications that chemical changes may occur within the microporosity of YP17 at these negative potentials in the PC-based electrolyte. However, since the data was collected over a time period of only a few hours, further work is needed to assess the importance of these changes in the context of aging in both the AN- and the PC-based electrolyte solution.

12.3. Conclusions

Using SAXS, it was possible to access a q range in which the electrolyte scattering contribution was negligible compared to that of the activated carbon YP17. Thus, in situ experiments could be performed at different electrode potentials for the AN- and PC-based EDLC electrolytes and the changes interpreted in terms of a scattering model for disordered two-phase systems with bimodal pore size distributions.

The obtained results indicate that the porous structure of YP17 remains essentially intact during extreme polarizations to -2.5 V and +2 V for durations in the order of 1 hour, with the notable exception in the case of YP17 in the AN-based electrolyte after polarization to +2 V. In this case, a modification of the pore structure was suggested by an irreversible decrease in the Debye correlation length a and pronounced variations in the electron density contrast on the length scale of micropores. To a lesser extent, similar variations were found for YP17 below -1.5 V in the PC-based electrolyte.

No evidence was obtained for a modification of the electron density fluctuation within the solid phase, thus supporting the hypothesis established in Chapter 11 according to which ion intercalation does not contribute significantly to structural degradation in YP17.

Due to irreversible changes in parameters describing the electron density contrast between carbon and electrolyte, it is likely that electrochemical modifications occur within either or both of the two phases. Thus, it may be proposed that these irreversible changes are an indication of the formation of degradation products in extended potential regions within both macro- and micropores.

Chapter 13.

Electrolyte degradation at the electrode surface

13.1. Motivation

The previous chapters have dealt with investigations primarily concerned with structural changes undergone by the electrode material, activated carbon, following electrochemical treatment in EDLC electrolytes at extreme negative and positive potentials. The results obtained in the present work indicate that the structure of activated carbon in terms of its porous $C-C$ bonded framework remains essentially intact during exposure to these strongly reducing and oxidizing potentials (Chapter 10).

As a consequence, it is of increasing importance to obtain insights into the possible degradation pathways of the electrolyte solution. In the extended potential ranges, electronic charge transfer may occur across the enormous interface between activated carbon and the electrolyte due to the large electric field established within the Helmholtz layer. The resulting redox reactions may in principle involve any electrolyte species within the double layer, i.e. cation, anion and solvent. Since the electronic charge on the carbon is relatively dilute (up to ca. 1 e per 50 carbon atoms), the presence of any ion at the electrified interface regardless of the sign of its charge must be considered.

The decomposition of electrolyte species may result in any of the following cases:

- formation of soluble reaction products,

- formation of gaseous reaction products and pressure build-up,

- formation of solid deposits on the electrode surface, and

- functionalization of the electrode surface with electrolyte species.

All of the above lead to a loss of ions or solvent molecules from the solution, which is detrimental to the EDLC performance in any case. Investigations into the accumulation of pressure within EDLC systems due to gas evolution [262, 272] have indicated that most of the irreversible charge loss in EDLCs at elevated voltages does not contribute towards gas formation, thus providing an important motivation to investigate the other degradation pathways listed above.

Out of the above possibilities, the formation of soluble degradation products might be predicted to have the least impact on the EDLC performance, as such species are expected to diffuse into the bulk solution and not accumulate specifically at the electrode/electrolyte interface (except if they are charged).

On the other hand, the formation of solid deposits or functionalization of the electrode surface is likely to directly influence the charge accumulation in the electrochemical double layer and thus represent a potentially critical aspect of EDLC aging. The formation of solid deposits on a model carbonaceous surface (HOPG) during negative polarization in $1\,M$ Et_4NBF_4/PC was shown to occur below ca. -2 V by Campana et al. [292].

In order to establish the relevance of these last two possible electrolyte degradation mechanisms for EDLCs on a more general basis, topographical and chemical analyses of HOPG were conducted after its electrochemical treatment in the AN- and PC-based electrolyte solutions.

Freshly cleaved HOPG was treated in solutions of $1\,M$ Et_4NBF_4 in AN and in PC, respectively, by performing potential sweeps at $10\,mV\,s^{-1}$ to extreme negative (-2.3 V) and positive (+2 V) potentials starting from the immersion potential of HOPG, which was close to 0 V. After a holding time of 30 minutes at maximum polarization, the potential was swept back to 0 V at the same sweep rate and held at 0 V for 5 minutes prior to disassembly of the cell. The treated HOPG surface was then rinsed with the pure anhydrous solvent (AN or PC) and subsequently dried gently under stream of dry nitrogen.

The treated samples were then immediately investigated by AFM and XPS, whereby each technique was applied to a separately prepared sample. All AFM measurements were performed in air under ambi-

ent conditions, and the XPS measurements were done following an air exposure of up to 10 minutes due to sample transfer.

13.2. Results and discussion

13.2.1. Electrochemical treatment

Typical current–potential curves obtained during the electrochemical treatment of HOPG are plotted in Figure 13.1. In the positive potential range, evidence for charge transfer in the form of ion intercalation into bulk HOPG or redox reactions involving the electrolyte was found close to +1.7 V in both electrolytes, whereby the irreversible current flow was markedly higher in the AN- compared to the PC-based electrolyte.
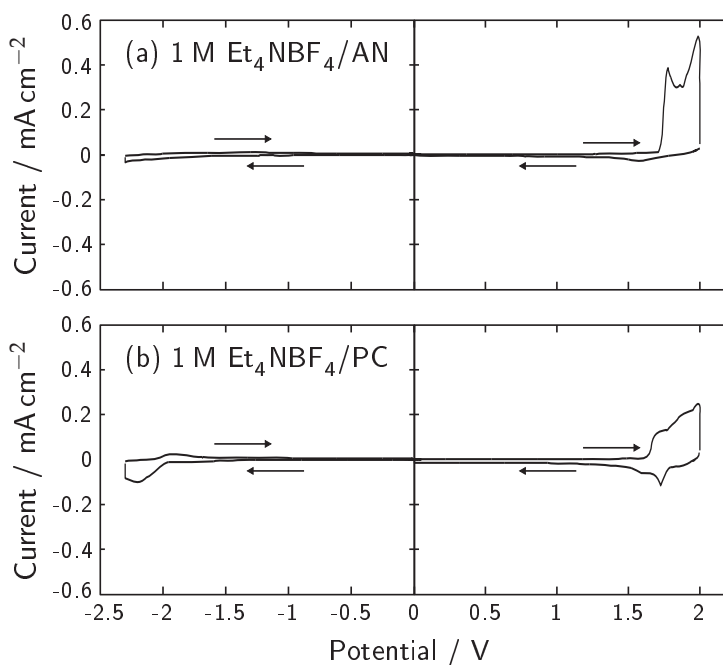
Figure 13.1.: Current–potential curves recorded during the electrochemical treatment of HOPG in (a) 1 M Et_4NBF_4/AN and (b) 1 M Et_4NBF_4/PC using a sweep rate of $10\,mV\,s^{-1}$ and a holding time of 30 minutes at -2.3 V or +2 V.

In the negative potential range, the onset of charge transfer was found near -2 V for the PC-based electrolyte. The onset potentials for charging of the HOPG electrode agree well with those obtained for microcrystalline graphite in the same electrolytes (Chapter 11) except for the AN-based electrolyte in the negative potential range (Figure 13.1a, left). In this case, the magnitude of current flow was significantly lower than in the other experiments despite the nominally identical exposed surface area of 0.785 cm^2. The double layer capacitance of HOPG determined prior to the electrochemical treatment via EIS was in the range of 3 ... 12 µF cm^{-2} at 100 mHz in all experiments. The different currents can therefore not be accounted for solely by a difference in the wetted electrode area. A possible explanation for the observed differences might be a slower rate of ion intercalation into the bulk of HOPG for Et$_4$N$^+$ in AN.

13.2.2. Topographical changes on HOPG

An AFM image of a freshly cleaved HOPG surface prior to electrochemical treatment is presented in Figure 13.2. The surface is smooth and exhibits different terraces which are separated by steps of typically 1 nm height (corresponding roughly to the stacking of three additional graphene sheets).
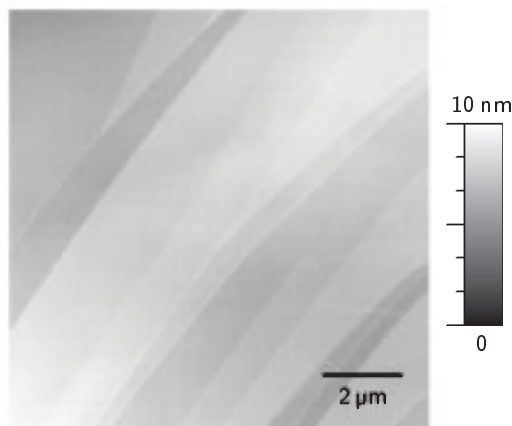
Figure 13.2.: AFM image of a freshly cleaved HOPG surface.

A selection of AFM images obtained from the treated samples are presented in Figures 13.3, 13.4, 13.5 and 13.6, and will be discussed in the following. Although the images provide clear evidence for significant topographical modification of HOPG and also indicate different mechanisms depending on the solvent and potential range, their interpretation is not straightforward.

AFM images obtained from the HOPG sample treated at -2.3 V in the AN-based electrolyte are presented in Figure 13.3. Compared to the pristine HOPG surface, the surface topography was considerably roughened and difficult to image, probably due to the presence of mobile surface species as indicated by the streaks in the fast scan direction. At higher magnifications (Figure 13.3c and d), the surface was found to consist of submicron-sized globular features. Repeated scanning with
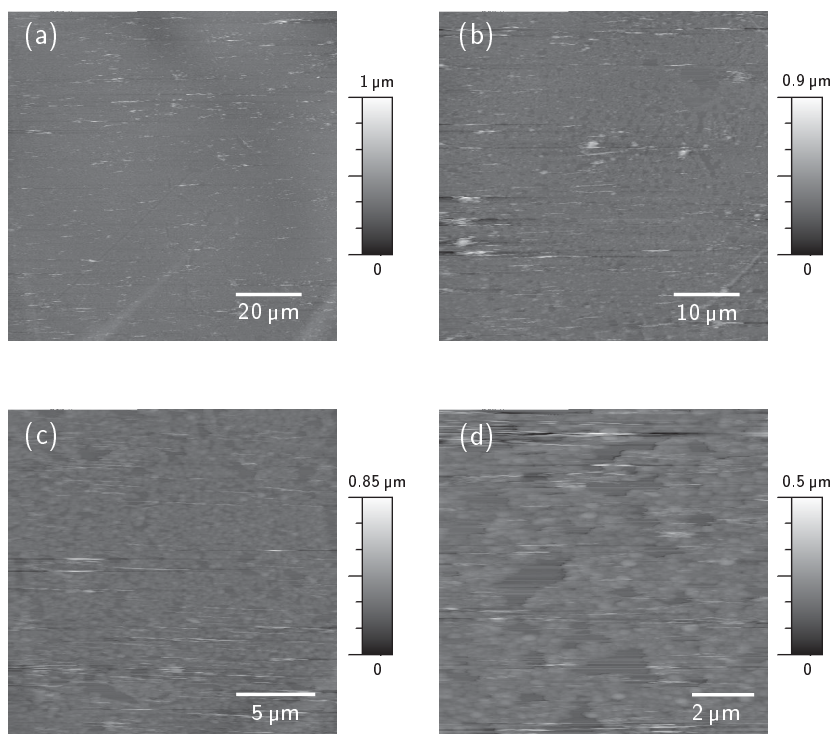
Figure 13.3.: AFM images of the HOPG surface after treatment at -2.3 V in 1 M Et_4NBF_4/AN.

maximum applied force did not displace or modify this structure in any noticeable way.

A completely different type of surface morphology was found following the treatment of HOPG at +2 V in the AN-based electrolyte (Figure 13.4). A network-like surface morphology was observed, with some large blisters (A) of up to several hundred nanometers in height and several micrometers in diameter protruding from the surface. The branched surface structure can be attributed either to electrolyte degradation deposits on top of the HOPG surface or to a swelling of the HOPG surface from beneath. Supporting evidence for the latter interpretation may be obtained by examining Figure 13.4d, in which steps of the HOPG surface (B) are visible. Clearly, the topographical features
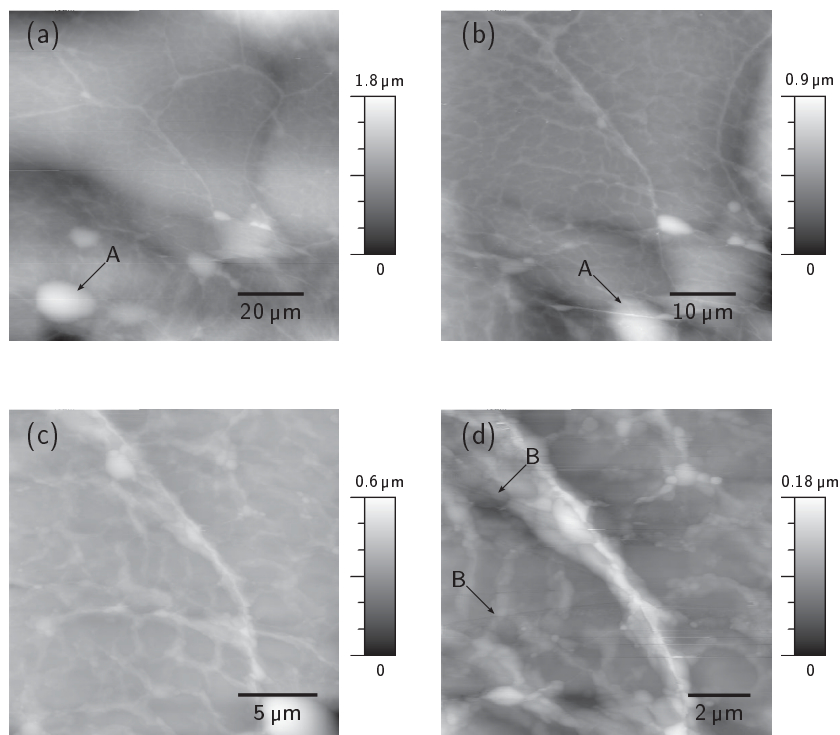
Figure 13.4.: AFM images of the HOPG surface after treatment at +2 V in 1 M Et$_4$NBF$_4$/AN.

arise from a pronounced local swelling of the HOPG surface, since solid deposits should cover the steps.

Similar features, although much less pronounced, were observed for the HOPG surface treated in the PC-based electrolyte at -2.3 V (Figure 13.5). Large blisters and pipe-like channels were visible at the surface, along with a crumpling of the uppermost graphene sheets as indicated in Figure 13.5c. In some regions of the sample, surface deposits were found, preferentially at step edges, which could be easily displaced by the AFM tip as shown by the white squares in Figure 13.5b. However, the underlying stepped structure of the HOPG remained visible after the treatment.
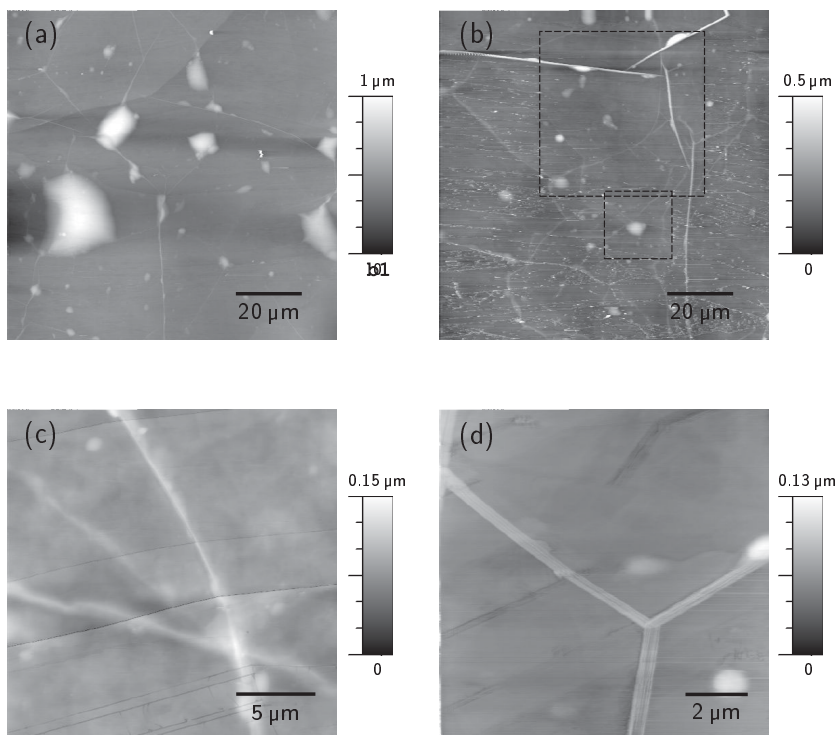
Figure 13.5.: AFM images of the HOPG surface after treatment at -2.3 V in 1 M Et$_4$NBF$_4$/PC. The squares in (b) mark regions in which repeated scanning with maximum applied force was performed.

Finally, a selection of AFM images of HOPG after exposure to 1 M Et$_4$NBF$_4$/PC at +2 V is shown in Figure 13.6. Besides the pipe-like surface structures visible in Figure 13.6b, highly faceted surface species of varying size were observed. A repeated measurement confirmed the presence of these deposits, as shown by the SEM images in Figure 13.7.

The characteristic topographical changes undergone by HOPG following electrochemical treatment at extreme potentials in the AN- and PC-based electrolytes are summarized Figure 13.8. Clearly, there are significant differences in the surface morphology depending on the type of solvent used and the polarity of the electrode. Significant modifications of the actual HOPG surface were observed for the treatments at +2 V in the AN-based electrolyte and -2.3 V in the PC-based electrolyte, leading to local swelling and the formation of large blisters and thinner
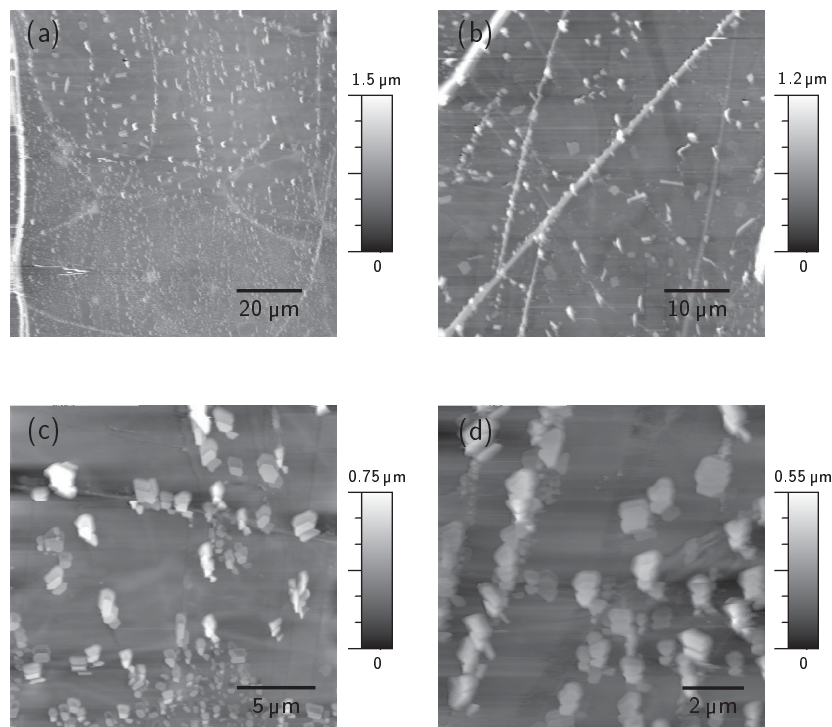
Figure 13.6.: AFM images of the HOPG surface after treatment at +2 V in 1 M Et$_4$NBF$_4$/PC.
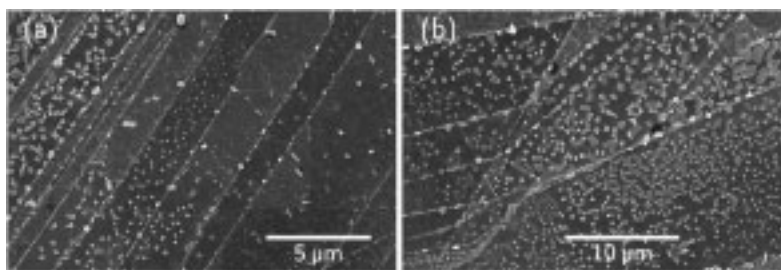
Figure 13.7.: SEM images of HOPG after treatment at +2 V in 1 M Et$_4$NBF$_4$/PC for two different magnifications.

pipe-like structures. Since the lines of step edges present in pristine HOPG were found to continue through these surface features, they can not be attributed to electrolyte degradation products deposited on top of the HOPG surface.

The mechanism for the formation of these observed HOPG surface features may be schematically depicted as in Figure 13.9. It has been established that ion intercalation into graphite occurs readily at the potentials applied in the present study (Chapter 11). As a consequence, any redox reactions involving the electrolyte solution are also likely to occur within the electrode itself, as illustrated by step 3 in Figure 13.9. The spatial requirement of the degradation products then dictates the amount of swelling observed subsequently in the AFM measurement. A similar interpretation of blister formation on a composite electrode in a Li-based electrolyte solution was proposed by Jeong et al. [494] in their in situ AFM study.

Step 5 in Figure 13.9 indicates the possibility of the removal of solid deposits on the HOPG surface due to the washing procedure employed in the present work. Numerous in situ AFM studies in carbonate-based electrolyte solutions have shown that the surface species formed during electrochemical charging can be easily removed by the AFM tip [273, 495–498]. Therefore, it can not be excluded that weakly adhering surface deposits are washed away during rinsing prior to AFM imaging in the present work. It is worth noting that the surface deposits as well as the pipe-like structures after treatment at -2.3 V in the

(a) Pristine HOPG

(b) 1 M Et$_4$NBF$_4$/AN

(c) 1 M Et$_4$NBF$_4$/PC
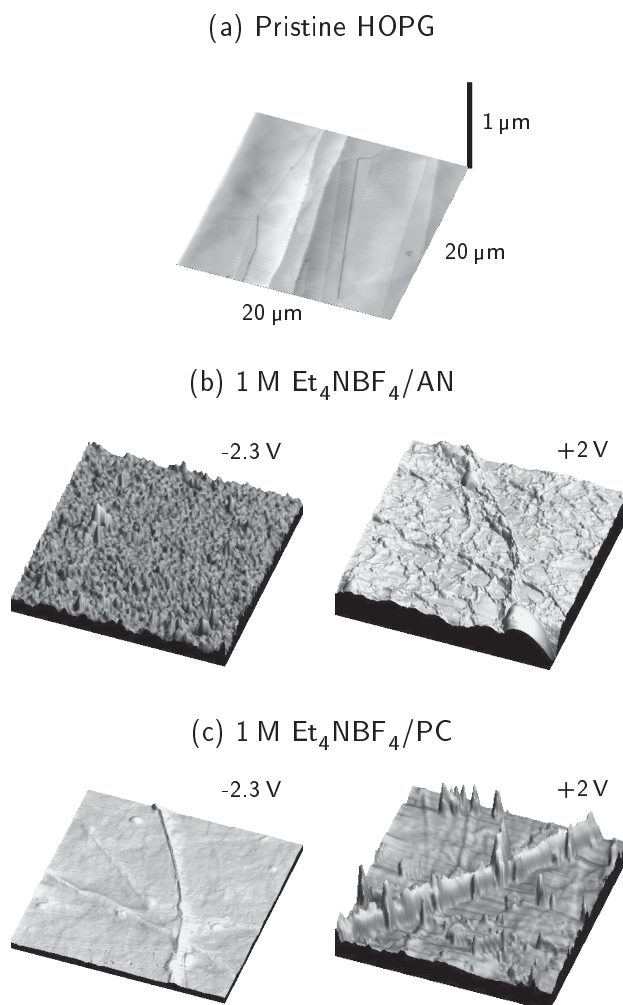
Figure 13.8.: Comparison of the surface morphology of HOPG after electrochemical treatment in the different cases studied in the present work.

PC-based electrolyte (Figure 13.5) agree well with the features reported in the in situ AFM study of Campana et al. [273].

Hence, the pronounced blister formation on HOPG treated in the AN-based electrolyte at +2 V and the PC-based electrolyte at -2.3 V is indicative of the degradation of intercalated electrolyte species. The electrode surface is obviously not passivated by a dense SEI-like film at
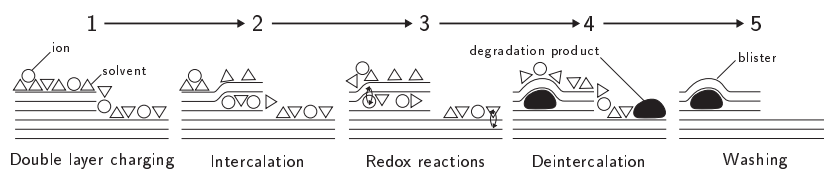
Figure 13.9.: Proposed mechanism for blister formation in HOPG through the degradation of intercalated electrolyte species. The possibility of removal of solid deposits through the washing procedure is indicated.

these potentials. The larger blisters in Figure 13.4a and 13.5a indicate a significant volume increase during electrolyte degradation which might be expected during gas evolution.

The features observed following treatment at -2.3 V in the AN-based electrolyte (Figure 13.3) are difficult to attribute unambiguously to either surface deposits or surface deformation of HOPG. Since the surface structure could not be modified by applying an increased tip load, the topography must be due to either hard, well-adhering deposits or bubble-like blisters formed by the HOPG surface itself. In both cases, a pronounced electrolyte degradation at the interface and in the electrode bulk would have taken place.

The nature of the faceted residues on the HOPG surface after treatment at +2 V in 1 M Et_4NBF_4/PC (Figure 13.6) is not well understood at the moment. The presence of salt remainders from dried electrolyte can be ruled out with a high likelihood according to the XPS analysis presented in the next section. Also, it is not clear why the washing procedure should be less effective in this case compared the others. The preferential adhesion of these deposits to step edges (Figure 13.6d) seems to indicate an electrochemical formation and not simply a drying of remaining electrolyte solution. In any case, no severe deformation of the HOPG surface underneath was observed, suggesting an improved stability of intercalated species in this case.

It should be mentioned that in all cases, modifications of the surface structures were observed during SEM imaging at high magnifications. For pristine HOPG, this was never the case. Thus, electron irradiation under high vacuum conditions appeared to result in a decomposition

of foreign surface species enclosed within the surface-near layers of HOPG, supporting the simplistic scheme in Figure 13.9.

13.2.3. Chemical analysis of degradation products

Prior to an investigation of the HOPG surfaces after electrochemical treatment, care was taken to establish the efficiency of the rinsing procedure in removing residual electrolyte. The photoelectron spectra of Et_4NBF_4 obtained after evaporation of the solvent (in this case AN) at room temperature are shown in Figure 13.10.

Due to the two different bonding environments of carbon in Et_4N^+, the C 1s signal of the dried salt exhibited two components centered at binding energies of 285.7 eV and 286.8 eV, respectively. The other peaks were centered at 686.5 eV (F 1s) and 194.6 eV (B 1s) for BF_4^- and 402.7 eV for the N 1s signal of Et_4N^+.
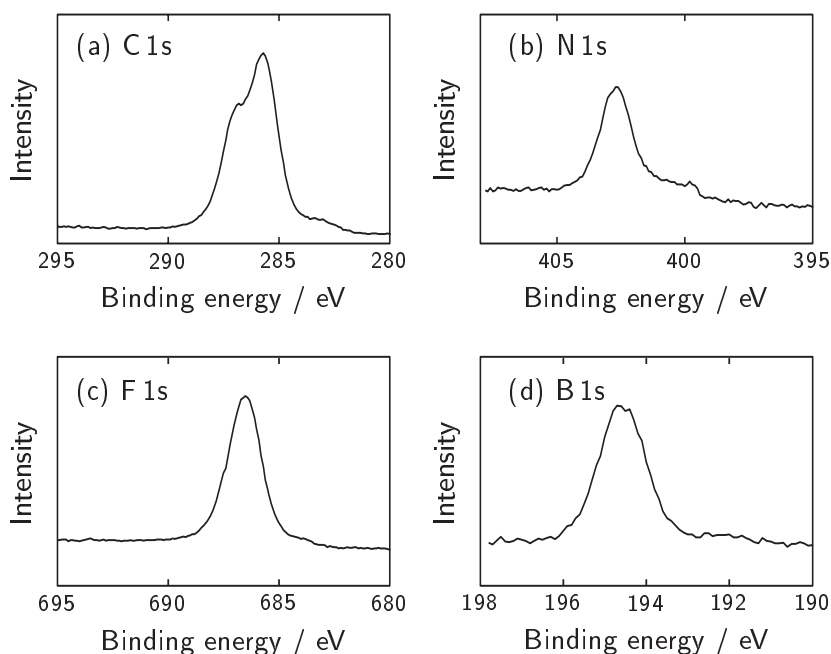
Figure 13.10.: Normalized XPS intensity of the (a) C 1s, (b) N 1s, (c) F 1s and (d) B 1s region of Et_4NBF_4.
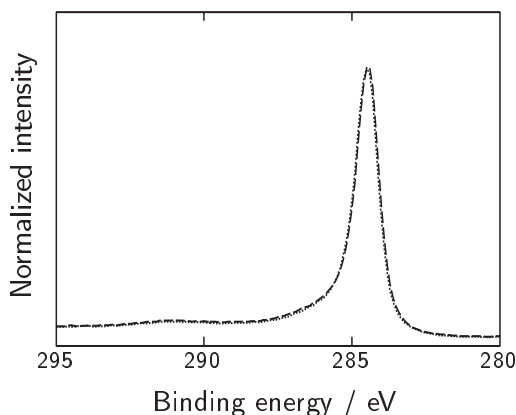
Figure 13.11.: C 1s spectra of HOPG after wetting with 1 M Et$_4$NBF$_4$ in AN (dotted line) and in PC (dashed line) and subsequent rinsing in the respective solvent.

In Figure 13.11, the C 1s spectra of HOPG are presented after exposure to the AN- and PC-based electrolyte solutions in the in situ cell without electrochemical polarization. The spectra exhibited a strong main peak at 284.5 eV as expected for HOPG [370, 499] and were identical for exposure to either electrolyte. No traces of Et$_4$N$^+$ were found in the C 1s region in the two cases, implying a successful removal of the electrolyte solution. Hence, the rinsing procedure was considered adequate for further investigation of electrochemically treated HOPG surfaces.

The elemental compositions of the rinsed HOPG samples both prior to and following the electrochemical treatments are summarized in Table 13.1. According to the above preliminary experiments, the detection of an element via XPS following the rinsing procedure points towards the involvement of the element in covalent bonding to the HOPG surface or in a well-adhering degradation product.

For the AN-based electrolyte following polarization to -2.3 V, boron, fluorine and oxygen were found to remain on the HOPG surface after washing. The complete absence of nitrogen implies that whether the cation, Et$_4$N$^+$, nor the solvent, AN, participate in the formation of cathodic deposits on HOPG or that these are easily removed through the washing procedure. The presence of boron and fluorine is unexpected,

Table 13.1.: Elemental composition (in at %) of the HOPG surface after electro-chemical treatment at the indicated potentials via XPS.

Element	$1\,M\,Et_4NBF_4/AN$			$1\,M\,Et_4NBF_4/PC$		
	0 V	-2.3 V	+2 V	0 V	-2.3 V	+2 V
B	0.0	3.1	1.2	0.3	0.3	1.4
C	98.3	73.6	92.3	96.7	89.0	85.5
N	0.0	0.0	1.3	0.2	1.3	1.3
O	1.6	9.8	2.1	1.5	7.3	6.0
F	0.1	5.6	3.2	1.4	2.2	5.9
Na	0.0	7.9[a]	0.0	0.0	0.0	0.0

[a] Attributed to impurities introduced after washing.

since the reduction of anions is usually considered negligible at negative electrodes in electrochemical systems [99]. The presence of BF_4^- near the negative electrode is not so surprising considering the relatively dilute electronic charge on the electrode. The enrichment of fluorine at negative activated carbon electrodes in AN-based EDLC electrolyte has been reported previously [265–268], in line with the present results. In fact, in the present study, boron and fluorine were observed in every case following electrochemical treatment, regardless of the polarity of the applied potential.

The increase in oxygen content, which was observed for all samples, could originate from a variety of sources, including molecular oxygen dissolved in the electrolyte solution, the decomposition of water or from ambient air during sample transfer, and will not be discussed in more detail here.

Upon examination of the C 1s spectrum of HOPG after cathodic treatment in the AN-based electrolyte, a distinct contribution at higher binding energies was found in addition to the main peak attributed to pristine HOPG (Figure 13.12). In the absence of nitrogen, this feature with a peak position of about 286.6 eV can be attributed to carbon in a one-oxygen environment as in C−O or C=O [268, 500, 501]) or possibly to semi-ionic C−F bonding [502].

For the positive potential range in the AN-based electrolyte, nitrogen was found on the HOPG surface (Table 13.1), which could originate
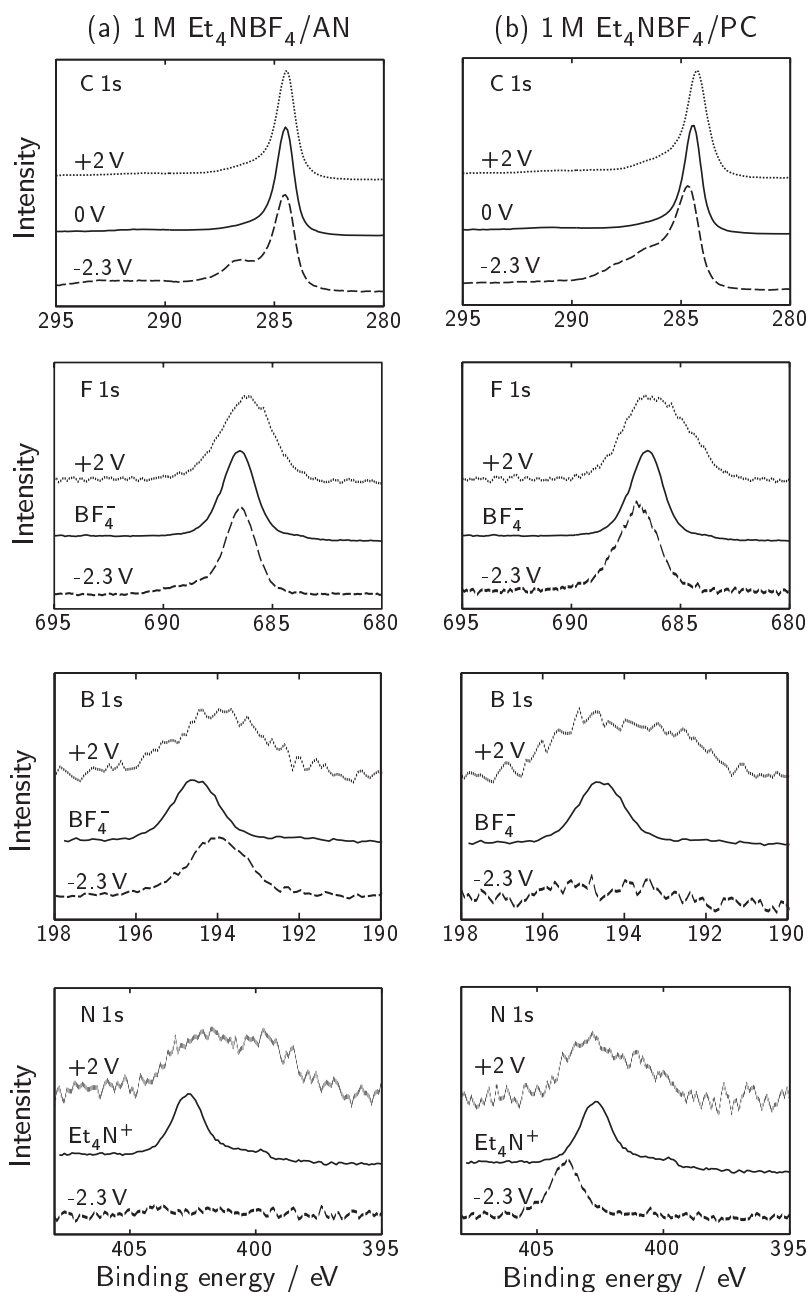
Figure 13.12.: Intensity-normalized XPS spectra of the HOPG surface at different binding energies before and after electrochemical treatment in (a) 1 M Et$_4$NBF$_4$/AN and (b) 1 M Et$_4$NBF$_4$/PC. The spectra have been offset along the y-axis for clarity.

from either Et_4N^+ or solvent degradation. The C 1s spectrum did not appear noticeably altered due to the electrochemical treatment in this case (Figure 13.12a), suggesting a low degree of functionalization of the HOPG itself and that the nitrogen is incorporated within degradation products on or beneath the electrode surface. The significant broadening of the N 1s signal (Figure 13.12a) suggests a complex bonding environment involving different atoms.

The electrochemical treatments of HOPG in the PC-based electrolyte solution resulted in similar features as for the AN-based system, and analogous interpretations apply. For the negative potential range, a functionalization of HOPG was indicated by the shape of the C 1s spectrum (Figure 13.12b), while no modification of the C 1s signal was observed in the positive range. Significant broadening of the fluorine, boron and nitrogen signals in the positive range imply degradation of BF_4^- as well as of Et_4N^+. The shift of the N 1s signal to higher binding energies for the negative polarization suggests bonding with oxygen in nitro groups, $-NO_2$. The bonding of such groups to carbon, $C-NO_2$, could also contribute to the signal of the C 1s spectrum in the region of 286.3 eV [267, 370] as observed in the present work (Figure 13.12b).

Evidently, the changes observed in all of the cases discussed above involve the participation of several different electrolyte species and result in a complex bonding environment which is not straightforwardly assigned to the topographical features presented in the previous section. Since the possible degradation pathways of the electrochemical systems studied here are numerous [99, 267, 271], a detailed interpretation of the obtained data in terms of electrochemical reaction mechanisms would be speculative at this point. Thus, the discussion of the results of the chemical analysis is not elaborated further here, but instead taken as a reference for the study of aged activated carbon electrodes presented in the next section, which bears greater practical relevance.

13.3. Conclusions

The polarization of HOPG to -2.3 V and +2 V in the AN- and PC-based EDLC electrolytes results in a notable degradation of electrolyte species and modification of the HOPG surface. The topographical changes of

HOPG depended on the potential range and the solvent used. In terms of a simple solvent cointercalation model proposed in this chapter, the topographical modifications should be most pronounced when the electrolyte degradation is most severe, leading to a permanent swelling of the HOPG surface due to the accumulation of degradation products beneath the uppermost graphene sheets.

From the chemical analysis of the rinsed samples after electrochemical treatment, it was clearly shown that all electrolyte species are likely to be involved in degradation processes at either electrode. For the AN-based electrolyte, however, it seemed as though whether the cation, Et_4N^+, nor the solvent contributed to solid surface deposits or surface functionalization in the negative potential range. Instead, it was found that anion degradation appears to contribute to the irreversible electrochemical processes occurring at the negative electrode by mechanisms which are not understood yet.

The accumulation of oxygen at the electrode surface and indications of $C-O$ functionalization for either electrolyte in the negative potential range suggest that oxygen-containing impurities are involved in redox reactions and may thus contribute towards the degradation of EDLCs.

For the positive potential range, surface functionalization or the formation of well-adhering deposits does not appear to be a significant degradation mechanism in either electrolyte, as evidenced by the unchanged C 1s signal in these cases (Figure 13.12).

In conclusion, the experiments presented in this chapter provide insight into the occurrence of electrolyte degradation at a model carbonaceous electrode at elevated potentials. However, it should be highlighted that the timescales involved in these investigations were very short compared to the duration of aging in EDLCs, and that an extrapolation of the present results to technical systems is far from straightforward. Nonetheless, a possible basis for discussion has been established for the investigation of the aging behavior of porous electrodes, which will be presented in the next chapter.

Chapter 14.

Aging characteristics of EDLCs

14.1. Motivation

The aging of EDLC devices at elevated voltages can be considered to involve irreversible phenomena beyond the idealized concept of pure double layer charging. In the previous chapters, it was shown that ion insertion into small micropores (Chapter 11) and decomposition of various electrolyte species (Chapter 13) are the main relevant aspects in this respect at high electrode polarizations. Yet, it is still unclear how these processes influence the electrochemical performance of an EDLC device consisting of highly porous activated carbon electrodes over a long period of time.

In order to apply the concepts established in this work to practically relevant systems at elevated voltages, the loss of the electrochemical performance of bound activated carbon electrodes was studied in laboratory cells as a function of cell voltage and aging time. The capacitance of each electrode was determined by incorporating a reference electrode for potential monitoring. A subsequent analysis of individual electrodes via nitrogen gas adsorption, XPS and SEM was performed in order to investigate the structural changes undergone by each electrode. Thus, the aim of the experiments summarized in the present chapter was to establish a correlation between the loss of performance and the electrochemical modification of the activated carbon electrodes.

14.2. Experimental conditions

A symmetric stack consisting of two YP17/PTFE electrodes of diameter 12 mm and thickness (500 ± 20) μm each with a proprietary paper-based separator (Maxwell Technologies, Switzerland) was assembled in the

electrochemical cell described in Section 7.1 in a three-electrode config-uration. To minimize contact resistance, a commercial carbon-coated aluminum foil (Gaia Akkumulatorenwerke, Germany) was used as an interlayer between the activated carbon electrodes and the titanium pis-ton current collectors. The thickness of this non-porous carbon coating was in the order of $5\,\mu m$.

The aging treatments were carried out at a constant floating voltage according to Table 14.1. The focus of the experimental series was placed on the degradation of the AN-based EDLC system, while additional experiments (labeled 10, 11 and 12 in Table 14.1) were conducted to investigate the effects of water contamination and the importance of the solvent in EDLC aging.

Before and after the aging protocols listed in Table 14.1, CVs were recorded for all cells in the two-electrode configuration between $0\,V$ and $2.5\,V$. Further, full cell EIS was performed in the frequency range between $100\,kHz$ and $10\,mHz$ at a cell voltage of $0\,V$.

Table 14.1.: Overview of experimental aging conditions applied to YP17/PTFE full cells in the present work. The electrolyte employed was always a $1\,M$ solution of Et_4NBF_4 in the indicated solvent.

Experiment number	Solvent	Float voltage V	Aging time hours
1	AN	4	10
2	AN	4	30
3	AN	4	60
4	AN	3.5	100
5	AN	3.5	300
6	AN	3.5	500
7	AN	3	100
8	AN	3	300
9	AN	3	500
10	AN + 1000 ppm H_2O	3.5	100
11	PC	3.5	100
12	PC	3.5	500

As indicated in Table 14.1, the aging of the cells was carried out by applying a constant floating voltage for a defined time. In time intervals of 10 hours, the capacitance was measured by three galvanostatic charge/discharge cycles of the full cell at $I/m = 0.28\,\mathrm{A\,g^{-1}}$ (referred to the total active mass m of both electrodes) between $0\,\mathrm{V}$ and $2.5\,\mathrm{V}$. Each capacitance measurement and subsequent scanning to the desired aging voltage took less than 30 minutes. For the full cell, the integral capacitance was calculated by

$$C_{\mathrm{cell}} = \frac{It}{\Delta U - 2IR_{\mathrm{cell}}} \tag{14.1}$$

where $It = \Delta Q$ is the total charge applied during the charging step of duration t, $\Delta U = 2.5\,\mathrm{V}$ is the voltage window explored during the galvanostatic cycling and R_{cell} is the resistance of the cell determined from the voltage drop during reversal of the current polarity at $U = 2.5\,\mathrm{V}$. The gravimetric capacitance was obtained by normalizing C_{cell} to the total active electrode mass m (excluding binder). The single electrode capacitances C_{pos} and C_{neg} were obtained accordingly by

$$C_{\mathrm{pos,neg}} = \frac{It}{\Delta E_{\mathrm{pos,neg}} - 2IR_{\mathrm{pos,neg}}} \tag{14.2}$$

in which ΔE_{pos} and ΔE_{neg} are the potential excursions of the positive and negative electrode, respectively, measured against the YP17/PTFE QRE, and R_{pos} and R_{neg} are the respective resistances. The gravimetric capacitances were obtained by normalizing each single electrode capacitance to the respective active electrode mass. Over the time period of the galvanostatic cycling, the reference potential of the QRE can be considered essentially constant (Section 9.2.6) regardless of its absolute value.

Following the aging treatments, the cells were disassembled under ambient conditions and the individual electrodes washed in a Soxhlet reactor for at least 6 hours using AN as the extraction solvent in order to remove residual electrolyte. Afterwards, the electrodes were placed in a desiccator and stored under a vacuum of $10^3\,\mathrm{Pa}$. For the subsequent analysis of the electrodes via nitrogen adsorption, XPS and SEM, separate pieces were cut out from the electrodes prior to the measurements.

14.3. Results and discussion

14.3.1. Electrochemical performance

With increasing aging voltage, the capacitance loss was found to be significantly enhanced (Figure 14.1a). At 3 V, the full cell capacitance dropped from an initial value of 25.6 F g^{-1} to 20.7 F g^{-1} after 500 hours, corresponding to a capacitance loss of 19 %. At 3.5 V and 4 V, an equivalent capacitance loss occurred after only 10 to 20 hours, respectively. Thus, in going from 3 V to 3.5 V, the initial rate of capacitance fading increased by a factor of 25–50, in relatively good agreement with the empirical rule of rate doubling per 0.1 V voltage increase [35] which predicts a rate increase by a factor of 32 in this case. It appears as though the initial rate of aging did not increase as significantly when augmenting the aging voltage further from 3.5 V to 4 V, although the rate of capacitance loss was clearly not constant over time. At 3.5 V, a rapid initial loss during the first 20 hours was followed by significantly slower aging.
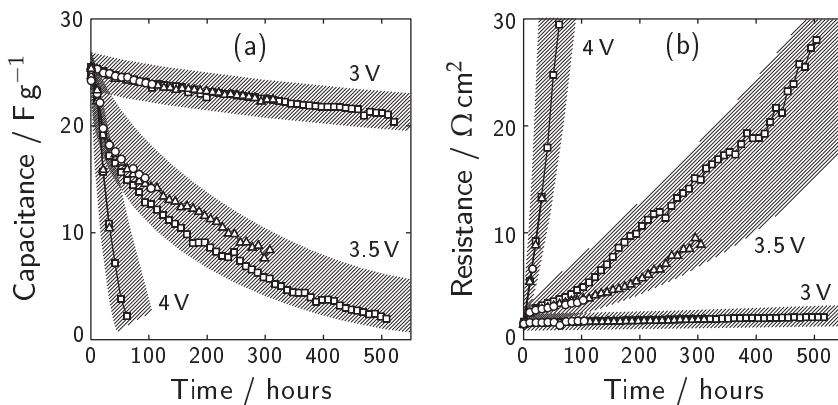
Figure 14.1.: Evolution of (a) full cell gravimetric capacitance and (b) specific resistance related to the geometric area of symmetric YP17/PTFE cells over time using 1 M Et$_4$NBF$_4$/AN as the electrolyte solution for aging at 3 V, 3.5 V and 4 V. The symbols denote results from different cells with varying aging times according to Table 14.1. The hatched regions are guides to the eye.

Also, the cell resistance was found to depend markedly on the aging voltage (Figure 14.1b). While the resistance remained relatively constant during aging at 3 V, it increased by one order of magnitude after about 300 hours at 3.5 V or about 50 hours at 4 V.

In order to relate the aging characteristics of these laboratory cells to practical devices, the capacitance fading and leakage current at 3.5 V were compared to the corresponding values of a commercially available EDLC (BCAP0350® from Maxwell Technologies, Switzerland). From Figure 14.2a, it is clear that the rate of capacitance loss of the laboratory cell was significantly greater than that of the commercial EDLC, particularly for aging times greater than 20 hours. Possible reasons for the improved stability of the commercial device include an optimized assembly and component selection, better sealing and asymmetric electrode masses to account for the varying stability window in each potential range. However, the leakage currents of both systems were comparable (Figure 14.2b), indicating similar contributions of irreversible charge losses in the two cases.
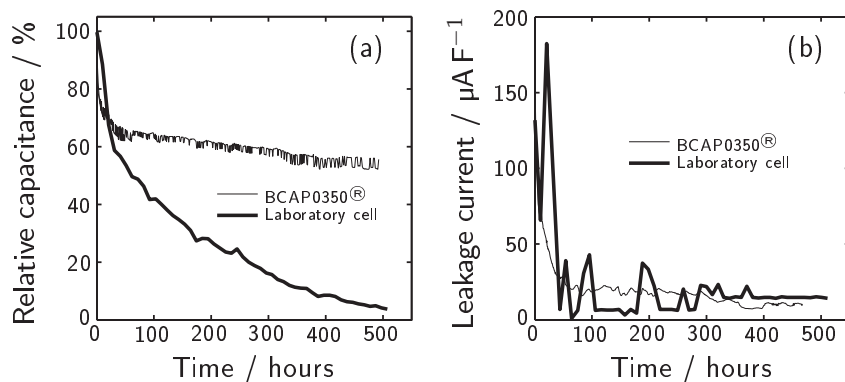
Figure 14.2.: Comparison of (a) the capacitance loss and (b) the leakage current of a laboratory cell (bold line) at room temperature with a commercial EDLC (BCAP0350®, thin line) at 30 °C and an applied voltage of 3.5 V. The leakage current was normalized to the initial full cell capacitance value or the nominal capacitance of 350 F in case of the commercial device. The significant noise of the laboratory cell leakage current was due to the limited resolution of the galvanostat employed.

The determination of the single electrode capacitances of the laboratory cells during aging revealed a marked difference in the capacitance fading for the positive and negative electrode depending on the aging voltage (Figure 14.3). The higher initial specific capacitance of the positive electrode compared to the negative electrode was already observed in the context of the electrochemical characterization presented in Section 9.2.6 and can be attributed to the electronic properties of YP17 (Section 10.4). At 3 V, where the capacitance fading of the full cell was not very pronounced compared to the higher voltages (Figure 14.1a), the single electrode capacitances dropped steadily from their initial values for both electrodes (Figure 14.3a). Further, the resistances evaluated from the respective IR drops were found to increase steadily for both electrodes at 3 V. For the cell aged during 500 hours, the capacitance of the positive electrode decreased from $113 \, \mathrm{F \, g^{-1}}$ to $91.1 \, \mathrm{F^{-1}}$, corresponding to a capacitance loss of 19 %, while the negative electrode lost 23 % of its initial capacitance (from $93.7 \, \mathrm{F \, g^{-1}}$ to $72.0 \, \mathrm{F \, g^{-1}}$).

However, at 3.5 V, the rate of capacitance fading for the positive electrode was significantly greater than that of the negative electrode (Figure 14.3b). For all investigated cells at this aging voltage, the capacitance of the positive electrode dropped below that of the negative electrode within 20 hours and faded to less than $5 \, \mathrm{F \, g^{-1}}$ after 500 hours. The capacitance of the negative electrode remained high at this aging voltage and was even found to increase over time. Further, the resistance of the negative electrode remained low during aging, while the resistance of the positive electrode increased dramatically over time and accounted for the entire resistance increase of the full cell.

In Figure 14.3b, a considerable spread of the evolution of the negative electrode capacitances can be seen, indicating a high sensitivity of the single electrode aging behavior to the experimental conditions. However, the lower rate of aging for the negative compared to the positive electrode was a common result for all cells tested at 3.5 V, indicating that the positive electrode is the weak pole of AN-based EDLCs at elevated voltages and is primarily responsible for the capacitance fading and resistance increase of the full cell.

At 4 V, a similar behavior was observed for the single electrodes, namely a rapid decline of the positive electrode capacitance along with
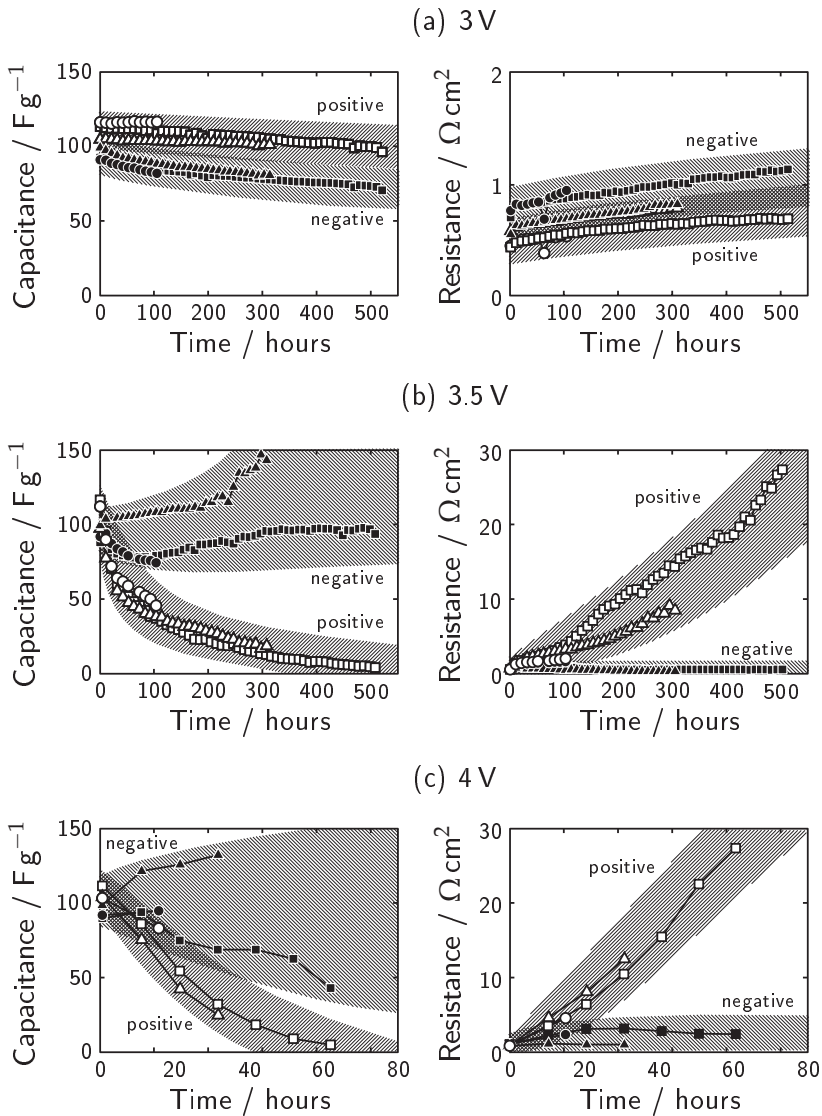
Figure 14.3.: Capacitance and resistance evolution of the negative (filled symbols) and positive (open symbols) electrodes for all experiments in 1 M Et$_4$NBF$_4$/AN over time at aging voltages of (a) 3 V, (b) 3.5 V and (c) 4 V. The hatched regions are guides to the eye.

a less pronounced deterioration of the negative electrode capacitance (Figure 14.3c) . Similar to the case at 3.5 V, the positive electrode was found to be the primary cause for capacitance loss and resistance increase of the full cell.

The apparent increase in the capacitance of the negative electrode over time during aging at 3.5 V and 4 V (Figure 14.3b, c) can be understood by considering the respective potential excursion of this electrode. The single electrode potentials were evaluated over time for the cells aged at 500 hours (3 V and 3.5 V) and 60 hours (4 V), with the results summarized in Figure 14.4. It is clear that the potential window of the negative electrode during the capacitance determination intervals was significantly reduced and shifted to more negative potentials during aging at 3.5 V and 4 V (Figure 14.4b, c). Since the electrode capacitance increases with increasingly remote potentials from 0 V (Section 9.2.6), the capacitance of the negative electrode during aging under these conditions increases as shown in Figure 14.3b and c.

The potential window shifts observed in Figure 14.4 can be understood by considering the potential change for a single electrode at elevated voltages:

$$\Delta E = \frac{\Delta Q_{\text{rev}} - \Delta Q_{\text{irr}}}{C} + IR \tag{14.3}$$

where ΔQ_{rev} is the reversible (capacitive) charge applied to the electrode and ΔQ_{irr} is amount of charge which is irreversibly consumed. In the absence of significant irreversible charge consumption ($\Delta Q_{\text{irr}} = 0$) and equal resistances R at each electrode, the difference in the potential excursions of the single electrodes during charging is simply given by the respective capacitances C_{pos} and C_{neg}. However, the potential excursion of either electrode is identical for each charge/discharge cycle, which appears to represent the case in Figure 14.4a.

Due to the significant capacitance loss and resistance gain of the positive electrode during aging at 3.5 V and 4 V, the potential excursion of this electrode during capacitance determination increased progressively with the extent of aging (Figure 14.4b, c). Accordingly, the potential excursion of the negative electrode decreased as described above. The potential spikes observed for the positive electrode following each capacitance determination (Figure 14.4b, c) are due to the greater re-
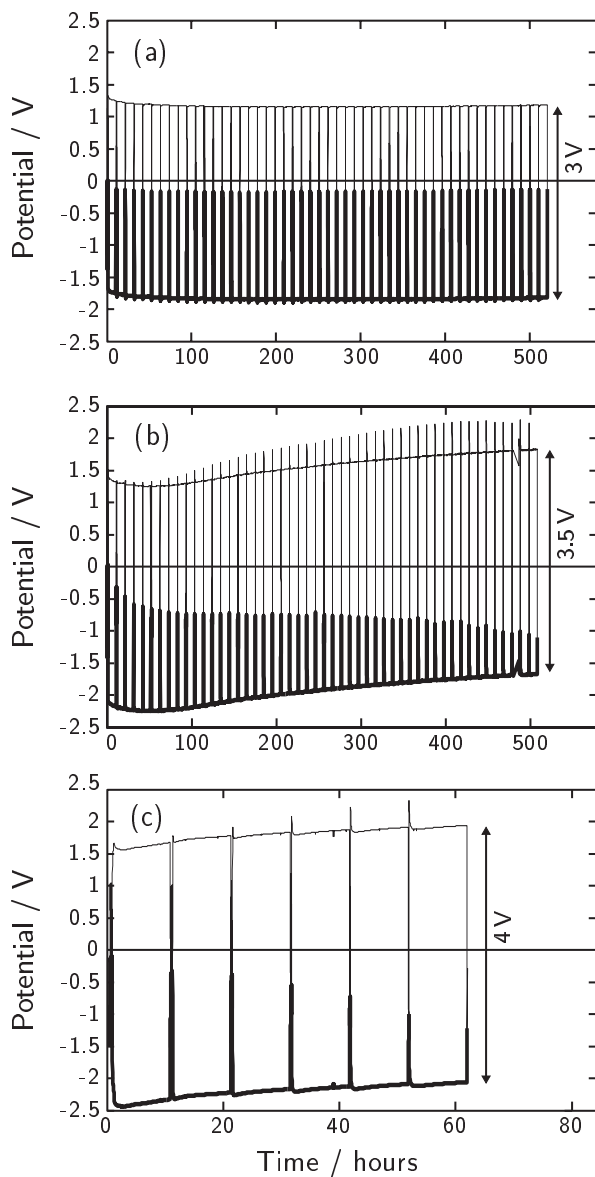
Figure 14.4.: Potentials of the positive (thin lines) and negative (bold lines) electrodes during aging in $1\,M\ Et_4NBF_4/AN$ at (a) $3\,V$, (b) $3.5\,V$ and (c) $4\,V$. The charge/discharge cycles for capacitance determination every 10 hours are visible as vertical lines on these timescales.

sistance R_{pos} of the aged electrode, resulting in a significant potential drop IR_{pos} during current flow. During the voltage hold periods, $I \rightarrow 0$ and the measured electrode potential decayed accordingly.

From Figure 14.4, further important observations can be made. At 3 V (Figure 14.4a), the potential limits of the single electrodes reached constant values close to -1.82 V and +1.18 V during the floating voltage periods. From the electrochemical characterization in Section 9.2.6, both electrodes can thus be stated to operate within the potential region of reversible capacitive charge storage under these conditions.

For different values of ΔQ_{irr} for the two electrodes, however, the potential excursion of the electrode with larger ΔQ_{irr} is reduced with respect the purely capacitive case. Also, during voltage hold periods, the electrode with larger ΔQ_{irr} will be charged less than the other electrode. In the case $\Delta Q_{irr} > \Delta Q_{rev}$, the electrode will actually be discharged. Thus, the initial downshift of the operating voltage window during aging at 3.5 V (Figure 14.4b) can be attributed to continuous irreversible charge consumption at the positive electrode. The subsequent upshift of the voltage window may then be attributed to the onset of significant charge consumption at the negative electrode. Indeed, according to the electrochemical characterization of YP17/PTFE in the AN-based electrolyte (Section 9.2.6), significant irreversible charge consumption was observed to take place at +1.4 V and -2.2 V for the positive and negative electrode, respectively.

The single electrode potential excursions at 4 V (Figure 14.4) are qualitatively similar to the case at 3.5 V, whereby the rate of shifting is significantly greater due to the larger applied cell voltages and correspondingly higher irreversible charge consumption at each electrode.

The influence of the different aging conditions on the CVs of the full cells is summarized in Figure 14.5. As expected from the single electrode potential excursions discussed above for aging at 3 V, the CVs remained essentially capacitive even after 500 hours (Figure 14.5a). A decreased response time at the vertex points was observed, particularly after aging at higher voltages, in agreement with the increased cell resistance discussed previously (Figure 14.1b).

The aging experiments conducted at 3.5 V had a marked influence on the CVs (Figure 14.5b) of the full cells. With increasing aging time, the
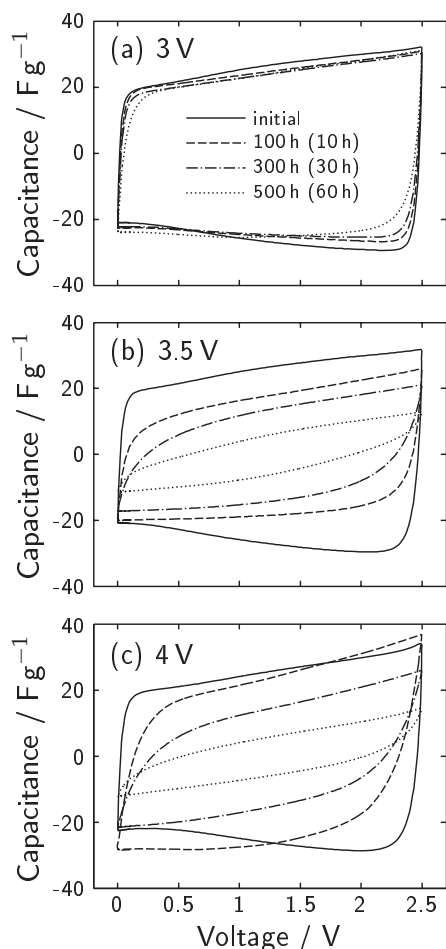
Figure 14.5.: Two-electrode CVs at $10\,\text{mV s}^{-1}$ before and after different aging times in $1\,\text{M Et}_4\text{NBF}_4/\text{AN}$ at (a) 3 V, (b) 3.5 V and (c) 4 V. The durations given in brackets are valid for aging at 4 V.

current response in the CV became slower and less capacitive, indicating both an increase in the equivalent series resistance and a decrease in the double layer capacitance.

The corresponding EIS measurements of the cells aged at 3 V (Figure 14.6a) indicated a slight increase in the electrolyte resistance and a high frequency arc which became more pronounced with increasing aging time. Several possible physical interpretations may be brought

(a) 3 V

(b) 3.5 V

(c) 4 V
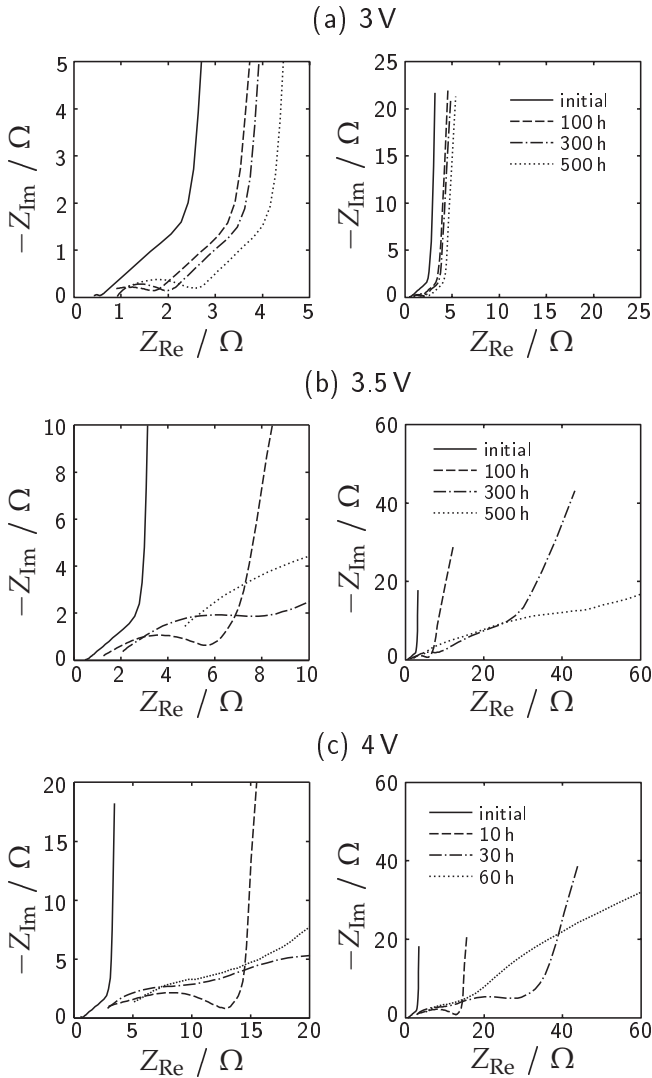
Figure 14.6.: Nyquist plots of the same cells as in Figure 14.5 between 100 kHz and 10 mHz at 0 V. The two different plots at a given voltage represent different regions of the same impedance spectrum.

forward to explain the meaning of the high frequency arc. Besides an increase in contact resistance between electrode and current collector, which would result in a well-defined semi-circle (Section 7.5), other

plausible explanations include a modification of the pore shape to generate bottle-neck type pores [112], trapping of ions in low energetic sites [503, 504] or slowed specific adsorption of ions due to hindered partial charge transfer [505]. It is not possible to differentiate between these different causes on the basis of the EIS data alone. It is worth noting that the electrolyte pore resistance (EDR) remained essentially constant during aging at 3 V (Figure 14.6a), indicating an intact porous network under these conditions.

After 100 hours at 3.5 V, the Nyquist plot (Figure 14.6b) exhibited similar features to the ones discussed above for aging at 3 V. However, a clear tilting of the low frequency tail could be observed, and the EDR region was no longer well-defined. With increasing aging time, a significant growth of the depressed semi-circle at high frequencies was observed along with a further tilting of the low frequency tail to lower impedance values. The tilting of the initially capacitive low frequency component of the Nyquist plot is usually represented by a constant phase element (CPE) [11], which is related to the distribution of adsorption time constants at the electrode/electrolyte interface as discussed by Pajkossy [506]. In effect, an increased tilting indicates an increased CPE contribution, which in turn suggests an increase in the heterogeneity of the electrode/electrolyte interface.

Two observations support the aspect of an increased contact resistance for both electrodes, namely the delamination of the carbonaceous coating from the aluminum interlayer as well as a pronounced embrittlement of the negative electrodes following aging at 3.5 V and 4 V. The latter point is particularly critical as it implies a degradation of the PTFE binder, possibly resulting in increased contact resistances within the negative electrode due to a loss of particle cohesion. The features observed following aging at 4 V are similar to those obtained after aging at 3.5 V, whereby the aging time differed by roughly one order of magnitude.

It follows from the single electrode data (Figure 14.3) that the changes observed in the full cell CVs (Figure 14.5) and EIS data (Figure 14.6) must be dominated by the aging of the positive electrode in terms of both capacitance and resistance.

In comparing the EIS data after aging at 3.5 V with a BCAP0350® cell aged under similar conditions, significantly less modifications may be identified in the Nyquist plot for the commercial cell (Figure 14.7). However, similarities exist in terms of the tilting of the low frequency capacitive component and the appearance of a depressed semi-circle at high frequencies. Thus, it is probable that the aging of the laboratory cells was driven at least in part by similar mechanisms as those encountered in commercial EDLCs.
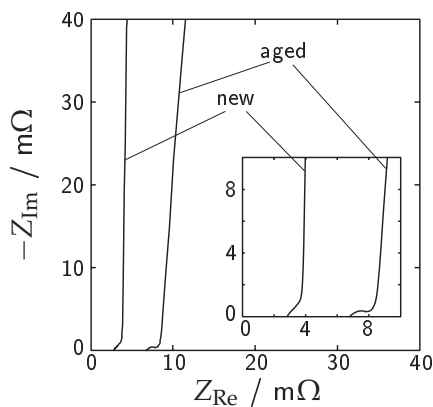
Figure 14.7.: Nyquist plots of the BCAP0350® EDLCs at 0 V after aging at 3.5 V and 30 °C for 500 hours. The inset is an enlargement of the high frequency region.

14.3.2. Morphological changes

Following the aging treatments, individual electrodes were studied via SEM in order to test for morphological changes. Due to the rather heterogeneous appearance of the YP17/PTFE starting material (Figure 14.8a), it is difficult to reliably assess the topographical modifications due to electrochemical aging. The micron-sized activated carbon particles were very heterogeneous in shape and size as well as surface topography. Clearly, it is not possible to resolve the microporosity of activated carbons via SEM.

Nonetheless, a few notable effects due to aging were noticed and are briefly described in the following for the electrodes aged at 3.5 V for

(a) YP17/PTFE

(b) 3.5 V / 500 hours / negative   (d) 3.5 V / 500 hours / positive

(c) 3.5 V / 500 hours / negative   (e) 3.5 V / 500 hours / positive
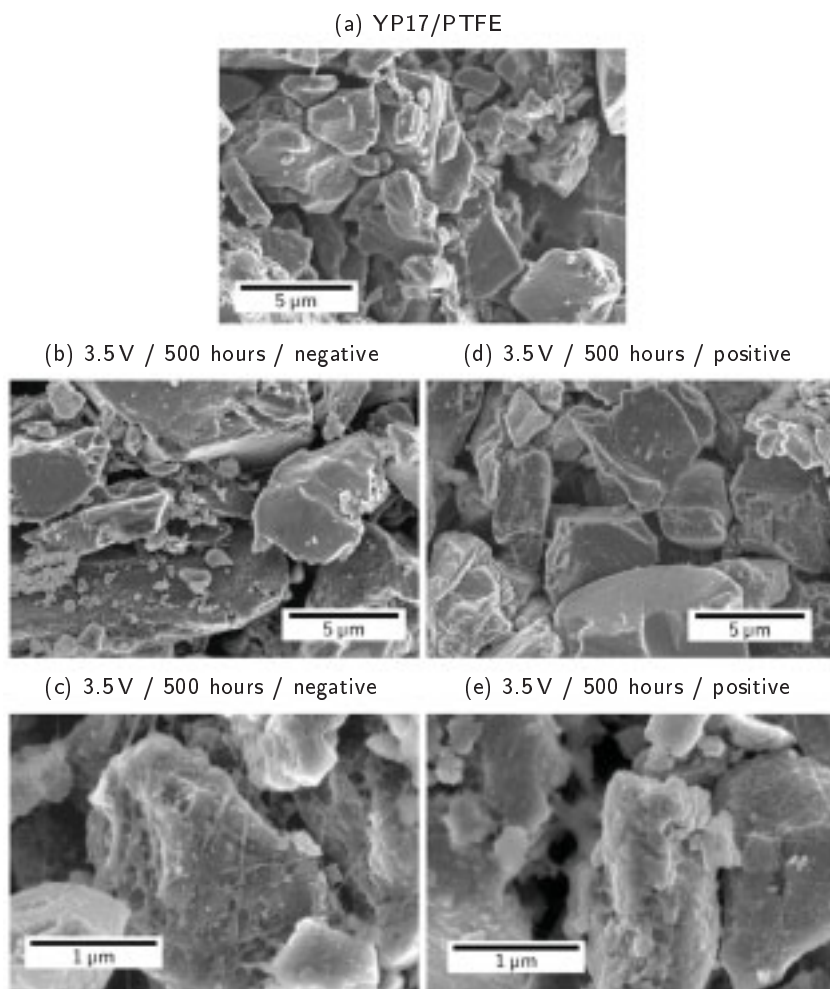
Figure 14.8.: SEM images of (a) YP17/PTFE prior to the electrochemical experiments, (b, c) negative electrode after aging at 3.5 V and 500 hours, and (d, e) positive electrode after aging at 3.5 V and 500 hours.

500 hours. At lower magnifications (Figure 14.8b, d), it is difficult to discern between the two electrodes and indeed also between the aged and the pristine electrode material. However, at larger magnifications (Figure 14.8c, e), certain features characteristic for each electrode can be identified.

For the negative electrode, a large number of particles which exhibited the peculiar surface texture shown in Figure 14.8c was observed. The thread-like web is attributed to the PTFE binder, but the contact points between these threads and the activated carbon particle in Figure 14.8c hint at a reaction between the two in terms of an electrochemical deterioration of the binder. In this context, the defluorination of PTFE is known to occur at negative potentials, resulting in a carbonaceous residue [392].

On the positive electrode, there was a large number of particles with the strongly textured surface shown in Figure 14.8e. The impression of a surface coverage is given, although the features might be suggested to be analogous to those observed on HOPG in the positive potential range in the AN-based electrolyte (Figure 13.4). These, on the contrary, were attributed to the swelling of surface-near regions due to the formation of degradation products from intercalated electrolyte species. In the absence of continuous stacked graphene sheets at the length scales relevant for Figure 14.8d, however, the sub-surface degradation mechanism does not satisfactorily account for the observed surface structure. Hence, the observed morphological change of the positive electrode is more likely to be the result of a surface coverage.

Neither of the particular features shown in Figure 14.8c and e were ever found in pristine YP17/PTFE electrodes, but were abundant on the electrodes aged under the indicated conditions.

14.3.3. Changes in electrode porosity

The nitrogen adsorption isotherms for negative and positive electrodes after aging at 3 V, 3.5 V and 4 V are summarized in Figure 14.9 for different aging durations. The most striking observation is the trend towards significantly lower nitrogen uptake for the positive electrode compared to the negative electrode, indicating a loss of porosity which is accessible to nitrogen gas.

An evaluation of the NLDFT and BET surface areas as well as the NLDFT and DA pore volumes is presented for all investigated samples in Table 14.2. An important finding is the significantly lower surface area and porosity of the positive electrode compared to the negative electrode for a given aging voltage and the longest aging time. Sim-
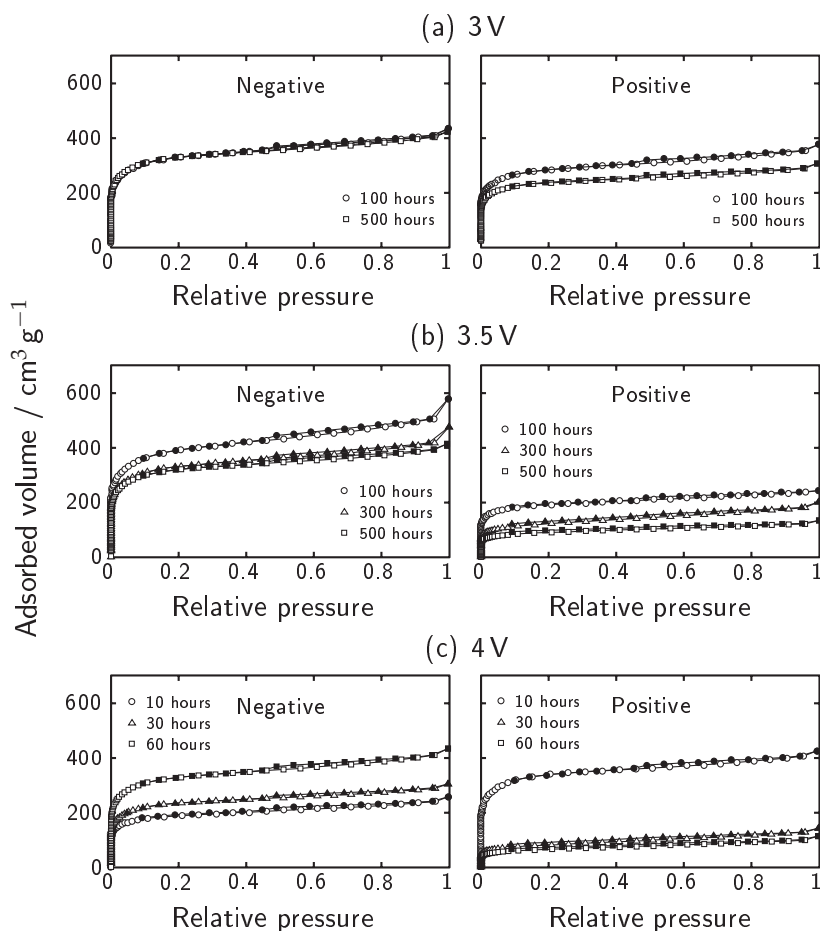
Figure 14.9.: Nitrogen adsorption isotherms for electrodes investigated after aging in 1 M Et$_4$NBF$_4$/AN at (a) 3 V, (b) 3.5 V and (c) 4 V. The adsorption volume was normalized to the total sample mass. Open symbols represent adsorption data while the filled symbols denote desorption data.

ilar results were obtained at elevated temperatures and cell voltages below 3 V by Azaïs et al. [265, 266] and Zhu et al. [267, 268]. In the present case, the NLDFT surface area of the negative electrode was always in excess of 1200 m^2 g^{-1} after prolonged aging in the AN-based electrolyte while that of the positive electrode decreased to values as low as 238 m^2 g^{-1} at 4 V after 60 hours.

Table 14.2.: Gravimetric surface areas (BET and NLDFT) as well as the total
pore volumes (NLDFT) and microporous volumes (NLDFT, DA) of
YP17/PTFE electrodes aged in 1 M solutions of Et_4NBF_4 in AN at
different cell voltages U for different durations t.

U V	t hours	Electrode	A_{NLDFT} (A_{BET}) $m^2 g^{-1}$	V_{NLDFT} $cm^3 g^{-1}$	$V_{mi,NLDFT}$ ($V_{mi,DA}$) $cm^3 g^{-1}$
3	100	neg	1261 (1230)	0.62	0.42 (0.41)
		pos	1126 (1062)	0.53	0.37 (0.36)
	500	neg	1250 (1235)	0.61	0.43 (0.41)
		pos	975 (888)	0.44	0.33 (0.31)
3.5	100	neg	1458 (1458)	0.79	0.48 (0.48)
		pos	783 (721)	0.36	0.28 (0.26)
	300	neg	1218 (1243)	0.65	0.41 (0.42)
		pos	431 (447)	0.27	0.16 (0.15)
	500	neg	1222 (1202)	0.59	0.42 (0.41)
		pos	319 (334)	0.18	0.13 (0.11)
4	10	neg	761 (709)	0.36	0.26 (0.26)
		pos	1294 (1274)	0.62	0.45 (0.43)
	30	neg	883 (880)	0.44	0.31 (0.30)
		pos	290 (295)	0.2	0.11 (0.09)
	60	neg	1239 (1231)	0.62	0.42 (0.44)
		pos	238 (240)	0.15	0.08 (0.08)

The only instance for which the aged negative electrode exhibited a
smaller specific surface area than the positive electrode was for aging
at 4 V after 10 hours. While the significance of this result is not clear, it
is interesting to note that the negative electrode experienced the most
negative polarization at this point (nearly -2.5 V, see Figure 14.4), while
the positive electrode had not yet spent a long time at excessively high
potentials. At longer aging times at 4 V, the voltage window shifted
towards more positive potentials along with the electrode potentials,
resulting in more irreversible charge consumption at the positive elec-
trode and less for the negative electrode, thus possibly enabling a re-
generation of the negative electrode surface area. However, this aspect
will not be discussed further here.

The reduction in pore volume of the positive electrode implies a de-
struction of accessible porosity. From a comparison of the micropore
volume with the total pore volume, the reduction in porosity occurs not
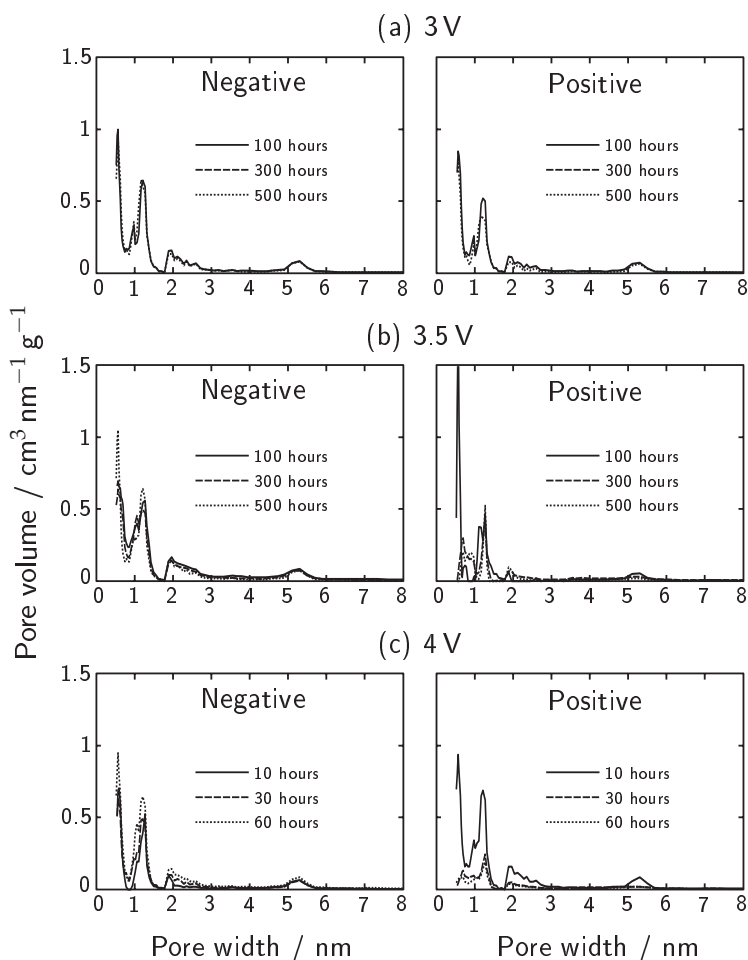
Figure 14.10.: NLDFT pore size distributions for electrodes investigated after aging in $1\,\mathrm{M}\ \mathrm{Et_4NBF_4/AN}$ at (a) $3\,\mathrm{V}$, (b) $3.5\,\mathrm{V}$ and (c) $4\,\mathrm{V}$.

only on the length scale of micropores but also for meso- and macropores.

Of course, the observed gravimetric surface area losses could be accounted for by an increase in the electrode mass during aging. Based on the hypothesis of surface coverage by electrolyte degradation products, the increase in the amount of non-porous mass is indeed expected to contribute to the values given in Table 14.2. Therefore, it is necessary

to consider the pore size distributions obtained via NLDFT analysis (Figure 14.10).

The pore size distributions in Figure 14.10 provide evidence for the integrity of the pore structure of the negative electrode at all investigated potentials. For the positive electrode, however, the case is the contrary. The pore volume is significantly reduced at sizes around and below 1 nm, with changes in the distribution of pore sizes indicating that the observed reduction in the gravimetric values as listed in Table 14.2 is not simply a mass effect.

In reference to the observed capacitance loss of the positive electrode and its apparent surface coverage (Section 14.3.2), it is tempting to correlate these results with the porosity loss by interpreting the latter as a consequence of the formation of dense, solid electrolyte degradation products within micro- and macropores. Due to the severe capacitance loss and high resistance suggested by EIS, the solid deposit must be both electronically insulating and a poor ionic conductor.

14.3.4. Chemical analysis of aged electrodes

The chemical changes undergone by the aged electrodes following the washing procedure were assessed by means of the C 1s spectra obtained by XPS (Figure 14.11). It was found that significant sample charging often affected the F 1s signal, as has been reported for PTFE in the past [507, 508], thus complicating the interpretation of this feature. Thus, the F 1s signal will not be discussed in the context of the present work, although it is noted that after aging at 3.5 V and 4 V, the charging effect for the F 1s signal disappeared and a single signal close to a binding energy of 686 eV remained. This value is less than the corresponding binding energy of F in uncharged PTFE, 690.2 eV [370, 508–510], thus hinting at a defluorination of the PTFE binder under these conditions.

The C 1s spectra exhibited marked differences as a function of electrode polarity and cell voltage (Figure 14.11). A main peak attributable to the carbon bonding environment in YP17 was found at 284.4 eV, as expected for sp^2 hybridized carbon in an essentially carbon-coordinated environment [370].

324
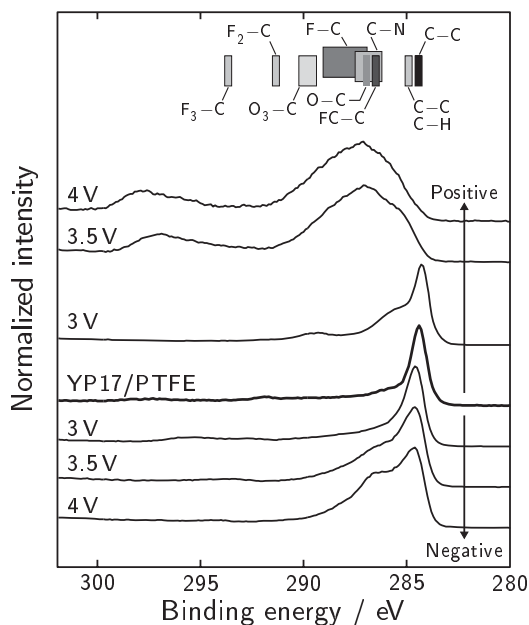
Figure 14.11.: C 1s spectra of YP17/PTFE after aging at the indicated full cell voltages after 100 hours (60 hours for 4 V). The assignment of chemical species to different binding energies is referred to in the text.

For all aged negative electrodes, this main signal remained the most intense feature of the C 1s spectrum. Under more severe aging conditions, the appearance of additional contributions between 285.5 eV and 288.5 eV was noted, suggesting a progressive functionalization or coverage of the carbon.

Possible assignments for the C 1s signal in this range include one-fluorine environments such as C−CF or CF−C [510], nitrogen functionalities such as C−N, C=N or C≡N [267, 370] as well as oxygen containing moieties such as C−O or O−C=O [500, 501]. In addition, an increase in the high energy shoulder of the main C 1s peak can arise from a reduction of the graphene edges to C−H and C−C, whereby the latter may be considered as the attachment of an alkyl group to the graphene-like framework [267, 268, 500, 501]. Since the presence of all of the elements involved in these hypothetical functionalization schemes was verified in all cases, it is not attempted to resolve the pre-

cise nature of the functionalization at this point. With high likelihood, contributions from all of the above are of relevance.

For the positive electrode, a markedly different chemical modification was noted under increasingly severe aging conditions. For the most significantly aged samples (3.5 V and 4 V), a drastic broadening and shift of the main C 1s peak to higher binding energies was observed. In these cases, there appeared to be no remaining component attributable to the pristine activated carbon, indicating either a completely dense surface coverage with well-adhering deposits from electrolyte degradation and/or a complete reaction of the carbon with heteroatoms. Although the possible functionalization schemes listed above for the negative electrode apply equally to the positive electrode, a dominating contribution may be expected from C$-$F type bonds due to the presence of the signal close to 298 eV. However, even within the bonding arrangement of CF$_3$, a maximum binding energy of about 293 eV [510] would be expected. Similarly, the maximum binding energy reported for sp^3 hybridized carbon atoms with covalent C$-$F bonds is 294.6 eV [502]. Therefore, it is likely that partial sample charging occurs for the positive electrodes aged under the most severe conditions, causing a shift of certain C 1s features to higher binding energies by a few eV. Of course, the increase in sample charging provides a further support for the hypothesis of a loss of electronically conductive carbon and/or a surface coverage by an electronically insulation film.

14.3.5. Effect of solvent and water—preliminary studies

The influence of the solvent nature and water impurities on the aging of EDLCs each deserves extensive studies in its own right. However, it is desirable to obtain first insights into the fundamental differences, if there are any, between the aging characteristics of the AN- and PC-based electrolyte solutions in order to assess the solvent contribution towards aging. Further, water impurities in the electrolyte solution have been reported to have a drastic effect on the EDLC lifetime [77, 511].

For these reasons, aging experiments under identical conditions as those described above for the AN-based electrolyte were conducted according to Table 14.1. A controlled water contamination of the AN-based electrolyte was achieved by adding a defined amount of ultra-

high purity water (Purelab UHQ from ELGA LabWater, UK) and determining the water content of this solution by coulometric Karl Fischer titration, which was was found to be (1000 ± 100) ppm.

Effect of water impurities in the electrolyte

Despite the limited number of experiments conducted in the present work towards understanding the influence of water on the aging behavior of EDCLs, some important insights can be gained from the selection of results presented below. Despite the significant water content of the electrolyte, the capacitance fading for the full cell was not observed to differ greatly from that of the as-received EDLC electrolyte (Figure 14.12a). Also, the capacitance and resistance changes of the individual electrodes (Figure 14.12b, c) exhibited the same trend as observed for the electrolyte with low water content. In both cases, the capacitance of the positive electrode diminished rapidly while its resistance increased notably, suggesting identical aging mechanisms.

During the electrochemical characterization before and after aging during 300 hours at 3.5 V, the change in the CVs did not appear to depend strongly on the water content of the electrolyte (Figure 14.13a). In both cases, a capacitance loss and an increase in resistance was observed.

The impedance spectra prior to aging (Figure 14.13b) were also very similar irrespective of the water content. However, a pronounced difference in the impedance spectra of the aged cells was noted (Figure 14.13c). The H_2O contaminated electrolyte solution exhibited a significantly higher ESR and imaginary part at low frequencies, indicating more pronounced modifications of the ion mobility and adsorption in the porous structure.

Hence, it is likely that water impurities contribute towards the formation of degradation products within micropores, which may be expected to affect the EIS spectra in such a significant way. Clearly, more work is required to confirm this hypothesis. For the sake of the present study, however, it is noted that water contaminations in the electrolyte do not appear to drastically modify the rate of capacitance loss or fundamental mechanism of aging in $1 M$ Et_4NBF_4/AN.
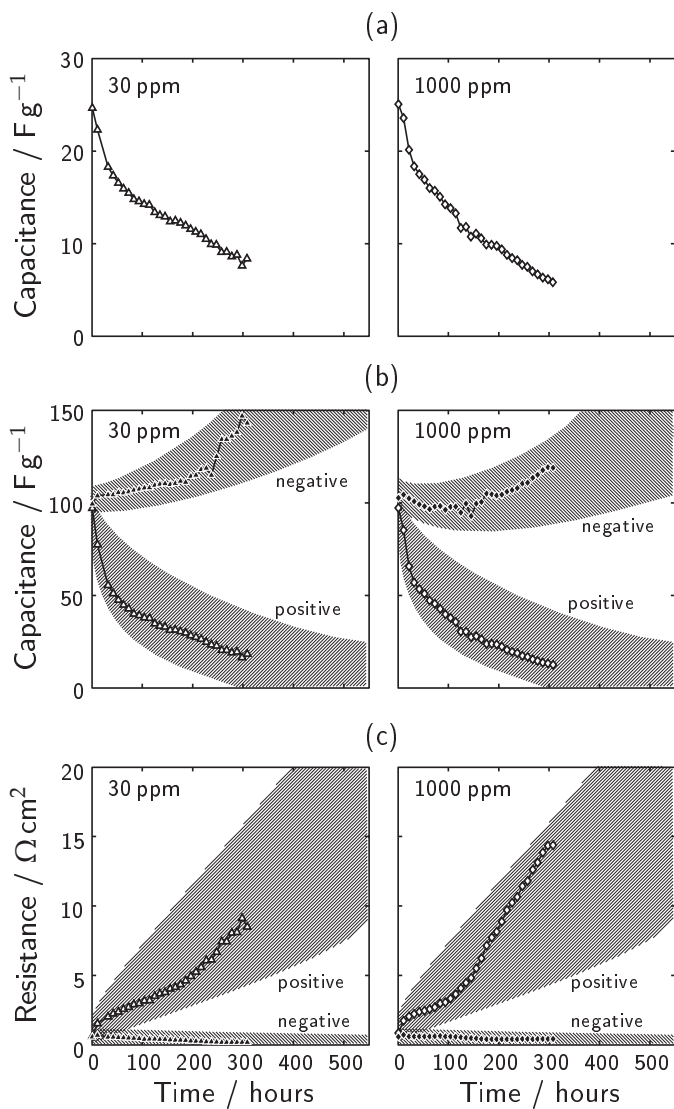
Figure 14.12.: (a) Full cell capacitance loss, (b) single electrode capacitance changes, and (c) single electrode resistance changes during aging at 3.5 V in 1 M Et$_4$NBF$_4$/AN with different water contents. The hatched regions are guides to the eye.
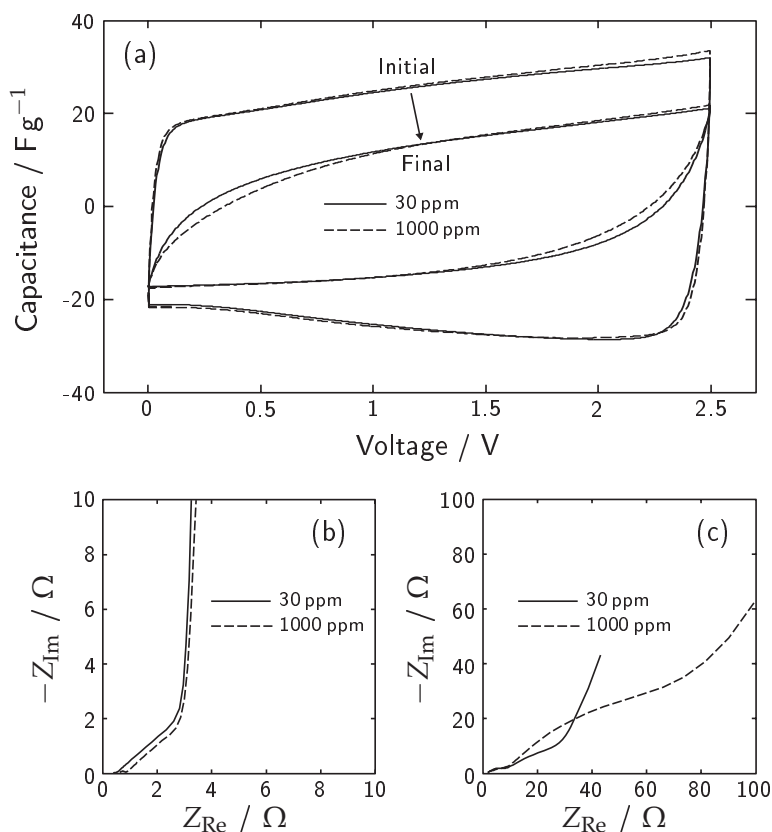
Figure 14.13.: Electrochemical performance loss of the full cells with 30 ppm H_2O (solid lines) and 1000 ppm H_2O (dashed lines) due to aging at 3.5 V for 500 hours. (a) CVs at $10\,\mathrm{mV\,s^{-1}}$, (b) EIS spectra prior to aging, and (c) EIS spectra after aging.

AN vs. PC as solvent

The capacitance fading of the YP17/PTFE full cell with the PC-based electrolyte is compared to that shown previously for the AN-based electrolyte at 3.5 V in Figure 14.14. The rate of capacitance loss was less pronounced for the PC-based electrolyte under the present aging conditions, with the capacitance dropping to 39 % of its initial value after 500 hours compared to 2 % for AN.

A fundamental difference in the aging behavior of the AN- and PC-based electrolytes at 3.5 V was the single electrode capacitance evolu-
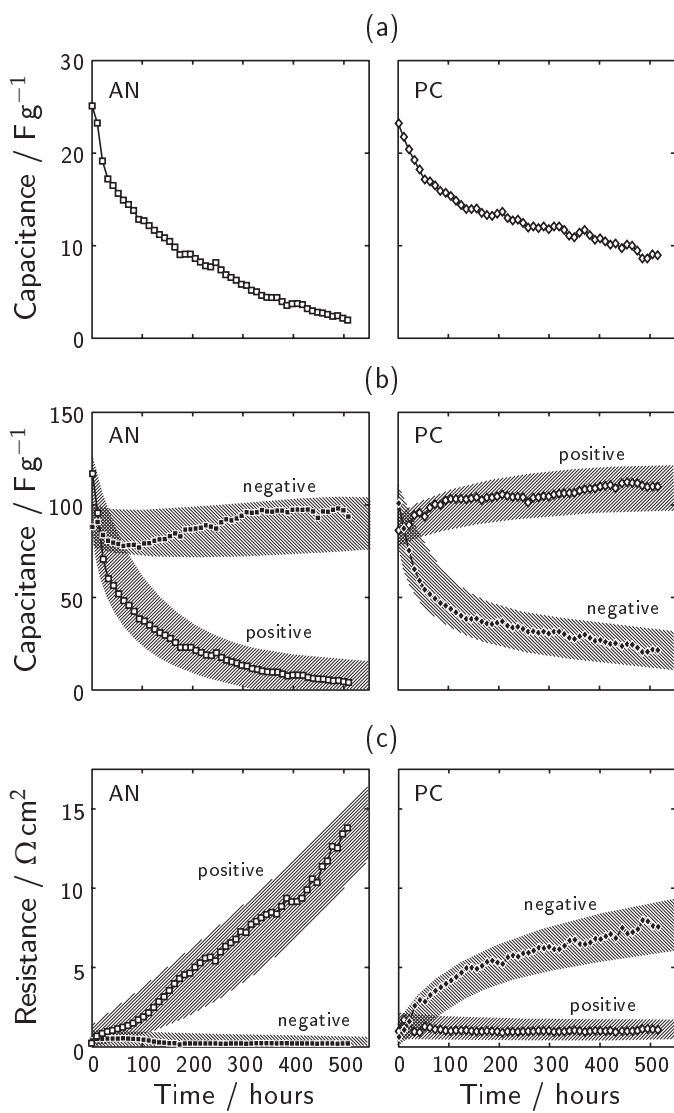
Figure 14.14.: Evolution of (a) the full cell and (b) single electrode capacitances as well as (c) the single electrode resistances for $1\,\text{M}$ Et_4NBF_4 in AN and in PC at $3.5\,\text{V}$ during 500 hours. The hatched regions are guides to the eye.

tion (Figure 14.14b). While the positive electrode was found to be the limiting electrode in a symmetric arrangement in $1\,M\,Et_4NBF_4/AN$, the situation was reversed for the PC-based electrolyte, in which the negative electrode was found to experience significant capacitance loss compared to the positive electrode. Similarly, the resistance increase in the PC-based electrolyte was dominated by the aging of the negative electrode (Figure 14.14c), which stands in contrast to the more pronounced aging of the positive electrode in AN. The results from the 100 hours aging experiment at 3.5 V confirmed these findings.

An examination of the potential excursions of the individual electrodes (Figure 14.15) revealed that the negative electrode was found to be polarized to potentials below -2 V, which would be expected to lead to irreversible charge loss according to the electrochemical characterization in Section 9.2.6. The potential spikes observed for the negative electrode in Figure 14.15 are in line with the increased *IR* drop at this electrode over time. The positive electrode was located close to +1.5 V, which is within the stable operating window for the PC-based electrolyte on YP17/PTFE (Section 9.2.6) and is in agreement with the capacitance retention of this electrode (Figure 14.14b).
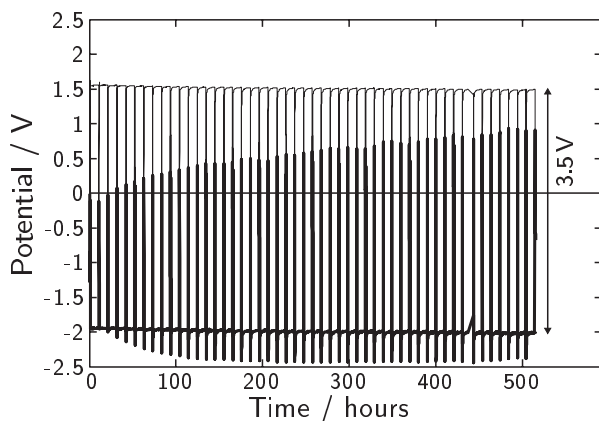
Figure 14.15.: Single electrode potential excursions in $1\,M\,Et_4NBF_4/PC$ during aging at 3.5 V for the positive (thin line) and negative (bold line) electrode.

The apparent increase in capacitance of the positive electrode in PC during aging (Figure 14.14b) can be attributed to the same effect which is responsible for the capacitance increase of the negative electrode in AN, namely an increase in the space charge capacitance of the electrode as the operational potential window is narrowed and shifted away from 0 V (Figure 14.15).

The improved stability of the PC-based electrolyte compared to the AN-based electrolyte under the present experimental conditions was clearly reflected by the corresponding CVs (Figure 14.16a) and Nyquist plots (Figure 14.16b and c).

Referring to the nitrogen adsorption data in Table 14.3, the effective gravimetric surface area was above $1000\,\text{m}^2\,\text{g}^{-1}$ for both electrodes even after 500 hours at 3.5 V. Thus, the blocking of porosity which was found to dominate the performance loss of the positive electrode in AN did not occur for the PC-based electrolyte solution, which is clearly evidenced by the pore size distributions in Figure 14.17. However, the possibility of removal of degradation products during the washing procedure in this case cannot be ruled out.

Finally, the electrodes aged in the PC-based electrolyte were analyzed by XPS. The C 1s spectra (Figure 14.18) exhibited some common features with the corresponding results from the AN-based electrolyte, notably the pronounced coverage of the positive electrode with fluorinated carbon species and also of the negative electrode with oxygen and/or nitrogen. However, an important difference exhibited by the

Table 14.3.: Gravimetric surface areas (BET and NLDFT) as well as the total pore volumes (NLDFT) and microporous volumes (NLDFT, DA) of YP17/PTFE electrodes aged in 1 M solutions of Et_4NBF_4 in PC at cell voltage U for duration t.

U V	t hours	Electrode	A_{NLDFT} (A_{BET}) $\text{m}^2\,\text{g}^{-1}$	V_{NLDFT} $\text{cm}^3\,\text{g}^{-1}$	$V_{mi,NLDFT}$ ($V_{mi,DA}$) $\text{cm}^3\,\text{g}^{-1}$
3.5	100	neg	1110 (1066)	0.54	0.38 (0.37)
		pos	1201 (1132)	0.57	0.40 (0.38)
	500	neg	1090 (1038)	0.52	0.37 (0.38)
		pos	1007 (947)	0.48	0.34 (0.33)
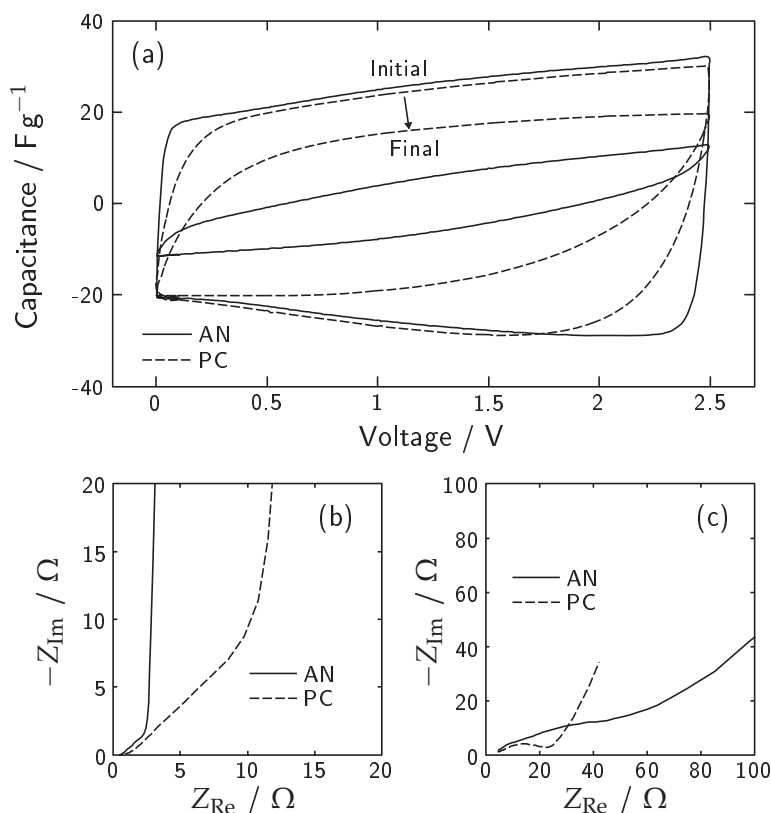
Figure 14.16.: Electrochemical performance loss of full cells based on $1\,M$ solutions of Et_4NBF_4 in AN or PC after aging at $3.5\,V$ for 500 hours. (a) CVs at $10\,mV\,s^{-1}$, (b) impedance spectra at $0\,V$ prior to aging, and (c) impedance spectra at $0\,V$ after aging.

positive electrode in the PC-based electrolyte was the presence of the C 1s feature attributable to the pristine activated carbon (Figure 14.18, top). Apparently, for the aged positive electrode in the PC-based electrolyte, a large amount of carbon remained within an sp^2 bonding arrangement with other carbon atoms and low surface coverage. This finding is in line with the electrochemical stability of the positive electrode in the PC-based electrolyte (Figure 14.14b, c).

In comparison to the electrodes aged in the AN-based electrolyte, those aged in the PC-based electrolyte typically contained 3–4 times more oxygen. A straightforward conclusion would be that the oxygen-
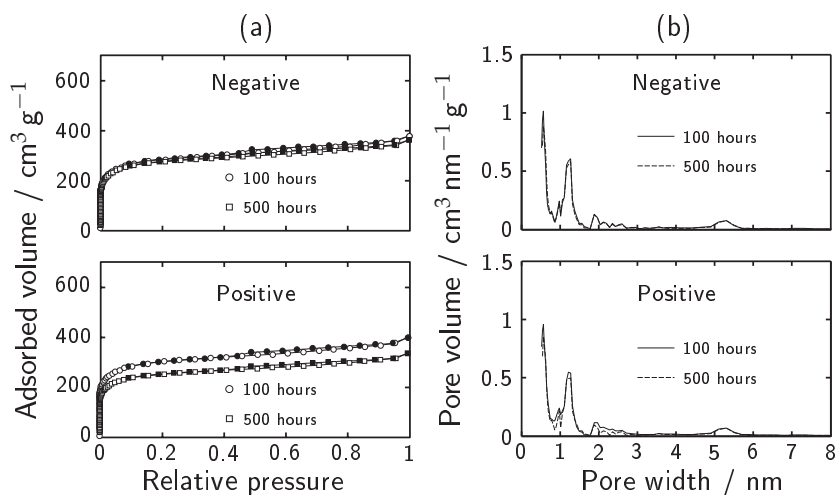
Figure 14.17.: (a) Nitrogen adsorption isotherms and (b) NLDFT pore size distributions of negative and positive electrodes aged at a cell voltage of 3.5 V in 1 M Et$_4$NBF$_4$/PC for different times. The open symbols represent adsorption data, while the full symbols denote desorption data.

containing solvent PC can act as a source of oxygen species for both electrodes. Ishimoto et al. [263] have indeed proposed the formation of poly(PC) films on both the negative and the positive electrode at elevated voltages. It appears likely that such polymeric films contribute at least in part towards the aging of the negative electrode in the PC-based electrolyte, as there were strong indications of oxygen functionalization in the C 1s spectrum (Figure 14.18, bottom).

Further, the nitrogen content of the electrodes aged in the PC-based electrolyte solution was between 8 and 10 times less than that of the electrodes aged in the AN-based electrolyte under identical conditions. Thus, it appears as though the primary nitrogen source for solid degradation products or surface functionalization in the case of AN is the decomposition of the solvent rather than a degradation of the cation Et$_4$N$^+$. Therefore, in all systems investigated in the present work, it is the degradation of the solvent which appears to be the limiting constraint for the performance loss of EDLCs at elevated voltages.
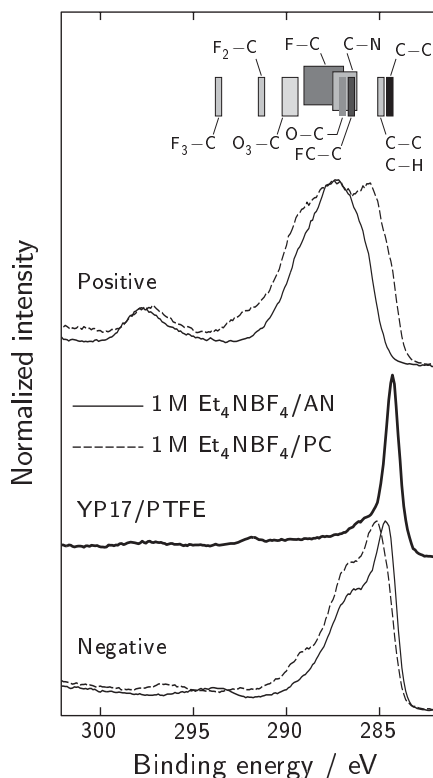
Figure 14.18.: C 1s spectra of the positive and negative electrodes after aging at 3.5 V during 500 hours in 1 M Et₄NBF₄ in AN and in PC. The assignment of chemical species to different binding energies was discussed in the context of Figure 14.11.

14.3.6. Discussion

From the present investigation, new insights into the phenomenology of EDLC aging have been obtained. Through examination of the range of data presented above, it is possible to propose the most likely causes for aging at each electrode, whereby a full description of all conceivable redox processes is beyond the scope of this study. A variety of feasible reaction mechanisms have been compiled by Zhu [267] and Kurzweil and Chwistek [271]. In the following, it is attempted to elicit the most significant mechanisms which may be expected to lead to changes in the solid state and to have a direct influence on the observed loss of

electrochemical performance, either by the formation of insoluble deposits on or the functionalization of the activated carbon electrode.

In the AN-based electrolyte, a significant increase in the rate of aging occurred when increasing the cell voltage from 3 V to 3.5 V. The observed loss of cell capacitance could be traced back mainly to the drastic loss of capacitance of the positive electrode, which was attributed to irreversible oxidative processes occurring at this electrode at potentials above +1.4 V. Also, the resistance of this electrode increased dramatically, accounting for the resistance increase of the entire cell. After aging, the positive electrode was found to be heavily fluorinated and contain significant amounts of carbon bonded to heteroatoms such as oxygen or nitrogen.

The fluorination of the positive electrode may principally arise from a degradation of BF_4^- or from a defluorination of the PTFE binder. However, a decomposition of the binder alone would not result in an increase in the measured fluorine content of the electrode. Also, the defluorination of PTFE is a reductive process [392] which is expected to occur at the negative rather than the positive electrode. However, the possibility of migration of negatively charged, fluorine-containing binder decomposition products from the negative to the positive electrode can not be ruled out. It is mentioned that Nozu et al. [264] observed a transfer of macroscopic amounts of material from the negative to the positive electrode, presumably due to electrophoresis.

The fluorination of the positive electrode is more likely to originate from the degradation of BF_4^-. Chandrasekaran et al. [512] have proposed the fluorination of glassy carbon electrodes in a solution of Bu_4NBF_4 in dimethylformamide at +0.8 V vs. SCE via the following mechanism:

$$C + BF_4^- \longrightarrow (C{-}F{\cdots}BF_3) + e^- \qquad (14.4)$$
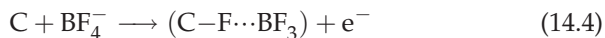
It is not clear whether further reactions of this type proceed to result in the presence of CF_3 species which was suggested by the XPS measurements. Only small traces of boron were found on the electrodes, indicating that the coordinated BF_3 might be released during the experiment or due to washing, as suggested by Suryanarayanan et al. [513]. At any rate, Reaction (14.4) has been shown to proceed in both AN

and in PC [513], thus providing a possible cause for the fluorine-related signals of the aged positive electrodes in either electrolyte.

However, in the PC-based electrolyte, the aging of the positive electrode was found to be significantly less than in AN. Therefore, another more important aging mechanism appears to act in the case of AN, most likely involving the solvent itself. Without going into details, the anodic decomposition of AN has been reported to mainly lead to the formation of CO_2, CH_3CNBF_3 and, in the presence of water, acetamide (CH_3CONH_2) [514, 515]. However, all of these compounds are present either in the dissolved or gaseous forms, making a correlation with the loss of capacitance and surface area difficult.

Tourillon et al. [516] have reported the anodic polymerization of AN at +2.6 V against a Ag/Ag^+ reference electrode. Zhu et al. [267, 268] have suggested this to be an important aging mechanism in AN-based electrolytes for EDLCs. Tourillon et al. [516] showed that the polymerization reaction was initiated by the oxidation of the anion, in their case ClO_4^- or BF_4^-:

$$BF_4^- \longrightarrow BF_4^{\cdot} + e^-$$ (14.5)

The radical leads to a deprotonation of the solvent according to

$$BF_4^{\cdot} + CH_3CN \longrightarrow CH_2CN^{\cdot} + H^+ + BF_4^-$$ (14.6)

Finally, the proton initiates the cationic polymerization by the reaction

$$CH_3CN + H^+ \longrightarrow CH_3C{=}NH^+$$ (14.7)
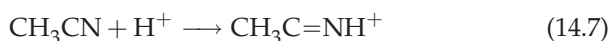
Further molecules of AN can add to the product of Reaction (14.7) to form poly(AN) [516]. The pronounced increase of the C 1s signal at binding energies between 285 eV and 288 eV observed in the present work might therefore be attributed in part to the formation of poly(AN). In particular, the polymerization within micropores or at their entrance can account for the pronounced loss of accessible pore volume determined by nitrogen gas adsorption and, therefore, also for the reduced capacitance and increased resistance of the positive electrode. However, it should be noted that Tourillon et al. [516] assigned a high ionic conductivity to their electrochemically prepared poly(AN) films on Pt.

Thus, the polymerization mechanism of AN within micropores of the positive activated carbon electrode and possible subsequent degradation steps remain to be confirmed.

For the negative electrode, the irreversible charge loss at potentials below -2 V was found to be dominated by the defluorination of PTFE (Section 9.2.6). Direct evidence for the cathodic carbonization of PTFE at the surface of activated carbon particles was observed via SEM (Figure 14.8c). The reductive defluorination of the PTFE binder had a less pronounced effect on the capacitance of the negative electrode than the degradation mechanism proposed above for the positive electrode. Yet, the occurrence of binder degradation is still of importance for several reasons. The loss of binder is expected to lead to a loss of cohesion between activated carbon particles, thus possibly contributing towards a higher equivalent series resistance. Further, the large amount of charge consumed irreversibly at the negative electrode causes its potential be be pinned at this point. As a result, any attempt to increase the cell voltage further leads to a larger excursion of the positive electrode to more oxidative potentials. Since the corresponding oxidative processes were found to lead to a dramatic loss of capacitance for the positive electrode, it can be stated that the binder decomposition at the negative electrode has an indirect, but significant effect on the capacitance loss of the full cell. Finally, although the negative electrode retained a significant portion of its capacitance in the particular stacked electrode arrangement employed in the present work, other cell arrangements might well suffer from loss of active material at the negative electrode during PTFE decomposition.

The preservation of the porosity of the negative electrode suggests that the aging mechanism differs fundamentally from that of the positive electrode. The documented electrolyte decomposition pathways in the negative potential range for the type of AN-based electrolyte used here include the degradation of AN to produce the 3-aminocrotonitrile anion, $(CH_3C(NH)CHCN)^-$ [514], and the Hofmann degradation of the cation Et_4N^+ by the cleavage of an alkyl group and corresponding release of ethene (C_2H_4) and formation of the amine Et_3N [267, 271]. Apart from a loss of electrolyte species, these mechanisms can not account for EDLC aging in terms of a modification of the carbonaceous

electrodes. However, the functionalization of edge sites or unsaturated sp^2 hybridized sites of the activated carbon by heteroatoms could be envisaged to lead to an increased electronic resistance within and between π bonded clusters, eventually leading to the isolation of individual fragments from the remaining conductive carbon network. However, further study is needed to support this hypothesis and establish the according reaction pathways.

In the PC-based electrolyte, the positive electrode remained highly capacitive even after 500 hours at a cell voltage of 3.5 V. Expected oxidation reactions of 1 M Et_4NBF_4/PC, apart from the defluorination of BF_4^- according to Reaction (14.4), include the decomposition of PC to CO_2 [261, 517, 518] and oxygen-containing species which may be deposited on the electrode [99, 263]. Apparently, these reactions at the positive electrode are not primarily responsible for the aging of the full cell in the PC-based electrolyte at 3.5 V.

Instead, it was observed that the negative electrode experienced a prominent capacitance loss under the present experimental conditions. Upon cathodic reduction, PC is expected to decompose to propene (CH_3CHCH_2) [261, 517] and carbonate deposits [99, 263, 517] on the electrode. The XPS spectra (Figure 14.11) appear to support the formation of signification oxygen-containing moieties. However, the surface area accessible by nitrogen gas adsorption (Table 14.2) remained above $1000 \, \mathrm{m^2 \, g^{-1}}$ for the negative electrode even after 500 hours at 3.5 V, suggesting that the reason for the capacitance loss is not a blockage of pores as was concluded for the positive electrode in the AN-based electrolyte.

Hence, the negative electrode in PC is likely to lose its capacitance via a similar route as the negative electrode in AN, i.e. through a loss of conductivity and isolation of conductive clusters. It is unclear whether this proceeds via a direct reduction of the activated carbon framework or via a deposition of electronically insulating carbonates, although the XPS analysis appears to favor the latter possibility. Since the electrode porosity did not correlate with the capacitance loss of the negative electrode, the solid degradation products must be either sparsely distributed, porous, permeable to gas or easily removable by the washing procedure. Currently, it is not possible to unambiguously rule out any of these possibilities.

Finally, the significant difference between the chemical composition of aged activated carbon electrodes and that of the electrochemically treated HOPG surface (Chapter 13) should be addressed. While the C 1s spectrum of positively polarized HOPG matched that of a freshly cleaved HOPG surface, the C 1s spectrum of the negatively polarized HOPG indicated functionalization of the surface with heteroatoms.

However, none of the features associated with the aging of the activated carbon positive electrodes in the AN- or PC-based electrolytes were found on HOPG. There may be several reasons for this, including the higher water concentration within micropores of activated carbon compared to the HOPG surface which might promote the degradation reactions, the abundance of surface functional groups on the activated carbon which could initiate these reactions and, finally, the possibility of easily washing away poorly adhering degradation products from the flat HOPG surface compared to the high retention capability of the microporous activated carbon structure. Therefore, considerable caution should be exercised when extrapolating results obtained on model electrode surfaces such as HOPG to other systems.

14.4. Conclusions

The capacitance loss and resistance increase of symmetric EDLC systems based on activated carbon electrodes at elevated voltages was resolved on the single electrode level. In $1\,M\,Et_4NBF_4/AN$ at $3.5\,V$, the capacitance of the positive electrode faded at a significantly higher rate than for the negative electrode, thus dominating the full cell capacitance loss. The applied cell voltage led to a defluorination of the binder at the negative electrode and a corresponding embrittlement of the electrode, while the gravimetric capacitance of this electrode was not significantly altered by the process. The potential pinning of the negative electrode potential during binder decomposition had the effect of promoting oxidative degradation at the positive electrode.

For the positive electrode in the AN-based electrolyte, the dominant degradation process at elevated cell voltages was attributed to the decomposition of AN, possibly via a polymerization mechanism as suggested in recent studies on the aging of AN-based EDLC systems at

elevated temperatures [267, 268]. The product formed by this process reduced the amount of accessible porosity of the positive electrode significantly, thus providing an explanation for the severe capacitance loss and resistance increase. Further, a significant fluorination of the positive electrode was observed, possibly due to the defluorination of BF_4^- or the migration of fluorine-containing binder decomposition products from the negative to the positive electrode. However, this does not seem to be the main degradation mechanism of the positive electrode in AN, since similar fluorination features were observed for the positive electrode in the PC-based electrolyte for which a significantly lower rate of aging was found.

First trials regarding the effect of H_2O in the AN-based electrolyte revealed that the aging mechanism at elevated voltages was not drastically altered compared to the as-received electrolyte solutions even for water contents as high as 1000 ppm. The most pronounced difference observed for the water-rich system was an increase in the low frequency impedance relative to the water-poor system, suggesting an enhanced modification of the pore electrolyte or interfacial chemistry due to the presence of H_2O.

Full cells aged in $1\,M\,Et_4NBF_4/PC$ exhibited completely different aging characteristics than the AN-based cells. The positive electrode was found to exhibit a markedly slower rate of aging than in the AN-based electrolyte, thus highlighting the critical role of the solvent. The rate of capacitance loss was much more pronounced for the negative electrode, which was tentatively attributed to a loss of conductive pathways due to surface functionalization and the deposition of carbonates on the electrode.

Part IV.

General discussion and conclusions

Chapter 15.

Discussion and conclusions

15.1. Electrochemical charge storage in EDLCs

The charge storage in EDLCs based on activated carbon electrodes and non-aqueous electrolyte solutions was shown to approach capacitive behavior over a wide range of potentials (Chapter 9). Electron and hole doping during charging of the negative and positive electrode is compensated by the accumulation of the corresponding counterions within the electrochemical double layer formed at the interface between electrode and electrolyte. In the present work, the electrochemical charge storage in a commercially available activated carbon derived from coconut shell, YP17 from Kuraray Chemical (Japan), in combination with a 1 M electrolyte solution of Et_4NBF_4 in AN was described.

Despite the symmetric arrangement of identical electrodes in EDLCs, the electrode capacitances are found to depend on the polarity, which is often ascribed to the inherent ionic asymmetry in the electrolyte. In Chapter 10, a pronounced asymmetry of the activated carbon electrode itself upon electron and hole doping was demonstrated using in situ Raman spectroscopy and relative resistance measurements. Deviations from the idealized graphene structure in activated carbon can account for the observed changes, with locally varying $C-C$ bonding arrangements resulting in an asymmetry of the DOS with respect to the Fermi level and also of the vibrational properties sampled in the Raman experiments upon electron and hole doping. Thus, a description of the asymmetric capacitance behavior of EDLCs must take into account the asymmetry of the electrode itself upon electron and hole doping, and not only that of the ions.

Studies of SWCNTs (HiPco SWCNTs from Carbon Nanotechnologies, USA) were performed both in terms of their feasibility as a viable electrode material in EDLCs and with respect to their relatively

well-defined geometric and electronic structure serving as a comparative standard for YP17. Despite the related structural basis of these two materials, significant differences in the doping behavior were clearly observed by Raman spectroscopy. Thus, the structure of activated carbon incorporates distinct differences to that of graphene-based systems in terms of significant in-plane disorder and cluster formation. While the SWCNTs studied in this work exhibited capacitive charging characteristics similar to YP17, their unique electronic structure enabled a differentiation between the doping behavior of semi-conducting and metallic SWCNTs. While semi-conducting SWCNTs were shown to be essentially undopable at low polarizations, as expected, an increase in capacitance upon increasing polarization in either potential range was observed which was steeper than that of YP17. Assuming a perfectly rigid electrode, this may be understood in terms of a higher DOS of the SWCNTs upon sufficiently large Fermi level shifts for the particular samples studied in this work.

However, evidence for another contribution to the increased capacitance upon polarization was obtained by studying the macroscopic expansion and capacitance enhancement of an entangled SWCNT mat (Chapter 11). It was found that a wetting of the interstitial bundle porosity could be achieved by polarizing the electrode to sufficiently negative or positive potentials, which was evidenced by a pronounced irreversible expansion of the electrode perpendicular to the bundle axis. Further, the varying occupation of the interstitial porosity of SWCNT bundles by ions depended on the electrode potential during charging, which could account for the measured reversible macroscopic height changes of the SWCNT electrode.

As an important consequence, it must be deduced that the effective interfacial area between electrode and electrolyte may depend significantly on the electrode potential for materials offering any kind of ion insertion sites. In graphite (SFG44 from TIMCAL, Switzerland), these insertion sites are defined by the crystalline lattice, resulting in ion intercalation at well-defined potentials. By investigating the charge storage in SFG44 using EDLC electrolytes, it was found that both cationic and anionic intercalation occurred readily at sufficiently large polarizations below -2.1 V and above +1.6 V on the potential scale of YP17. In

graphite, at least the intercalation of the anion, BF_4^-, was found to occur under cointercalation of the solvent using in situ XRD. Thus, the intercalation of solvated species in this case appeared to be favorable despite the more demanding steric requirements during insertion into the graphite lattice.

For YP17, a macroscopic electrode expansion during charging similar to that of SWCNTs was observed. The immediate expansion response during polarization implies the presence of ion insertion sites which are more easily accessible than the interlayer spacing in graphite. First trial experiments conducted on a GO-derived, expanded graphite lattice revealed that an increase in the interlayer spacing between graphene sheets may significantly facilitate the insertion of ions, expressed by a shift in the onset potential for intercalation, despite the presence of turbostratic disorder. However, the ion insertion sites in YP17 must be even more accessible than those of the GO-derived sample, leading to an identification of the microporosity as the most facile insertion location. The pore size distribution of YP17 (Chapter 9) was found to exhibit a range of pore sizes in the sub-nanometer regime, thus providing a distribution of ion insertion sites. The ion insertion between neighboring graphene sheets is, of course, also expected at suitable electrode potentials, but was estimated to provide a very small contribution towards the total charge storage and dimensional changes of the electrodes due to the low abundance of parallel graphene sheets in YP17. On this premise, the absence of distinct insertion peaks during cyclic voltammetry can also be explained.

Not only the nature of the insertion sites but also the characteristics of the electrode framework can influence the ion insertion mechanism. A comparison of the cathodic and anodic expansions resulted in very different apparent relative ion size ratios for the crystalline graphite, SFG44, and the two microporous carbons, SWCNTs and YP17. This might be taken as an indication for different solvent coordination of the inserted ions in the two cases. Given that the ion diameters approach the pore sizes of the activated carbon, it is perhaps not surprising that the solvent coordination of the ions is different than in the bulk. However, the cause for the apparently different spatial requirements of the ions within graphite and within micropores, which both represent con-

fined insertion sites, is not well understood yet and could be the target of future studies. Motivations in this respect include a slowing of aging processes by excluding solvent molecules from the interfacial area within micropores or an optimization of ion insertion capability within a given potential window.

At any rate, it is important to emphasize that the effective interfacial area between an electrode with insertion sites, be they well-defined as in crystalline lattices or broadly distributed as in disordered activated carbons, depends on the electrode potential. The determination of the accessible pore volume for a certain ion size by ex situ means can not be considered rigorous in the context of electrochemical systems, since electrostatically driven ion insertion can force ions to occupy insertion sites which are smaller than the ions themselves.

The above discussion suggests a possible increase of charge storage capability of EDLCs by efficiently utilizing ion insertion processes within the operating voltage window. Since it is desirable to preserve the fast charge and discharge characteristic of double layer charging, it may be proposed to tune the micropore size (rather than to provide crystalline intercalation sites) in order to establish a distribution of insertion sites which can be entirely utilized within the region of potential stability of the electrolyte solution. While similar strategies have been followed using templating techniques [329, 519], ion insertion mechanisms in these materials are usually not explicitly considered or discussed. A systematic investigation of the dependence of the onset potential for ion insertion on the nature of the insertion site would aid in the strategic design of EDLCs in which the utilization of interfacial area is maximized with respect to mass and volume in a given potential window.

15.2. Aging mechanisms of EDLCs

By elucidating the supposedly reversible charge storage mechanisms in EDLCs in the previous section, deviations from the idealized electrostatic charging of a rigid electrode/electrolyte interface without charge transfer were already established. A systematic categorization of interfacial charge transfer processes is convenient for the discussion of

the most important aging mechanisms in EDLCs at elevated voltages (Figure 15.1).

In general terms, the aging of EDLCs must involve irreversible processes beyond double layer charging in order to account for the loss of electrochemical performance. In other words, charge transfer across the electrode/electrolyte interface must occur, whereby this can be further refined to ionic (Figure 15.1a, b) or electronic (Figure 15.1c, d) charge transfer.

As discussed in the previous section, the occupation of all kinds of insertion sites by ions and solvent molecules must be considered as a function of the electrode potential. At electrode potentials near -2.1 V and +1.6 V, the onset potentials for intercalation of EDLC electrolyte species in graphite (Chapter 11), it may be estimated that every carbon atom in YP17 is accessible to electrolyte species. It was shown that the intercalation/deintercalation processes of EDLC electrolytes into the interlayer spacings of crystalline graphite resulted in a severe loss of crystallinity (Chapter 11). Correspondingly, a fatigue of the electrode upon repeated charge–discharge cycles might eventually lead to fracturing and the according consequences, namely a loss of conductive pathways or even active material, and must be considered an important aging mechanism in crystalline electrodes.
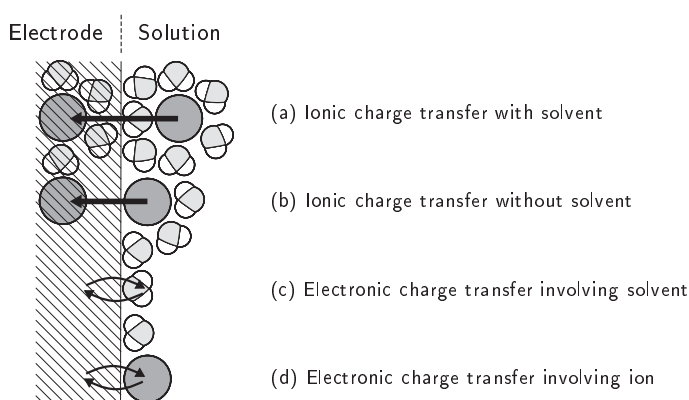
Figure 15.1.: Schematic overview of possible modes of interfacial charge transfer.

However, for activated carbon, the amount of strain introduced into the material by the simple insertion and extraction of ions as in Figure 15.1a and b is significantly less than for graphite, as evidenced by the much smaller macroscopic expansions (Chapter 11). Using in situ SAXS (Chapter 12), it was found that the characteristic length scale of the porous carbon framework remained essentially constant even following exposure to extremely negative or positive potentials (except for the positive electrode in the AN-based electrolyte, which will be discussed later). A possible explanation for the apparent robustness of the activated carbon framework against permanent structural modifications due to ion insertion and deinsertion cycles is the significant cohesion between cross-linked localized clusters as well as the presence of intermittent void space, in contrast to the weak interplanar forces between stacked graphene sheets and long-range strain mediation in high-density samples.

Upon combination of ionic and electronic charge transfer, the decomposition of intercalated or inserted electrolyte species may result in a very different situation. Certainly, the probability of fracture is greater for graphite when the intercalated species undergo redox reactions which result in an abrupt change in volume. An extreme case in this respect would be the formation of gaseous reaction products from intercalated electrolyte species, which was found to lead to the drastic changes in the surface morphology of HOPG (Chapter 13). The occurrence of similar reactions within activated carbon might therefore well lead to a fracturing of the electrode and the corresponding detrimental effects.

From the aging studies conducted in the present work (Chapter 14), the capacitance loss of a symmetric YP17/PTFE full cell based on $1\,M$ Et_4NBF_4/AN at $3.5\,V$ was dominated by the rapid aging of the positive electrode, which in turn was associated with a loss of porosity linked to the oxidation of AN to dense, insoluble degradation products within pores. At this cell voltage, the PTFE binder was decomposed at the negative electrode, which is certainly detrimental for the interparticle cohesion, but was found to contribute negligibly towards the full cell aging compared to the capacitance loss of the positive electrode. Evidently, the primary cause for aging in AN-based, symmetric EDLCs at elevated

voltages is electronic charge transfer at the positive electrode involving AN, whereby the degradation of BF_4^- or migration of PTFE decomposition products from the negative to the positive electrode might also contribute to the aging process as implied by the significant fluorination of the positive electrode.

The use of PC as a solvent instead of AN resulted in an improved anodic stability, and at 3.5 V the capacitance loss of the full cell was in fact found to be dominated by the aging of the negative electrode. The capacitance loss of the negative electrode is tentatively explained by the formation of carbonates at the electrode surface from the reductive decomposition of PC, which is supported by the chemical analysis via XPS (Chapter 14) and the imaging of surface deposits at step edges on HOPG (Chapter 13). While not resulting in a blockage of porosity, these carbonates may electronically (perhaps also ionically) insulate the interfacial area, thus preventing double layer charging.

In comparing the aging characteristics of the two different solvents, it appears as though the present results have contributed towards understanding the low rate of gas formation and simultaneous high irreversible charge consumption in AN compared to PC [272]. More specifically, anodic reactions in the AN-based system tend to result in the formation of solid degradation products which adhere to the positive electrode, while in the PC-based system the formation of such reaction products appears to be less pronounced, with a correspondingly higher fraction of irreversible charge contributing to gas evolution.

In summary, the aging of EDLCs is obviously determined by the entire system and its components. The primary causes for aging in this work were linked to the decomposition of electrolyte species and, to a lesser extent, the reaction of active material with electrolyte species to form covalently bonded functionalities. It was illustrated that the voltage window of an EDLC may easily shift during constant voltage periods due to the different irreversible charge consumption rates at each electrode, thus causing unexpectedly strong oxidative or reductive potentials to act upon the single electrodes. Due to this interdependence of the positive and negative electrode, a precise knowledge of the processes occurring at different electrode potentials for each electrode is vital in order to understand the aging phenomena.

Due to the complexity of possible successive degradation reactions, it is difficult to predict the effect of modifying even a single component of the electrolyte solution and to make according recommendations. In particular, it is unclear to which extent the electronic properties and functional groups of the carbon influence the electrolyte degradation. Even though the mechanisms discussed in Chapter 14 do not explicitly involve carbon surface functionalities, it has been suggested that their presence accelerates the aging processes [259, 265, 266]. Hence, a complete understanding of the role of the carbon electrode in the degradation of electrolyte species is lacking and represents an important field of research in this respect. In the current situation, the experimental determination of the stability windows of entire EDLC systems will remain invaluable in the selection of components for degradation-resistant EDLCs at elevated voltages.

This work has contributed towards establishing an understanding of the voltage limitations of present day EDLCs. As a general note, the double layer capacitance of highly porous electrodes was found to be extremely sensitive towards the formation of insoluble degradation products which adhere to the electrode and are likely to obstruct the migration of ions.

15.3. Conclusions

The aim of the present work was to elucidate the charge storage mechanisms in EDLCs beyond the classical model of double layer charging and to identify the processes which result in a significant loss of EDLC lifetime in technically relevant systems at elevated voltages.

Concerning the reversible storage of charge in EDLCs, the following key findings were established:

- The approximation of the structure of activated carbon by graphene fragments is insufficient to explain the asymmetric doping behavior during electrochemical charging; rather, the existence of in-plane disorder and a C−C bond length distribution must be taken into account.

- The capacitance of carbonaceous electrodes depends sensitively on the electronic DOS near the Fermi level, which is most clearly demonstrated by the electrochemical doping behavior of semiconducting and metallic SWCNTs in EDLC electrolytes.

- The effectively accessible interfacial area of a carbonaceous electrode depends significantly on the electrode potential and the nature of its insertion sites. Compared to the well-defined intercalation sites in crystalline graphite, the insertion sites in microporous carbons such as activated carbon or SWCNTs may be thought to have a broad distribution of site energies. With increasing electrode polarization, successively more narrow insertion sites can be utilized for charge storage.

With regard to the phenomena which limit the voltage window of present day EDLCs, the following conclusions can be drawn:

- In AN- and PC-based EDLC electrolytes, ion intercalation into graphite results in a rapid degradation of the periodicity perpendicular to the graphene sheets, thus representing a possible fatigue mechanism. In particular, redox reactions involving cointercalated solvent molecules are expected to enhance this degradation.

- For activated carbon, the intercalation of ions into interlayer spacings between neighboring graphene sheets was found to contribute negligibly towards structural degradation. Instead, the insertion of ions into narrow micropores was found to dominate the dimensional changes of the material, resulting in a low strain and correspondingly less fatigue during cycling.

- Through standard electrochemical procedures, the potential onsets of irreversible charge consumption for a commercial activated carbon in $1\,M$ solutions of Et_4NBF_4 in AN and in PC were established, forming the basis for the interpretation of aging phenomena in these electrolytes.

- Based on systematic studies of the aging behavior in symmetric EDLCs consisting of PTFE-bound activated carbon electrodes and the AN-based electrolyte mentioned above, the cell voltage of EDLCs was found to be limited by the combination of PTFE defluorination on the negative electrode and AN decomposition on the positive electrode, whereby the latter mechanism leads to a drastic loss of electrode capacitance due to the blockage of pores by insoluble degradation products and consequently to a rapid decline of the cell capacitance.

- Due to the interdependence of solvent, salt and activated carbon in the aging process, the degradation mechanism is very system-specific. Generally, however, it appears as though the single electrode capacitance is affected most severely by a coverage of the electrode by insoluble electrolyte degradation products which obstruct ion migration.

15.4. Outlook

The continuation of several experimental approaches initiated in the present work is recommended. In particular, the effect of residual water on the degradation rate requires further study, not only in the form of electrolyte contamination, but also trapped water within the activated carbon microporosity remaining after conventional drying procedures.

In addition, several insights were obtained which warrant further investigations. The most interesting topics with a certain degree of novelty include:

- Tailoring of the DOS of activated carbon in order to maximize the space charge capacitance through the incorporation of heteroatoms or the introduction of additional disorder.

- Controlled modification of the pore size or graphene sheet separation distance in order to establish the potential onset of ion insertion processes and thereby optimized charge storage well within the stability limits of the electrolyte solution.

- Development of alternative binder chemistries for EDLC electrodes, possibly dedicated to a specific electrode polarity, or self-supporting electrodes in order to avoid the reductive defluorination of PTFE.

- Introduction of electrolyte additives to prevent the formation of insoluble degradation products, scavenge radicals or provide reversible redox shuttles to avoid excursions to critical potential regions.

It is believed that the application of in situ techniques such as those employed in the present work can aid research in the above fields by providing potential-dependent information, which may be considered essential for a complete understanding of the electrochemical processes in electrochemical energy storage devices.

Part V.

Appendix

Bibliography

[1] International Energy Agency. *Key world energy statistics 2008*. Available online at http://www.iea.org (Last visited on 15.01.2009).

[2] Shell International BV. *Shell energy scenarios to 2050*. Available online at http://www.shell.com (Last visited on 15.01.2009).

[3] Intergovernmental Panel on Climate Change. *The Physical Science Basis. Contribution of Working Group I to the Fourth Assessment Report of the Intergovernmental Panel on Climate Change*. Cambridge University Press, Cambridge, United Kingdom (2007).

[4] H. Ibrahim, A. Ilinca and J. Perron. *Renewable and Sustainable Energy Reviews* **12** (5), 1221–1250 (2008).

[5] B. Sørensen. *Renewable energy. Its physics, engineering, environmental impacts, economics & planning*. Elsevier, 3rd edition (2004).

[6] International Energy Agency. *Empowering variable renewables*. Available online at http://www.iea.org (Last visited on 15.01.2009).

[7] Electricity Storage Association. *Technology comparisons*. Available online at http://www.electricitystorage.org (Last visited on 15.01.2009).

[8] A. Burke. *Electrochimica Acta* **53** (3), 1083–1091 (2007).

[9] D. Ragone. *SAE Transactions* **77**, 680 453 (1968).

[10] T. Christen and M. W. Carlen. *Journal of Power Sources* **91** (2), 210–216 (2000).

[11] R. Kötz and M. Carlen. *Electrochimica Acta* **45** (15-16), 2483–2498 (2000).

[12] M. Conte, P. Prosini and S. Passerini. *Materials Science and Engineering B* **108** (1-2), 2–8 (2004).

[13] D. A. Scherson and A. Palencsár. *The Electrochemical Society Interface* **15** (1), 17–22 (2006).

[14] I. Plitz, A. DuPasquier, F. Badway, J. Gural, N. Pereira, A. Gmitter and G. Amatucci. *Applied Physics A* **82** (4), 615–626 (2006).

[15] P. Simon and Y. Gogotsi. *Nature Materials* **7** (11), 845–854 (2008).

[16] C. Ashtiani, R. Wright and G. Hunt. *Journal of Power Sources* **154** (2), 561–566 (2006).

[17] R. Kötz, J.-C. Sauter, P. Ruch, P. Dietrich, F. Büchi, P. Magne and P. Varenne. *Journal of Power Sources* **174** (1), 264–271 (2007).

[18] M. Ortúzar, J. Moreno and J. Dixon. *IEEE Transactions on Industrial Electronics* **54** (4), 2147–2156 (2007).

[19] A. F. Burke. *Proceedings of the IEEE* **95** (4), 806–820 (2007).

[20] J. Baumann and M. Kazerani. *IEEE Transactions on Vehicular Technology* **57** (2), 760–769 (2008).

[21] J. M. Carrasco, L. G. Franquelo, J. T. Bialasiewicz, E. Galván, R. C. P. Guisado, M. A. M. Prats, J. I. León and N. Moreno-Alfonso. *IEEE Transactions on Industrial Electronics* **53** (4), 1002–1016 (2006).

[22] F. I. Simjee and P. H. Chou. *IEEE Transactions on Power Electronics* **23** (3), 1526–1536 (2008).

[23] J. R. Miller and P. Simon. *Science* **321** (5889), 651–652 (2008).

[24] J. Jia, G. Whang, Z. Zhu, Y. Cham and M. Han. *IEEE International Conference on Sustainable Energy, Singapore, November 24-27* (2008).

[25] A. Schneuwly. *Ultracapacitors improve reliability for wind turbine pitch systems*. Available online at http://www.maxwell.com (Last visited on 20.01.2009).

[26] A. Burke. *2nd European Symposium on Super Capacitors & Applications, Lausanne, Switzerland, November 2-3* (2006).

[27] W. Evers. *2nd European Symposium on Super Capacitors & Applications, Lausanne, Switzerland, November 2-3* (2006).

[28] J. Baba, K. Nishikawa, E. Shimoda, S. Numata, S. Suzuki, Y. Ueda, T. Nitta and E. Masada. *2nd European Symposium on Super Capacitors & Applications, Lausanne, Switzerland, November 2-3* (2006).

[29] P. Degobert, S. Kreuawan, P. Li and B. François. *2nd European Symposium on Super Capacitors & Applications, Lausanne, Switzerland, November 2-3* (2006).

[30] P. Binduhewa, A. Renfrew and M. Barnes. *4th International Conference on Power Electronics, Machines and Drives, York, UK, April 2-4* (2008).

[31] M. Steiner and S. Pagiela. *Eisenbahntechnische Rundschau (ETR)* **4**, 207–214 (2005).

[32] M. Steiner, M. Klohr and S. Pagiela. *12th European Conference on Power Electronics and Applications, Aalborg, Denmark, September 2-5* (2007).

[33] R. Barrero, X. Tackoen and J. van Mierlo. *13th International Power Electronics and Motion Control Conference, Poznań, Poland, September 1-3* (2008).

[34] S.-M. Kim and S.-K. Sul. *IEEE Transactions on Power Electronics* **21** (5), 1420–1427 (2006).

[35] R. Kötz, M. Hahn and R. Gallay. *Journal of Power Sources* **154** (2), 550–555 (2006).

[36] A. Burke. *Journal of Power Sources* **91** (1), 37–50 (2000).

[37] J. Miller. *Batteries and Energy Storage Technology* (October), 61–78 (2007).

[38] Nippon Chemi-Con Corporation. *Products catalog*. Available online at http://www.chemi-con.co.jp/e/ (Last visited on 22.01.2009).

[39] J. R. Miller and A. F. Burke. *The Electrochemical Society Interface* **17** (1), 53–57 (2008).

[40] H. I. Becker. Low voltage electrolytic capacitor. U.S. Patent 2,800,616 (to General Electric) (1957).

[41] R. A. Rightmire. Electrical energy storage apparatus. U.S. Patent 3,288,641 (to Standard Oil Company of Ohio) (1966).

[42] D. L. Boos. Electrolytic capacitor having carbon paste electrodes. U.S. Patent 3,536,963 (to Standard Oil Company of Ohio) (1970).

[43] I. D. Raistrick. In: *Electrochemistry of semiconductors and electronics: processes and devices*, J. McHardy and F. Ludwig, eds., 297–355. Noyes Publications, New Jersey (1992).

[44] B. Conway. *Electrochemical supercapacitors: scientific fundamentals and technological applications*. Kluwer Academic, New York (1999).

[45] E. Frackowiak and F. Béguin. *Carbon* **39** (6), 937–950 (2001).

[46] J. Zheng, P. Cygan and T. Jow. *Journal of the Electrochemical Society* **142** (8), 2699–2703 (1995).

[47] K. Naoi and M. Morita. *The Electrochemical Society Interface* **17** (1), 44–48 (2008).

[48] P. Taberna, C. Portet and P. Simon. *Applied Physics A* **82** (4), 639–646 (2006).

[49] N. Mushiake and K. Inoue. Process for manufacturing electric double layer capacitor. U.S. Patent 6,134,760 (2000).

[50] C. Nanjundiah, P. Bendale, M. R. Malay, J. M. Dispennette and E. Chaney. Electrochemical double layer capacitor having carbon powder electrodes. U.S. Patent 6,643,119 B2 (to Maxwell Technologies) (2003).

[51] R. Parsons. *Pure and Applied Chemistry* **21** (1), 499–516 (1970).

[52] S. Trasatti. *Electroanalytical Chemistry and Interfacial Electrochemistry* **52** (3), 313–329 (1974).

[53] N. W. Ashcroft and N. D. Mermin. *Solid state physics*. Harcourt College Publishers, Fort Worth (1976).

[54] S. Trasatti. In: *The Double Layer*, J. O. Bockris, B. E. Conway and E. Yeager, eds., volume 1, 45–81. Plenum Press, New York (1980).

[55] P. Atkins and J. D. Paula. *Atkin's Physical Chemistry*. Oxford University Press, 7th edition (2002).

[56] S. Trasatti. *Electrochimica Acta* **28** (8), 1083–1093 (1983).

[57] S. Trasatti. *Electrochimica Acta* **35** (1), 269–271 (1990).

[58] J. O. Bockris and A. K. Reddy. *Modern Electrochemistry*, volume 2A. Kluwer Academic, 2nd edition (2002).

[59] S. Trasatti. *Pure and Applied Chemistry* **58** (7), 955–966 (1986).

[60] A. J. Bard and L. R. Faulkner. *Electrochemical methods - fundamentals and applications*. John Wiley & Sons, 2nd edition (2001).

[61] P. Rüetschi and P. Delahay. *Journal of Chemical Physics* **23** (4), 697–699 (1955).

[62] S. Trasatti and R. Parsons. *Pure and Applied Chemistry* **55** (8), 1251–1268 (1983).

[63] D. C. Grahame. *Chemical Reviews* **41** (3), 441–501 (1947).

[64] D. Halliday, R. Resnick and J. Walker. *Fundamentals of Physics*. Wiley & Sons, 8th (extended) edition (2008).

[65] A. Bard, R. Memming and B. Miller. *Pure and Applied Chemistry* **63** (4), 569–596 (1991).

[66] H. Gerischer, R. McIntyre, D. Scherson and W. Storck. *Journal of Physical Chemistry* **91** (7), 1930–1935 (1987).

[67] J. Côté, D. Brouillette, J. E. Desnoyers, J. Rouleau, J.-M. St-Arnaud and G. Perron. *Journal of Solution Chemistry* **25** (12), 1163–1173 (1996).

[68] J. Huang, B. G. Sumpter and V. Meunier. *Angewandte Chemie International Edition* **47** (3), 520–524 (2007).

[69] S. Ergun, J. Yasinsky and J. Townsend. *Carbon* **5**, 403–408 (1967).

[70] H. Gerischer. *Journal of Physical Chemistry* **89** (20), 4249–4251 (1985).

[71] D. Chung. *Journal of Materials Science* **37** (8), 1475–1489 (2002).

[72] J. Bockris, M. Devanathan and K. Müller. *Proceedings of the Royal Society of London A* **274** (August), 55–79 (1963).

[73] M. Devanathan and B. Tilak. *Chemical Reviews* **65** (6), 635–684 (1965).

[74] N. Mott and R. Watts-Tobin. *Electrochimica Acta* **4** (2-4), 79–107 (1961).

[75] M. Müller and B. Kastening. *Journal of Electroanalytical Chemistry* **374**, 149–158 (1994).

[76] S. Trasatti and E. Lust. In: *Modern aspects of electrochemistry*, R. White, ed., volume 33, 1–215. Kluwer Academic/Plenum Publishers, New York (1999).

[77] M. Ue. *The 8*[th] *International Seminar on Double Layer Capacitors and Hybrid Energy Storage Devices, Deerfield Beach, Florida, December 7-9* (1998).

[78] C. H. Hamann and W. Vielstich. *Elektrochemie*. Wiley-VCH, Weinheim, 4th edition (2005).

[79] H. Strehlow, W. Knoche and H. Schneider. *Berichte der Bunsen-Gesellschaft* **10** (11), 760–771 (1973).

[80] K. Izutsu. *Electrochemistry in non-aqueous solutions*. Wiley-VCH, Weinheim (2002).

[81] J. Chmiola, C. Largeot, P.-L. Taberna, P. Simon and Y. Gogotsi. *Angewandte Chemie International Edition* **47** (18), 3392–3395 (2008).

[82] K. Xu, S. P. Ding and T. R. Jow. *Journal of the Electrochemical Society* **146** (11), 4172–4178 (1999).

[83] K. Xu, M. S. Ding and T. R. Jow. *Electrochimica Acta* **46** (12), 1823–1827 (2001).

[84] K. Xu, M. S. Ding and T. R. Jow. *Journal of the Electrochemical Society* **148** (3), A267–A274 (2001).

[85] A. B. McEwen, H. L. Ngo, K. LeCompte and J. L. Goldman. *Journal of the Electrochemical Society* **146** (5), 1687–1695 (1999).

[86] A. Jänes and E. Lust. *Journal of Electroanalytical Chemistry* **588** (2), 285–295 (2006).

[87] M. Galiński, A. Lewandowski and I. Stępniak. *Electrochimica Acta* **51** (26), 5567–5580 (2006).

[88] M. Ue, M. Takeda, A. Toriumi, A. Kominato, R. Hagiwara and Y. Ito. *Journal of the Electrochemical Society* **150** (4), A499–A502 (2003).

[89] A. Balducci, F. Soavi and M. Mastragostino. *Applied Physics A* **82** (4), 627–632 (2006).

[90] T. Centeno, M. Hahn, J. Fernández, R. Kötz and F. Stoeckli. *Electrochemistry Communications* **9** (6), 1242–1246 (2007).

[91] B. Kastening and M. Heins. *Electrochimica Acta* **50** (12), 2487–2498 (2005).

[92] P. Liu, M. Verbrugge and S. Soukiazian. *Journal of Power Sources* **156** (2), 712–718 (2005).

[93] J.-L. Abboud and R. Notario. *Pure and Applied Chemistry* **71** (4), 645–718 (1999).

[94] D. R. Lide, ed. *CRC Handbook of Chemistry and Physics (Internet Version)*. CRC Press/Taylor and Francis, Boca Raton, FL, 89$^{\text{th}}$ edition (2009).

[95] H. O. House, E. Feng and N. P. Peet. *Journal of Organic Chemistry* **36** (16), 2371–2375 (1971).

[96] M. Ue. *Electrochimica Acta* **39** (13), 2083–2087 (1994).

[97] J. Besenhard, M. Winter, J. Yang and W. Biberacher. *Journal of Power Sources* **54** (2), 228–231 (1995).

[98] D. Aurbach, M. D. Levi, E. Levi and A. Schechter. *Journal of Physical Chemistry B* **101** (12), 2195–2206 (1997).

[99] K. Xu. *Chemical Reviews* **104** (10), 4304–417 (2004).

[100] E. Peled. *Journal of the Electrochemical Society* **126** (12), 2047–2051 (1979).

[101] O. Barbieri, M. Hahn, A. Herzog and R. Kötz. *Carbon* **43** (3), 1303–1310 (2005).

[102] E. Raymundo-Piñero, K. Kierzek, J. Machnikowski and F. Béguin. *Carbon* **44** (12), 2498–2507 (2006).

[103] R. Lin, P. Taberna, J. Chmiola, D. Guay, Y. Gogotsi and P. Simon. *Journal of the Electrochemical Society* **156** (1), A7–A12 (2009).

[104] G. Salitra, A. Soffer, L. Eliad, Y. Cohen and D. Aurbach. *Journal of the Electrochemical Society* **147** (7), 2486–2493 (2000).

[105] L. Eliad, G. Salitra, A. Soffer and D. Aurbach. *Journal of Physical Chemistry B* **105** (29), 6880–6887 (2001).

[106] L. Eliad, E. Pollak, N. Levy, G. Salitra, A. Soffer and D. Aurbach. *Applied Physics A* **82** (4), 607–613 (2006).

[107] E. Pollak, I. Genish, G. Salitra, A. Soffer, L. Klein and D. Aurbach. *Journal of Physical Chemistry B* **110** (14), 7443–7448 (2006).

[108] M. Hahn, M. Baertschi, O. Barbieri, J.-C. Sauter, R. Kötz and R. Gallay. *Electrochemical and Solid-State Letters* **7** (2), A33–A36 (2004).

[109] J. Zheng and T. Jow. *Journal of the Electrochemical Society* **144** (7), 2417–2420 (1997).

[110] R. De Levie. *Electrochimica Acta* **8** (10), 751–80 (1963).

[111] R. De Levie. *Electrochimica Acta* **9** (9), 1231–1245 (1964).

[112] H. Keiser, K. Beccu and M. Gutjahr. *Electrochimica Acta* **21** (8), 539–543 (1976).

[113] Y. Hu, O. A. Shenderova and D. W. Brenner. *Journal of Computational and Theoretical Nanoscience* **4** (2), 199–221 (2007).

[114] H. O. Pierson. *Handbook of carbon, graphite, diamond and fullerenes*. Noyes Publications, New Jersey (1993).

[115] E. Yasuda, M. Inagaki, K. Kaneko, M. Endo, A. Oya and Y. Tanabe, eds. *Carbon alloys. Novel concepts to develop carbon science and technology*. Elsevier, Amsterdam (2003).

[116] J. Robertson. *Advances in Physics* **35** (4), 317–374 (1986).

[117] A. Cuesta, P. Dhamelincourt, J. Laureyns, A. Martínez-Alonso and J. Tascón. *Journal of Materials Chemistry* **8** (12), 2875–2879 (1998).

[118] E. Fitzer, K.-H. Köchling, H. Boehm and H. Marsh. *Pure and Applied Chemistry* **67** (3), 473–506 (1995).

[119] J. G. Speight. *Handbook of coal analysis*. Wiley-Interscience, New Jersey (2005).

[120] T. Wigmans. *Carbon* **27** (1), 13–22 (1989).

[121] J. Robertson and E. O'Reilly. *Physical Review B* **35** (6), 2946–2957 (1987).

[122] A. Pandolfo and A. Hollenkamp. *Journal of Power Sources* **157** (1), 11–27 (2006).

[123] A. Geim and K. Novoselov. *Nature materials* **6** (3), 183–191 (2007).

[124] B. Partoens and F. Peeters. *Physical Review B* **74** (7), 075 404 (2006).

[125] I. Forbeaux, J.-M. Themlin and J.-M. Debever. *Physical Review B* **58** (24), 16 396–16 406 (1998).

[126] T. Ohta, A. Bostwick, T. Seyller, K. Horn and E. Rotenberg. *Science* **313** (5789), 951–955 (2006).

[127] S. Stankovich, D. A. Dikin, R. D. Piner, K. A. Kohlhaas, A. Kleinhammes, Y. Jia, Y. Wu, S. T. Nguyen and R. S. Ruoff. *Carbon* **45** (7), 1558–1565 (2007).

[128] D. Pandey, R. Reifenberger and R. Piner. *Surface Science* **602** (9), 1607–1613 (2008).

[129] H. K. Chae, D. Y. Siberio-Pérez, J. Kim, Y. Go, M. Eddaoudi, A. J. Matzger, M. O'Keeffe and O. M. Yaghi. *Nature* **427** (6974), 523–527 (2004).

[130] P. Wallace. *Physical Review* **71** (9), 622–634 (1947).

[131] J.-C. Charlier, X. Gonze and J.-P. Michenaud. *Carbon* **32** (2), 289–299 (1994).

[132] R. Saito, G. Dresselhaus and M. Dresselhaus. *Physical Review B* **61** (4), 2981–2990 (2000).

[133] A. Hashimoto, K. Suenaga, A. Gloter, K. Urita and S. Iijima. *Nature* **430** (7002), 870–873 (2004).

[134] N. Peres, F. Guinea and A. C. Neto. *Physical Review B* **73** (12), 125 411 (2006).

[135] A. El-Barbary, R. Telling, C. Ewels, M. Heggie and P. Briddon. *Physical Review B* **68** (14), 144 107 (2003).

[136] J. McClure. *Physical Review* **108** (3), 612–618 (1957).

[137] J. Slonczewski and P. Weiss. *Physical Review* **109** (2), 272–279 (1958).

[138] R. Tatar and S. Rabii. *Physical Review B* **25** (6), 4126–4141 (1982).

[139] M. D. Stoller, S. Park, Y. Zhu, J. An and R. S. Ruoff. *Nano Letters* **8** (10), 3498–3502 (2008).

[140] S. Vivekchand, C. S. Rout, K. Subrahmanyam, A. Govindaraj and C. Rao. *Journal of Chemical Sciences* **120** (1), 9–13 (2008).

[141] D. Ugarte. *Nature* **359** (6397), 707–709 (1992).

[142] H. Marsh and F. Rodríguez-Reinoso. *Activated carbon*. Elsevier (2006).

[143] G. Moss, P. Smith and D. Tavernier. *Pure and Applied Chemistry* **67** (8-9), 1307–1375 (1995).

[144] H. Kroto, J. Heath, S. O'Brien, R. Curl and R. Smalley. *Nature* **318** (6042), 162–163 (1985).

[145] A. Oberlin, M. Endo and T. Koyama. *Journal of Crystal Growth* **32** (3), 335–349 (1976).

[146] S. Iijima. *Nature* **354** (6348), 56–58 (1991).

[147] S. Iijima and T. Ichihashi. *Nature* **363** (6430), 603–605 (1993).

[148] D. Bethune, C. Kiang, M. de Vries, G. Gorman, R. Savoy, J. Vazquez and R. Beyers. *Nature* **363** (6430), 605–607 (1993).

[149] A. Rinzler, J. Liu, H. Dai, P. Nikolaev, C. Huffman, F. Rodríguez-Macías, P. Boul, A. Lu, D. Heymann, D. Colbert, R. Lee, J. Fischer, A. Rao, P. Eklund and R. Smalley. *Applied Physics A* **67** (1), 29–37 (1998).

[150] C. Journet, W. Maser, P. Bernier, A. Loiseau, M. Lamy de la Chapelle, S. Lefrant, P. Deniard, R. Lee and J. Fischer. *Nature* **388** (6644), 756–758 (1997).

[151] H. Dai, A. G. Rinzler, P. Nikolaev, A. Thess, D. T. Colbert and R. E. Smalley. *Chemical Physics Letters* **260** (3-4), 471–475 (1996).

[152] P. Nikolaev, M. J. Bronikowski, R. K. Bradley, F. Rohmund, D. T. Colbert, K. Smith and R. E. Smalley. *Chemical Physics Letters* **313** (1-2), 91–97 (1999).

[153] M. J. Bronikowski, P. A. Willis, D. T. Colbert, K. Smith and R. E. Smalley. *Journal of Vacuum Science & Technology A: Vacuum, Surfaces, and Films* **19** (4), 1800–1805 (2001).

[154] A. M. Cassell, J. A. Raymakers, J. Kong and H. Dai. *Journal of Physical Chemistry B* **103** (31), 6484–6492 (1999).

[155] P. J. Harris. *Carbon* **45** (2), 229–239 (2007).

[156] W.-F. Du, L. Wilson, J. Ripmeester, R. Dutrisac, B. Simard and S. Dénommée. *Nano Letters* **2** (4), 343–346 (2002).

[157] I. Chiang, B. Brinson, A. Huang, P. Willis, M. Bronikowski, J. Margrave, R. Smalley and R. Hauge. *Journal of Physical Chemistry B* **105** (35), 8297–8301 (2001).

[158] M. Cinke, J. Li, B. Chen, A. Cassell, L. Delzeit, J. Han and M. Meyyappan. *Chemical Physics Letters* **365** (1-2), 69–74 (2002).

[159] E. Bekyarova, K. Kaneko, M. Yudasaka, D. Kasuya, S. Iijima, A. Huidobro and F. Rodriguez-Reinoso. *Journal of Physical Chemistry B* **107** (19), 4479–4484 (2003).

[160] A. Kuznetsova, D. B. Mawhinney, V. Naumenko, J. T. Y. Jr., J. Liu and R. Smalley. *Chemical Physics Letters* **321** (3-4), 292–296 (2000).

[161] I. Stepanek, G. Maurin, P. Bernier, J. Gavillet, A. Loiseau, R. Edwards and O. Jaschinski. *Chemical Physics Letters* **331** (2-4), 125–131 (2000).

[162] A. Thess, R. Lee, P. Nikolaev, H. Dai, P. Petit, J. Robert, C. Xu, Y. H. Lee, S. G. Kim, A. G. Rinzler, D. T. Colbert, G. E. Scuseria, D. Tománek, J. E. Fischer and R. E. Smalley. *Science* **273** (5274), 483–487 (1996).

[163] L. Lafi, D. Cossement and R. Chahine. *Carbon* **43** (7), 1347–1357 (2005).

[164] A. Peigney, C. Laurent, E. Flahaut, R. Bacsa and A. Rousset. *Carbon* **39** (4), 507–514 (2001).

[165] A. Fujiwara, K. Ishii, H. Suematsu, H. Kataura, Y. Maniwa, S. Suzuki and Y. Achiba. *Chemical Physics Letters* **336** (3-4), 205–211 (2001).

[166] M. Dresselhaus, G. Dresselhaus, R. Saito and A. Jorio. *Physics Reports* **409** (2), 47–99 (2005).

[167] C. Dekker. *Physics Today* **52** (5), 22–28 (1999).

[168] R. Saito, M. Fujita, G. Dresselhaus and M. Dresselhaus. *Applied Physics Letters* **60** (18), 2204–2206 (1992).

[169] J. Mintmire, D. Robertson and C. White. *Journal of Physics and Chemistry of Solids* **54** (12), 1835–1840 (1993).

[170] A. Jorio, M. Pimenta, A. S. Filho, R. Saito, G. Dresselhaus and M. Dresselhaus. *New Journal of Physics* **5**, 139.1–139.17 (2003).

[171] H. Kataura, Y. Kumazawa, Y. Maniwa, I. Umezu, S. Suzuki, Y. Ohtsuka and Y. Achiba. *Synthetic Metals* **103** (1-3), 2555–2558 (1999).

[172] C. Fantini, A. Jorio, M. Souza, M. Strano, M. Dresselhaus and M. Pimenta. *Physical Review Letters* **93** (14), 147 406 (2004).

[173] A. Rao, J. Chen, E. Richter, U. Schlecht, P. Eklund, R. Haddon, U. Venkateswaran, Y.-K. Kwon and D. Tománek. *Physical Review Letters* **86** (17), 3895–3898 (2001).

[174] S. Reich, C. Thomsen and P. Ordejón. *Physical Review B* **65** (15), 155 411 (2002).

[175] M. S. Strano. *Journal of the American Chemical Society* **125** (51), 16 148–16 153 (2003).

[176] S. Shiraishi, H. Kurihara, K. Okabe, D. Hulicova and A. Oya. *Electrochemistry Communications* **4** (7), 593–598 (2002).

[177] D. N. Futaba, K. Hata, T. Yamada, T. Hiraoka, Y. Hayamizu, Y. Kakudate, O. Tanaike, H. Hatori, M. Yumura and S. Iijima. *Nature Materials* **5** (12), 987–994 (2006).

[178] R. W. Wyckoff. *Crystal structures*, volume 1. Interscience, New York, 2nd edition (1963).

[179] T. D. Burchell, ed. *Carbon materials for advanced technologies*. Elsevier, Oxford (1999).

[180] M. Wissler. *Journal of Power Sources* **156** (2), 142–150 (2006).

[181] L. B. Ebert. *Annual Review of Materials Science* **6**, 181–211 (1976).

[182] A. Hérold. In: *Intercalated Layered Materials*, F. A. Lévy, ed., volume 6, 321–421. D. Reidel Publishing Company, Dordrecht (1979).

[183] M. Dresselhaus and G. Dresselhaus. *Advances in Physics* **30** (2), 139–326 (1981).

[184] S. Solin. *Advances in Chemical Physics* **49**, 455–532 (1982).

[185] R. Fong, U. von Sacken and J. Dahn. *Journal of the Electrochemical Society* **137** (7), 2009–2013 (1990).

[186] M. Winter, J. O. Besenhard, M. E. Spahr and P. Novák. *Advanced Materials* **10** (10), 725–763 (1998).

[187] J.-M. Tarascon and M. Armand. *Nature* **414** (6861), 359–367 (2001).

[188] J. Dahn, T. Zheng, Y. Liu and J. Xue. *Science* **270** (5236), 590–593 (1995).

[189] M. E. Spahr, H. Wilhelm, F. Joho, J.-C. Panitz, J. Wambach, P. Novák and N. Dupont-Pavlovsky. *Journal of the Electrochemical Society* **149** (8), A960–A966 (2002).

[190] M. Hahn, O. Barbieri, F. Campana, R. Kötz and R. Gallay. *Applied Physics A* **82** (4), 633–638 (2006).

[191] M. Hahn, H. Buqa, P. Ruch, D. Goers, M. Spahr, J. Ufheil, P. Novák and R. Kötz. *Electrochemical and Solid-State Letters* **11** (9), A151–A154 (2008).

[192] H. Wang, M. Yoshio, A. K. Thapa and H. Nakamura. *Journal of Power Sources* **169** (2), 375–380 (2007).

[193] L. J. Hardwick. *In situ Raman microscopy of insertion electrodes for lithium-ion batteries and supercapacitors*. Ph.D. thesis, ETH Zurich (2006).

[194] L. J. Hardwick, M. Hahn, P. Ruch, M. Holzapfel, W. Scheifele, H. Buqa, F. Krumeich, P. Novák and R. Kötz. *Electrochimica Acta* **52** (2), 675–680 (2006).

[195] L. J. Hardwick, P. W. Ruch, M. Hahn, W. Scheifele, R. Kötz and P. Novák. *Journal of Physics and Chemistry of Solids* **69** (5-6), 1232–1237 (2008).

[196] R. E. Franklin. *Proceedings of the Royal Society of London Series A - Mathematical and Physical Sciences* **209** (1097), 196–218 (1951).

[197] G. Jenkins and K. Kawamura. *Nature* **231** (5299), 175–176 (1971).

[198] H. Kuroda and H. Akamatu. *Bulletin of the Chemical Society of Japan* **32** (2), 142–149 (1959).

[199] C. Houska and B. Warren. *Journal of Applied Physics* **25** (12), 1503–1509 (1954).

[200] D. Van Krevelen. *Organic Geochemistry* **6**, 1–10 (1984).

[201] P. J. Hall, H. Marsh and K. M. Thomas. *Fuel* **67** (6), 863–866 (1988).

[202] P. H. Given, A. Marzec, W. A. Barton, L. J. Lynch and B. C. Gerstein. *Fuel* **65** (2), 155–163 (1986).

[203] H. Marsh, M. Martínez-Escandell and F. Rodríguez-Reinoso. *Carbon* **37** (3), 363–390 (1999).

[204] H. F. Stoeckli. *Carbon* **28** (1), 1–6 (1990).

[205] S. Townsend, T. Lenosky, D. Muller, C. Nichols and V. Elser. *Physical Review Letters* **69** (6), 921–926 (1992).

[206] L. Bursill and L. N. Bourgeois. *Modern Physics Letters B* **9** (22), 1461–1470 (1995).

[207] H. Marsh, D. Crawford, T. O'Grady and A. Wennerberg. *Carbon* **20** (5), 419–426 (1982).

[208] P. J. Harris. *Critical Reviews in Solid State and Materials Sciences* **30** (4), 235–253 (2005).

[209] H. Marsh. *Fuel* **52** (3), 205–212 (1973).

[210] I. Mochida, Y. Korai, C.-H. Ku, F. Watanabe and Y. Sakai. *Carbon* **38** (2), 305–328 (2000).

[211] J. Brooks and G. Taylor. *Nature* **206** (4985), 697–699 (1965).

[212] A. Oberlin. *Carbon* **22** (6), 521–541 (1984).

[213] H. Marsh. *Carbon* **29** (6), 703–704 (1991).

[214] G. Fug, H. Gasparoux and A. Pacault. *Carbon* **11** (6), 591–597 (1973).

[215] K. Kawamura and R. Bragg. *Carbon* **24** (3), 301–309 (1986).

[216] H. Blayden, H. Riley and A. Taylor. *Journal of the American Chemical Society* **62** (1), 180–186 (1940).

[217] H. Akamatu, H. Inokuchi, H. Takahashi and Y. Matsunaga. *Bulletin of the Chemical Society of Japan* **29** (5), 574–581 (1956).

[218] H. Marsh and W. Wynne-Jones. *Carbon* **1** (3), 269–279 (1964).

[219] M. Endo, Y. Kim, K. Osawa, K. Ishii, T. Inoue, T. Nomura, N. Miyashita and M. Dresselhaus. *Electrochemical and Solid-State Letters* **6** (2), A23–A26 (2003).

[220] A. Ahmadpour and D. Do. *Carbon* **34** (4), 471–479 (1996).

[221] F. Rodríguez-Reinoso and M. Molina-Sabio. *Carbon* **30** (7), 1111–1118 (1992).

[222] F. Rodríguez-Reinoso, M. Molina-Sabio and M. González. *Carbon* **33** (1), 15–23 (1995).

[223] D. Everett. *Pure and Applied Chemistry* **21** (1), 578–638 (1970).

[224] Z. Hu, M. Srinivasan and Y. Ni. *Carbon* **39** (6), 877–886 (2001).

[225] J. Laine and S. Yunes. *Carbon* **30** (4), 601–604 (1992).

[226] H. Marsh, D. S. Yan, T. M. O'Grady and A. Wennerberg. *Carbon* **22** (6), 603–611 (1984).

[227] M. Lillo-Ródenas, D. Cazorla-Amorós and A. Linares-Solano. *Carbon* **41** (2), 267–275 (2003).

[228] Y. Gogotsi, A. Nikitin, H. Ye, W. Zhou, J. E. Fischer, B. Yi, H. C. Foley and M. W. Barsoum. *Nature Materials* **2** (9), 591–594 (2003).

[229] D. Hulicova, J. Yamashita, Y. Soneda, H. Hatori and M. Kodama. *Chemistry of Materials* **17** (5), 1241–1247 (2005).

[230] J. Lee, S. Yoon, T. Hyeon, S. M. Oh and K. B. Kim. *Chemical Communications* (21), 2177–2178 (1999).

[231] C. Vix-Guterl, S. Saadallah, K. Jurewicz, E. Frackowiak, M. Reda, J. Parmentier, J. Patarin and F. Beguin. *Materials Science and Engineering B* **108** (1-2), 148–155 (2004).

[232] M. Jung, H. Kim, J. Lee, O. Joo and S. Mho. *Electrochimica Acta* **50** (2-3), 857–862 (2004).

[233] Z. Ma, T. Kyotani, Z. Liu, O. Terasaki and A. Tomita. *Chemistry of Materials* **13** (12), 4413–4415 (2001).

[234] J. Lee, J. Kim and T. Hyeon. *Advanced Materials* **18** (16), 2073–2094 (2006).

[235] T. Kyotani. *Carbon* **38** (2), 269–286 (2000).

[236] L. R. Radovic and B. Bockrath. *Journal of the American Chemical Society* **127** (16), 5917–5927 (2005).

[237] H. Boehm. *Carbon* **32** (5), 759–769 (1994).

[238] C. Leon y Leon, J. Solar, V. Calemma and L. Radovic. *Carbon* **30** (5), 797–811 (1992).

[239] J. Figueiredo, M. Pereira, M. Freitas and J. Órfão. *Carbon* **37** (9), 1379–1389 (1999).

[240] H. Tobias and A. Soffer. *Journal of Electroanalytical Chemistry* **148** (2), 221–232 (1983).

[241] R. Panzer and P. Elving. *Electrochimica Acta* **20** (9), 635–647 (1975).

[242] D. Qu. *Journal of Power Sources* **179** (1), 310–316 (2008).

[243] F. Béguin, M. Friebe, K. Jurewicz, C. Vix-Guterl, J. Dentzer and E. Frackowiak. *Carbon* **44** (12), 2392–2398 (2006).

[244] K. Jurewicz, E. Frackowiak and F. Béguin. *Applied Physics A* **78** (7), 981–987 (2004).

[245] T. Centeno and F. Stoeckli. *Journal of Power Sources* **154** (1), 314–320 (2006).

[246] J. Pels, F. Kapteijn, J. Moulijn, Q. Zhu and K. Thomas. *Carbon* **33** (11), 1641–1653 (1995).

[247] E. Frackowiak, G. Lota, J. Machnikowski, C. Vix-Guterl and F. Béguin. *Electrochimica Acta* **51** (11), 2209–2214 (2006).

[248] T. Aida, K. Yamada and M. Morita. *Electrochemical and Solid-State Letters* **9** (12), A534–A536 (2006).

[249] V. Khomenko, E. Raymundo-Piñero and F. Béguin. *Journal of Power Sources* **177** (2), 643–651 (2008).

[250] H. Wang and M. Yoshio. *Journal of Power Sources* **177** (2), 681–684 (2008).

[251] A. Du Pasquier, I. Plitz, S. Menocal and G. Amatucci. *Journal of Power Sources* **115** (1), 171–178 (2003).

[252] D. Bélanger, T. Brousse and J. W. Long. *The Electrochemical Society Interface* **17** (1), 49–52 (2008).

[253] V. Khomenko, E. Raymundo-Piñero and F. Béguin. *Journal of Power Sources* **153** (1), 183–190 (2006).

[254] V. Khomenko, E. Raymundo-Piñero, E. Frackowiak and F. Béguin. *Applied Physics A* **82** (4), 567–573 (2006).

[255] W. G. Pell and B. E. Conway. *Journal of Power Sources* **136** (2), 334–345 (2004).

[256] A. Laforgue, P. Simon, J. Fauvarque, J. Sarrau and P. Lailler. *Journal of the Electrochemical Society* **148** (10), A1130–A1134 (2001).

[257] A. Lewandowski and M. Galinski. *Journal of Power Sources* **173** (2), 822–828 (2007).

[258] D. Linzen, S. Buller, E. Karden and R. W. D. Doncker. *IEEE Transactions on Industry Applications* **41** (5), 4435–4431 (2005).

[259] T. Morimoto, K. Hiratsuka, Y. Sanada and K. Kurihara. *Journal of Power Sources* **60** (2), 239–247 (1996).

[260] T. Umemura, Y. Mizutani, T. Okamoto, T. Taguchi, K. Nakajima and K. Tanaka. *Proceedings of the 7th International Conference on Properties and Applications of Dielectric Materials, Nagoya, Japan, June 1-5* 944–948 (2003).

[261] M. Hahn, A. Würsig, R. Gallay, P. Novák and R. Kötz. *Electrochemistry Communications* **7** (9), 925–930 (2005).

[262] M. Hahn, R. Kötz, R. Gallay and A. Siggel. *Electrochimica Acta* **52** (4), 1709–1712 (2006).

[263] S. Ishimoto, Y. Asakawa, M. Shinya and K. Naoi. *Journal of the Electrochemical Society* **156** (7), A563–A571 (2009).

[264] R. Nozu, M. Iizuka, M. Nakanishi and M. Kotani. *Journal of Power Sources* **186** (2), 570–579 (2009).

[265] P. Azaïs. *Recherche des causes du vieillissement de supercondensateurs à électrolyte organique à base de carbones activés*. Ph.D. thesis, Université d'Orléans (2003).

[266] P. Azaïs, L. Duclaux, P. Florian, D. Massiot, M.-A. Lillo-Rodenas, A. Linares-Solano, J.-P. Peres, C. Jehoulet and F. Béguin. *Journal of Power Sources* **171** (2), 1046–1053 (2007).

[267] M. Zhu. *Ageing of porous carbon electrodes*. Ph.D. thesis, École Polytechnique Fédérale de Lausanne (2006).

[268] M. Zhu, C. Weber, Y. Yang, M. Konuma, U. Starke, K. Kern and A. Bittner. *Carbon* **46** (14), 1829–1840 (2008).

[269] O. Bohlen, J. Kowal and D. U. Sauer. *Journal of Power Sources* **172** (1), 468–475 (2007).

[270] O. Bohlen, J. Kowal and D. U. Sauer. *Journal of Power Sources* **173** (1), 626–632 (2008).

[271] P. Kurzweil and M. Chwistek. *Journal of Power Sources* **176** (2), 555–567 (2008).

[272] R. Kötz, M. Hahn, P. Ruch and R. Gallay. *Electrochemistry Communications* **10** (3), 359–362 (2008).

[273] F. Campana, M. Hahn, A. Foelske, P. Ruch, R. Kötz and H. Siegenthaler. *Electrochemistry Communications* **8** (8), 1363–1368 (2006).

[274] W. Lajnef, J.-M. Vinassa, O. Briat, H. E. Brouji, S. Azzopardi and E. Woirgard. *2nd European Symposium on Super Capacitors & Applications, Lausanne, Switzerland, November 2-3* (2007).

[275] J. Schiffer, D. Linzen and D. U. Sauer. *Journal of Power Sources* **160** (1), 765–772 (2006).

[276] N. Rizoug, P. Bartholomeüs, B. Vulturescu and P. L. Moigne. *35th Annual IEEE Power Electronics Specialists Conference, Aachen, Germany, June 20-25* (2004).

[277] N. Rizoug, P. Bartholomeüs and P. L. Moigne. *2ⁿᵈ European Symposium on Super Capacitors & Applications, Lausanne, Switzerland, November 2-3* (2006).

[278] Y. Asakawa, M. Shinya, S. Ishimoto, N. Ogihara and K. Naoi. *214ᵗʰ Meeting of the Electrochemical Society, Honolulu, Hawaii, October 12-17* (2008).

[279] K. Naoi. *214ᵗʰ Meeting of the Electrochemical Society, Honolulu, Hawaii, October 12-17* (2008).

[280] K. Naoi. *59ᵗʰ Annual Meeting of the International Society of Electrochemistry, Seville, Spain, September 7-12* (2008).

[281] M. Okamura, H. Hasuike, M. Yamagishi and S. Araki. *Electrochemistry* **69** (6), 414–421 (2001).

[282] Y. Oren, I. Glatt, A. Livnat, O. Kafri and A. Soffer. *Journal of Electroanalytical Chemistry* **187** (1), 59–71 (1985).

[283] A. Moore. In: *Chemistry and physics of carbon*, P. L. Walker and P. A. Thrower, eds., volume 11, 69–187. Marcel Dekker, New York (1973).

[284] S. Ng, J. Wang, Z. Guo, J. Chen, G. Wang and H. Liu. *Electrochimica Acta* **51** (1), 23–28 (2005).

[285] G. Gritzner and J. Kůta. *Pure and Applied Chemistry* **56** (4), 461–466 (1984).

[286] E. Barsoukov and J. Ross Macdonald, eds. *Impedance spectroscopy: theory, experiment and applications*. Wiley & Sons, New Jersey (2005).

[287] J. Winkler, P. Hendriksen, N. Bonanos and M. Mogensen. *Journal of the Electrochemical Society* **145** (4), 1184–1182 (1998).

[288] M. Hahn, O. Barbieri, R. Gallay and R. Kötz. *Carbon* **44** (12), 2523–2533 (2006).

[289] G. Binnig, C. Quate and C. Gerber. *Physical Review Letters* **56** (9), 930–934 (1986).

[290] Y. Gan. *Surface Science Reports* **64** (3), 99–121 (2009).

[291] H.-J. Butt, B. Cappella and M. Kappl. *Surface Science Reports* **59** (1-6), 1–152 (2005).

[292] F. Campana. *Investigation of dimensional changes and film morphology at graphite electrodes in aprotic solutions by in situ atomic force microscopy*. Ph.D. thesis, University of Bern (2005).

[293] B. Cullity. *Elements of X-ray diffraction*. Addison-Wesley, Reading, Massachusetts, 2ⁿᵈ edition (1978).

[294] H. Saisho and Y. Gohshi, eds. *Applications of Synchrotron Radiation to Materials Analysis*. Elsevier Science (1996).

[295] B. Warren. *Physical Review* **59** (9), 693–698 (1941).

[296] B. Patterson, R. Abela, H. Auderset, Q. Chen, F. Fauth, F. Gozzo, G. Ingold, H. Kühne, M. Lange, D. Maden, D. Meister, P. Pattison, T. Schmidt, B. Schmitt, C. Schulze-Briese, M. Shi, M. Stampanoni and P. Willmott. *Nuclear Instruments and Methods in Physics Research A* **540** (1), 42–67 (2005).

[297] B. Schmitt, C. Brönnimann, E. Eikenberry, F. Gozzo, C. Hörmann, R. Horisberger and B. Patterson. *Nuclear Instruments and Methods in Physics Research A* **501** (1), 267–272 (2003).

[298] F. Rosciano, M. Holzapfel, H. Kaiser, W. Scheifele, P. Ruch, M. Hahn, R. Kötz and P. Novák. *Journal of Synchrotron Radiation* **14** (6), 487–491 (2007).

[299] F. Rosciano. *In situ synchrotron and neutron diffraction based methods for the characterization of cathodic materials for lithium-ion batteries*. Ph.D. thesis, ETH Zurich (2008).

[300] P. Ruch, M. Hahn, F. Rosciano, M. Holzapfel, H. Kaiser, W. Scheifele, B. Schmitt, P. Novák, R. Kötz and A. Wokaun. *Electrochimica Acta* **53** (3), 1074–1082 (2007).

[301] A. Guinier and G. Fournet. *Small-angle scattering of X-rays*. Wiley, New York (1955).

[302] O. Glatter and O. Kratky, eds. *Small-angle X-ray scattering*. Academic Press, London (1982).

[303] L. Feigin and D. Svergun. *Structure analysis by small-angle X-ray and neutron scattering*. Plenum Press, New York (1987).

[304] P. Debye and A. Bueche. *Journal of Applied Physics* **20** (6), 518–525 (1949).

[305] P. Debye, J. H.R. Anderson and H. Brumberger. *Journal of Applied Physics* **28** (6), 679–683 (1957).

[306] P. Debye. *Annalen der Physik* **351** (6), 809–823 (1915).

[307] K. Nishikawa. In: *Carbon alloys—novel concepts to develop carbon science and technology*, E. Yasuda, M. Inagaki, K. Kaneko, M. Endo, A. Oya and Y. Tanabe, eds., 175–188. Elsevier, Oxford (2003).

[308] M. Kalliat, C. Kwak and P. Schmidt. In: *New approaches in coal chemistry*, B. D. Blaustein, B. C. Bockrath and S. Friedman, eds., 3–22. American Chemical Society, Washington, D.C. (1981).

[309] H. D. Bale, M. L. Carlson and H. H. Schobert. *Fuel* **65** (9), 1185–1189 (1986).

[310] A. Gibaud, J. Xue and J. Dahn. *Carbon* **34** (4), 499–503 (1996).

[311] T. Zheng, J. Xue and J.R.Dahn. *Chemistry of Materials* **8** (2), 389–393 (1996).

[312] G. Laudisio, R. K. Dash, J. P. Singer, G. Yushin, Y. Gogotsi and J. E. Fischer. *Langmuir* **22** (21), 8945–8950 (2006).

[313] D. Stevens and J. Dahn. *Journal of the Electrochemical Society* **147** (12), 4428–4431 (2000).

[314] D. Stevens and J. Dahn. *Journal of the Electrochemical Society* **148** (8), A803–A811 (2001).

[315] W. Ruland. *Journal of Applied Crystallography* **4**, 70–73 (1971).

[316] R. Jenkins and J. P.L. Walker. *Carbon* **14** (1), 7–11 (1976).

[317] K. Masters and B. McEnaney. *Carbon* **22** (6), 595–601 (1984).

[318] H. D. Bale and P. W. Schmidt. *Physical Review Letters* **53** (6), 596–599 (1984).

[319] P. Pfeifer and D. Avnir. *Journal of Chemical Physics* **79** (7), 3558–3565 (1983).

[320] P. W. Schmidt. *Journal of Applied Crystallography* **24**, 414–435 (1991).

[321] S. Polarz and B. Smarsly. *Journal of Nanoscience and Nanotechnology* **2** (6), 581–612 (2002).

[322] W. Ruland. *Carbon* **39** (2), 287–324 (2001).

[323] R. Perret and W. Ruland. *Journal of Applied Crystallography* **1** (5), 308–313 (1968).

[324] R. Perret and W. Ruland. *Journal of Applied Crystallography* **5** (3), 183–187 (1972).

[325] C. Broennimann, E. Eikenberry, B. Henrich, R. Horisberger, G. Huelsen, E. Pohl, B. Schmitt, C. Schulze-Briese, M. Suzuki, T. Tomizaki, H. Toyokawa and A. Wagner. *Journal of Synchrotron Radiation* **13** (2), 120–130 (2006).

[326] T. Huang, H. Toraya, T. Blanton and Y. Wu. *Journal of Applied Crystallography* **26** (2), 180–184 (1993).

[327] H. Marsh. *Carbon* **25** (1), 49–58 (1987).

[328] H. Shi. *Electrochimica Acta* **41** (10), 1633–1639 (1996).

[329] J. Chmiola, G. Yushin, Y. Gogotsi, C. Portet, P. Simon and P. Taberna. *Science* **313** (5794), 1760–1763 (2006).

[330] S. Gregg and K. Sing. *Adsorption, surface area and porosity*. Academic Press, London (1982).

[331] S. Brunauer, L. S. Deming, W. E. Deming and E. Teller. *Journal of the American Chemical Society* **62** (7), 1723–1732 (1940).

[332] M. Dubinin. *Carbon* **27** (3), 457–467 (1989).

[333] B. McEnaney. *Carbon* **25** (1), 69–75 (1987).

[334] P. Carrott, R. Roberts and K. Sing. *Carbon* **25** (1), 59–68 (1987).

[335] M. Dubinin and H. Stoeckli. *Journal of Colloid and Interface Science* **75** (1), 34–42 (1980).

[336] P. I. Ravikovitch, A. Vishnyakov, R. Russo and A. V. Neimark. *Langmuir* **16** (5), 2311–2320 (2000).

[337] J. Jagiello and M. Thommes. *Carbon* **42** (7), 1227–1232 (2004).

[338] S. Brunauer, P. Emmett and E. Teller. *Journal of the American Chemical Society* **60** (2), 309–319 (1938).

[339] K. Sing, D. Everett, R. Haul, L. Moscou, R. Pierotti, J. Rouquérol and T. Siemieniewska. *Pure and Applied Chemistry* **57** (4), 603–619 (1985).

[340] E. P. Barrett, L. G. Joyner and P. P. Halenda. *Journal of the American Chemical Society* **73** (1), 373–380 (1951).

[341] J. de Boer, B. Lippens, B. Linsen, J. Broekhoff, A. van den Heuvel and T. J. Osinga. *Journal of Colloid and Interface Science* **21**, 405–414 (1966).

[342] J. R. Ferraro, K. Nakamoto and C. W. Brown. *Introductory Raman spectroscopy*. Elsevier, San Diego, 2nd edition (2003).

[343] R. Loudon. *Advances in Physics* **50** (7), 813–864 (2001).

[344] M. Pimenta, G. Dresselhaus, M. Dresselhaus, L. Cançado, A. Jorio and R. Saito. *Physical Chemistry Chemical Physics* **9** (11), 1276–1291 (2007).

[345] S. Reich and C. Thomsen. *Philosophical Transactions of the Royal Society A* **362** (1824), 2271–2288 (2004).

[346] J. Maultzsch, S. Reich, C. Thomsen, H. Requardt and P. Ordejón. *Physical Review Letters* **92** (7), 075 501 (2004).

[347] G. G. Samsonidze, E. B. Barros, R. Saito, J. Jiang, G. Dresselhaus and M. S. Dresselhaus. *Physical Review B* **75** (15), 155 420 (2007).

[348] C. Mapelli, C. Castiglioni, G. Zerbi and K. Müllen. *Phys. Rev. B* **60** (18), 12 710–12 725 (1999).

[349] A. Ferrari and J. Robertson. *Physical Review B* **61** (20), 14 095–14 107 (2000).

[350] A. Ferrari and J. Robertson. *Physical Review B* **64** (7), 075 414 (2001).

[351] F. Tuinstra and J. Koenig. *The Journal of Chemical Physics* **53** (3), 1126–1130 (1970).

[352] Y. Wang, D. C. Alsmeyer and R. L. McCreery. *Chemistry of Materials* **2** (5), 557–563 (1990).

[353] R. Vidano, D. Fischbach, L. Willis and T. Loehr. *Solid State Communications* **39** (2), 341–344 (1981).

[354] M. Matthews, M. Pimenta, G. Dresselhaus, M. Dresselhaus and M. Endo. *Physical Review B* **59** (10), R6585–R6588 (1999).

[355] C. Thomsen and S. Reich. *Physical Review Letters* **85** (24), 5214–5217 (2000).

[356] C. Castiglioni, C. Mapelli, F. Negri and G. Zerbi. *Journal of Chemical Physics* **114** (2), 963–974 (2001).

[357] F. Negri, E. di Donato, M. Tommasini, C. Castiglioni, G. Zerbi and K. Mullen. *Journal of Chemical Physics* **120** (24), 11 889–11 900 (2004).

[358] G. A. Zickler, B. Smarsly, N. Gierlinger, H. Peterlik and O. Paris. *Carbon* **44** (15), 3239–3246 (2006).

[359] A. Ferrari, J. Meyer, V. Scardaci, C. Casiraghi, M. Lazzeri, F. Mauri, S. Piscanec, D. Jiang, K. Novoselov, S. Roth and A. Geim. *Physical Review Letters* **97** (18), 187 401 (2006).

[360] A. C. Ferrari. *Solid State Communications* **143** (1-2), 47–57 (2007).

[361] S. Piscanec, M. Lazzeri, F. Mauri, A. C. Ferrari and J. Robertson. *Phys. Rev. Lett.* **93** (18), 185 503 (2004).

[362] S. Pisana, M. Lazzeri, C. Casiraghi, K. S. Novoselov, A. Geim, A. C. Ferrari and F. Mauri. *Nature Materials* **6** (3), 198–201 (2007).

[363] A. Das, S. Pisana, B. Chakraborty, S. Piscanec, S. Saha, U. Waghmare, K. Novoselov, H. Krishnamurthy, A. Geim, A. Ferrari and A. Sood. *Nature Nanotechnology* **3** (4), 210–215 (2008).

[364] M. Kalbac, L. Kavan, L. Dunsch and M. Dresselhaus. *Nano Letters* **8** (4), 1257–1264 (2008).

[365] J. Tsang, M. Freitag, V. Perebeinos, J. Liu and P. Avouris. *Nature Nanotechnology* **2** (11), 725–730 (2007).

[366] A. Das, A. Sood, A. Govindaraj, A. M. Saitta, M. Lazzeri, F. Mauri and C. Rao. *Physical Review Letters* **99** (13), 136 803 (2007).

[367] R. F. Egerton. *Physical properties of electron microscopy. An introduction to TEM, SEM and AEM.* Springer, New York (2005).

[368] A. Einstein. *Annalen der Physik* **17** (6), 132–148 (1905).

[369] B. Feuerbacher, B. Fitton and R. Willis, eds. *Photoemission and the electronic properties of surfaces.* Wiley, Chichester (1978).

[370] National Institute of Standards and Technology. *NIST X-ray Photoelectron Spectroscopy Database.* Available online at http://srdata.nist.gov/xps (Last visited on 23.03.2009).

[371] B. Kastening, M. Hahn and J. Kremeskötter. *Journal of Electroanalytical Chemistry* **374** (1-2), 159–166 (1994).

[372] B. Kastening, M. Hahn, B. Rabanus, M. Heins and U. zum Felde. *Electrochimica Acta* **42** (18), 2789–2800 (1997).

[373] E. Pollak, A. Anderson, G. Salitra, A. Soffer and D. Aurbach. *Journal of Electroanalytical Chemistry* **601** (1-2), 47–52 (2007).

[374] L. Strebkova, O. Potekhin and V. Romanov. *Industrial Laboratory* **45** (1), 42–44 (1979).

[375] H. Ye, N. Naguib and Y. Gogotsi. *JEOL News* **39** (2), 2–7 (2004).

[376] R. J. Mashl, S. Joseph, N. R. Aluru and E. Jakobsson. *Nano Letters* **3** (5), 589–592 (2003).

[377] N. Shimodaira and A. Masui. *Journal of Applied Physics* **92** (2), 902–909 (2002).

[378] R. Escribano, J. Sloan, N. Siddique, N. Sze and T. Dudev. *Vibrational Spectroscopy* **26** (2), 179–186 (2001).

[379] P. Lespade, A. Marchand, M. Couzi and F. Cruege. *Carbon* **22** (4-5), 375–385 (1984).

[380] A. Cuesta, P. Dhamelincourt, J. Laureyns, A. Martínez-Alonso and J. Tascón. *Carbon* **32** (8), 1523–1532 (1994).

[381] P. Hirsch. *Proceedings of the Royal Society of London A* **226** (1165), 143–169 (1954).

[382] W. Ruland and B. Smarsly. *Journal of Applied Crystallography* **35**, 624–633 (2002).

[383] L. Lu, V. Sahajwalla, C. Kong and D. Harris. *Carbon* **39** (12), 1821–1833 (2001).

[384] H. Fujimoto and M. Shiraishi. *Carbon* **39** (11), 1753–1761 (2001).

[385] H. Shi, J. Reimers and J. Dahn. *Journal of Applied Crystallography* **26** (6), 827–836 (1993).

[386] C.-M. Yang, Y.-J. Kim, M. Endo, H. Kanoh, M. Yudasaka, S. Iijima and K. Kaneko. *Journal of the American Chemical Society* **129** (1), 20–21 (2007).

[387] L. Gerasimova, I. Kedrinskii and S. Oleinikov. *Zhurnal Prikladnoi Khimii* **63** (9), 2053–2055 (1990).

[388] O. Duschek and V. Gutmann. *Monatshefte für Chemie* **104** (4), 990–997 (1973).

[389] G. Gritzner. *Inorganica Chimica Acta* **24**, 5–12 (1977).

[390] Y. Marcus. *Pure and Applied Chemistry* **57** (8), 1129–1132 (1985).

[391] E. Lust, A. Jänes and M. Arulepp. *Journal of Electroanalytical Chemistry* **562** (1), 33–42 (2004).

[392] L. Kavan. *Chemical Reviews* **97** (8), 3061–3082 (1997).

[393] J.-P. Randin and E. Yeager. *Journal of Electroanalytical Chemistry and Interfacial Electrochemistry* **36** (2), 257–276 (1972).

[394] C. Chan, K. Ho and W. Kamitakahara. *Physical Review B* **36** (6), 3499–3522 (1987).

[395] Y. N. Gartstein, A. Zakhidov and R. Baughman. *Physical Review Letters* **89** (4), 045 503–1–4 (2002).

[396] E. Margine, P. E. Lammert and V. H. Crespi. *Physical Review Letters* **99** (19), 196 803 (2007).

[397] L. Kavan and L. Dunsch. *ChemPhysChem* **8** (7), 974–998 (2007).

[398] C. Liu, A. J. Bard, F. Wudl, I. Weitz and J. R. Heath. *Electrochemical and Solid-State Letters* **2** (11), 577–578 (1999).

[399] E. Frackowiak, K. Jurewicz, S. Delpeux and F. Béguin. *Journal of Power Sources* **97-98**, 822–825 (2001).

[400] K. An, W. Kim, Y. Park, J. Moon, D. Bae, S. Lim, Y. Lee and Y. Lee. *Advanced Functional Materials* **11** (5), 387–392 (2001).

[401] F. Picó, J. Rojo, M. Sanjuán, A. Ansón, A. Benito, M. Callejas, W. Maser and M. Martínez. *Journal of the Electrochemical Society* **151** (6), A831–A837 (2004).

[402] R. Signorelli, J. Schindall and J. Kassakian. *Proceedings of the 14th International Seminar on Double Layer Capacitors and Hybrid Energy Storage Devices, Deerfield Beach, Florida, December 6-8* (2004).

[403] S. Arepalli, H. Fireman, C. Huffman, P. Moloney, P. Nikolaev, L. Yowell, C. Higgins, K. Kim, P. Kohl, S. Turano and W. Ready. *Journal of the Metals, Minerals & Materials Society* **57** (12), 26–31 (2005).

[404] B. Xu, F. Wu, F. Wang, S. Chen, G.-P. Cao and Y.-S. Yang. *Chinese Journal of Chemistry* **24** (11), 1505–1508 (2006).

[405] C. E. Banks, T. J. Davies, G. G. Wildgoose and R. G. Compton. *Chemical Communications* (7), 829–841 (2005).

[406] K. Hata, D. N. Futaba, K. Mizuno, T. Namai, M. Yumara and S. Iijima. *Science* **306** (5700), 1362–1364 (2004).

[407] M. Stoll, P. Rafailov, W. Frenzel and C. Thomsen. *Chemical Physics Letters* **375** (5-6), 625–631 (2003).

[408] J. N. Barisci, G. G. Wallace and R. H. Baughman. *Journal of the Electrochemical Society* **147** (12), 4580–4583 (2000).

[409] J. N. Barisci, G. G. Wallace and R. H. Baughman. *Journal of Electroanalytical Chemistry* **488** (2), 92–98 (2000).

[410] G. Sumanasekera, J. Allen, S. Fang, A. Loper, A. Rao and P. Eklund. *Journal of Physical Chemistry B* **103** (21), 4292–4297 (1999).

[411] A. Claye, S. Rahman, J. Fischer, A. Sirenko, G. Sumanasekera and P. Eklund. *Chemical Physics Letters* **333** (1-2), 16–22 (2001).

[412] R. H. Baughman, C. Cui, A. A. Zakhidov, Z. Iqbal, J. N. Barisci, G. M. Spinks, G. G. Wallace, A. Mazzoldi, D. D. Rossi, A. G. Rinzler, O. Jaschinski, S. Roth and M. Kertesz. *Science* **284** (5418), 1340–1344 (1999).

[413] A. Rao, P. Eklund, S. Bandow, A. Thess and R. Smalley. *Nature* **388** (6639), 257–259 (1997).

[414] L. Kavan, P. Rapta and L. Dunsch. *Chemical Physics Letters* **328** (4-6), 363–368 (2000).

[415] C. An, Z. Vardeny, Z. Iqbal, G. Spinks, R. Baughman and A. Zakhidov. *Synthetic Metals* **116** (1-3), 411–414 (2001).

[416] P. Corio, P. Santos, V. Brar, G. G. Samsonidze, S. Chou and M. Dresselhaus. *Chemical Physics Letters* **370** (5-6), 675–682 (2003).

[417] S. Cronin, R. Barnett, M. Tinkham, S. Chou, O. Rabin, M. Dresselhaus, A. Swan, M. Ünlü and B. Goldberg. *Applied Physics Letters* **84** (12), 2052–2054 (2004).

[418] S. Gupta, M. Hughes, A. Windle and J. Robertson. *Journal of Applied Physics* **95** (4), 2038–2048 (2004).

[419] K. Okazaki, Y. Nakato and K. Murakoshi. *Surface Science* **566** (Part 1), 436–442 (2004).

[420] P. Rafailov, M. Stoll and C. Thomsen. *Journal of Physical Chemistry B* **108** (50), 19 241–19 245 (2004).

[421] N. Takeda and K. Murakoshi. *Analytical and Bioanalytical Chemistry* **388** (1), 103–108 (2007).

[422] L. Kavan, P. Rapta, L. Dunsch, M. J. Bronikowski, P. Willis and R. E. Smalley. *Journal of Physical Chemistry B* **105** (44), 10 764–10 771 (2001).

[423] L. Kavan and L. Dunsch. *ChemPhysChem* **4** (9), 944–950 (2003).

[424] L. Kavan and L. Dunsch. *Nano Letters* **3** (7), 969–972 (2003).

[425] L. Kavan, M. Kalbáč, M. Zukalová and L. Dunsch. *Journal of Physical Chemistry B* **109** (13), 19 613–19 619 (2005).

[426] L. Kavan, M. Kalbáč, M. Zukalová and L. Dunsch. *Physica Status Solidi B* **243** (13), 3130–3133 (2006).

[427] L. Pietronero and S. Strässler. *Physical Review Letters* **47** (8), 593–596 (1981).

[428] M. Kertesz. *Molecular Crystals and Liquid Crystals* **126** (1), 103–110 (1985).

[429] G. Sun, M. Kertesz, J. Kürti and R. H. Baughman. *Physical Review B* **68** (12), 125 411 (2003).

[430] G. Chen, C. Furtado, S. Bandow, S. Iijima and P. Eklund. *Physical Review B* **71** (4), 045 408 (2005).

[431] M. Lazzeri and F. Mauri. *Physical Review Letters* **97** (26), 266 407 (2006).

[432] S. Piscanec, M. Lazzeri, J. Robertson, A. C. Ferrari and F. Mauri. *Physical Review B* **75** (3), 035 427 (2007).

[433] H. Telg, J. Maultzsch, S. Reich, F. Hennrich and C. Thomsen. *Physical Review Letters* **93** (17), 177 401 (2004).

[434] S. M. Bachilo, M. S. Strano, C. Kittrell, R. H. Hauge, R. E. Smalley and R. B. Weisman. *Science* **298** (5602), 2361–2367 (2002).

[435] M. S. Strano, H. Agarwal, J. Pedrick, D. Redman and H. C. Foley. *Carbon* **41** (13), 2501–2508 (2003).

[436] I. Heller, J. Kong, K. A. Williams, C. Dekker and S. G. Lemay. *Journal of the American Chemical Society* **128** (22), 7353–7359 (2006).

[437] M. Burghard. *Surface Science Reports* **58** (1-4), 1–109 (2005).

[438] W. Zhou, J. Vavro, N. Nemes, J. Fischer, F. Borondics, K. Kamarás and D. Tanner. *Physical Review B* **71** (20), 205 423–205 429 (2005).

[439] D. Paolucci, M. M. Franco, M. Iurlo, M. Marcaccio, M. Prato, F. Zerbetto, A. Pénicaud and F. Paolucci. *Journal of the American Chemical Society* **130** (23), 7393–7399 (2008).

[440] J. Maultzsch, R. Pomraenke, S. Reich, E. Chang, D. Prezzi, A. Ruini, E. Molinari, M. Strano, C. Thomsen and C. Lienau. *Physical Review B* **72** (24), 241 402(R) (2005).

[441] G. D. Scholes and G. Rumbles. *Nature Materials* **5** (9), 683–696 (2006).

[442] Z. Wang, H. Pedrosa, T. Krauss and L. Rothberg. *Physical Review Letters* **96** (4), 047 403 (2006).

[443] L. Kavan, M. Kalbáč, M. Zukalová and L. Dunsch. *Physical Review Letters* **98** (1), 019 701 (2007).

[444] Z. Wang, H. Pedrosa, T. Krauss and L. Rothberg. *Physical Review Letters* **98** (1), 019 702 (2007).

[445] P. Rafailov, C. Thomsen, U. Dettlaf-Weglikowska, B. Hornbostel and S. Roth. *Physica Status Solidi B* **244** (11), 4060–4063 (2007).

[446] P. M. Rafailov, C. Thomsen, U. Dettlaff-Weglikowska and S. Roth. *Journal of Physical Chemistry B* **112** (17), 5368–5373 (2008).

[447] A. Pénicaud, P. Poulin, A. Derré, E. Anglaret and P. Petit. *Journal of the American Chemical Society* **127** (1), 8–9 (2005).

[448] F. Bonhomme, J. Lassègues and L. Servant. *Journal of the Electrochemical Society* **148** (11), E450–E458 (2001).

[449] M. Dumont, G. Chollon, M. Dourges, R. Pailler, X. Bourrat, R. Naslain, J. Bruneel and M. Couzi. *Carbon* **40** (9), 1475–1486 (2002).

[450] A. Sadezky, H. Muckenhuber, H. Grothe, R. Niessner and U. Pöschl. *Carbon* **43** (8), 1731–1742 (2005).

[451] A. C. Ferrari and J. Robertson. *Philosophical Transactions of the Royal Society A* **362** (1824), 2477–2512 (2004).

[452] M. Hahn. *Ladungsspeicherung und -transport in Aktivkohle-Elektroden*. Ph.D. thesis, University of Hamburg (1997).

[453] J. Robertson. *Progress in Solid State Chemistry* **21** (4), 199–333 (1991).

[454] W. Anderson and W. Hansen. *Journal of the Electrochemical Society* **121** (12), 1570–1575 (1974).

[455] W. N. Hansen. *Surface Science* **101** (1-3), 109–122 (1980).

[456] M. Milnera, J. Kürti, M. Hulman and H. Kuzmany. *Physical Review Letters* **84** (6), 1324–1327 (2000).

[457] O. Kimizuka, O. Tanaike, J. Yamashita, T. Hiraoka, D. N. Futaba, K. Hata, K. Machida, S. Suematsu, K. Tamamitsu, S. Saeki, Y. Yamada and H. Hatori. *Carbon* **46** (14), 1999–2001 (2008).

[458] J. D. W. Madden, J. N. Barisci, P. A. Anquetil, G. M. Spinks, G. G. Wallace, R. H. Baughman and I. W. Hunter. *Advanced Materials* **18** (7), 870–873 (2006).

[459] A. Soffer and M. Folman. *Journal of Electroanalytical Chemistry and Interfacial Electrochemistry* **38** (1), 25–43 (1972).

[460] J. O. Besenhard and H. P. Fritz. *Angewandte Chemie International Edition* **22** (12), 950–75 (1983).

[461] M. Noel and R. Santhanam. *Journal of Power Sources* **72** (1), 53–65 (1998).

[462] J. Vetter, P. Novák, M. Wagner, C. Veit, K.-C. Möller, J. Besenhard, M. Winter, M. Wohlfahrt-Mehrens, C. Vogler and A. Hammouche. *Journal of Power Sources* **147** (1-2), 269–281 (2005).

[463] M. Takeuchi, K. Koike, T. Maruyama, A. Mogami and M. Okamura. *Electrochemistry* **66** (12), 1311–7 (1998).

[464] M. Takeuchi, T. Maruyama, K. Koike, A. Mogami, T. Oyama and H. Kobayashi. *Electrochemistry* **69** (6), 487–492 (2001).

[465] M. Okamura and M. Takeuchi. Carbon material for electric double layer capacitor, method of producing same, electric electric double layer capacitor and method of fabricating same. U.S. Patent 6,310,762 B1 (to Jeol) (2001).

[466] M. Takeuchi, K. Koike, A. Mogami and T. Maruyama. Electric double-layer capacitor and carbon material therefor. U.S. Patent 2002/0039275 A1 (to Jeol) (2002).

[467] A. S. Claye, J. E. Fischer, C. B. Huffman, A. G. Rinzler and R. E. Smalley. *Journal of the Electrochemical Society* **147** (8), 2845–2852 (2000).

[468] H. Shimoda, B. Gao, X. Tang, A. Kleinhammes, L. Fleming, Y. Wu and O. Zhou. *Physical Review Letters* **88** (1), 015 502 (2002).

[469] R. T. Carlin, H. C. D. Long, J. Fuller and P. C. Trulove. *Journal of the Electrochemical Society* **141** (7), L73–L76 (1994).

[470] R. Santhanam and M. Noel. *Journal of Power Sources* **66** (1-2), 47–54 (1997).

[471] L. Wang, M. Fujita and M. Inagaki. *Electrochimica Acta* **51** (19), 4096–4102 (2006).

[472] J. Besenhard and H. Fritz. *Journal of Electroanalytical Chemistry and Interfacial Electrochemistry* **53**, 329–333 (1974).

[473] J. Schön, D. Adler and G. Dresselhaus. *Journal of Physics C* **21** (33), 5595–5614 (1988).

[474] J. Dahn, D. Dahn and R. Haering. *Solid State Communications* **42** (3), 179–183 (1982).

[475] V. Mordkovich. *Synthetic Metals* **63** (1), 1–6 (1994).

[476] A. Metrot. *Synthetic Metals* **7** (3-4), 177–184 (1983).

[477] H.-P. Boehm, R. Setton and E. Stumpp. *Pure and Applied Chemistry* **66** (9), 1893–1901 (1994).

[478] D. Billaud, J. Mareche, E. McRae and A. Herold. *Synthetic Metals* **2** (1), 37–46 (1980).

[479] J. Seel and J. Dahn. *Journal of the Electrochemical Society* **147** (3), 892–8 (2000).

[480] Z. Zhang and M. M. Lerner. *Journal of the Electrochemical Society* **140** (3), 742–746 (1993).

[481] A. Jobert, P. Touzain and L. Bonnetain. *Carbon* **19** (3), 193–198 (1981).

[482] Y. Marcus. *Chemical Reviews* **88** (8), 1475–1498 (1988).

[483] H. Ohtaki and T. Radnai. *Chemical Reviews* **93** (3), 1157–1204 (1993).

[484] H. Ohtaki. *Monatshefte für Chemie* **132** (11), 1237–1268 (2001).

[485] Y. Liu, J. Xue, T. Zheng and J. Dahn. *Carbon* **34** (2), 193–200 (1996).

[486] W. Xing, J. X. T. Zheng, A. Gibaud and J. Dahn. *Journal of the Electrochemical Society* **143** (11), 3482–3491 (1996).

[487] J. Xue and J. Dahn. *Journal of the Electrochemical Society* **142** (11), 3668–3677 (1995).

[488] T. Zheng and J. Dahn. *Synthetic Metals* **73** (1), 1–7 (1995).

[489] T. Zheng, J. Reimers and J. Dahn. *Physical Review B* **51** (2), 734–741 (1995).

[490] J. Chmiola, G. Yushin, R. Dash and Y. Gogotsi. *Journal of Power Sources* **158** (1), 765–772 (2006).

[491] M. Endo, Y. Kim, H. Ohta, K. Ishii, T. Inoue, T. Hayashi, Y. Nishimura, T. Maeda and M. Dresselhaus. *Carbon* **40** (14), 2613–2626 (2002).

[492] T. Kim, C. Ham, C. K. Rhee, S.-H. Yoon, M. Tsuji and I. Mochida. *Electrochimica Acta* **53** (19), 5789–5795 (2008).

[493] H. Boehm and W. Scholz. *Justus Liebigs Annalen der Chemie* **691**, 1–8 (1966).

[494] S.-K. Jeong, M. Inaba, Y. Iriyama, T. Abe and Z. Ogumi. *Journal of Power Sources* **119-121**, 555–560 (2003).

[495] K. A. Hirasawa, T. Sato, H. Asahina, S. Yamaguchi and S. Mori. *Journal of the Electrochemical Society* **144** (4), L81–L84 (1997).

[496] D. Alliata, R. Kötz, P. Novák and H. Siegenthaler. *Electrochemistry Communications* **2** (6), 436–440 (2000).

[497] S.-K. Jeong, M. Inaba, T. Abe and Z. Ogumi. *Journal of the Electrochemical Society* **148** (9), A989–A993 (2001).

[498] M. Inaba, H. Tomiyasu, A. Tasaka, S.-K. Jeong and Z. Ogumi. *Langmuir* **20** (4), 1348–1355 (2004).

[499] H. Estrade-Szwarckopf and B. Rousseau. *Synthetic Metals* **23** (1-4), 191–198 (1988).

[500] S. Leroy, F. Blanchard, R. Dedryvère, H. Martinez, B. Carré, D. Lemordant and D. Gonbeau. *Surface and Interface Analysis* **37** (10), 773–781 (2005).

[501] L. E. Ouatani, R. Dedryvère, J.-B. Ledeuil, C. Siret, P. Biensan, J. Desbrières and D. Gonbeau. *Journal of Power Sources* **189**, 72–80 (2009).

[502] Y.-S. Lee. *Journal of Fluorine Chemistry* **128** (4), 392–403 (2007).

[503] J. Bisquert. *Electrochimica Acta* **47** (15), 2435–2449 (2002).

[504] J. Bisquert and V. S. Vikhrenko. *Electrochimica Acta* **47** (24), 3977–3988 (2002).

[505] A. Jänes and E. Lust. *Journal of the Electrochemical Society* **153** (1), A113–A116 (2006).

[506] T. Pajkossy. *Journal of Electroanalytical Chemistry* **364** (1-2), 111–125 (1994).

[507] D. Wheeler and S. Pepper. *Journal of Vacuum Science and Technology* **20** (2), 226–232 (1982).

[508] D. Clark and W. Brennan. *Journal of Electron Spectroscopy and Related Phenomena* **41** (3-4), 399–410 (1986).

[509] D. Clark, W. Feast, D. Kilcast and W. Musgrave. *Journal of Polymer Science A* **11** (2), 389–411 (1973).

[510] S. Tasker, R. Chambers and J. Badyal. *Journal of Physical Chemistry B* **98** (47), 12 442–12 446 (1994).

[511] M. Ue, K. Ida and S. Mori. *Journal of the Electrochemical Society* **141** (11), 2989–2996 (1994).

[512] M. Chandrasekaran, M. Noel and V. Krishnan. *Talanta* **37** (7), 695–699 (1990).

[513] V. Suryanarayanan, S. Yoshihara and T. Shirakashi. *Electrochimica Acta* **51** (5), 991–999 (2005).

[514] J. K. Foley, C. Korzeniewski and S. Pons. *Canadian Journal of Chemistry* **66** (1), 201–206 (1988).

[515] P. Krtil, L. Kavan and P. Novák. *Journal of the Electrochemical Society* **140** (12), 3390–3395 (1993).

[516] G. Tourillon, P.-C. Lacaze and J.-E. Dubois. *Journal Electroanalytical Chemistry* **100**, 247–262 (1979).

[517] G. Eggert and J. Heitbaum. *Electrochimica Acta* **31** (11), 1443–1448 (1986).

[518] P. Novák, P. Christensen, T. Iwasita and W. Vielstich. *Journal of Electroanalytical Chemistry* **263** (1), 37–48 (1989).

[519] M. Arulepp, J. Leis, M. Lätt, F. Miller, K. Rumma, E. Lust and A. Burke. *Journal of Power Sources* **162** (2), 1460–1466 (2006).

Abbreviations, symbols and constants

Abbreviations		
Abbreviation	Meaning	Reference
AFM	Atomic force microscopy	p. 84
AN	Acetonitrile	p. 40
BDDT	Brunauer, Deming, Deming and Teller	p. 133
BET	Brunauer, Emmett and Teller	p. 137
BJH	Barrett, Joyner and Halenda	p. 140
BWF	Breit-Wigner-Fano	p. 203
CAES	Compressed air energy storage	p. 7
CCD	Charge-coupled device	p. 149
CDE	Coulombic discharge efficiency	p. 38
CE	Counter (or auxiliary electrode)	p. 101
CMC	Carboxymethylcellulose	p. 85
CPE	Constant phase element	p. 317
CV	Cyclic voltammetry or voltammogram	p. 105
CVD	Chemical vapor deposition	p. 58
DA	Dubinin-Astakhov	p. 135
DC	Direct current	p. 155
DOS	Density of states	p. 29
DR	Dubinin-Radushkevich	p. 135
DTA	Differential thermal analysis	p. 250
EDLC	Electrochemical double layer capacitor	p. 3
EDR	Equivalent distributed resistance	p. 111
EIS	Electrochemical impedance spectroscopy	p. 88
EPDM	Ethylene propylene diene M-class rubber	p. 102
ESCA	Electron spectroscopy for chemical analysis	p. 152
ESR	Equivalent series resistance	p. 111
FWHM	Full width at half maximum	p. 97
GIC	Graphite intercalation compound	p. 66
GO	Graphite oxide	p. 236
HiPco	High-pressure decomposition of CO	p. 98
HOPG	Highly oriented pyrolytic graphite	p. 86
ICE	Internal combustion engine	p. 8
IHP	Inner Helmholtz plane	p. 26
IT	Information technology	p. viii
iTO	In-plane transverse optical	p. 143
IUPAC	International Union of Pure and Applied Chemistry	p. 21
LA	Longitudinal acoustic	p. 143
LCAO	Linear combination of atomic orbitals	p. 54
LIB	Lithium-ion battery	p. 40
LO	Longitudinal optical	p. 143
MWCNT	Multi-walled carbon nanotube	p. 58
NIST	National Institute of Standards and Technology	p. 154
NLDFT	Non-local density functional theory	p. 136
NMP	N-methyl-2-pyrrolidone	p. 96

Abbreviations (cont.)		
Abbreviation	Meaning	Reference
OHP	Outer Helmholtz plane	p. 26
OPA	Oriented polyamide	p. 125
oTA	Out-of-plane transverse acoustic	p. 143
oTO	Out-of-plane transverse optical	p. 143
PAN	Poly(acrylonitrile)	p. 77
PC	Propylene carbonate	p. 38
PE	Poly(ethylene)	p. 124
PEEK	Poly(aryletheretherketone)	p. 103
PFA	Poly(furfuryl alcohol)	p. 72
PTFE	Poly(tetrafluoroethylene)	p. 17
PVDC	Poly(vinylidene chloride)	p. 72
PVDF	Poly(vinylidene fluoride)	p. 96
pzc	Potential of zero charge	p. 34
QRE	Quasi-reference electrode	p. 104
RBM	Radial breathing mode	p. 99
RE	Reference electrode	p. 101
SAXS	Small-angle X-ray scattering	p. 121
SCE	Saturated calomel electrode	p. 174
SDS	Sodium dodecyl sulfate	p. 202
SEI	Solid electrolyte interphase	p. 41
SEM	Scanning electron microscopy	p. 90
SHE	Standard hydrogen electrode	p. 24
SLS	Swiss Light Source	p. 124
SMES	Superconducting magnetic energy storage	p. 8
SWCNT	Single-walled carbon nanotube	p. 58
TA	Transverse acoustic	p. 143
TEM	Transmission electron microscopy	p. 58
TG	Thermogravimetry	p. 250
TO	Transverse optical	p. 143
UHV	Ultra-high vacuum	p. 153
UPS	Uninterruptable power supply	p. 11
UV	Ultraviolet	p. 119
vHs	Van Hove singularity or singularities	p. 62
WAXS	Wide-angle X-ray scattering	p. 121
WE	Working (or indicator) electrode	p. 101
XPS	X-ray photoelectron spectroscopy	p. 84
XRD	X-ray diffraction	p. 121

	Symbols and units	
Symbol	Meaning	Units
A	(a) Area	m^2
	(b) Specific area	$m^2\,g^{-1}$
	(c) Molar work of adsorption	$J\,mol^{-1}$
	(d) Empirical RBM frequency parameter	$nm\,cm^{-1}$
	(e) SAXS fitting coefficient	a.u.
A_{BET}	BET surface area	$m^2\,g^{-1}$
A_{NLDFT}	NLDFT surface area	$m^2\,g^{-1}$
a	Debye correlation length	m
$\boldsymbol{a_1, a_2}$	Graphene lattice vectors	m
a_i	Activity of species i	–
a_{Ox}	Activity of oxidized species	–
a_{Red}	Activity of reduced species	–
B	(a) FWHM of diffraction peak	rad
	(b) Empirical RBM frequency parameter	cm^{-1}
	(c) SAXS fitting coefficient	a.u.
$\boldsymbol{b_1, b_2}$	Reciprocal graphene lattice vectors	m^{-1}
C	(a) Capacitance	F
	(b) BET constant	–
C_H	Capacitance of the Helmholtz layer	$F\,m^{-2}$
C_S	Specific capacitance	$F\,m^{-2}$
C_{SC}	Capacitance of the space charge layer	$F\,m^{-2}$
$C_{SC,M}$	Capacitance of the space charge layer for a metallic electrode	$F\,m^{-2}$
$C_{SC,S}$	Capacitance of the space charge layer for a semi-conducting electrode	$F\,m^{-2}$
C_c	Capacitance of current collector	F
C_{cell}	Cell capacitance	F
C_d	Capacitance of the diffuse layer	$F\,m^{-2}$
$\boldsymbol{C_h}$	Chiral vector	m
C_{neg}	Capacitance of the negative electrode	F
C_{pore}	Capacitance of a single pore	F
C_{pos}	Capacitance of the positive electrode	F
C_{single}	Single electrode capacitance	F
c	(a) Langmuir constant	–
	(b) Volume fraction	–
c_A	Volume fraction in two-phase system A	–
c_B	Volume fraction in two-phase system B	–
c_{Ox}	Concentration of oxidized species	$mol\,L^{-1}$
c_{Red}	Concentration of reduced species	$mol\,L^{-1}$
D	(a) Density of electronic states	$eV^{-1}\,cm^{-3}$
	(b) Fractal dimension	–
DN	Solvent donicity	$kcal\,mol^{-1}$
d	(a) Distance	m
	(b) Bragg spacing	m
d_{001}	(a) Interlayer spacing of turbostratic planes	m
	(b) Bragg spacing of 0 0 1 diffraction peak	m

Symbol	Meaning	Units
d_{002}	Interlayer spacing of graphite	m
d_1	Repeat distance of stage 1 GIC	m
d_{C-C}	C−C bond length	m
d_H	Helmholtz layer thickness	m
d_g	Distance between two adjacent layers of graphene in GICs	m
d_i	Distance between two successive layers of intercalate in GICs	m
d_{slit}	Width of slit pore	m
d_t	SWCNT diameter	m
E	(a) Electrode potential	V
	(b) Potential	V
E_0	(a) Characteristic energy of adsorption	J mol^{-1}
	(b) Potential at bottom of pore	V
E^0	Standard electrode potential	V
$E^{0\prime}$	Formal electrode potential	V
$E_{1/2}$	Half-wave potential	V
E_B	Electron binding energy	eV
E_{hf}	Half-filling potential	V
$E_{ii}^{M,S}$	SWCNT electronic transition energy	eV
E_{im}	Immersion potential	V
E_{kin}	Kinetic energy of photoelectrons	eV
E_{laser}	Laser energy	eV
E_{neg}	Potential of the negative electrode	V
$E_{p,a}$	Potential of peak anodic current	V
$E_{p,c}$	Potential of peak cathodic current	V
E_{pos}	Potential of the positive electrode	V
E_T	Solvent polarity	kcal mol^{-1}
F	Force	N
f	(a) Frequency	Hz
	(b) Normalized pore size distribution	m^{-1}
	(c) Fermi-Dirac distribution	–
h	Height	m
h_0	Initial height	m
$h\,k\,l$	Miller indices	–
I	Current	A
I_0	Current amplitude	A
I_D	D band intensity	a.u.
I_G	G band intensity	a.u.
I_e	Intensity of X-rays scattered by one electron	a.u.
i	Intensity of scattered X-rays	a.u.
i_{fl}	Scattered intensity fluctuation due to inhomogeneous electron density in space	a.u.
j	(a) Current density	A m^{-2}
	(b) Integer	–
K	Shape factor	–

	Symbols and units (cont.)	
Symbol	Meaning	Units
K_{sp}	Solubility product	$mol^2\,L^{-2}$
k	(a) Order of diffraction peak	–
	(b) Wavenumber	m^{-1}
$\boldsymbol{k}$	Wave vector	m^{-1}
k_{gr}	Order of GIC diffraction peak closest to 002 peak of graphite	–
L_a	Length scale of in-plane order	m
L_c	Length scale of stacking order	m
L_D	Debye length	m
L_{TF}	Thomas-Fermi screening length	m
l	Pore depth	m
M_W	Molecular mass	$g\,mol^{-1}$
m	(a) Mass	g
	(b) SWCNT chiral index	–
m_{single}	Active mass of single electrode	g
N	Whole number	–
N_S	Single pore isotherm (NLDFT)	$m^3\,g^{-1}$
N_{exp}	Experimental isotherm	$m^3\,g^{-1}$
n	(a) Charge carrier density	m^{-3}
	(b) Positive number	–
	(c) SWCNT chiral index	–
	(d) SAXS scattering exponent	–
	(e) Number of mols of adsorbed gas	–
	(f) DA exponent	–
	(g) Stage index of GIC	–
n^+	Number concentration of cations	m^{-3}
n^-	Number concentration of anions	m^{-3}
$n_1,\,n_2$	SAXS scattering exponents	–
n_{Av}	Average electron density	m^{-3}
n_e	Electron density	m^{-3}
$\Delta n_{e,A}$	Electron density contrast in two-phase system A	m^{-3}
$\Delta n_{e,B}$	Electron density contrast in two-phase system B	m^{-3}
n_i	Number concentration of species i	m^{-3}
n_i^0	Bulk number concentration of species i	m^{-3}
n_m	Number of mols in one monolayer	–
P_L	Power at load	W
P_S	Power at source	W
P_{max}	Power at matched impedance	W
p	Pressure	Pa
p^0	Saturation vapor pressure	Pa
Q	Charge	C
Q_{irr}	Irreversibly consumed charge	C
Q_{rev}	Reversible charge	C
q	(a) Charge per charge carrier	C

Symbol	Meaning	Units
	(b) Momentum transfer	m^{-1}
	(c) Bjerrum critical distance	m
$\boldsymbol{q}$	Phonon wavevector	m^{-1}
R	Resistance	Ω
R'	Resistance per unit pore length	$\Omega\,m^{-1}$
R_L	Load resistance	Ω
R_S	Internal resistance of source	Ω
R_c	Contact resistance	Ω
R_{cell}	Cell resistance	Ω
R_e	Electrolyte resistance	Ω
R_g	Radius of gyration	m
R_{neg}	Resistance at negative electrode	Ω
R_P	Parallel resistance	Ω
R_{pore}	Resistance of a single pore	Ω
R_{pos}	Resistance at positive electrode	Ω
R_s	Series resistance	Ω
r	(a) Pore radius	m
	(b) Distance	m
	(c) Effective ion radius	m
r_1, r_2	Characteristic radii of liquid meniscus	m
r_{cyl}	Radius of cylindrical pore	m
r_i	Effektive radius of species i	m
r_K	Kelvin radius	m
S	Interfacial area determined by SAXS	a.u.
S_A	Interfacial area of two-phase system A	a.u.
S_B	Interfacial area of two-phase system B	a.u.
$\boldsymbol{s}$	Scattering vector	–
T	Temperature	K
$\boldsymbol{T}$	SWCNT unit cell vector	m
t	(a) Time	s
	(b) Thickness	m
	(c) Crystallite size	m
U	Voltage	V
U_0	Voltage amplitude	V
U_{nom}	Nominal voltage	V
V	(a) Volume	m^3
	(b) Potential energy	J
V_L	Molar volume of adsorbate gas	$m^3\,mol^{-1}$
V_{NLDFT}	NLDFT pore volume	$cm^3\,g^{-1}$
$V_{mi,DA}$	DA micropore volume	$cm^3\,g^{-1}$
$V_{mi,NLDFT}$	NLDFT micropore volume	$cm^3\,g^{-1}$
v	Drift velocity	$m\,s^{-1}$
v_{max}	Terminal velocity	$m\,s^{-1}$
v_{max}^+	Terminal velocity of cations	$m\,s^{-1}$
v_{max}^-	Terminal velocity of anions	$m\,s^{-1}$
W	(a) Energy	J

	Symbols and units (cont.)	
Symbol	Meaning	Units
	(b) Filled micropore volume	m^3
W_0	Total micropore volume	m^3
W_{nom}	Energy at nominal voltage	J
w	Pore width	m
w_{max}	Maximum pore width	m
w_{min}	Minimum pore width	m
X_C	Capacitive reactance	Ω
x	(a) Distance coordinate	m
	(b) Interlayer expansion ratio for GICs	–
Z	(a) Atomic number	–
	(b) Impedance	Ω
Z'	Impedance per unit pore length	$\Omega\,m^{-1}$
Z_{Im}	Imaginary impedance	Ω
Z_{Re}	Real impedance	Ω
Z_n	Impedance of n pores	Ω
Z_{pore}	Impedance of a single pore	Ω
z	Valency	–
z^+	Valency of cation	–
z^-	Valency of anion	–
z_i	Valency of species i	–
β	Adsorbate affinity coefficient	–
γ	(a) Correlation function	–
	(b) Surface tension	$N\,m^{-1}$
γ_0	C$-$C overlap integral	eV
$\mathcal{E}$	Electric field	$V\,m^{-1}$
$\mathcal{E}_H$	Electric field in the Helmholtz layer	$V\,m^{-1}$
ϵ	Relative permittivity	–
ϵ_H	Relative permittivity of the Helmholtz layer	–
$\epsilon_{SC,M}$	Relative permittivity of the space charge layer for a metallic electrode	–
$\epsilon_{SC,S}$	Relative permittivity of the space charge layer for a semi-conducting electrode	–
ϵ_d	Relative permittivity of the diffuse layer	–
ε	Electron energy	eV
ε_F	Fermi level	eV
ε_{hf}	Half-filling energy	eV
ε_{vac}	Vacuum level	eV
ζ_W	Energetic efficiency	–
η	(a) Dynamic viscosity	Pa s
	(b) Local variations in the average electron density	m^{-3}
η_A	Electron density at point A	m^{-3}
η_B	Electron density at point B	m^{-3}
θ	(a) SWCNT chiral angle	°
	(b) Scattering angle	°
λ	(a) Penetration depth	m

	Constants		
Symbol	Description	Value	Units
e	Elementary charge	$1.60 \cdot 10^{-19}$	C
ϵ_0	Permittivity of vacuum	$8.85 \cdot 10^{-12}$	$F\,m^{-1}$
F	Faraday constant	$96\,485$	$C\,mol^{-1}$
h	Planck constant	$6.63 \cdot 10^{-34}$	$J\,s$
$\hbar$	Reduced Planck constant	$1.05 \cdot 10^{-34}$	$J\,s$
k_B	Boltzmann constant	$1.38 \cdot 10^{-23}$	$J\,K^{-1}$
N_A	Avogadro constant	$6.02 \cdot 10^{23}$	mol^{-1}
R	Universal gas constant	8.314	$J\,K^{-1}\,mol^{-1}$

List of publications

R. Kötz, P.W. Ruch and Dario Cericola. Aging and failure mode of electrochemical double layer capacitors during accelerated constant load tests. *Journal of Power Sources* **195** (3), 923–928 (2009).

J.L. Gómez Cámer, J. Morales, L. Sánchez, P. Ruch, S.H. Ng, R. Kötz and P. Novák. Nanosized Si/cellulose fiber/carbon composites as high capacity anodes for lithium-ion batteries: a galvanostatic and dilatometric study. *Electrochimica Acta* **54** (26), 6713–6717 (2009).

P.W. Ruch, R. Kötz and A. Wokaun. Electrochemical characterization of single-walled carbon nanotubes for electrochemical double layer capacitors using non-aqueous electrolyte. *Electrochimica Acta* **54** (19), 4451–4458 (2009).

P.W. Ruch, L.J. Hardwick, M. Hahn, A. Foelske, R. Kötz and A. Wokaun. Electrochemical doping of single-walled carbon nanotubes in double layer capacitors studied by in situ Raman spectroscopy. *Carbon* **47** (1), 38–52 (2009).

R. Kötz, M. Hahn, P. Ruch and R. Gallay. Comparison of pressure evolution in supercapacitor devices using different aprotic solvents. *Electrochemistry Communications* **10** (3), 359–362 (2008).

L.J. Hardwick, P.W. Ruch, M. Hahn, W. Scheifele, R. Kötz and Petr Novák. *In situ* Raman spectroscopy of insertion electrodes for lithium-ion batteries and supercapacitors: first cycle effects. *Journal of Physics and Chemistry of Solids* **69** (5–6), 1232–1237 (2008).

M. Hahn, H. Buqa, P.W. Ruch, D. Goers, M.E. Spahr, J. Ufheil, P. Novák and R. Kötz. A dilatometric study of lithium intercalation into powder-type graphite electrodes. *Electrochemical and Solid-State Letters* **11** (9), A151–A154 (2008).

P.W. Ruch, M. Hahn, F. Rosciano, M. Holzapfel, H. Kaiser, W. Scheifele, B. Schmitt, P. Novák, R. Kötz and A. Wokaun. *In situ* X-ray diffraction of the intercalation of $(C_2H_5)_4N^+$ and BF_4^- into graphite from acetonitrile and propylene carbonate based supercapacitor electrolytes. *Electrochimica Acta* **53** (3), 1074–1082 (2007).

F. Rosciano, M. Holzapfel, H. Kaiser, W. Scheifele, P. Ruch, M. Hahn, R. Kötz and Petr Novák. A multi-sample automatic system of *in situ* electrochemical

X-ray diffraction synchrotron measurements. *Journal of Synchrotron Radiation* **14** (6), 487–491 (2007).

R. Kötz, J.-C. Sauter, P. Ruch, P. Dietrich, F.N. Büchi, P.A. Magne and P. Varenne. Voltage balancing: long-term experience with the 250 V supercapacitor module of the hybrid fuel cell vehicle HY-LIGHT. *Journal of Power Sources* **174** (1), 264–271 (2007).

P.W. Ruch, O. Beffort, S. Kleiner, L. Weber and P.J. Uggowitzer. Selective interfacial bonding in Al(Si)-diamond composites and its effect on thermal conductivity. *Composites Science and Technology* **66** (15), 2677–2685 (2006).

S. Kleiner, F.A. Khalid, P.W. Ruch, S. Meier and O. Beffort. Effect of diamond crystallographic orientation on dissolution and carbide formation in contact with liquid aliminium. *Scripta Materialia* **55** (4), 291–294 (2006).

L.J. Hardwick, M. Hahn, P. Ruch, M. Holzapfel, W. Scheifele, H. Buqa, F. Krumeich, P. Novák and R. Kötz. An in situ Raman study of the intercalation of supercapacitor-type electrolyte into microcrystalline graphite. *Electrochimica Acta* **52** (2), 675–680 (2006).

F.P. Campana, M. Hahn, A. Foelske, P. Ruch, R. Kötz and Siegenthaler, H. Intercalation into and film formation on pyrolytic graphite in a supercapacitor-type electrolyte $(C_2H_5)_4NBF_4$/propylene carbonate. *Electrochemistry Communications* **8** (8), 1363–1368 (2006).

O. Beffort, F.A. Khalid, L. Weber, P. Ruch, U.E. Klotz, S. Meier and S. Kleiner. Interface formation in infiltrated Al(Si)/diamond composites. *Diamond and Related Materials* **15** (9), 1250–1260 (2006).

D.R. McKenzie, K. Newton-McGee, P. Ruch, M.M. Bilek and B.K. Gan. Modification of polymers by plasma-based ion implantation for biomedical applications. *Surface and Coatings Technology* **186** (1–2), 239–244 (2004).

M.M.M. Bilek, D.R. McKenzie, R.N. Tarrant, T.W.H. Oates, P. Ruch, K. Newton-McGee, Yang Shi, D. Tompsett, H.C. Nguyen, B.K. Gan and D.T. Kwok. Practical plasma immersion ion implantation for stress regulation and treatment of insulators. *Contributions to Plasma Physics* **44** (5–6), 465–471 (2004).

List of selected presentations

P. Ruch, D. Cericola, A. Foelske and R. Kötz. Electrochemical in situ studies of supercapacitor electrodes—comparing activated carbon, single-walled carbon nanotubes and graphite.
Electrochemistry: Crossing Boundaries (German Chemical Society), Giessen, Germany, October 6–8 (2008)

P. Ruch, D. Cericola, A. Foelske and R. Kötz. In situ studies of single-walled carbon nanotubes and activated carbon in nonaqueous supercapacitor electrolytes.
59th Annual Meeting of the International Society of Electrochemistry, Seville, Spain, September 7–12 (2008)

P. Ruch, M. Hahn, A. Foelske and R. Kötz. In situ Raman spectroscopy and electrochemical dilatometry of sp^2-hybridized carbons during charging in supercapacitors.
Annual Meeting of the German Chemical Society (Wissenschaftsforum 2007), Ulm, Germany, September 16–19 (2007)

P. Ruch, M. Hahn and R. Kötz. The increase of supercapacitor energy density by utilizing insertion type reactions.
Carbon for Energy Storage and Environment Protection 2007, Krakow, Poland, September 2–6 (2007)

P. Ruch, L. Hardwick, M. Hahn, O. Barbieri, A. Foelske, P. Novák, R. Kötz and A. Wokaun. In situ Raman and X-ray diffraction studies of carbons for supercapacitors.
57th Annual Meeting of the International Society of Electrochemistry, Edinburgh, UK, August 26–September 6 (2006)

Curriculum vitae

Name	Patrick Wolfgang Ruch
Date of birth	17 March 1981
Place of birth	Atlanta, GA, USA
Nationality	Germany / USA

Primary schools	Local schools in Norway and Denmark (1987–1995)
Secondary school	British School of Paris, France (1995–1999)
Higher education	ETH Zurich, Switzerland (1999–2005)
	2005 M.Sc. in Materials Science
	Paul Scherrer Institut, Switzerland (2005–2009)
	2009 Dr. sc. ETH Zurich
Other studies	Visiting student, University of Sydney, Australia (2003)